Design and Analysis of Smart Building Envelope Materials and Systems

Qiliang Lin

Submitted in partial fulfillment of the
requirements for the degree of
Doctor of Philosophy
under the Executive Committee
of the Graduate School of Arts and Sciences

COLUMBIA UNIVERSITY

2020

Abstract

Design and Analysis of Smart Building Envelope Materials and Systems

Qiliang Lin

As the largest consumer of electricity, the buildings sector accounts for about 76% of electricity use and 40% of all U.S. primary energy use and associated greenhouse gas (GHG) emissions. Research shows that a potential energy saving of 34.78% could be achieved by the smart buildings comparing to conventional buildings. Therefore, a smart management of building sectors becomes significantly important to achieve the optimal interior comfort with minimal energy expenditure. The ability of adaptation to the dynamic environments is considered the central aspect in smart building systems, which can be segmented into the passive adaptation and the active adaptation. The passive adaptation refers to the designs that do not change with the dynamic environment but improve the building overall performance by the integration of originally separated components, or by the application of advanced engineering materials. The active adaptation refers to the building management system (BMS) that actively responds and evolves with the changing environment, through the continuous monitoring of the surroundings via the sensor network, and the smart response through the controlling algorithms in the central controlling unit.

This Ph.D. dissertation focuses on developing materials and systems for the smart building envelope, including a photovoltaic integrated roof with passive adaptation, and self-powered

window systems with active responses environment. As the skin of a building, the building envelope provides the first level resistance towards air, water, heat, light and noise, which makes it the ideal target for the passive adaptation to the environments, as well as the perfect sensing location in the building management system for the active adaptation.

This dissertation starts with a discussion of the building integrated photovoltaic thermal (BIPVT) roofing panel, including the fabrication, performance demonstration, and micromechanics-based theoretical modeling. The panel is structurally supported by a functionally graded material (FGM) panel made with high-density polyethylene as the matrix and aluminum particles as reinforcement. It prevents the heat from entering the building and directs the heat to the water tubes embedded inside the panel for the thermal energy harvesting, such that the overall energy efficiency is significantly improved. The design, fabrication and performance of the system is discussed, and an innovative non-destructive analysis method is developed to captures the authentic particle distribution of the FGM.

As the main structural component, functionally graded material is comprehensively tested and modeled in elastic, thermoelastic, elastoplastic, and thermo-elastoplastic performance, based on the equivalent inclusion based method. An ensemble average approach was used to convert the particles' interaction in the microscope to the averaged relation in the macroscope, such that both particle to matrix influence and particle to particle pair-wise interactions are characterized. The idea of the equivalent inclusion method extends to the plastic modeling of the FGM, by formulating an ensemble average form of the matrix stress norm in the macroscale that incorporate the local disturbance of particle reinforcement in the microscale. The accuracy of the proposed algorithm is verified and validated by comparing with another theory in homogeneous composite and experiments, respectively. To the best of the author's knowledge, no prior theoretical algorithm

has been proposed for the elastoplastic modeling of functionally graded materials. Therefore, the proposed algorithm can be used as a foundation and reference for further investigation and industry prediction of graded composites.

Based on the theoretical modeling of the mechanical properties, a high order plate theory is also proposed in this dissertation to study for the thermo-mechanical performance of the FGM panel, to provide structural design guideline for the BIPVT panels. The shearing and bending behaviors are decomposed, solved independently, and combined to formulate the final solution. The shear strain components are assumed to follow a parabolic variation across the thickness, while the bending components follow the solution from classical plate theory. Closed-form solutions for the circular panel under different loadings are provided, with verification by comparing to other models and validation to experiments.

Two smart window systems are proposed and demonstrated in this dissertation to actively monitor the building environment with active responses, and energy harvesting techniques are investigated to harvest energy from ambient environment the eternal power supply to the system. The thermoelectric powered wireless sensor network (TPWSN) platform is first demonstrated and discussed, where the energy is harvested from the temperature difference across the window frame. The TPWSN sits completely inside the window/façade frame with no compromise of the outlook and continuously monitors the building environment for the optimal control of the building energy consumption and indoor comfort. The energy harvesting technique grants eternal battery lifetime and significantly simplifies the installation and maintenance of the system with considerable saving of time and cost. In addition, the platform provides energy to various types of sensors for different kinds of sensing needs and store the data to the Google cloud for permanent storage and advanced analytics.

The thermoelectric powered system works well for the sensors and microcontrollers but fails to provide enough power to the actuators. A novel sun-powered smart window blinds (SPSWB) system is designed, prototyped, and tested in this dissertation with solar energy harvesting on window blinds which provides enough power for the actuators. The thin-film photovoltaic cells are attached on one side of slats for energy harvesting and a PVdF-HFP coating is attached on the other side for the passive cooling. The voltage regulation and battery management systems are designed and tested, where a stable 55% energy efficiency from the PV into the battery has been achieved. The automatic control of the window blinds is accomplished with the help of sensors and a microcontroller. The energy equilibrium analysis is proposed and demonstrated with the local solar data to incorporate the influence of local weather conditions and solar zenith angle, from which we demonstrated that much more power than needed can be harvested. The abundant energy harvested validates the feasibility and the robustness of the system and proves its wide application potentials to various sensors and applications.

In conclusion, both passive and active adaptations to the environment are investigated to build up the next generation of smart building envelope systems. The building integrated photovoltaic thermal roof is designed, fabricated, tested, and modeled in detail, which provides structural support to the external loads and improves the energy efficiency of buildings. The smart window/façade systems serve as a platform for various sensors and actuators via the energy harvesting from the ambient environment, and could significantly improve the energy expenditure with minimal impact of internal comfort.

Table of Contents

List of Figures

List of Tables

ACKNOWLEDGEMENTS

I am sincerely grateful to my advisor, Professor Huiming Yin, for the valuable support he had given to me throughout my Ph.D. study and research. I am sure this dissertation would never have been accomplished without his help. It is my great pleasure to be his students at Columbia University.

Besides my advisor, I would like to thank the rest of my dissertation committee, Professor Haim Waisman, Professor Shiho Kawashima, Professor Arvind Narayanaswamy of Columbia University, and Dr. Tejav DeGanyar from Schuco Virtual Construction Lab for taking their valuable time to participate my defense, and to read and comment on this dissertation.

My sincere thanks also go to Dr. Tejav DeGanyar for offering me the internship opportunities in the Schuco Virtual Construction Lab and his continuously patient guidance to my professional development.

Over the past five years at Columbia University, I have received support from a great number of individuals. I am grateful to my colleagues Dr. Fangliang Chen, Dr. Liangliang Zhang, Dr. Siyu Zhu, Dr. Liming Li, Dr. Xiaokong Yu, Dr. Xin He, Dr. Gan Song, Dr. Liang Wang, Dr. Junhui Lou, Dr. Zhenhua Wei, Mr. Zhenyu Shou, Mr. Tengxiang Wang, Mr. Chunlin Wu, Mr. Mehdi Zadshir, and Mr. Yanchu Zhang at Columbia University, and Professor Yi-Chung Chen from Tennessee State University, who helped me in both my research and daily life.

I also would like to dedicate this dissertation to my girlfriend Yeqing Xia. Thank you for your continuously love, patience and support throughout my Ph.D. study. No matter what happens in the future, your love is the driving source to make me move forward bravely.

Last but never the least, I want to thank my parents, my father Jianyun Lin and my mother Xiuying Lin, for their endless love, support and encouragement, without which I'd never be the person I am today.

Chapter 1 Introduction

1.1 Modern building envelope systems

In the past decades, a grand challenge that has been emerging in energy system is to simultaneously address the nation's most fundamental need -- energy security, economic competitiveness, environmental responsibility, as well as smart serviceability and workability [1]. As the largest consumer of electricity, the buildings sector accounts for about 76% of electricity use and 40% of all U.S. primary energy use and associated greenhouse gas (GHG) emissions [2]. Globally, about 30% of total energy and 60% of electricity are consumed on buildings [3]. The major areas of energy consumption in buildings are heating, ventilation, air conditioning, lighting, and other appliances, such as water heating, refrigerators, dryers, etc [4]. The share of electricity use in building sectors has grown dramatically in the past five decades from 25% of U.S. annual electricity consumption in the 1950s to the 40% in the early 1970s, and to more than 76% by this decade [5]. Therefore, a smart management of building sectors becomes significantly important to achieve the optimal interior comfort with minimal energy expenditure, which makes it necessary to revisit the way how the building envelope components and the building management systems are designed and developed.

The concept of the smart building emerged at the beginning of 1980s and has been continuously evolving during the past decades [6]–[8], where the ability of adaptation to the dynamic environments is considered as the central aspect in its definition [9]. Research shows that a potential energy saving of 34.78% could be achieved by the smart buildings comparing to conventional buildings, through the optimal control of the major building components [10]. The smart building has attracted significant attention in the civil engineering industry during the recent

decade. The topics of recent research and development can be segmented into the passive adaptation and the active adaptation. The passive adaptation refers to the designs that do not change with the dynamic environment but improve the building overall performance by the deep integration of originally separated components, or by the application of advanced engineering materials. The active adaptation refers to the building management system (BMS) that actively responds and evolves with the changing environment, through the continuous monitoring of the surroundings via the sensor network, and the smart response through the controlling algorithms in the central controlling unit. In both active and passive adaptation, the building envelope can play an important role for keeping the building smart. It is like the skin of a building and provide the first level resistance towards air, water, heat, light and noise, which makes it the ideal target for the passive adaptation to the environments, as well as the perfect sensing location in the building management system for the active adaptation. Therefore, the smart building envelope design and development plays an important role for the next generation of smart building and smart city development.

The majority of the research and development of the passive adaptation for smart buildings were carried out by incorporating advanced materials and composite structures in the building envelope. Unlike the structural components, such as columns and beams, providing structural resistance towards external loading, the building envelope refers to the peripheral physical separators between the indoor and outdoor environments, such as the roof, walls, window and façade. Roofs are a critical part and account for the majority amounts of heat gain/loss of the building envelopes with large roof area such as low-rise buildings, auditoriums and sports complexes etc., thereby, influencing the indoor comfort for the occupants. In the past decades, different cooling techniques have been investigated and implemented for the better temperature control and energy

performance, which includes but not limited to the cellular layout for the minimum solar exposure [11], natural or mechanical roof ventilation [12], the vegetation roof cover for humidity and shade [13], [14], advanced coating for solar reflectance and thermal emissivity [15], [16], the phase change materials (PCM) with high thermal capacity [17]–[20], and the building integrated photovoltaic/thermal (BIPVT) roofing panels [21]–[25]. Among them the investigation of PCM and BIPVT for roof application have attracted a lot of research interest during the recent years. The PCM leverages the high latent heat during the phase change process to store the excessive heat and to release when it is needed, for a more stabilized temperature distribution over a time cycle. The BIPVT takes advantage of the additional thermal energy absorbed by the photovoltaic cells and converts it into usable form such as the hot/warm water or air. Similar to roof, walls are a predominant fraction of a building envelope and are expected to provide thermal comfort for the building. The thermal resistance of wall, which is usually quantified by the R-value, is a crucial factor to the energy consumption of a building, especially for high rise buildings where the wall takes the majority of building envelope surface. Apart from the traditional solid walls, recent innovative wall designs mainly focus on the composite design with multiple layers for specific functionalities. The solar wall was proposed with multiple layers to better utilize the solar energy for room heating [26], [27]. The lightweight concrete wall with miniscule air bubbles generated by aluminum powder was tested to have superior thermal resistance for the heat prevention [28]–[30]. The phase change material is also involved in some designs with porous concrete to store excessive heat and stabilize the temperature [31]–[33]. The double skin wall/façade utilizes an air gap to enhance passive cooling of buildings [34]–[36]. The natural or mechanical ventilation is used to circulate the air flow inside the cavity to take away the unwanted heat. Usually glass, rather than concrete, is involved in the double skin façade, therefore making it similar to the window

system. The openings, majorly windows, of buildings also have a vital role in providing optimum thermal comfort and illumination levels. They are important from an architectural standpoint by adding aesthetics to the design. The study for window system focuses on the glazing, aiming to provide the high-performance insulation, solar gain, daylighting or a combination. Double glazing or multiple glazing systems are applied in the market to provide good sound and thermal insulation [37]. Advanced coatings have been investigated to either increase the transparency or reflection [38]–[41]. The space between multiple glazing layers is usually vacuumed. In some application, suspended particle devices film has been placed between two glass panes, to control transparency by adjusting the applied voltage [42]–[44]. As for the window frame, the research is much less active than the glazing. The rule of thumb is to choose one with low conductance to minimize the thermal bridging and infiltration losses [11].

The building envelope is the perfect location for the sensing and monitoring of the surroundings and is therefore also important for the active adaptation to the dynamic environment, by contributing to the building management system. The building management system (BMS), also known as building automation system (BAS), refers to an active computer-based control in the building that monitors and manipulates mechanical and electrical equipment such as heating, ventilation and air conditioning. The BMS functions like the brain of a building, collecting sensed data of the surroundings and reacting for the most comfort and energy efficient environment. It is further segmented into the sensor network (hardware), which is usually deployed on the building envelopes, and the controlling algorithms (software) implemented within the central controlling unit. Significant attentions were paid to the controlling algorithms thanks to the recent boom of the artificial intelligence, with a lot of discussions about the energy consumption forecast [45]–[47], the smart grid technology [48], and the in-room occupancy detection [49]. The importance

of the sensor network was relatively underestimated with fewer researches and discussions. Traditional systems rely heavily on wired sensors to monitor the environment, which comes with substantial costs of manpower and time during both installation and maintenance. Thanks to the recent developments of wireless communication technology, the concept of wireless sensor network (WSN) becomes more and more popular in the BMSs with many advantages, including cost elimination of hard-wiring, enhanced flexibility in or dangerous areas, ease of installation and reduced maintenance costs of sensor deployments [50]. The main challenge of the WSN is how to maximize the lifetime of a node with a limited-sized battery, for the energy consumption of data acquisition, processing, and wireless communication [51]. For some applications in the building environment, it could be very hard to reach the WSN node for the battery replacement, which means it is not only for energy costs but also for the enormous scale of maintenance expenses. The energy harvesting technologies provide a good solution to elongate the battery lifetime and reduce the maintenance cost of the WSN. Energy harvesting technologies use power generating elements such as solar cells [52]–[54], piezoelectric elements [55]–[57], and thermoelectric elements [58]–[60] to convert light, vibration, and heat energy into electricity. The building envelope, as the barrier between the interior and the exterior of a building, features considerably exposure to the interior and exterior of buildings and is therefore crucial to the energy harvesting applications to solve the energy problem in the smart building design [61].

In conclusion, the building envelope plays an important role in the smart building management for a better energy efficiency of the building sector. Advanced materials and novel structures in the building envelope have been designed for the passive adaptation to the environment, where the phase change materials and the building integrated structures made of composite materials have been widely investigated. In terms of active adaptation, the building envelope is also perfect place

for the implementation of wireless sensor nodes, where the energy supply is the bottle neck for the long-term application. The energy harvesting techniques provide a solution to the limited battery life and deserve a wider investigation.

1.2 Composite materials and applications in building envelope

Many modern technologies require materials with special combination of properties that cannot be met by conventional materials. They will usually refer to composite materials for the tailored and outstanding performance in a specific area. This is especially true for materials that are needed for aerospace, robotics, transportation and civil application. In the recent decades, a lot of researches and applications of composite materials to the building envelope design have been observed, specifically they can increase the building's passive adaptivity to the dynamic environment, and thus increase the overall energy efficiency without compromising the interior comfort.

Composite is a type of material consisted of two or more separate components with significantly different physical or chemical properties, so that when combined their overall performance can be remarkably improved compared to each individual phase along in both mechanical and economic aspects. Most composites are made of two components, with one of them being the matrix or binder to surrounds and binds together the other reinforcing component. One of the earliest applications of composite is the brick made of mud and straw many thousand years ago. The mud with a strong compression strength is reinforced with straw for its weak tensile performance, so that the bricks would be resistance to both squeezing and tearing and make excellent building blocks. Similar idea is applied to the modern building techniques by placing metal rods or wires into the concrete for the reinforcement of its weak tensile strength. There are many types of

composite. As is shown in Figure 1, one simple scheme of classification is through their form of reinforcement [62]–[65], into the following three categories: 1. Structural composites; 2. Fiber reinforced polymer composite, and; 3. Particle reinforced composite.

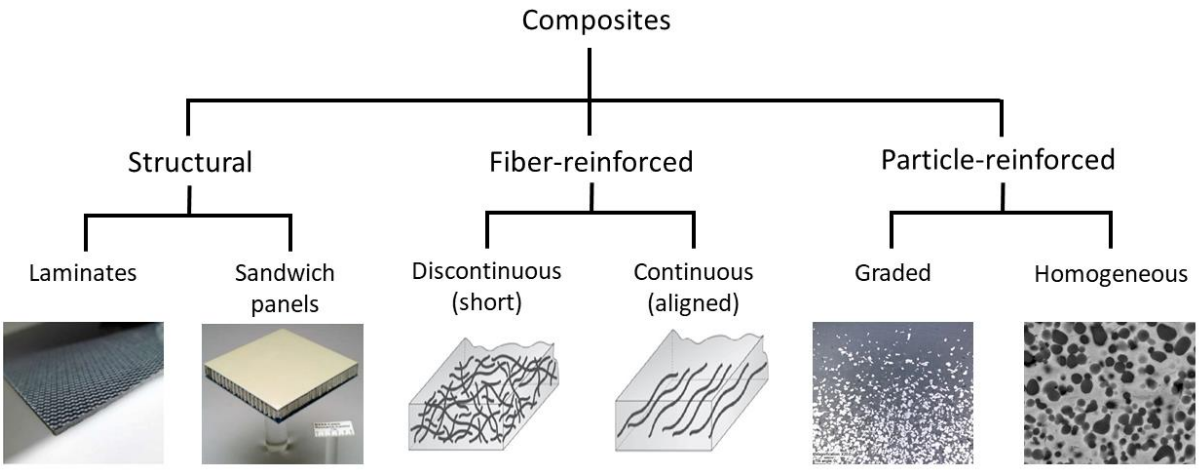

Figure 1 Classification of composite materials

The structural composite refers to the material combination from structural level and can be further divided into laminate composite and sandwich composite. Laminate composite is an assembly of layers of fibrous materials to provide strong in-plane stiffness. Each individual layer is generally orthotropic, but the whole laminate can exhibit anisotropic, orthotropic or quasi-isotropic properties depending on engineering requirements. The sandwich-structured composite is usually fabricated by attaching two thin but stiff skins to a lightweight but thick core, with the thick core providing enough moment distance for bending resistance. The skins are usually made with laminate composites to provide strong in-plane strength. Wide applications of laminated and sandwiched composites have been investigated and developed in the building envelope [66], especially to the roof and wall structure, for the energy efficiency enhancement [67]–[69] and the fire resistance improvement [70], [71]. Since the structural composites are usually attached from structural perspectives, the connections between components are usually the weak places and will

easily trigger stress concentration, delamination and structural failure. Such problems can be alleviated by the material combination from a smaller scale, with the help from the fiber reinforced polymer composites and particle reinforced composites.

Fiber reinforced polymer composite (FRPC) is a commonly used composite made of polymer matrix and fibers reinforcement. The polymer usually includes epoxy, vinyl ester or polyester thermosetting plastic, while the reinforcement usually includes graphite, glass fiber, boron, or silicon carbide. Unlike the laminated structure, the FRPC refers to distributed fibers inside the matrix rather than a layer. The idea behind FRPC is to increase the strength of the material in certain directions, so that the composite is highly tailored towards a specific stress configuration. By arranging the direction appropriately, the fiber reinforced composites can achieve both high in-plane stiffness, out-of-plane bending strength and excellent strength-weight ratio. The fiber-reinforced concrete has been a hot research topic for the sustainable and energy-efficient building in the recent decades, with applications to the façade [72], [73] and roofing [74].

If the reinforcement is changed from fibers to particles, the composites are named the particle reinforced composites (PRC). The particle shape can be spherical, spheroidal, ellipsoidal or even random [75], [76]. Similar to FRPC, PRC has the advantages of stronger material properties and continuous composition and therefore enjoys a wide application in civil engineering. For example, the polymer foam particles can be added to concrete matrix to formulate the lightweight concrete (LWC), which can significantly reduce the weight of traditional concrete and have wide application in the building envelope [77], [78]. The motivation is to decrease the dead load of the concrete structure, so that more space can be freed by reducing the size of columns, beams and other load bearing elements [78]–[80]. For the most applications of PRC, the material composition is homogeneous over the space and the material properties are uniform. Its efficiency can also be

improved by tailoring particle gradations over specific direction(s) towards the applied stress configuration. The functionally graded materials (FGMs) are thus developed to fulfill that objective to fully utilize the material strength.

Conventional laminated composite materials exhibit a discontinuity of material properties at the interface, which commonly results in stress concentrations and thus damage in the form of delamination, matrix cracking and adhesive bond separation when they are subjected to environmental and mechanical loadings. Functionally graded materials, as a special type of particle-reinforced composite, are designed for the tailored morphologies and material properties through a continuing gradation of constituent phases, such as metals, ceramics and polymers, in specific spatial directions [81]. It was first invented and developed in Japan in 1984 during a space plane project in the form of a proposed thermal barrier capable of withstanding a surface temperature of 2000 K and temperature gradient of 1000 K across a cross section smaller than 10mm [82]–[84]. With the promising performance, the researches on the FGMs are emerging in recent years and have gained much attention as advanced structural materials with wide applications in aerospace, electric engineering, biomedical engineering, nuclear and civil engineering [85]–[87]. Its applications involve the thermal barrier coatings [88], thermal protectors [89], piezoelectric actuators [90], [91], high-precision sensors [92], [93] and high current connectors and capacitors [94], [95]. The typical two-phase FGM with gradation in one direction is schematically plotted in Figure 2 for illustration [96], where two materials are perfectly mixed with a continuous gradation of volume fraction.

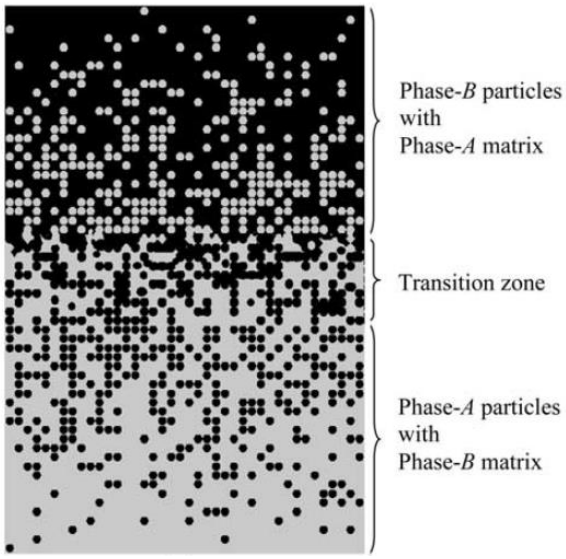

Figure 2 Schematically drawing of a two-phase functionally graded material

The highly tailored material composition requires the advanced fabrication techniques for the FGMs, which can be classified via the material phases into gas, liquid and solid based techniques [81]. Among them the gas-based thermal spray method and the liquid-based sedimentation method are two of the most widely used methods in the fabrication. The thermal spray technique is normally used to fabricate the thermal barrier coatings, the most important applications of FGMs. The technique is easy and mature, but the mismatch of thermal expansion rate between the base and the coating is a serious challenge and will introduce surface and interfacial cracks during the thermal cycling [97]. The liquid-based sedimentation method is normally used in the production of particle-reinforced composites, where the proper level of vibration and gravity is utilized to formulate the gradation along the thickness [98], [99]. Combined with water tubes and photovoltaic cells, the functionally graded material panel can formulate the building-integrated photovoltaic-thermal roofing panels (BIPVT), which is an active field for researches and application developments. The BIPVT system leverages the building envelope for solar energy

collection to produce both electrical and thermal energy, and thus greatly improves the energy efficiency of both residential and commercial buildings. It is an innovative and practical application of composite materials, specifically the functionally graded materials, to the civil industry.

1.3 Energy harvesting techniques and applications in building envelope

The wireless sensor network (WSN) technology plays an important role in the smart building management by providing the environmental monitoring for the optimal control of building components. The major problem for the WSN is the continuous energy consumption from sensors and processors versus the limited battery energy storage, which makes the sensor node suffer from limited battery lifetime. However, the energy density and capacity of batteries have not improved as much as the increase of the energy consumption from smart electronic devices in the WSN. In some civil engineering applications, the battery is very difficult to reach and replace, which will drastically increase the maintenance cost and limit the potential applications of the WSN. The energy harvesting techniques provide a good solution to elongate the battery lifetime and reduce the maintenance cost of the WSN.

The energy harvesting technologies is the process to convert, capture and store the energy from ambient environment into energy storage element for the power supply, where light, radio frequency radiation, heat, mechanical vibration and etc. could all be the energy source. The energy harvesting from living creatures and industrial applications have been developing rapidly during the recent decade. The energy harvesting from the livings can be segmented into wearable devices and the implantable biomedical devices, while the energy source for both applications are either from thermal source [100]–[102] or mechanical motion [103]–[105]. The research and

development of human wearable devices attracted a lot of attention in the most recent decade, with many prototypes implemented with wristband [106], shoes [107] and backpacks [108]. The energy harvesting for implantable biomedical devices has been demonstrated under in vitro [109] and in vivo [110] conditions through the breath and heartbeat of live rats. Unlike the nano and micro-watt level energy harvesting from living creatures, the harvesting in industrial applications has bigger power output and is usually above the micro-watt level. Civil engineering is one of the most widely developed field for energy harvesting, with a lot of widely seen solar cells attached on the roadway lamps, traffic lights, building roofs, and façade surfaces. Apart from the solar cells, electromagnetic harvester has been proposed for the railroad transportation [111], electromagnetic or piezoelectric harvesters have been applied for the structural health monitoring of highway bridges [112], and geothermal energy harvesting has been studied for the district heating [113].

The energy harvesting can serve as an uninterrupted power supply for a specific sensor node and for the overall system, and therefore enjoys a wide application in the wireless sensor network. The building envelope, as the barrier between the interior and the exterior of a building, features considerably exposure to the interior and exterior of buildings and is therefore crucial to the energy harvesting application in the smart building management. A comprehensive review of energy harvesting techniques in the building application can be found in [114]. The building envelope usually involves the solar energy harvesting through the building integrated photovoltaic-thermal devices [115] and the wind energy harvesting within the double skin façade [116]. The thermal energy harvesting from the building envelope, although rarely seen as an independent energy harvesting approach, is also a good source for the wireless sensor platform.

1.4 Scope

The primary objective of this dissertation is to design, develop and test the next generation of smart building envelope systems, in order to increase the overall energy efficiency performance of the building management system. Chapter 2 to Chapter 4 will focus on the fabrication, characterization, modeling, and structural analysis of the building integrated photovoltaic thermal roofing system, which passively adapt to the environment for an optimal harvesting efficiency of solar energy without compromising the internal comfort. Chapter 5 and Chapter 6 will introduce the smart window systems with thermal and solar energy harvesting techniques, which provide the power supply to the sensor and microprocessor embedded inside the window frame. The smart window will continuously monitor the environmental data and send out the information wirelessly to the building management system for the active environmental adaptations accordingly.

In Chapter 2, the building integrated photovoltaic thermal roofing system will be introduced, and a brief review of the recent researches and developments will be conducted. The design, fabrication and properties of a special BIPVT system made of Al/HDPE functionally graded material will be discussed. A novel image-based, non-destructive analysis method is developed and introduced in this chapter, to statistically captures the authentic particle distribution of the FGM, which was difficult to obtain for the small FGM samples. Since the external load for building roof is usually quasi-static with small temperature change, classical elastoplastic models such as the von-Mises model and Drucker-Prager model are used to characterize the mechanical properties of the matrix material, the high-density polyethylene. For deformation speed and temperature sensitive applications, the Johnson Cook plasticity model can be applied to incorporate the plastic strain rate and temperature change [117], [118].

The Al/HDPE functionally graded material used in the BIPVT design grants the excellent thermal, mechanical, and energy harvesting performance to the smart building roof system, but also casts challenges to the modeling and structural analysis for the design and engineering. Therefore, a micromechanics-based modeling algorithm is introduced and discussed in Chapter 3, to predict the elastoplastic, thermo-elastoplastic behavior of the particle-reinforced Al/HDPE FGM. The proposed approach uses the equivalent inclusion to model the inhomogeneities inside matrix materials and considers the pair-wise particle effect to improve the modeling accuracy. The fundamentals of the algorithm are discussed at the beginning. The detailed assumptions, formulation, implementation, verification, and validation are discussed in detail in the following subchapters. The algorithm provides theoretical and fundamental understanding of the particle-reinforced FGM, and serves as important reference and guideline for future researches and engineering designs.

In Chapter 4, a high order plate theory is proposed to study for the thermo-mechanical performance of the circular FGM panel made of Al/HDPE FGM, in order to provide structural design guideline for the BIPVT panels. The material characterizations of the FGM panel is conducted and discussed, and its deflections subjected to thermo-mechanical loading are measured with laser displacement sensor. In the theoretical modeling, the deflections from bending and shearing are separated, with the shear strain components following a parabolic variation across the thickness. Temperature induced thermal strain is integrated into the constitutive equations, and the governing equations are formulated via variational principle on extension, bending deflection and shearing deflection. Theoretical solutions are obtained with the help of the modified Bessel function under different loading and boundary conditions. Finite element model is constructed to verify the theoretical

prediction and good agreement is observed. The compression test is conducted to flatten the curvature from the thermal effect and serves as the validation for the proposed theory.

In Chapter 5, a thermoelectric-powered wireless sensor platform designed for the next generation of the smart building envelope is proposed and prototyped within a window frame. The platform was designed entirely inside the frame with no wired connections to the outside, therefore having no compromise of the outlook. With a slight modification of the internal profile and thermal performance, the platform achieves energy equilibrium between energy consumption and harvesting and provides the solution to the limited battery lifetime of the wireless sensor network. Comprehensive discussions of the design methodology are conducted and elaborated for both the energy harvesting and the wireless sensing subsystems. Corresponding lab tests are conducted rigorously to prove the feasibility and to demonstrate the performance of the platform. An energy equilibrium algorithm is proposed based on the field test result to predict the battery energy level, such that the self-powered feature can be achieved in any environment by proper engineering of key design parameters. The optimal battery capacity can also be determined through the cyclic amplitude of the battery energy projection. The design methodology and the energy equilibrium algorithm serve as a valuable guidance for the future design and engineering of the energy harvesting based wireless sensor network. The success of this project provides the continuous monitoring of the environment and valuable information for the optimal control of the building management system, such that significant savings can be achieved without jeopardizing the interior comfort.

Chapter 6 will introduce the design, fabrication and performance of a sun-power smart window system, which can harvest solar energy through the photovoltaic cells attached on the window blinds. The harvested solar energy is regulated and stored in the battery system to generate a 24

volts power supply for the motor that implemented inside the window. An innovative porous coating is coated on the other side of the window blinds to eject the heat out when the temperature is too high. An Arduino-based microcontroller is used to continuously monitor the temperature data on the window blinds. When the temperature is too high, the microcontroller will send signal to the motor to rotate the coating to face outside for the system cooling when the temperature is high, and rotate the PV side back when the temperature is low, such that the energy harvesting is proceeded in a high efficiency without jeopardizing the in-room comfort. The system generates more energy than needed from the motor and the micro-controller and will provide additional power supply for other sensors and actuators for the smart window and smart building management, which serves as an important platform for the next generation of smart building envelope system.

Chapter 2 Material fabrication and modeling for a building integrated photovoltaic thermal (BIPVT) roofing panel

2.1 Overview

The building-integrated photovoltaic-thermal (BIPVT) system was first proposed in the early 1990s [119] in order to improve the energy efficiency of buildings and houses. It was installed in North Carolina on the roof of a Applebee's restaurant for electricity and water heating [120]. The concept was then rapidly developed since 2000 [23], [121]–[125], due to its potential to facilitate the design of energy independent house. The BIPVT system is a successful improvement of traditional roofing systems, with optimal utilization of available energy and a passive adaptation to the environment. The rationale behind the BIPVT concept is to not only convert solar energy into electricity but also harvest the heat generated by the PV for building usage. It is known that the photovoltaic cells convert solar energy into electricity, with efficiency mostly less than 20% [126]. The rest of the solar irradiation is either reflected (about 10%) or transferred into heat [24]. It means about 70% of the solar energy is wasted and absorbed by the PV cells as the thermal energy in the form of higher temperature. Like all other semiconductors, the PV cell's efficiency is sensitive to temperature and decrease linearly at about 0.5% per ℃ for most silicon-based PV cells. Therefore, by harvesting the thermal energy from PV cells, both the solar-electricity efficiency can be increase and significant amount of thermal energy can be used or stored for the building/house owners.

In BIPVT design, the heat transfer from the PV cells and the harvesters is usually designed through air, water or phase change materials (PCM). For the air-based, both active [127]–[129] and passive [130]–[132] systems have been investigated and developed. The air-based systems are lightweight

and easy to transfer, giving the flexibility for integration with various building elements like roofs, facades, windows and skylights. But it also suffers from the relatively lower heat transfer efficiency and need higher temperature to operate comparing to other systems. The water-based systems have the advantage of working in low to medium temperature applications, such as pool heating [133], direct floor heating [134] and warm water supply [135]. Different types of structural configurations have been investigated for the heat transfer, with the designs of sheet-and-tube, rectangular water channel, or aluminum flat-box. Usually a homogeneous thermal absorber is used to take the heat from PV cells and then transfer to the water, and an insulative layer is applied below the water to prevent the heat from entering the building/house. The thermal absorber and the insulation are separate materials with different material properties and will introduce deformation mismatch under thermal or mechanical loadings. Unlike the previous two systems involving a single-phase material, the PCM-based system leverages large thermal capacity of a material during the phase change period to store the heat and stabilize the PV temperature at a certain range [136]–[139]. They possess great potential for cooling PV modules. Back in 2004, an application in the southeast England has successfully maintain the PV temperature below 35℃ during the summer daytime [140]. However, since most PCMs are organic materials, they usually come with an unpleasant smell and can be highly combustible. The inorganic PCMs normally have much less latent heat and thus undermine the performance. The strict fire safety requirements in the civil industry will be important issue for the PCM-based BIPVT system to address before a wide application. In the case of thermal energy harvesting, the PCMs only store the heat and maintain the PV temperature, the harvesting process will still require other techniques to take the energy out.

Recently, an innovative water-based BIPVT roofing system was proposed to solve the issues resulted from the material discontinuity [21], [99], [141], [142]. As is schematically illustrated in Figure 3, the photovoltaic cells are attached to a functionally graded material panel made with aluminum and high-density polyethylene (HDPE). A gradually material transition from metal dominated to polymer dominated is observed along the thickness. The double-serpentine shaped water tubes are implemented inside the FGM panel during the fabrication stage, to take away the heat from the PV cells. The aluminum heavy side will enjoy high thermal conductivity to transfer the heat while the HDPE heavy side will prevent the heat entering the building, thanks to its great thermal resistance. Although the performance depends on the speed of water flow, a drastic PV temperature drop and significant thermal energy harvesting have been observed during the lab tests.

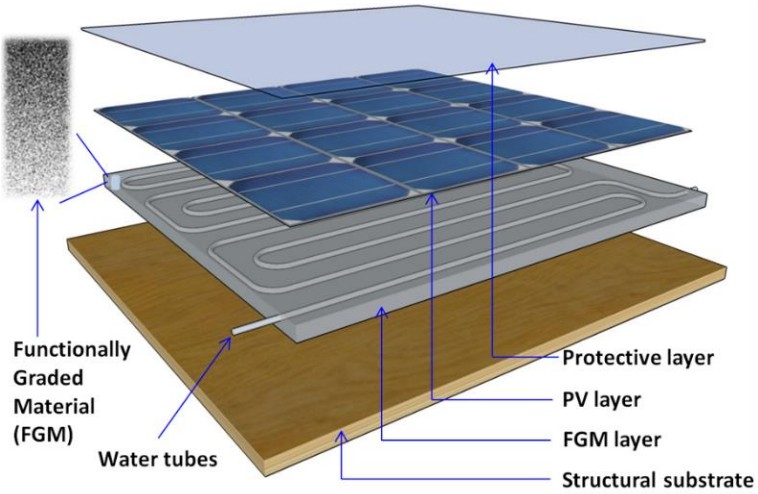

Figure 3. A hybrid solar roofing panel integrating an FGM plate with other layers for heat harvesting and temperature control

The successful application of functionally graded materials into building integrated photovoltaic thermal roofing not only contribute to the conversion efficiency of PV cells and the thermal energy harvesting, but also resolve the potential delamination and cracks of the layered BIPVT system in the traditional design. Since the BIPVT roofing system is designed to replace the traditional roof,

the building construction code is applied and both dead load and live load shall be considered. The long-time exposure to the solar irradiation will also heat up the surface and introduce potential thermal stress. Therefore, a theoretical model for the thermal and mechanical behavior of the BIPVT system is needed, specifically for the FGM substrate. The micromechanics-based models are perfect tools to analyze and predict the performance of the composite materials, and will be briefly introduced in the next chapter.

In this chapter, the design and fabrication of the Al/HDPE based functionally graded material panel is discussed step by step, and a complete BIPVT prototype is demonstrated with water tubes and PV cells. An image-based nondestructive measurement for the particle volume fraction distribution is proposed to statistically capture the Al particle volume fraction. The method is applicable to any composites comprised of metallic and nonmetallic materials. The mechanical tests are conducted and documented to obtain the elastoplastic behavior of the HDPE, which is the matrix material of the proposed FGM panel. A discussion of classical plastic models is carried out for an accurately modeling of the HDPE's elastoplastic behavior, in order to accurate predict the FGM's performance in the next chapter.

2.2 Fabrication of FGM-based BIPVT

In recent years, a sedimentation-based method for the manufacturing of functionally graded material panel has been developed, in which the combined vibration and sedimentation method is used to create the graded microstructure of the mixture [141]. In this method, coarse aluminum (Al) particles (with the size ranging from 100-600 μm and median of 300 μm) and fine high-density polyethylene (HDPE) powder (with the size 1-100 μm and median of 25 μm) are mixed thoroughly with 100% ethanol to fabricate the functionally graded panels for the BIPVT system.

The reason of using ethanol instead of water is because of the following two reasons: (a) the water's specific gravity is between the Al and HDPE and thus will lead to a laminated deposition instead of graded structure; (b) a chemical reaction between Al and water has been observed when the sedimentation time is long, creating hydrogen and alumina.

Since the two types of particles have significantly different specific gravity (2.7 for Al and 0.95 for HDPE) and size distribution, the velocity of sedimentation under the vibration inside the ethanol solution will also be different, thus creating a graded microstructure. The mix design of Al and HDPE is determined after a series of tries and comparison, with the result of volume ratio between Al to HDPE as 1:3 and the ethanol as weight ratio of 28% of the total mixed powder. Three steps are needed for the manufacture: (a) mixing; (b) sedimentation; (c) baking. In the mixing procedure, the hand mix is needed first for an even distribution of Al and HDPE particles inside the container, which is then placed onto a Hobart mixer for the total mixing time of about 6 mins with a pause at every 2 mins. The weighted ethanol is divided evenly into three fractions and added separated before the machine and during the following two pauses. The solid loadings attached on the container surface during the mixing shall be returned to the solution during the pause. The mixed suspension is then transferred to an aluminum mold clamped onto a Syntron vibration table with model VP-51 for the sedimentation process. The mold containing the mixture is then vibrated for 30 s at the power level of 80 and frequency of 75 Hz. It is noted that the sedimentation depends heavily on the machine and the size of the mold. The process described is suitable for a 2 ft × 2 ft mold with the depth of about 3 in. The mold shall be placed at the center of the shaking table for the even vibration. If clamps and stiffeners were used to fix the mold, extra attention shall be paid to make sure they were aligned and centered. Thereafter, the suspension is kept in the mold allowing further sedimentation of particles and open to the air for evaporation of

ethanol. During this process, the ethanol will completely be drained off in about 24 h. It is noted that the formula is obtained through the test of a 2 ft × 2 ft size. For the panel of other sizes, the amount of mixing and the shaking time shall be slightly modified through trial.

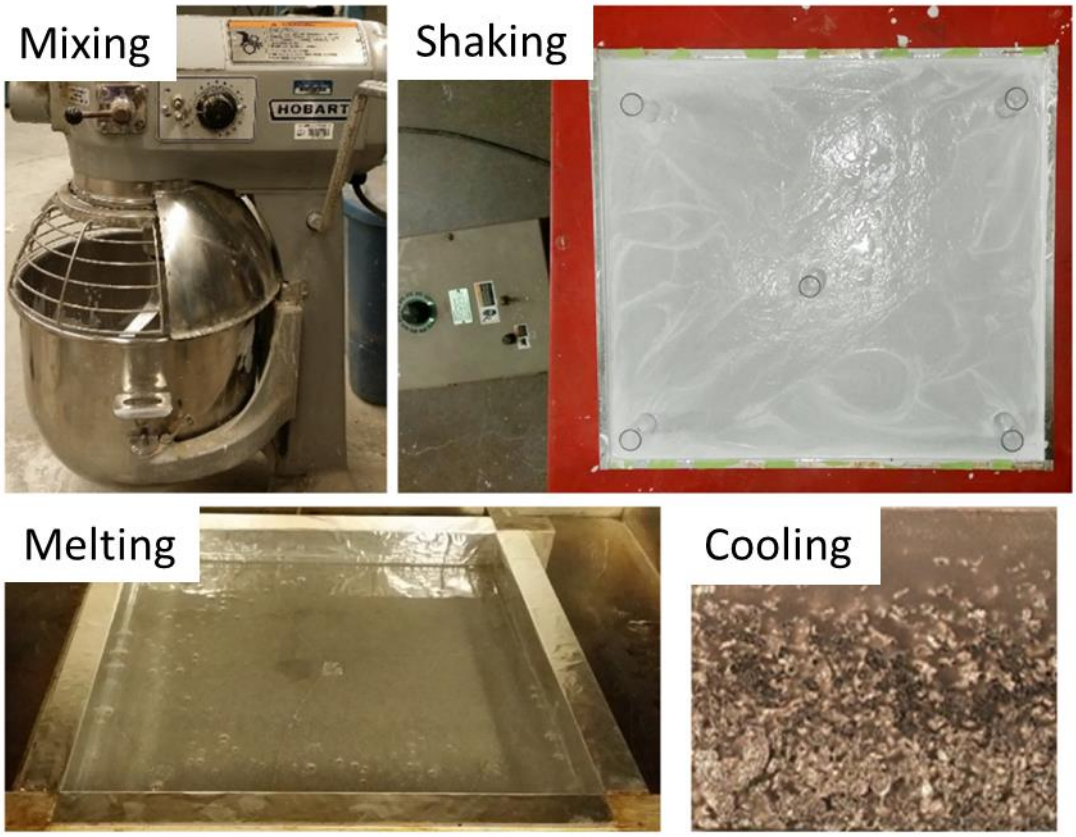

Figure 4 The procedures in functionally graded material manufacturing

The mold with the solid-state mixture will then be transferred into a vacuum oven for melting and vacuum process. The oven is preheated to 170 ℃ and the mixture will be baked for 8 hours, until all the HDPE particles have been melted shown in Figure 4, so as to form a composite of Al particles dispersed in the HDPE matrix with a graded microstructure. The air voids in the melted composite resulted from the particle mixing and residual ethanol are degassed by applying the vacuum process for about 8 hours, after which the sample surface will be full of holes generated by the air void inside the panel. The sample surface is flattened by applying the mold top with

heavy metals and put inside the 170 ℃ chamber for another 4 hours. The oven temperature is then reduced to 110 ℃, right below the melting point of the HDPE, for another 8 hours to gradually solidify the liquid HDPE, after which the whole set up is turned off and FGM sample is removed from the mold and cooled down into room temperature. The cross section of sample elements cut from the FGM panel is shown in Figure 5, where a well-controlled gradation is achieved along the cross section.

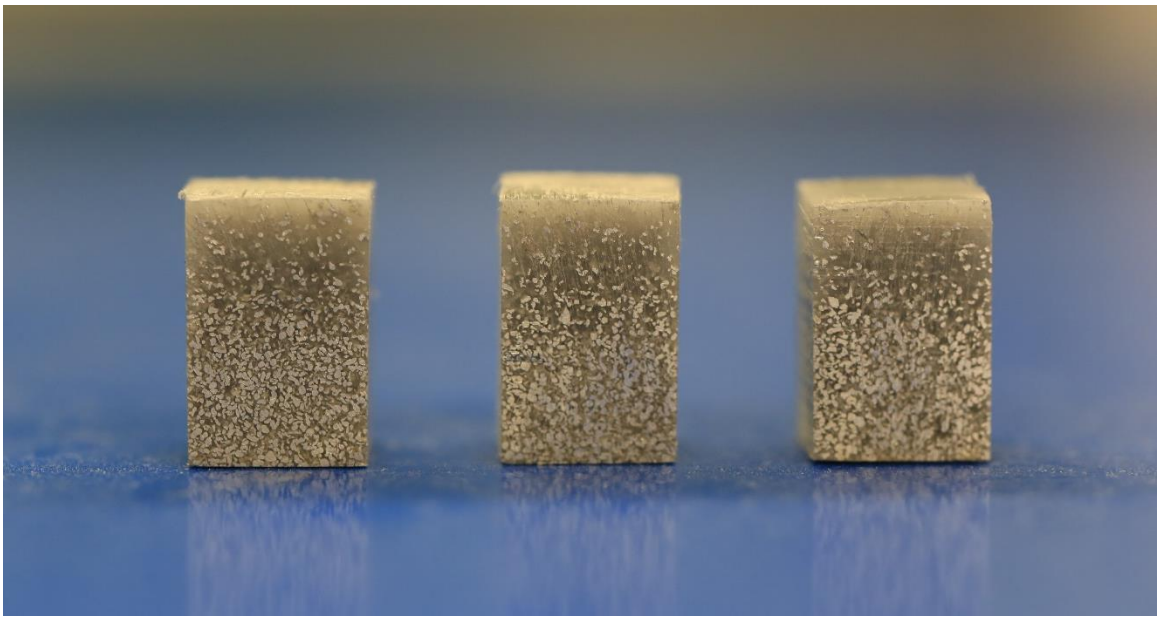

Figure 5 Cross section of functionally graded material panel

The functionally graded material panel can also be manufactured with pre-assembled water tubes to formulate the supporting substrate for the BIPVT system, as is shown in Figure 6a and Figure 6b, such that the heat is transferred efficiently through the aluminum particles into the flowing water while prevented from entering the room, thanks to the strong heat resistant of HDPE. Double serpentine shape of the water tubes is designed to remove the heat more uniformly. The panel can be made into different sizes, and the dimensions the authors investigated include 2 ft × 2 ft, 1 ft × 1 ft and 0.6 ft × 0.6 ft. After taken out from the oven, the panel is glued onto a fire-retardant

plywood through a moisture resistant epoxy adhesive as shown in Figure 6c. Solar panels are then attached on top (aluminum heavy) side of the FGM panel to formulate the complete BIPVT system prototype shown in Figure 6d.

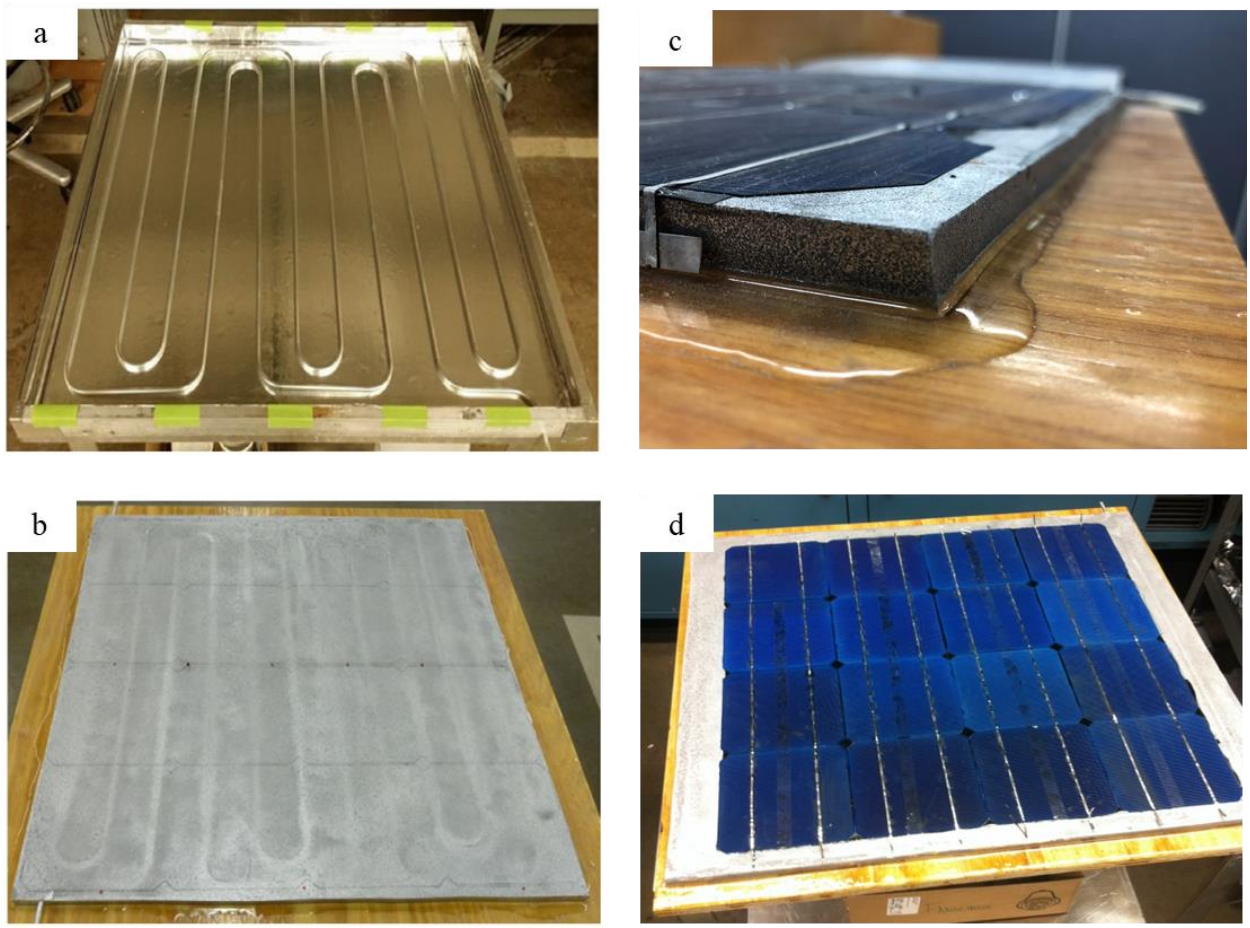

Figure 6 Illustration of the FGM BIPVT panel fabrication and testing: a. built-in water tubes inside the mold; b. functionally graded panel with built-in water tubes; c. adhesive epoxy for FGM panel fixing onto a plywood panel; d. FGM panel prototype

2.3 Performance of the FGM-based BIPVT

The Aluminum-rich side can transfer the heat absorbed by the PV cells into the water tubes integrated inside the panel and the HDPE-rich side can prevent the excessive heat from entering the building, thus increasing the overall energy efficiency of the building. The thermal and

electronical improvement is described in detail in [98] and briefly introduced in this section. The overall performance of the FGM panel is quantified by the lab test under the solar simulator as shown in Figure 7. The solar simulator is established in a purpose-built room with a temperature-controlled exhaust system, which cools the room by forced-air ventilation as shown in Figure 7(a). The irradiance intensity of the metal lamp is controlled by the simulator controller shown in Figure 7(b), together with a flow-meter controlling the water flow rate inside the water tube, which cools down the surface temperature of the FGM panel as well as the solar cell. The temperature measurement and the generated power were collected by the LabVIEW data acquisition (DAQ) system in Figure 7(c) with a pyranometer in Figure 7(d) to measure and to calibrate the solar irradiation density of the solar simulator.

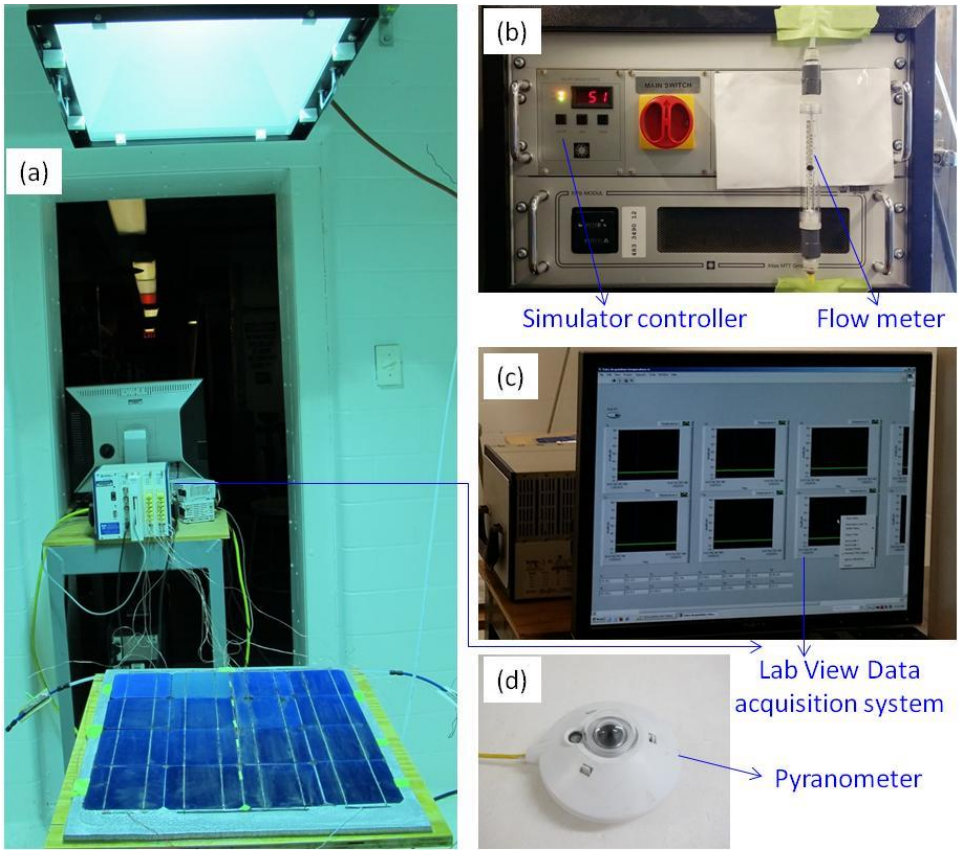

Figure 7 Performance evaluation of the BIPVT: (a) test setup; (b) simulator controller and flow meter; (c) data acquisition system; and (d) Pyranometer.

Fourteen thermal couples were applied to examine the temperature distribution throughout the whole panel surface, where twelve of them (6 located at the two edges of the panel and other 6 were distributed at the center line on the solar panel) were attached on the FGM panel, and the other two were attached on the inlet (No. 1) and outlet (No. 15) of the aluminum water tubes. The detailed distributions of the thermocouples were shown in Figure 8.

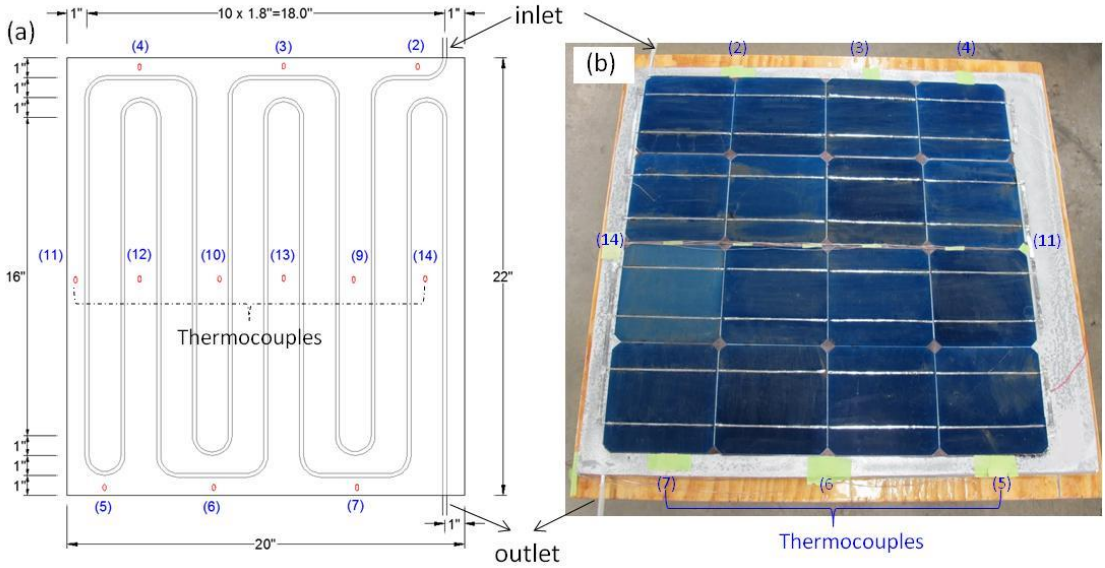

Figure 8 Thermal couple distributions: (a) schematic illustration; and (b) real BIPVT panel

The test consists of two stages. In the first stage, the BIPVT was exposed to the solar radiation without water flowing inside until a stable state was reached; while in the second stage, a stable water flow was introduced and controlled by the flow meter until another stable state was reached. Three different solar irradiation levels are tested, each with four different water flow speeds. The thermal performance is demonstrated in Table 1 and the electrical performance is demonstrated in Table 2.

To quantify the thermal performance, the thermal energy and the thermal efficiency collected by the BIPVT will be evaluated. The thermal energy collected by the water per second (E_{water} (W)) is defined as

$$E_{water} = m_{water} \times C_{water} \times \Delta T_{water} \tag{2.1}$$

where m_{water} is the mass of the flowing water per second and $C_{water} = 4.19$ (kJ/kg · ℃) is the specific heat capacity of water. The thermal efficiency of the BIPVT panel $\eta_{thermal}$ can be determined by Eq. (2)

$$\eta_{thermal} = \frac{E_{water}}{E_{IN}} = \frac{E_{water}}{I_R \cdot A} \tag{2.2}$$

where E_{IN} is the product of the irradiance intensity measured in W/m^2, I_R is the irradiance intensity, *A* is the total area of the BIPVT including the frame area, which is 0.28 m^2 (20"×22") for the prototype BIPVT.

Table 1 The thermal performance of the BIPVT

Solar radiation (w/m2)	Water flow rate (ml/min)	ΔT_{water} (ºC)	ΔT_{panel} (ºC)	E_{water} (W)	$\eta_{thermal}$ (%)
620	30	26.5	-12.7	55.52	31.54
	60	22.94	-18.6	93.86	53.33
	90	17.6	-21.8	110.62	62.85
	120	14.1	-23.9	119.83	67.14
800	30	32.2	-15.7	67.46	29.71
	60	25.6	-20.8	107.26	47.23
	90	20.3	-24.2	127.59	56.18
	150	13.6	-28.1	142.46	62.73
1000	30	37.5	-14.3	78.56	27.68
	60	29.5	-22.9	123.61	43.54
	90	23.7	-27.8	148.95	52.47
	150	16.1	-32	168.65	59.41

As shown in Table 1, the increased temperature of the outlet water over the inlet water decreases as the water flowing rate increases and the overall harvesting efficiency of the thermal energy is between 30% to 67%. A desired flowing rate can be adjusted based on a customer's need in terms of the harvested heat energy collected by the warm water or the enhanced electricity generation efficiency from the PV module. It is expected to guide regular residents to select a proper water flowing rate at different seasons to meet their household needs on both warm water and output electricity from the present multifunctional roofing system.

A circuit shown in Figure 9 was set up with the data acquisition system to measure the maximum output power by the solar cells, in order to quantify the enhanced performance, where an adjustable resistor was applied in the circuit to control the output load. The current was measured by a digital multimeter and the voltage was obtained via the DAQ. The current reaches its maximum (I_{SC}) in a short-circuit when the resistance is zero, while the voltage reaches its maximum (V_{OC}) in an open-circuit where the resistance can be considered as infinite through which no current flows. By setting different values of resistance in between, the I-V curve can be traced, and the panel can be characterized at different irradiance intensities with different water flowing rates. The electric measurements are recorded in Table 2 for comparison under different solar irradiations and water flow rates. The I_{MPP} and V_{MPP} are the current and the voltage corresponding to the maximum power point tracking with the adjustable resistor. The E_{pv} is the maximum output power. The FF stands for the fill factor, which is essentially an index of the BIPVT quality and calculated by comparing the maximum output energy to the theoretical one (E_T) that would be generated at both the open circuit voltage and short circuit current together.

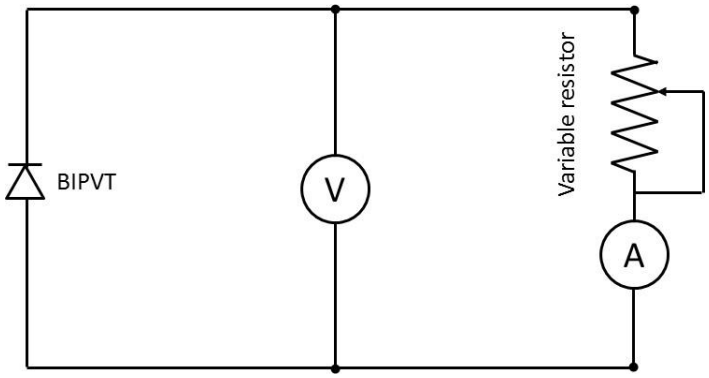

Figure 9 Circuit diagram for the I-V characteristics determination.

Table 2 The electric performance of the BIPVT

Solar irradiance (w/m2)	Water flow rate (ml/min)	ISC (ADC)	VOC (VDC)	IMPP (ADC)	VMPP (VDC)	E_{pv} (W)	FF (%)	η_{pv} (%)
620	0	3.69	7.86	2.83	6.52	18.45	63.62	10.48
	30	3.92	8.23	3.21	6.39	20.51	63.58	11.65
	60	4.17	8.41	3.17	6.73	21.32	60.83	12.11
	90	4.2	8.54	3.19	6.88	21.96	61.19	12.48
	120	4.24	8.6	3.29	6.89	22.65	62.11	12.87
800	0	4.69	9.28	3.64	7.47	27.21	62.51	11.98
	30	5.09	9.47	3.98	7.62	30.35	62.96	13.36
	60	5.27	9.56	4.09	7.67	31.37	62.27	13.81
	90	5.31	9.57	4.13	7.72	31.88	62.74	14.04
	150	5.39	9.71	4.22	7.81	32.96	62.97	14.51
1000	0	5.68	10.02	4.52	8.01	36.22	63.61	12.76
	30	6.17	10.31	4.91	8.24	40.46	63.60	14.25
	60	6.26	10.42	5.09	8.32	42.35	64.92	14.92
	90	6.38	10.57	5.18	8.43	43.67	64.75	15.38
	150	6.62	10.83	5.24	8.57	44.91	62.64	15.82

It is seen in Table 2 that the output electric energy E_{pv} increases as the solar radiation increases, and the output power, ISC, VOC, IMP and VMP increases with the water flowing rates. A significant increase of the PV efficiency is observed with the water-cooling process. The enhancements of 21.1% and 24.0% are observed for the solar irradiance of 800 and 1000 $\mathrm{W/m^2}$

under the water flow rate of 150 $\mathrm{ml/min}$, where the maximum output power reaches 32.96 W and 44.91 W, respectively. Based on the thermal and electric performances provided in Tables 1 and 2, the total energy efficiencies $\eta_T = \eta_{thermal} + \eta_{pv}$ of the present BIPVT roofing panel can be evaluated as 79.8%, 77.3% and 75.2% under the solar irradiance of 620 $\mathrm{W/m^2}$, 800 $\mathrm{W/m^2}$, and 1000 $\mathrm{W/m^2}$, respectively. Therefore, a significant energy harvesting efficiency is observed for the FGM based BIPVT, where both the photovoltaic and solar thermal energy could be harvested for both electricity and warm water supply in the house.

2.4 Image-based nondestructive measurement for volume fraction

In the modeling of the functionally graded material panel, it is assumed that the material gradation is only along the thickness direction, i.e. the particle volume fraction remains the same within a horizontal plane of a given thickness location. The equivalent performance in each layer can thus be obtained, as long as the particle volume fraction distribution is known. Therefore, in order to fully quantify the thermo-mechanical behavior of the functionally graded material panel, the first and foremost task is to determine the volume fraction distribution of the Al particle inside the HDPE matrix, after which the proposed micromechanics model can be used to predict the corresponding behavior under the thermal and mechanical loading.

There are many ways to quantify the particle volume fraction for a homogeneous composite system. The most straightforward way is to measure the volume through water displacement method and the weight on an electronic scale, so that the equivalent density can be obtained to calculate the mass ratio of the Al over HDPE. For graded material, however, the measurement is more complicated. The equivalent density shall be measured in every thickness location, by slicing the

FGM into multiple pieces, to obtain a discrete volume fraction of Al at different thickness location. Curve fitting is then needed to achieve a smooth function to represent the volume fraction distribution. Since the particle distribution can be arbitrary over the same horizontal plane, multiple samples are usually needed for an accurate representation. Moreover, since the thickness to length ratio of the FGM panel is very small, it is hard to slice the FGM without harming the microstructure. In order to accurately measure the samples' particle volume fraction distribution, a novel image-based nondestructive method is proposed and applied to statistically measure the particle volume fraction distribution along the gradation. Since it is nondestructive, measurements and tests can be conducted at the same time for each sample to incorporate individuality. The samples are tested with the Instron 5984 34k Universal Testing Machine inside the Carleton Laboratory of Columbia University. In the meantime, a high-resolution photo is taken at the beginning of each loading test, with the Canon DSLR 6D camera and the Tamron 90mm f/2.8 macro lens. The YongNuo YN-14EX macro flashlight is mounted onto the Tamron macro lens to provide additional light in the macro photographing. The experiment setup is shown in Figure 10(a). The macro lens allows a much closer shooting distance such that the photo frame can be filled as much as possible by the small FGM sample, in order to reveal more detail of the FGM cross section. The cross-section photo is seen on Figure 10(b), with approximately 4 million effective pixels included in the area of the 0.25 in^2 cross-section surface. The cross-section photos are used to statistically retrieve the particle volume fraction distributions through the image analysis.

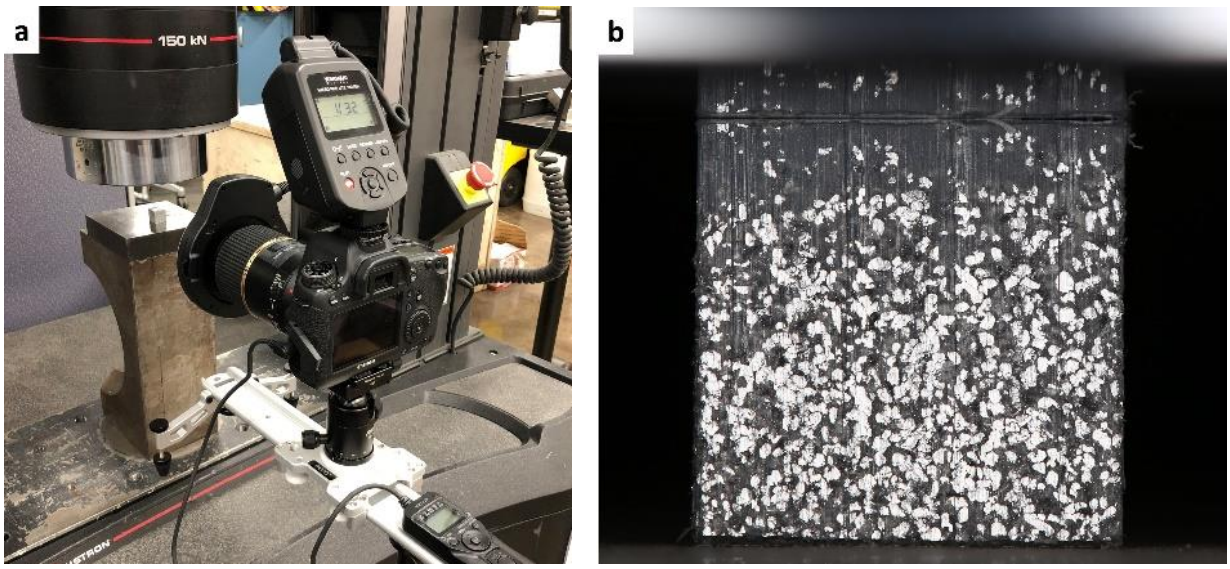

Figure 10 Microstructure acquisition: (a). Experimental setup; (b). Macro photo of the FGM sample's cross section

The functionally graded materials usually are mostly designed with a single gradation direction, which is usually the thickness direction. The number of particles within a specific horizontal plane depends on its corresponding volume fraction, but the particle distribution is uniform over the horizontal plane. Therefore, if the particle size is relatively small comparing to the horizontal cross section, enough number of particles can be distributed over the plane to generate the statistical significance of using the 2D surface distribution to represent the 3D distribution. Statistically speaking, the distribution of one cross section will represent the distribution of the sample, which means that the two dimensional surface in Figure 10(b) can be used to statistically represent the three dimensional particle distribution of the sample. The volume fraction distribution is achieved through image analysis by dividing the sample image into multiple layers and counting the relative area of aluminum to the overall area at the specific layer. The problem is how to distinguish the pixels belonged to Al with the pixels belonged to HDPE. Aluminum, with the surface color of grey, will show very close pixel value with HDPE when the photo is converted to grey scale. Moreover,

the solid HDPE is partially transparent, making the Al particles in the deeper layer also showing up in the image, which will hinder the recognition process of the surface Al particles. The trick is the application of the macro flash light during the photographing. Aluminum, as a metal, has a very high reflection rate to the flashed light, while HDPE, as a plastic, absorbs most of the light and thus shows much darker in Figure 10(b), making it easier to be distinguished from aluminum. Since the surface HDPE will absorb much of the light, the aluminum in deeper layer will not reflect light anymore, and thus will not show up in the image. Therefore, the flash light greatly contributes to the differentiation of Al and HDPE by making the surface aluminum particle "shine" in the photo.

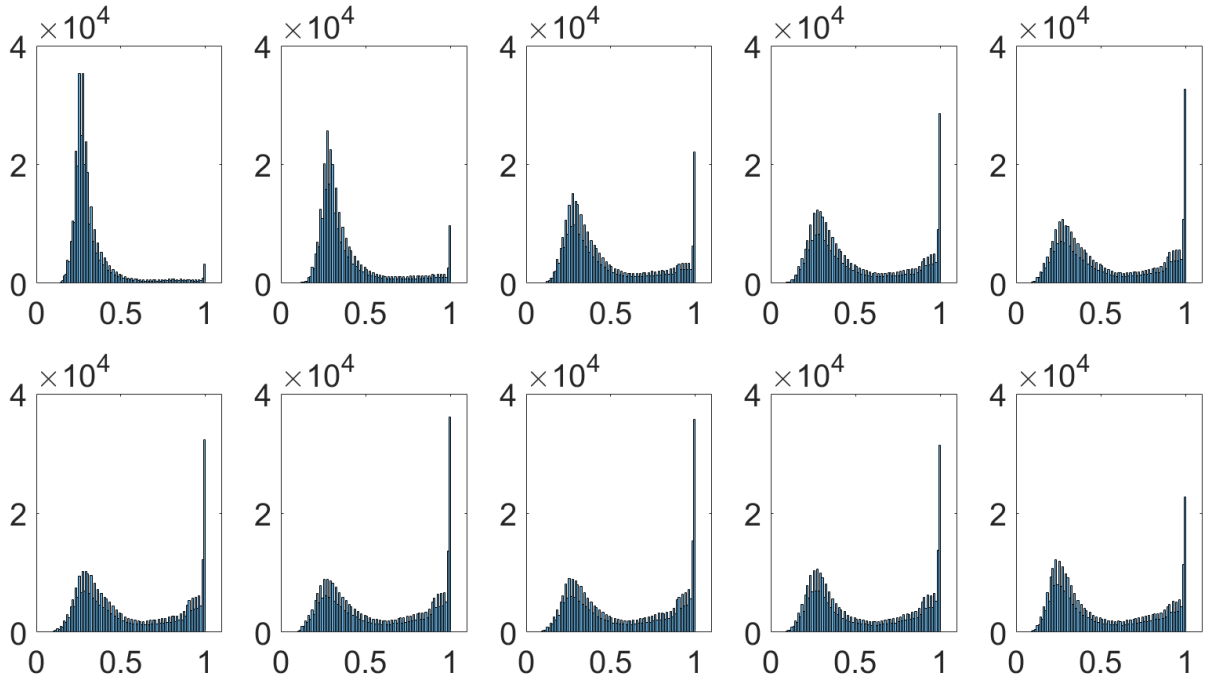

Figure 11 The histograms along the gradation of the FGM sample in the 10 different sections along the gradation

Specifically, the captured image is first converted from RGB to the gray scale, where each pixel location has a number ranging from 0 to 1, representing the intensity of the light reflected to the

camera. The value 1 means totally white, i.e. all the light is reflected, while the value 0 means totally black, i.e. no light is reflected. The FGM sample part is cropped from the whole photo and divided into 10 sections along the gradation and the histograms in each section are plotted as shown in Figure 11, where sequence from the upper left to the bottom right represent the top layer to the bottom one, respectively. The gray scale light intensity from 0 to 1 is divided into 100 sections with accuracy of 0.01 for the histogram plot. The histogram counts the number of occurrences within a certain light intensity range. It is clearly seen that from top to bottom, the number of occurrences from brighter pixels (pixel information close to 1) increases along the gradation, in accordance with the gradual increase of aluminum particle volume fraction from the top toward bottom.

A light intensity threshold is settled to distinguish aluminum pixels from HDPE pixels, which is determined by calibrating the predicted weight of the sample to the measured average. Let us first assume that the light intensity threshold is set as 0.86, such that any pixel's light intensity larger than or equal to 0.86 is considered as part of aluminum particle, while smaller than 0.86 is considered as HDPE. The identification of aluminum or HDPE can thus be easily accomplished. The comparison of original image and Al-recognized image is shown in Figure 12. It is seen that all the aluminum particles in the original photo are successfully recognized, while the vertical scratches from the sample-cutting and the aluminum particles hidden in deeper layer are mostly filtered out.

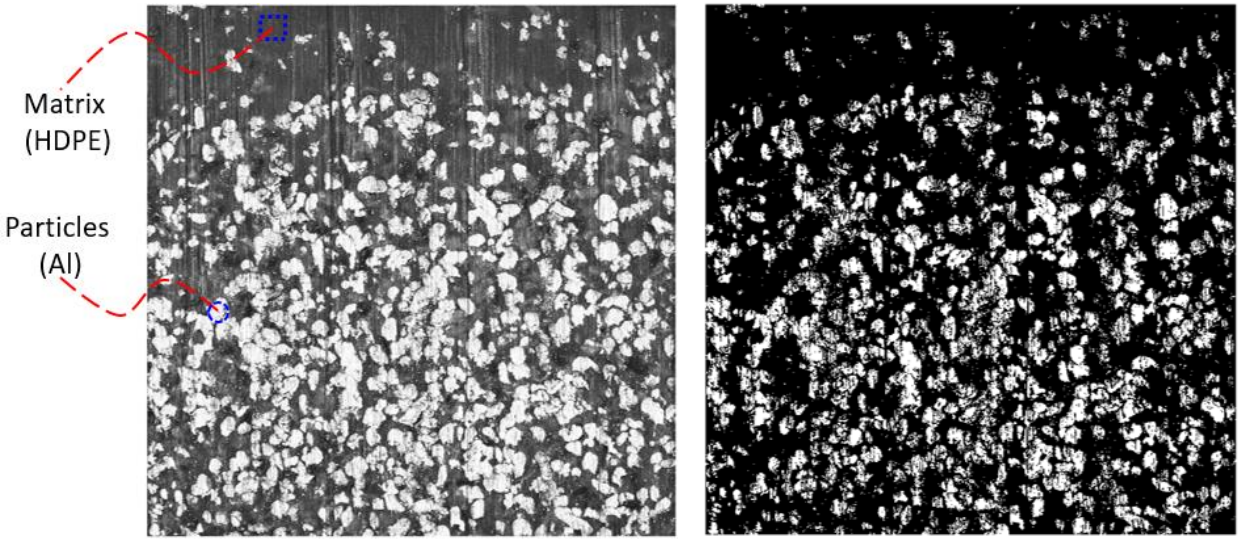

Figure 12 FGM sample original photo (left) and Al-recognized photo (right)

Ten layers are divided along the gradation and the corresponding particle volume fraction is calculated by dividing the number of bright pixels to the total number of pixels. Such image analysis is repeated for all four FGM samples and the averaged particle volume fraction distribution is plotted Figure 13. The blue dots represent the averaged volume fraction while the error bar represents the maximum deviation retrieved from all four FGM samples. A quadratic function with forced zero interception is used to fit the volume fraction distribution. The area below the fitted curve is the averaged particle volume fraction. Given the sample dimension in Figure 13, the weight corresponding to the averaged volume fraction is calculated as 3.3112 g, which matches well with the measured average sample weight 3.3205 g, such that the light intensity threshold 0.86 is validated. It is seen from Figure 13 that when the relative location is smaller than 0.6, the particle volume fraction gradually increases in convex form until approximately 30% and then stabilizes with a slight decrease. The retrieved particle volume fraction distribution is slightly different with the linear distribution assumption in the paper of Chen et al (2016) and has a slight decrease at the bottom of the sample. The reason for the decrease is the boundary effect of the

mold. The gradation is resulted from the sedimentation process, where the mold containing the sample solution is fixed to a shaking table with vertical vibration. Since the bottom surface is fixed to the shaking table, the particles close to the bottom surface are forced to bounce back, and therefore the bottom layer is formulated with less particles. The layer close to the bottom will accumulate both the particles fallen from the top and the particles bounced back from the bottom, and therefore has the largest volume fraction across the thickness.

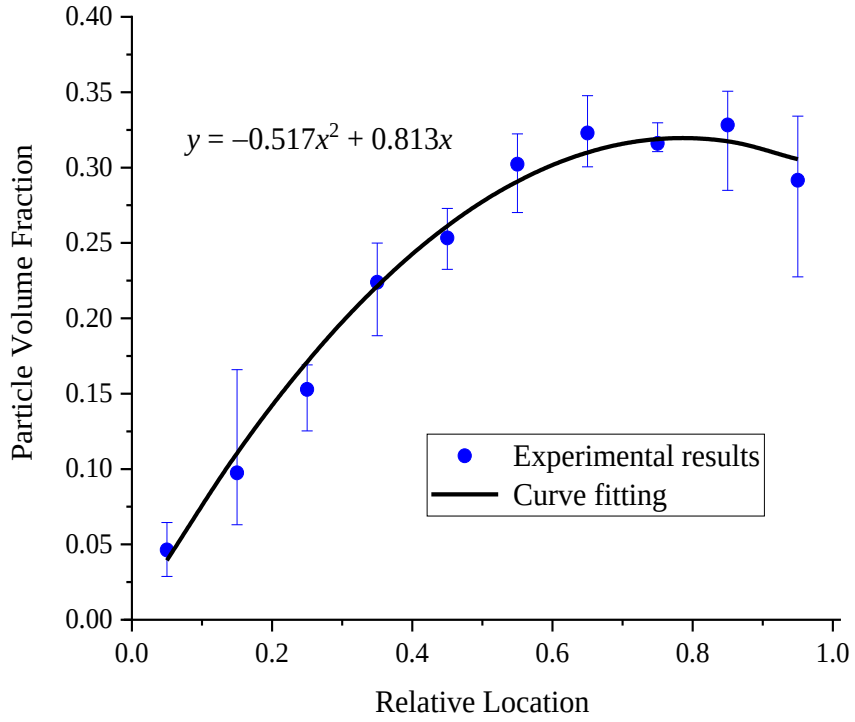

Figure 13 Aluminum volume fraction distribution in the gradation direction

Once the volume fraction distribution is achieved, algorithms can be applied to predict the thermo-mechanical behavior of FGMs. It is worth to mention that the above-mentioned image analysis method can incorporate the individuality of each sample. If the sedimentation is not even across the panel, verification of every individual sample can be carried out for an accurate measurement and comparison.

2.5 Mechanical properties and models of HDPE

The yielding and plastic flow of HDPE plays an important role in the wear and failure mechanisms of the building-integrated photovoltaic-thermal roofing panel (BIPVT). The primary objective of this section is to capture the yielding and plastic flow behavior of the LyondellBasell microfine high-density polyethylene powder (HDPE) used in the manufacturing of BIPVT roofing panel. The first part of this section described the monotonic loading behavior of HDPE in both compression and tension. The second part explores performance of von-Mises model and Drucker-Prager model in capturing the elastoplastic behavior of HDPE and the material properties for both elastic and plastic region.

2.5.1 Tension and compression tests of HDPE

Both tension and compression samples are cut from a HDPE panel casted following the same manufacturing steps of BIPVT, without the sedimentation process. The HDPE panel rests for about 3 weeks after the manufacture and is machined into special shapes according to the test standard. The tension test samples are cut into dog-bone shape, as shown in Figure 14, following the ASTM D638-14 standard for tensile properties of plastics. Five samples are machines and the detailed dimensions are shown in Table 3.

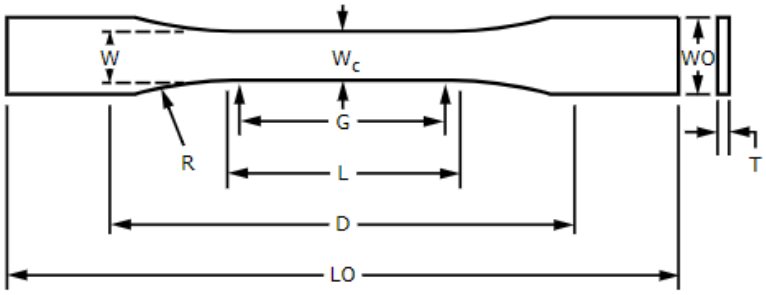

Figure 14 Tension test sample shape

Table 3 Tension samples' dimensions

Samples	Length L0 (in)	Grip dist. D (in)	Gauge L (in)	Width Wc (in)	Thickness T (in)
1	6.56	4.52	2.01	0.806	0.163
2	6.53	4.55	2.03	0.792	0.162
3	6.48	4.44	1.95	0.856	0.169
4	6.42	4.48	1.98	0.852	0.159
5	6.50	4.54	2.02	0.779	0.149

The compression test samples are cut into cubic shape following the ASTM D695-15 standard for compressive properties of rigid plastics. Five samples are machines and the detailed dimensions are shown in Table 4.

Table 4 Compression samples' dimensions

Samples	Length (in)	Width (in)	Thickness (in)
1	1.000	0.509	0.505
2	1.023	0.508	0.504
3	0.965	0.507	0.494
4	0.996	0.505	0.512
5	0.982	0.503	0.508

Both tension and compression tests are carried out in MTS Criterion Model 43 universal testing machine. The samples rest for about 4 hours after being machined and sanded to specific shape. The tension and compressions configurations are shown in Figure 15. An extensometer with gauge length of 1 in is attached to the tension test samples for the strain measurement. Since the HDPE is highly viscous, the loading speed plays an important role in its elastoplastic behavior. The loading speed for both tension and compression tests are set as 1×10^{-3} /s. The data sampling frequency is set as 20 Hz.

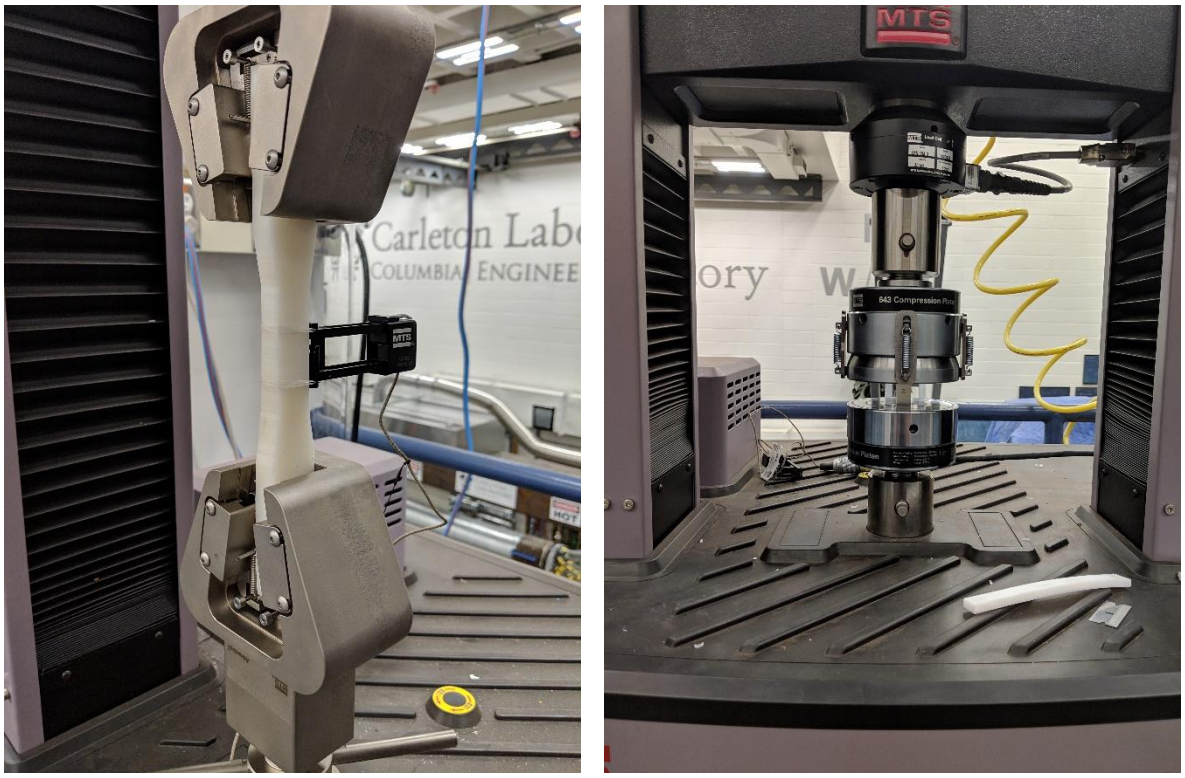

Figure 15 Tension and compression test comfiguration

Both nominal stress-strain and true stress-strain relations are plotted from the test data. The nominal stress and strain are identical to the engineering stress and strain. The true stress and strain are derived considering the change of the loading area, assuming the unchanged total volume before and after the test. The Poisson ratio of HDPE is normally 0.45, which is close to the Poisson ratio of impressible solid. Therefore, the plot of true stress and strain curve is reasonable and will generate more valuable results considering to the large deformation of HDPE. The equations for nominal stress and strain as well as true stress and strain are listed below:

$$\boldsymbol{\varepsilon_N = \frac{l - l_0}{l_0}} \qquad \boldsymbol{\varepsilon_T = \ln(1 + \varepsilon_N)} \tag{2.3}$$

$$\boldsymbol{\sigma_N = \frac{P}{A_0}} \qquad \boldsymbol{\sigma_T = \sigma_N(1 + \varepsilon_N)} \tag{2.4}$$

where l and l_0 are the final and initial length of the extensometer, P represents the load and A_0 is the initial undeformed cross-sectional area.

Both the nominal and true stress and strain curves are plotted, as shown in Figure 16 and Figure 17 respectively. The plot is based on the averaged data of 5 samples, with the error bars indicating the ranges of variations. The stress strain curves are only plotted up till strain equaling to 6.5%, because a brittle failure was observed for tension test of HDPE. Normally HDPE has very good ductility and can reach a deformation up to 300% of original length. However, all tension test samples showed the same brittle failure mode during the tests, with critical failure strain ranging from 4% to 7%. The reason for this switch of failure mode has not been investigated yet, but the manufacturing processes could be the major reason for this change of performance. The compression test samples were pressed to about 15% of deformation.

It is seen that all 5 samples' behaviors agree with each other very well for both tension and compression tests, with variation much smaller than the average value. For nominal stress and strain relation, the tension and compression curves are quite different in plastic region, while the elastic region share some similarity but not identical. When the nominal stress and strain are converted to its true counterparts, the stress and strain relations are almost identical in plastic region between tension and compression. The two curves converge to a single curve when the true strain reaches about 2.8%. For the stress strain relations with true strain below 2%, the trends are very similar with the value slightly different with each other.

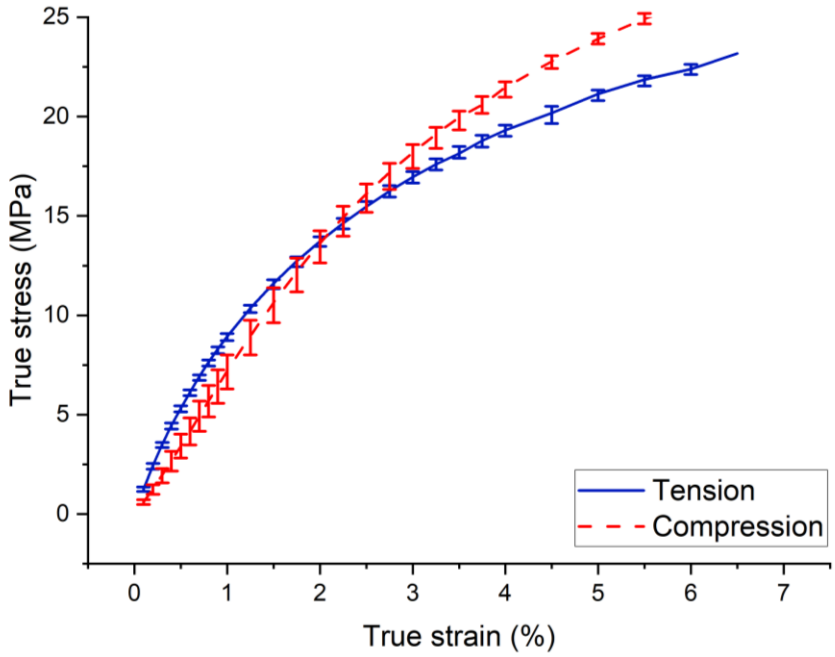

Figure 16 Nominal stress and strain curve for both tension and compression

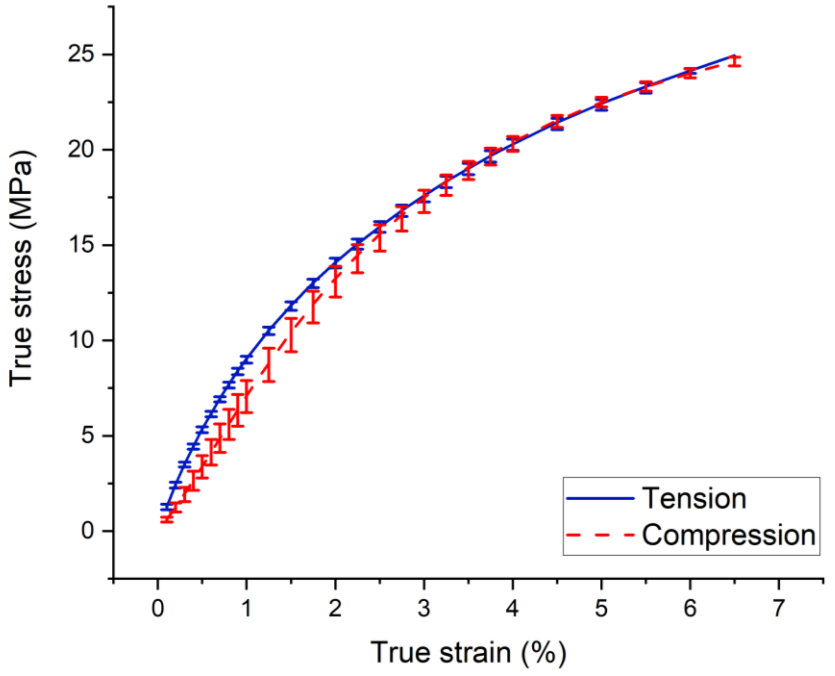

Figure 17 True stress and strain curve for both tension and compression

There has been some argue whether we should differentiate the tension and compression in the study of HDPE elastoplastic behaviors. It is argued in [143] that polymers could be pressure sensitive and that the Drucker-Prager model shall be applied to incorporate the pressure dependency of HDPE in the characterization of elastoplastic behavior. While some studies also showed that the high molecular weight polyethylene would have identical tension and compression behavior and the commonly used von-Mises model is capable of capturing its behavior [144], [145]. In our case, as shown in Figure 17, the tension and compression behaviors look identical in plastic region and quite alike in elastic region. The tangents in the elastic region, however, have quite large difference. If one combines the tension and compression data into a single curve, it will look like the plot in Figure 18, which still looks quite reasonable with limited variation as indicated by the error bar. In order to quantify the elastoplastic behavior and determine which model to use, the following parameters are defined from the loading curve: the Young's modulus is defined as the averaged tangent value of true strain up to 0.5%, as an indicator for elastic behavior; the commonly used 0.2% strain offset method is applied to define the region for elastic and plastic deformation and the corresponding yield stress, which are plotted in Figure 18 for better understanding. The above defined parameters are calculated for pure tension, pure compression and combined test data and are listed in Table 5 for comparison.

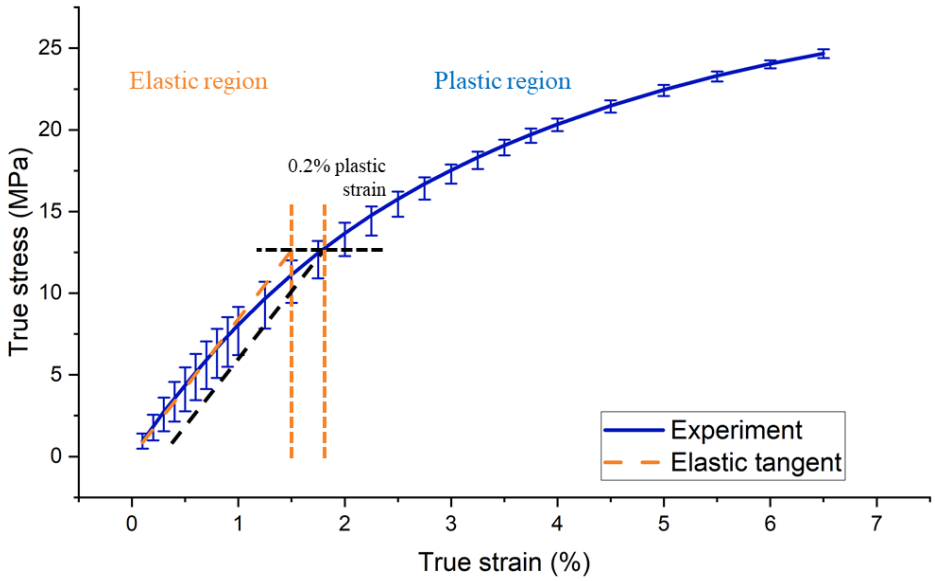

Figure 18 Combined true stress strain loading curve

Table 5 Elastic and plastic parameters from loading curves

Test	Young's modulus/MPa	Yield strain/%	Yield stress/MPa
Pure tension	978.3	1.26	12.35
Pure compression	703.8	2.25	15.85
Combined data	841	1.56	13.15

Table 5 shows that that the elastic and plastic parameters are considerably different for pure tension and pure compression, although the large plastic deformations are almost identical. However, the combined data curve also looks reasonable with limited variation. The next subsection shows two models and compares their difference in fitting the experimental data.

2.5.2 The von-Mises elastoplastic model

The commonly-used elastoplastic model, the von-Mises elastoplastic model with isotropic hardening, is applied to fit the loading curve of the combined data described in Figure 18. Although von-Mises model cannot characterize a lot of special characteristics of HDPE, it is the simplest

plastic model that can capture the monotonic loading behavior, and has been applied in multiple studies with high molecular weight polyethylene before [144], [145].

An exponential hardening function is utilized to describe the true stress strain behavior of the HDPE, with the constitutive relation characterized as the following two segments:

A power law hardening function is utilized to describe the true stress strain behavior of the HDPE, with the constitutive relation characterized in Eq. (2.5):

$$\sigma(\varepsilon) = \begin{cases} E\varepsilon & \varepsilon \le \varepsilon_y \\ \sigma_y + h \cdot (\varepsilon_p)^q & \varepsilon_y < \varepsilon \le 0.12 \end{cases} \tag{2.5}$$

Where h and q are the hardening parameters for the plastic strain ε_p, with ε_y and σ_y indicating yield strain and yield stress, respectively. The power law hardening is commonly used in material hardening analysis and has been applied in the FGM studies as well [146]. The combined data is used in the model to obtain the parameters listed in Table 6. The simulated loading curve is plotted in Figure 19 with the experimental data, with the coefficient of determination $r^2 = 0.994$. It is seen that the power hardening function has a straighter curve when the strain gets large, comparing to the experimental data. To solve this issue, an exponential hardening function can be used to better fit the curve. However, the performance of exponential hardening in the Drucker-Prager model, which will be shown in the next section, is not good, so we will stay with the power law hardening function for the comparison.

Table 6 Parameters for power hardening function

Parameters	E/MPa	$\boldsymbol{\varepsilon_y}$	$\boldsymbol{\sigma_y}$/MPa	h/MPa	q
Value	841	1.56%	13.15	109.8	0.74

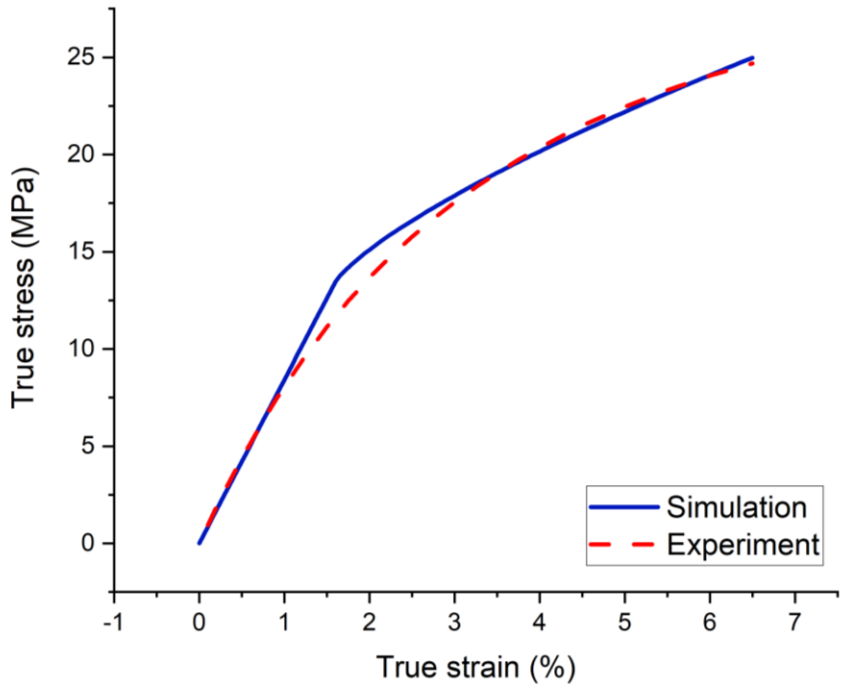

Figure 19 Elastoplastic behavior of HDPE based on power hardening model

2.5.3 The Drucker-Prager elastoplastic model

If the tension and compression behaviors are considered different, then the traditional von-Mises based model no longer applies. The difference in tension and compression could be resulted from the pressure dependency of HDPE, where the hydrostatic compression will tighten the molecular connection and increase the yielding stress. The Drucker-Prager yield criterion is a pressure dependent model that considers the hydrostatic pressure to the plastic modeling. It was first introduced to deal with the plastic deformation of soils, where the tensile strength is much weaker than the compression strength. The criterion is based on the assumption that the octahedral shear stress at failure depends linearly on the octahedral normal stress through material constants [147]. Some polymer materials also exhibit the similar behavior with soils, such that the tensile performance is different with the compression, and the Drucker-Prager model was investigated to

incorporate the hydrostatic pressure effect [143]. Therefore, the Drucker-Prager model is also investigated in this study to compare with the von-Mises model.

The yield function for the Drucker-Prager model is written in Eq. (2.6), with the isotropic power law hardening considered:

$$F = \sqrt{3J_2} + aI_1 - \sigma_y - h(e^p)^q \tag{2.6}$$

where I_1 indicates the hydrostatic stress with definition $I_1 = \frac{1}{3}\sigma_{kk}$; h and q are the hardening parameters; and a stands for the coefficient for the hydrostatic pressure. It is noted that the pressure dependency only influences the yield stress in tension and compression. It will not have contribution towards elastic behavior, i.e. the absolute value of Young's modulus will not be affected. Since tension and compression have different performance in elastic range, as shown in Figure 17, the average Young's modulus listed in Table 5 of 841 MPa is chosen for the elastic simulation. Since the compressive yield stress is σ^c =15.85 MPa, while the tensile yield stress is σ^t =12.35MPa, the following two equations can be formulated right at the yielding points for both compression and tension

$$\sigma^c - \frac{a}{3}\sigma^c = \sigma_y \tag{2.7}$$

$$\sigma^t + \frac{a}{3}\sigma^t = \sigma_y \tag{2.8}$$

By plugging the numbers into the above equations, we have $a = 3\frac{\sigma^c - \sigma^t}{\sigma^c + \sigma^t} = 0.37$, $\sigma_y = 13.88$ MPa. The hardening parameters can be determined by curve fitting of plastic deformation data for both compression and tension. For uniaxial loading, the external stress is σ_{ext}, making the $\sqrt{3J_2} = \sqrt{\sigma_{ext}^2} = |\sigma_{ext}|$. The yielding function is always zero during the strain hardening process, resulting in the following equation for the curve fitting:

$$|\sigma_{ext}| + \frac{a}{3}\sigma_{ext} - \sigma_y = h(e^p)^q \tag{2.9}$$

The determined parameters are listed in Table 7 with the simulated true stress strain curve plotted in Figure 20, together with experimental data. The r^2 for the curve fitting reaches 0.997. The fitted curve is considered as the average of tension and compression and will overestimate stress in compression and underestimate stress in tension, as is seen in Figure 20.

Table 7 Parameters for Drucker-Prager model with power hardening function

Parameters	$\boldsymbol{\sigma_y}$/MPa	a	h/MPa	q
Value	13.883	0.372	188	0.9107

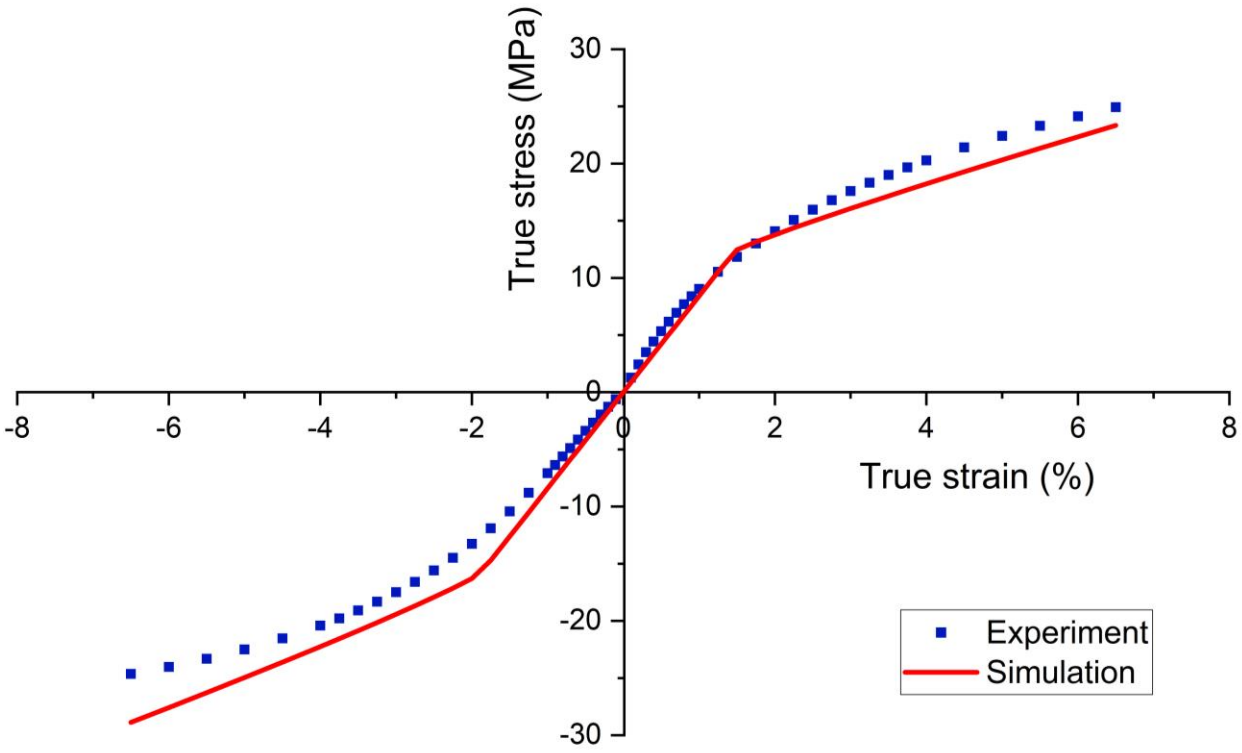

Figure 20 Elastoplastic behavior of HDPE based on Drucker-Prager model with power hardening function

Comparing the result in Figure 19 and Figure 20 we see that although the pressure sensitivity is considered in the Drucker-Prager model, the estimation error is large when the plastic deformation

is large. The pressure sensitivity will not contribute to the elastic performance, which is where the HDPE performances differ. Therefore, the von-Mises model with power law isotropic hardening is chosen in the FGM modeling of next chapter, thanks to its simplicity and accuracy.

2.6 Conclusions

The fabrication process of a building integrated photovoltaic thermal (BIPVT) roofing panel made of Al/HDPE-based functionally graded material is discussed in detail in this chapter, where a clear and continuous gradation of the material is observed along the thickness. The enhanced performance of the thermal energy harvesting and the photovoltaic efficiency is tested and recorded with the data acquisition system under the solar simulator. Significant improvements of the PV efficiency are observed with the water cooling inside the panel. The overall efficiency could reach more than 75% combining the thermal and PV energy harvesting. In order to prepare for the mechanical testing in the next chapter, a novel nondestructive testing methodology based on the image analysis is introduced in this chapter, to statistically capture the volume fraction distribution of the FGM sample along the thickness. The recognized particle distribution pattern keeps the same as the original image. This method can be extended to any composite measurements where the reinforcement phase and the matrix phase have significant difference of the light reflectance rate. The tension and compression test of the high-density polyethylene is conducted following the testing standard, to obtain the elastoplastic properties for the modeling in the next chapter. Both von-Mises and the Drucker-Prager models are used to fit the measurement. The von-Mises model enjoys a better performance and shall be used for the future modeling.

Chapter 3 Micromechanics based elastoplastic behavior of functionally graded materials in BIPVT

3.1 Overview

As is discussed in Chapter 2, the functionally graded material plays an important role in the design and fabrication of the BIPVT system, by transferring the excessive heat into the water tubes for the energy harvesting and not jeopardizing the in-door comfort. Since the BIPVT system is designed to be implemented into the building structure, a comprehensive investigation of its thermal and mechanical performance is needed before the application.

The elastoplastic behavior is an essential problem for the optimal design and application of composite materials. It has been investigated vastly for many decades and all the approaches can be classified into the following three categories [148]: 1. computational micromechanics method, 2. variational approach for upper and lower bounds, and 3. analytical homogenization models. The analytical homogenization models provide physic-based analysis to formulate the relations of field parameters between matrix and reinforcement in microscope so that homogenization schemes can be utilized to provide a macroscale behavior prediction. Although it is appreciated that the actual yielding process will start from some local area, its contribution to the macro plastic strain of the composite, thanks to its negligible volume fraction, is practically insignificant [149]. Therefore, the average, or homogenization process, should be a reasonable approximation to the determination of yield point of the composites. Since the relations between field parameters are derived from the physics, deeper interpretations can be made from the explicit results. The analytical approaches require much less computation, give deterministic predictions rather than a range of results, and therefore exhibit advantages over the other two approaches.

In the past decades, many researchers focus on the analytical elastoplastic modeling of fiber-reinforced composites and homogeneous particulate-reinforced composites. The research work on the elastoplastic modeling of functionally graded materials (FGMs) is quite limited. Due to the spatial variation of phase volume fraction, FGMs are essentially heterogeneous, which leads to limited analytical schemes to tackle the spatial variation of each phase. Historically, Zuiker (1995) considered the Mori-Tanaka [151], self-consistent [152] and Tamura's [153] models among comparisons of standard micromechanical techniques. After that, a comparison between the Mori-Tanaka, self-consistent models and the finite element simulation of FGM was also presented in Refs [154], [155]. However, those models did not directly analyze the interaction between particles. When the variation is relatively smooth, standard homogenization methods such as Mori-Tanaka model and self-consistent model can be applied, while higher order generalized theories should be used [156], [157] when the gradation is sharp. In addition, finite element models [158], [159] based on micromechanics have been used to predict the material properties of FGMs. These methods were computationally intensive and inconvenient to be implemented for engineering structural analysis, when considering the local particle interactions.

The micromechanics based homogenization has been widely utilized to analyze the elastoplastic [160]–[164] and viscoplastic [165]–[170] problems of two-phase composites. In recent years, it is considered an effective approach to analyze the FGMs [171], [172], where the materials are homogenized locally in the representative volume element (RVE) scale to achieve globally heterogeneous behavior in the macroscopic scale. Eshelby [173], [174] developed the equivalent inclusion method (EIM) to study the elastic field of a single inhomogeneity within an infinite matrix domain, in which the difference of material properties mismatch between particle and matrix is represented by the eigenstrain. Moschovidis and Mura [175] further modified and

extended this method to address the multi-particle problem and ellipsoidal shape. The EIM is a powerful tool which can give out the detailed stress and strain fields for both particles and matrix. By using the EIM, Ju and Chen [176], [177] presented the elastic prediction of particle-reinforced metal matrix composites (PRMMC) with spherical and spheroidal particles. After that, Ju and Chen [178] also studied the effective elastoplastic deformations and responses of PRMMC by introducing the "effective yield criterion", which is derived micromechanically by considering effects of elastic spherical particles embedded in the elastoplastic matrix. Ju and Tseng [179], [180] further extended this theory by considering the pair-wise spherical particle interaction in particle reinforced ductile matrix composites, and they derived analytical expressions for the bulk and shear moduli of a two-phase composite. Built upon this, Ju and Sun [181] and Sun and Ju [182] proposed an expression for the overall elastoplastic stress-strain of randomly located, aligned spheroid reinforced metal matrix composites. Furthermore, elastoplastic responses of metal matrix composites with more complicated particle distribution (i.e., randomly located and randomly oriented particles in the matrix) were developed by Sun and Ju [183].

Majority of studies mentioned above were mainly developed for homogeneous composites with uniform particle distribution, i.e. material gradation being zero. When FGMs with polymeric matrix are subjected to externally applied mechanical or thermal loadings, plastic deformation is commonly developed in the polymeric matrix. Therefore, the elastoplastic analysis of the FGMs is highly desired to accurately characterize their elastoplastic behavior. By comparing with the micromechanical model of FGMs, Gasik [184] provided a Gasik-Ueda model to characterize the elastoplastic properties of FGMs, which works for dilute distribution of particles in a uniform matrix without considering the particle interactions. After that, Yin et al. [185] proposed an elastic algorithm that contains the coupling effect of neighboring layers and particle pair-wise interaction

in the micromechanics scheme to accommodate the graded nature of FGMs, which has been extended to interfacial debonding [186] and thermomechanical [187] behaviors.

In this chapter, the micromechanics-based theoretical algorithm is discussed for the thermo and elastoplastic modeling of the functionally graded materials with particle reinforcement. A brief review is given in Section 3.2 to introduce the equivalent inclusion method, which is the foundation to the proposed micromechanics modeling. Section 3.3 and Section 3.4 discuss the elastic and thermo-elastic formulations of a two-phase particle reinforced functionally graded materials, based on our previous work [172], [185]. The spherical particle shape is assumed, and the pair-wise particle interaction effect is taken into consideration. The elastoplastic modeling is then introduced in Section 3.5 following the elastic scheme, by assuming that the plastic deformation only occurs in the matrix phase (HDPE phase). The ensemble average yield function is introduced with the stress norm from micromechanics-based scheme. The corresponding plastic algorithm is discussed. Both von-mises and Drucker-Prager yielding conditions are assumed and derived. The thermo elastoplastic modeling is studied in Section 3.6 as an extension to the elastoplastic modeling, by considering the quasi-static temperature effect. The theoretical verification and the experimental validation are conducted and discussed in Section 3.7. Case studies of particle volume fraction and distribution function are studied in Section 3.8 and serve as the guideline for the future research and engineering.

3.2 Formulation of the Equivalent Inclusion Method

Due to the local disturbance from existing inhomogeneities, the mechanical response of composite is much more complicated than that of homogeneous material. Particularly, when a composite

material is under a uniform far-field strain ε_{ij}^0 or stress σ_{ij}^0, the distribution of stress and strain in local domain is no longer uniform anymore. In order to accurately model the local disturbance due to the inhomogeneities, J. D. Eshelby in 1959 proposed a micromechanical approach call the Equivalent Inclusion Method (EIM), to investigate the elastic field inside and outside of an elliptical inhomogeneity in the infinite domain.

The case of a single spherical inhomogeneity Ω embedded inside an infinite matrix domain *D* is considered as an example, with a prescribed uniform far-field strain $\boldsymbol{\varepsilon}^0$. The material properties of the matrix are denoted as a fourth order tensor $\boldsymbol{C}_0$ and the inhomogeneity's as $\boldsymbol{C}_1$.

Due to the existence of the inhomogeneity, the strain field in the local neighborhood is no longer uniform due to the material properties mismatch. In order to quantify the difference, the local strain field is decomposed into a part identical to the prescribed uniform far-field strain and another part for the disturbed local strain field,

$$\boldsymbol{\varepsilon} = \boldsymbol{\varepsilon}^{\boldsymbol{0}} + \boldsymbol{\varepsilon}' \tag{3.1}$$

where the disturbed strain $\boldsymbol{\varepsilon}'$ represents the influence of elastic material mismatch between the inhomogeneity and the matrix. Therefore, the constitutive relations for both inside and outside of the inhomogeneity domain are written as:

$$\begin{cases} \sigma_{ij}^0 + \sigma_{ij}' = C_{ijkl}^1(\varepsilon_{kl}^0 + \varepsilon_{kl}') & x \in \Omega \\ \sigma_{ij}^0 + \sigma_{ij}' = C_{ijkl}^0(\varepsilon_{kl}^0 + \varepsilon_{kl}') & x \in D - \Omega \end{cases} \tag{3.2}$$

The influence of material properties mismatch is taken into consideration in the Eshelby's equivalent inclusion method, through a so-called eigenstrain $\boldsymbol{\varepsilon}^*$. As is depicted in Figure 21, the original configuration of an inhomogeneity inside a uniform matrix is decomposed into the combination of two cases: one with pure matrix configuration under the same strain field $\boldsymbol{\varepsilon}^0 + \boldsymbol{\varepsilon}'$, and an additional one with pure matrix configuration under the influence of the eigenstrain $\boldsymbol{\varepsilon}^*$

inside the inhomogeneity domain. In such a way the original composite configuration is then converted into a homogeneous matrix configuration with the eigenstrain "storing" the material mismatch information, and the original inhomogeneity problem is converted to an inclusion problem within pure matrix phase. The constitutive relations for both inside and outside the inhomogeneity are then converted to:

$$\begin{cases} \sigma_{ij}^0 + \sigma_{ij}' = C_{ijkl}^0(\varepsilon_{kl}^0 + \varepsilon_{kl}' - \varepsilon_{kl}^*) & x \in \Omega \\ \sigma_{ij}^0 + \sigma_{ij}' = C_{ijkl}^0(\varepsilon_{kl}^0 + \varepsilon_{kl}') & x \in D - \Omega \end{cases} \tag{3.3}$$

The eigenstrain $\boldsymbol{\varepsilon}^*$, now as the proxy of the material properties mismatch, is responsible for the disturbance of the local strain field and shall be related to the $\boldsymbol{\varepsilon}'$.

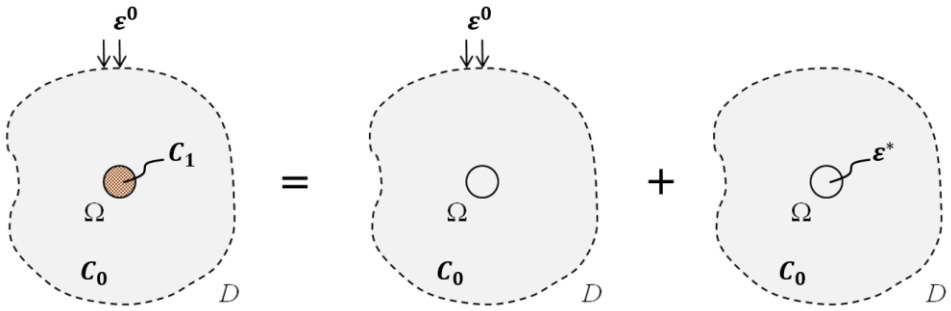

Figure 21 Eshelby's equivalent inclusion method – using an eigenstrain in an inclusion to represent the inhomogeneity

Since the eigenstrain is an inclusion inside the inhomogeneity's domain, it can be considered as a body force to the matrix. The influence of an inclusion is a classical solid mechanics problem and can be theoretically addressed with the help of Green's function. For the case with spherical inhomogeneity domain, the corresponding Green's function is written as

$$G_{ij}(\boldsymbol{x}, \boldsymbol{x}') = \frac{1}{4\pi\mu}\frac{\delta_{ij}}{|\boldsymbol{x}-\boldsymbol{x}'|} - \frac{1}{16\pi\mu(1-\nu)}\frac{\partial^2|\boldsymbol{x}-\boldsymbol{x}'|}{\partial x_i \partial x_j} \tag{3.4}$$

where δ_{ij} is the Kronecker delta function and μ and ν are shear modulus and Poisson ratio of matrix phase, respectively. Using the Kelvin's approach, the distributed body force effect from the eigenstrain $\boldsymbol{\varepsilon}^*$ can be derived and linked to the disturbed strain field $\boldsymbol{\varepsilon}'$ as:

$$\boldsymbol{\varepsilon}' = -\int_{\Omega} \boldsymbol{G}(\boldsymbol{x}, \boldsymbol{x}') \cdot \boldsymbol{C}_0 : \boldsymbol{\varepsilon}^*(\boldsymbol{x}') d\boldsymbol{x}' \tag{3.5}$$

Plug the Green's function in Eq. (3.4) into the derivation will arrive at a concise presentation of Eq. (3.5) as

$$\boldsymbol{\varepsilon}' = -\boldsymbol{D} : \boldsymbol{C}_0 : \boldsymbol{\varepsilon}^* \tag{3.6}$$

where the fourth order tensor $\boldsymbol{D}$ is given in the Appendix at the end of this chapter and consisted of two cases, one within the inhomogeneity domain $\boldsymbol{D}^{\Omega}$ and one outside the domain $\boldsymbol{D}^{\bar{\Omega}}$. Eq. (3.6) between disturbed strain and the eigenstrain is connected with the stress equivalent condition from the equivalent inclusion method as

$$\boldsymbol{C}_1 : (\boldsymbol{\varepsilon}^0 + \boldsymbol{\varepsilon}') = \boldsymbol{C}_0 : (\boldsymbol{\varepsilon}^0 + \boldsymbol{\varepsilon}' - \boldsymbol{\varepsilon}^*) \tag{3.7}$$

to generate the relation to the prescribed far-field strain $\boldsymbol{\varepsilon}^0$ as

$$\boldsymbol{\varepsilon}^* = \boldsymbol{C}_0^{-1} \cdot (\boldsymbol{D}^{\Omega} - \Delta \boldsymbol{C}^{-1})^{-1} : \boldsymbol{\varepsilon}^0 \tag{3.8}$$

In Eq. (3.4), $\Delta \boldsymbol{C} = \boldsymbol{C}_1 - \boldsymbol{C}_0$ is the stiffness difference. It is noted that the fourth order tensor $\boldsymbol{D}^{\Omega}$, as described in Eq. (3.6), is not a function of location and remains constants over the inhomogeneity domain. With the help of Eq. (3.3), (3.6) and (3.7), the one spherical inhomogeneity problem is fully defined under equivalent inclusion method domain and the total strain inside the inhomogeneity domain $\bar{\boldsymbol{\varepsilon}}$ is a uniform value with the equation

$$\bar{\boldsymbol{\varepsilon}} = (\boldsymbol{I} - \boldsymbol{D}^{\Omega} \cdot \Delta \boldsymbol{C})^{-1} : \boldsymbol{\varepsilon}^0 \tag{3.9}$$

where $\boldsymbol{I}$ signified the fourth-rank identity tensor $I_{ijkl} = \frac{1}{2}\left(\delta_{ik}\delta_{jl} + \delta_{il}\delta_{jk}\right)$.

Such algorithm was extended to the case of two spherical particles inside an infinite matrix domain by [175]. By using the polynomial expansion, the total strain within each particle domain is derived as:

$$\bar{\bar{\boldsymbol{\varepsilon}}} = \frac{1}{V_{\boldsymbol{\Omega}}}\int_{\boldsymbol{\Omega}} \boldsymbol{\varepsilon}\, d\boldsymbol{\Omega} = \left(\boldsymbol{I} - \boldsymbol{D}^{\Omega}\cdot\Delta\boldsymbol{C} - \boldsymbol{D}^{\bar{\Omega}}\cdot\Delta\boldsymbol{C}\right)^{-1} : \boldsymbol{\varepsilon^0} + O(\tilde{\rho}^8) \tag{3.10}$$

where $\tilde{\rho} = a/b$ and $V_{\boldsymbol{\Omega}} = 4\pi a^3/3$ with a and b being the particle radius and the center-to-center distance between the two particles centered at $\boldsymbol{x_1}$ and $\boldsymbol{x_2}$, respectively. The precision of Eq. (3.10) can reach the order of $O(\tilde{\rho}^8)$ where $\tilde{\rho}$ is not higher than 0.5. Since Eq. (3.10) represents the volume average strain within one of the two particles with the influence of the other, by subtracting Eq. (3.9) the average influence of one particle to the other one can be addressed as:

$$\boldsymbol{d}(\boldsymbol{x_1}, \boldsymbol{x_2}) = \bar{\bar{\boldsymbol{\varepsilon}}} - \bar{\boldsymbol{\varepsilon}} = \Delta\boldsymbol{C}^{-1}\cdot\boldsymbol{L}(\boldsymbol{x_1}, \boldsymbol{x_2}) : \boldsymbol{\varepsilon}^0 \tag{3.11}$$

where the particle pair-wise interaction tensor $\boldsymbol{L}(\boldsymbol{x_1}, \boldsymbol{x_2})$ is:

$$\boldsymbol{L}(\boldsymbol{x_1}, \boldsymbol{x_2}) = \left(\left[\Delta\boldsymbol{C}^{-1} - \boldsymbol{D}^{\Omega} - \boldsymbol{D}^{\bar{\Omega}}\right]^{-1} - \left[\Delta\boldsymbol{C}^{-1} - \boldsymbol{D}^{\Omega}\right]^{-1}\right) + O(\tilde{\rho}^8) \tag{3.12}$$

The explicit expression of $\boldsymbol{L}$ can be found in the Appendix at the end of this chapter.

It is noted that Eq. (3.11) can be extended to represent the pair-wise interactions of multiple particles P_i $(i = 2,3, \dots)$ to one particle $P_1(\boldsymbol{x_1})$, such that for a given particle configuration $\mathcal{G}$ with N particles. The average strain in $P_1(\boldsymbol{x_1})$ domain is derived through a linear summation of all the pair-wise interactions from neighboring particles as:

$$\tilde{\boldsymbol{\varepsilon}}(\boldsymbol{x}_1) = \bar{\boldsymbol{\varepsilon}} + \sum_{i=2}^{N} \boldsymbol{d}(\boldsymbol{x}_1, \boldsymbol{x}_i) \tag{3.13}$$

The pair-wise interaction between particles is a simplified approximation to the real multi-body interaction in the composite. Good agreement has been observed between the pair-wise interaction and the Finite Element simulation for the multi-body interaction, when the volume fraction is less than 35%. For the composite with volume fraction larger than 35%, more than 10% difference can

be expected for the modulus prediction [188]. For large particle volume fraction, the multi-body interactions can be modeled by considering the each individual particles instead of doing the ensemble average, with the help of the inclusion-based boundary element method (iBEM), which is also based on the equivalent inclusion method [189].

3.3 Elastic modeling of functionally graded materials

The equivalent inclusion method mentioned above can be applied for the elastic modeling of functionally graded materials. The typical macro and micro structure of a two phase functionally graded material is shown in Figure 22, with the macro coordinate represented by $X_i(i = 1, 2, 3)$ and micro coordinate by $x_i(i = 1, 2, 3)$. The gradation is assumed along the $X_3(x_3)$ direction, for both macro and micro scales. If one zoomed in from a macroscopic point $\boldsymbol{X}^0$ to the corresponding microstructure, the representative volume element will look like the right-hand-side of Figure 22, with multiple randomly located particles embedded inside the matrix phase. Without loss of generality, it is assumed that one particle P_1 existed right at the center $\boldsymbol{x} = \boldsymbol{0}$ of the RVE.

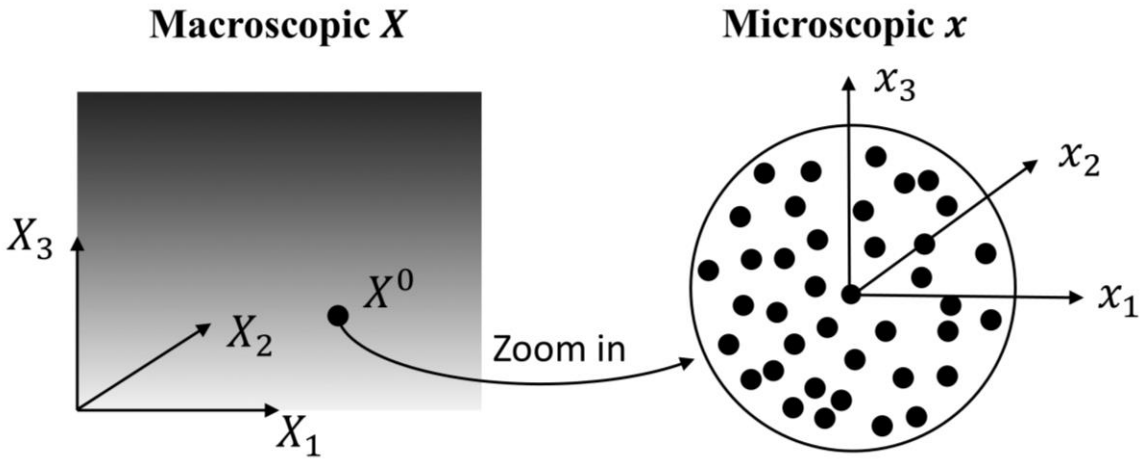

Figure 22 A micromechanics-based model of FGM to predict the effective behavior considering the microstructural aspects

With the help of Eq. (3.13), the averaged strain inside the P_0 domain can be determined considering the influence from all other neighboring particles as:

$$\langle \boldsymbol{\varepsilon} \rangle^{P_1} = (\boldsymbol{I} - \boldsymbol{D}^{\Omega} \cdot \Delta \boldsymbol{C})^{-1} : \boldsymbol{\varepsilon}^0(P_1) + \sum_{i=2}^{\infty} \Delta \boldsymbol{C}^{-1} \cdot \boldsymbol{L}(P_1, P_i) : \boldsymbol{\varepsilon}^0(P_i) \tag{3.14}$$

where $\boldsymbol{\varepsilon}^0(P_i)$ represents the prescribed far field strain corresponding to the particle P_i at the microscopic location $\boldsymbol{x}_i$, such that the above equation can be further written as:

$$\langle \boldsymbol{\varepsilon} \rangle(\mathbf{0}) = (\boldsymbol{I} - \boldsymbol{D}^{\Omega} \cdot \Delta \boldsymbol{C})^{-1} : \boldsymbol{\varepsilon}^0(\mathbf{0}) + \sum_{i=2}^{\infty} \Delta \boldsymbol{C}^{-1} \cdot \boldsymbol{L}(\mathbf{0}, \boldsymbol{x}^{\boldsymbol{i}}) : \boldsymbol{\varepsilon}^0(x_3^i) \tag{3.15}$$

It is noted that for the single particle case, the prescribed far field strain is uniform across the whole domain, while for the case of multiple particles with a gradation, the prescribed far field strain is only uniform within the transverse plane of the gradating direction, and varies with the gradation in the microscope. Therefore the $\boldsymbol{\varepsilon}^0(x_3^i)$ can be related to the RVE center $\boldsymbol{\varepsilon}^0(0)$ through Taylor expansion to the first order, as:

$$\boldsymbol{\varepsilon}^0\left(x_3^i\right) \cong \boldsymbol{\varepsilon}^0(\mathbf{0}) + \boldsymbol{\varepsilon}^0_{,3}(\mathbf{0})\left(x_3^i - \mathbf{0}\right) = \boldsymbol{\varepsilon}^0(\mathbf{0}) + \boldsymbol{\varepsilon}^0_{,3}(\mathbf{0}) x_3^i \tag{3.16}$$

So far, all the derivations are conducted in the microscope of the FGM. In order to characterize the general behavior of the FGM for the macroscopic performance prediction, theoretically the summation of pair-wise interactions over all possible particles are needed for the strain calculation of a single particle location. A particle probability density function $P(\boldsymbol{x}|\mathbf{0})$ is introduced to convert the summation to an integration, to arrive at the ensemble average form of Eq. (3.15). Physically, the $P(\boldsymbol{x}|\mathbf{0})$ means the probability of a particle's existence at a certain location $\boldsymbol{x}$, given the existence of another particle's existence at the center location $\mathbf{0}$. Therefore, the summation of the pair-wise interaction is converted into the integral over all possible particle positions as follows:

$$\langle \boldsymbol{d} \rangle(\mathbf{0}) = \sum_{i=1}^{\infty} \Delta \boldsymbol{C}^{-1} \cdot \boldsymbol{L}(\mathbf{0}, \boldsymbol{x}^{\boldsymbol{i}}) : \boldsymbol{\varepsilon}^0(x_3^i) = \int_D P(\boldsymbol{x}|\mathbf{0}) \Delta \boldsymbol{C}^{-1} \cdot \boldsymbol{L}(\mathbf{0}, \boldsymbol{x}^{\boldsymbol{i}}) : \boldsymbol{\varepsilon}^0(x_3^i) d\boldsymbol{x} \tag{3.17}$$

There have been may discussions about the formula of the particle probability density function $P(\boldsymbol{x}|\boldsymbol{0})$, [176], [181]. The simplest assumption is that the all particles are located independently, such that a particle's pre-existence will not influence another one's probability of existence at any locations. The corresponding probability density function would be simply $\frac{3\phi}{4\pi a^3}$ for homogeneous composite. For functionally graded materials, however, a new formulation is proposed to incorporate the effect of gradation effect, i.e. the derivations of the particle volume fraction, following the first order Taylor expansion form:

$$P(\boldsymbol{x}|\boldsymbol{0}) = \frac{3}{4\pi a^3}\left[\phi(X_3) + e^{-\frac{x}{\delta}}\phi_{,3}(X_3)\cdot x_3\right] \tag{3.18}$$

The δ is the parameter to control the attenuation rate such that the probability function remains within a reasonable range inside the RVE. Eqs. (3.16) to (3.18) are plugged into Eq. (3.15) to formulate the explicit relation between particle strain and prescribed far field strain:

$$\langle\boldsymbol{\varepsilon}\rangle(X_3) = (\boldsymbol{I} - \boldsymbol{D^{\Omega}}\cdot\Delta\boldsymbol{C})^{-1}\colon\boldsymbol{\varepsilon}^0(X_3) + \phi\Delta\boldsymbol{C}^{-1}\cdot\boldsymbol{\mathcal{D}}\colon\boldsymbol{\varepsilon}^0(X_3) + \phi_{,3}\Delta\boldsymbol{C}^{-1}\cdot\boldsymbol{\mathcal{F}}\colon\boldsymbol{\varepsilon}^0_{,3}(X_3) \tag{3.19}$$

The explicit expressions of $\boldsymbol{\mathcal{D}}$ and $\boldsymbol{\mathcal{F}}$ are introduced in the Appendix at the end of this chapter. The tensor $\boldsymbol{\mathcal{D}}$ addresses the pair-wise interaction effect between particles, while the tensor $\boldsymbol{\mathcal{F}}$ specially accounts for the coupling effect of neighboring layers along the gradation direction. In Eq. (3.19), it is noticed that $\boldsymbol{\varepsilon}^0(X_3)$ is used to represent the $\boldsymbol{\varepsilon}^0(\boldsymbol{0})$, the prescribed far field strain at the microscopic center of the RVE. It is based on the Mori-Tanaka assumption that the macroscopic matrix strain $\boldsymbol{\varepsilon}^0(X_3)$ functions as the far field strain at its corresponding microscopic RVE center. Eq. (3.19) gives the ensemble average relation between particle strain $\langle\boldsymbol{\varepsilon}\rangle(X_3)$ and matrix strain $\boldsymbol{\varepsilon}^0(X_3)$ in the macroscope, and is further coupled with the volumetric relation of stress and strain

$$\overline{\boldsymbol{\sigma}} = \phi(X_3)\boldsymbol{C}_1\colon\langle\boldsymbol{\varepsilon}\rangle(X_3) + [1-\phi(X_3)]\boldsymbol{C}_0\colon\boldsymbol{\varepsilon}^0(X_3) \tag{3.20}$$

to solve whole system at any location, where $\bar{\boldsymbol{\sigma}}$ represents the applied external load along the thickness direction. Given $\bar{\boldsymbol{\sigma}}$, Eqs. (3.19) and (3.20) formulate an ordinary differential equation which can be solved by backward Euler's method, such that the elastic behavior of FGMs considering the pair-wise particle interaction is well defined.

It is noted that in the study of Yin et al (2004), three material zones in the gradation are introduced with the two zones containing the reverse of matrix and particle phases to accommodate for the composite with high particle volume fraction, and a transition zone to bridge the results from two sides. Since the FGMs used in the present study are typically having volume fraction of aluminum particles less than 60% in the HDPE matrix [190], only one zone is considered in scope of this chapter.

3.4 Thermo-elastic modeling of functionally graded materials

The functionally graded material was first invented as the thermal barrier in a spaceplane project in Japan in 1984, which need to sustain a temperature gradient of 1000 K across a section less than 10 mm. Therefore, the thorough understanding of the thermal performance is very important for the application of FGM. In this section, the effect of the thermal influence to the formulation of equivalent inclusion method is discussed, followed by the model of thermo-elastic analysis for functionally graded materials. The derivation shares some similarities with previous sections but has its own specialties.

It is known that the local strain field would be disturbed by the inhomogeneity under pre-applied mechanical field, as is shown in Eq. (3.1). If the applied loading is not only a mechanical field $\boldsymbol{\sigma}^0$ but also a thermal field, e.g. a quasi-static temperature difference of T is applied to the composite,

the relation between stress and strain is no longer simply related by the stiffness. The far field matrix strain now becomes:

$$\boldsymbol{\varepsilon}^0 = (\boldsymbol{C}_0)^{-1}\colon \boldsymbol{\sigma}^0 + \alpha_0 T\boldsymbol{\delta} \tag{3.21}$$

where α_0 is the coefficient of thermal expansion (CTE) for matrix and the $\boldsymbol{\delta}$ is the Kronecker delta function.

The constitutive relations for both inside and outside of the inhomogeneity are the similar with Eq. (3.1) and is written below with the temperature effect:

$$\begin{cases} \sigma_{ij}^0 + \sigma_{ij}' = C_{ijkl}^1(\varepsilon_{kl}^0 + \varepsilon_{kl}' - \varepsilon_{kl}^T) & x \in \Omega \\ \sigma_{ij}^0 + \sigma_{ij}' = C_{ijkl}^0(\varepsilon_{kl}^0 + \varepsilon_{kl}') & x \in D - \Omega \end{cases} \tag{3.22}$$

where $\varepsilon_{kl}^T = (\alpha_1 - \alpha_0)T\delta_{kl}$ is the thermal equivalent eigenstrain, and α_1 is the CTE for the inhomogeneity.

Following the equivalent inclusion method, the material mismatch between the matrix and inhomogeneity will be replaced with the eigenstrain ε_{kl}^*, making the constitutive relation written as:

$$\begin{cases} \sigma_{ij}^0 + \sigma_{ij}' = C_{ijkl}^0(\varepsilon_{kl}^0 + \varepsilon_{kl}' - \varepsilon_{kl}^* - \varepsilon_{kl}^T) & x \in \Omega \\ \sigma_{ij}^0 + \sigma_{ij}' = C_{ijkl}^0(\varepsilon_{kl}^0 + \varepsilon_{kl}') & x \in D - \Omega \end{cases} \tag{3.23}$$

By comparing Eq. (3.23) with Eq. (3.3), one can easily arrive at the conclusion that the disturbed strain $\boldsymbol{\varepsilon}'$ can be related to the eigenstrain and thermal difference strain through the Green's function $\boldsymbol{G}(\boldsymbol{x}, \boldsymbol{x}')$ as:

$$\boldsymbol{\varepsilon}' = -\int_{\boldsymbol{\Omega}} \boldsymbol{G}(\boldsymbol{x}, \boldsymbol{x}') \cdot \boldsymbol{C}_0\colon [\boldsymbol{\varepsilon}^*(\boldsymbol{x}') + \boldsymbol{\varepsilon}^T]\boldsymbol{dx}' = -\boldsymbol{D}^{\boldsymbol{\Omega}}\colon \boldsymbol{C}_0\colon [\boldsymbol{\varepsilon}^*(\boldsymbol{x}') + \boldsymbol{\varepsilon}^T] \tag{3.24}$$

where $\boldsymbol{\Omega}$ represents the particle domain, $\boldsymbol{C}_0$ and $\boldsymbol{C}_1$ are the elastic stiffness tensor of the matrix and the particle, respectively, and $\boldsymbol{D}^{\boldsymbol{\Omega}}$ signifies the integral of the modified Green's function within the spherical particle domain $\boldsymbol{\Omega}$ and has the same expression in Eq. (3.6).

As is indicated in the equivalent inclusion method in Section 2.2, the inhomogeneity problem is transformed into an inclusion problem through the stress equivalent condition in the inhomogeneity domain, such that:

$$\boldsymbol{C}_1 : [\boldsymbol{\varepsilon}^0 + \boldsymbol{\varepsilon}' - \boldsymbol{\varepsilon}^T] = \boldsymbol{C}_0 : [\boldsymbol{\varepsilon}^0 + \boldsymbol{\varepsilon}' - \boldsymbol{\varepsilon}^T - \boldsymbol{\varepsilon}^*] \tag{3.25}$$

The combination of Eqs. (3.23 – 2.25) yields the local eigenstrain field $\boldsymbol{\varepsilon}^*$ and is derived as:

$$\boldsymbol{\varepsilon}^* = \boldsymbol{C}_0^{-1} \cdot (\boldsymbol{D}^{\Omega} - \Delta \boldsymbol{C}^{-1})^{-1} : (\boldsymbol{\varepsilon}^0 - \alpha_1 T \boldsymbol{\delta} - \boldsymbol{D}^{\Omega} \cdot \boldsymbol{C}_0 : \boldsymbol{\varepsilon}^T) \tag{3.26}$$

where $\Delta \boldsymbol{C} = \boldsymbol{C}_1 - \boldsymbol{C}_0$ is the stiffness difference.

Combining Eqs. (3.24) and (3.26), the strain field within the spherical particle domain is shown to be uniform as:

$$\bar{\boldsymbol{\varepsilon}} = \alpha_1 T \boldsymbol{\delta} + (\boldsymbol{I} - \boldsymbol{D}^{\Omega} \cdot \boldsymbol{\Delta C})^{-1} : (\boldsymbol{\varepsilon}^0 - \alpha_1 T \boldsymbol{\delta} - \boldsymbol{D}^{\Omega} \cdot \boldsymbol{C}_0 : \boldsymbol{\varepsilon}^T) \tag{3.27}$$

Such scheme is extended to the case with two spherical particles embedded in an infinite matrix domain. By using the polynomial expansion, the averaged strain field within each particle domain is derived as:

$$\begin{gathered} \bar{\bar{\boldsymbol{\varepsilon}}} = \alpha_1 T \boldsymbol{\delta} + \{\boldsymbol{I} - [\boldsymbol{D}^{\Omega} + \boldsymbol{D}(\boldsymbol{x}_1)] \cdot \Delta \boldsymbol{C}\}^{-1} : \\ \{\boldsymbol{\varepsilon}^0 - \alpha_1 T \boldsymbol{\delta} - [\boldsymbol{D}^{\Omega} + \boldsymbol{D}(\boldsymbol{x}_1)] \cdot \boldsymbol{C}_0 : \boldsymbol{\varepsilon}^T\} + O(\rho^8) \end{gathered} \tag{3.28}$$

where the parameters have been described in Eq. (3.1). The precision also reaches the order of $O(\tilde{\rho}^8)$ where $\tilde{\rho}$ is not higher than 0.5. Subtracting Eq. (3.27) from Eq. (3.28), the average influence of one particle to the other one particle is derived as:

$$\boldsymbol{d}(\boldsymbol{0}, \boldsymbol{x}_1) = \bar{\bar{\boldsymbol{\varepsilon}}} - \bar{\boldsymbol{\varepsilon}} = \Delta \boldsymbol{C}^{-1} \cdot \boldsymbol{L}(\boldsymbol{0}, \boldsymbol{x}_1) : (\boldsymbol{\varepsilon}^{\boldsymbol{0}} - \alpha_1 T \boldsymbol{\delta} - \Delta \boldsymbol{C}^{-1} \cdot \boldsymbol{C}_0 : \boldsymbol{\varepsilon}^T) + O(\rho^8) \tag{3.29}$$

where the particle pair-wise interaction tensor $\boldsymbol{L}(\boldsymbol{x}_1, \boldsymbol{x}_2)$ is the same with Eq. (3.12). Therefore, Eq. (3.29) can be extended to represent the pair-wise interactions of multiple particles P_i ($i = 2,3, \ldots$) to one particle $P_1(\boldsymbol{x}_1)$, such that for a given particle configuration $\mathcal{G}$ with N particles. The average strain of $P_1(\boldsymbol{x}_1)$ domain is given with the pair-wise particle interactions as:

$$\bar{\bar{\boldsymbol{\varepsilon}}}(\boldsymbol{x}_1) = \bar{\boldsymbol{\varepsilon}} + \sum_{i=2}^{N} \boldsymbol{d}(\boldsymbol{x}_1, \boldsymbol{x}_i) \tag{3.30}$$

Following the same procedure as described in Section 2.3, for a microscopic representative volume element of FGM with a particle P_1 sitting at the center, the average strain inside the particle domain with pair-wise particle interaction is give as

$$\begin{aligned} \langle \boldsymbol{\varepsilon} \rangle^{P_1} = \alpha_1 T \boldsymbol{\delta} + (\boldsymbol{I} - \boldsymbol{D}^{\Omega} \cdot \boldsymbol{\Delta C})^{-1} : [\boldsymbol{\varepsilon}^0(P_1) - \alpha_1 T \boldsymbol{\delta} - \boldsymbol{D}^{\Omega} \cdot \boldsymbol{C}_0 : \boldsymbol{\varepsilon}^T] \\ + \sum_{i=2}^{\infty} \boldsymbol{\Delta C}^{-1} \cdot \boldsymbol{L}(P_1, P_i) : (\boldsymbol{\varepsilon}^{\boldsymbol{0}}(P_i) - \alpha_1 T \boldsymbol{\delta} - \Delta \boldsymbol{C}^{-\boldsymbol{1}} \cdot \boldsymbol{C}_0 : \boldsymbol{\varepsilon}^{\boldsymbol{T}}) \end{aligned} \tag{3.31}$$

Since $\boldsymbol{\varepsilon}^0(P_i)$ represents the prescribed far field strain at the same height of the corresponding particle P_i, and varies along the microscopic field with particle volume fraction, the above equation can be further written as:

$$\begin{aligned} \langle \boldsymbol{\varepsilon} \rangle(\boldsymbol{0}) = \alpha_1 T \boldsymbol{\delta} + (\boldsymbol{I} - \boldsymbol{D}^{\Omega} \cdot \boldsymbol{\Delta C})^{-1} : [\boldsymbol{\varepsilon}^0(\boldsymbol{0}) - \alpha_1 T \boldsymbol{\delta} - \boldsymbol{D}^{\Omega} \cdot \boldsymbol{C}_0 : \boldsymbol{\varepsilon}^T] \\ + \sum_{i=2}^{\infty} \boldsymbol{\Delta C}^{-1} \cdot \boldsymbol{L}(\boldsymbol{x}_1 = \boldsymbol{0}, \boldsymbol{x}_i) : \left(\boldsymbol{\varepsilon}^{\boldsymbol{0}}(x_{i,3}) - \alpha_1 T \boldsymbol{\delta} - \Delta \boldsymbol{C}^{-\boldsymbol{1}} \cdot \boldsymbol{C}_0 : \boldsymbol{\varepsilon}^{\boldsymbol{T}}\right) \end{aligned} \tag{3.32}$$

The prescribed far field strain $\boldsymbol{\varepsilon}^0\left(x_3^i\right)$ is related to the far field strain at the center of the RVE $\boldsymbol{\varepsilon}^0(\boldsymbol{0})$ by the Taylor expansion to the first order:

$$\boldsymbol{\varepsilon}^0\left(x_{i,3}\right) \cong \boldsymbol{\varepsilon}^0(\boldsymbol{0}) + \boldsymbol{\varepsilon}^0_{,3}(\boldsymbol{0})(\boldsymbol{x}_i - \boldsymbol{0}) = \boldsymbol{\varepsilon}^0(\boldsymbol{0}) + \boldsymbol{\varepsilon}^0_{,3}(\boldsymbol{0}) x_3 \tag{3.33}$$

Combined with the probability function $P(\boldsymbol{x}|\boldsymbol{0})$ in Eq. (3.18), the summation of the pair-wise interaction is converted into integral over all possible particle positions as follows:

$$\begin{aligned} \langle \boldsymbol{d} \rangle(\boldsymbol{0}) = \sum_{i=1}^{\infty} \boldsymbol{\Delta C}^{-1} \cdot \boldsymbol{L}(\boldsymbol{0}, \boldsymbol{x}_i) : \left[\boldsymbol{\varepsilon}^0\left(x_{i,3}\right) - \alpha_1 T \boldsymbol{\delta} - \Delta \boldsymbol{C}^{-\boldsymbol{1}} \cdot \boldsymbol{C}_0 : \boldsymbol{\varepsilon}^{\boldsymbol{T}}\right] \\ = \int_D P(\boldsymbol{x}|\boldsymbol{0}) \boldsymbol{\Delta C}^{-1} \cdot \boldsymbol{L}(\boldsymbol{0}, \boldsymbol{x}_i) : \left[\boldsymbol{\varepsilon}^0(\boldsymbol{0}) + \boldsymbol{\varepsilon}^0_{,3}(\boldsymbol{0}) x_3 - \alpha_1 T \boldsymbol{\delta} - \Delta \boldsymbol{C}^{-\boldsymbol{1}} \cdot \boldsymbol{C}_0 : \boldsymbol{\varepsilon}^{\boldsymbol{T}}\right] d\boldsymbol{x} \end{aligned} \tag{3.34}$$

Eqs. (3.12) and (3.18) are plugged into Eq. (3.34) to formulate the explicit relation between particle strain and prescribed far field strain:

$$\begin{aligned} \langle \boldsymbol{\varepsilon} \rangle(X_3) = \alpha_1 T \boldsymbol{\delta} + (\boldsymbol{I} - \boldsymbol{D}^{\boldsymbol{\Omega}} \cdot \boldsymbol{\Delta C})^{-1} : [\boldsymbol{\varepsilon}^0(X_3) - \alpha_1 T \boldsymbol{\delta} - \boldsymbol{D}^{\Omega} \cdot \boldsymbol{C}_0 : \boldsymbol{\varepsilon}^T] \\ + \phi \Delta \boldsymbol{C}^{-1} \cdot \boldsymbol{\mathcal{D}} : [\boldsymbol{\varepsilon}^0(X_3) - \alpha_1 T \boldsymbol{\delta} - \boldsymbol{D}^{\Omega} \cdot \boldsymbol{C}_0 : \boldsymbol{\varepsilon}^T] + \phi_{,3} \Delta \boldsymbol{C}^{-1} \cdot \boldsymbol{\mathcal{F}} : \boldsymbol{\varepsilon}^0_{,3}(X_3) \end{aligned} \tag{3.35}$$

The definition and expression of $\boldsymbol{\mathcal{D}}$ and $\boldsymbol{\mathcal{F}}$ are the same with Eq. (3.19), with the tensor $\boldsymbol{\mathcal{D}}$ addressing the pair-wise interaction between particles, and the tensor $\boldsymbol{\mathcal{F}}$ specially accounting for the coupling of layers along the gradation direction. Eq. (18) relates the macroscopic ensemble average particle strain $\langle\boldsymbol{\varepsilon}\rangle(X_3)$ with its corresponding matrix strain $\boldsymbol{\varepsilon}^0(X_3)$, after which the overall macroscopic stress $\overline{\boldsymbol{\sigma}}$ can be derived as the volumetric average of the particle and matrix stress as

$$\overline{\boldsymbol{\sigma}} = \phi(X_3)\boldsymbol{C}_1 : \langle\boldsymbol{\varepsilon}\rangle(X_3) + [1-\phi(X_3)]\boldsymbol{C}_0 : \langle\boldsymbol{\varepsilon}\rangle^0(X_3) \tag{3.36}$$

Given $\overline{\boldsymbol{\sigma}}$, Eqs. (3.35) and (3.36) formulate an ordinary differential equation which can be solved by backward Euler's method, such that the thermo-elastic behavior of FGMs considering the pair-wise particle interaction is well defined.

3.5 Plastic modeling of functionally graded materials

3.5.1 von-Mises yielding, associate flow rule and isotropic hardening

In the plastic analysis of two-phase FGMs [191], it is assumed that plasticity only occurs in the matrix phase. In this section, the von Mises yielding criteria with associated flow rule is assumed, together with the isotropic hardening [192], such that the yielding function is written as:

$$F(\boldsymbol{\sigma}, e^p) = \sqrt{H} - \sqrt{\frac{2}{3}}K(e^p) \tag{3.37}$$

For an isotropic homogeneous material, the stress norm H takes the form $H = \boldsymbol{\sigma} : \boldsymbol{I_d} : \boldsymbol{\sigma}$, and the isotropic hardening function usually takes the form $K(e^p) = \sigma_Y + h(e^p)^q$, where σ_Y is the yield stress, h and q are the hardening parameters and e^p is the effective plastic strain. Such stress norm definition is suitable for isotropic homogeneous material. However, when it comes to composite materials, especially the particle reinforced functionally graded materials, it cannot be directly

applied for the plastic modeling due to the influence from reinforcements. How to accurately define the stress norm H become a little more complicated.

One easy way is to simply use the macroscopic matric stress $\boldsymbol{\sigma}^0$, which can be directly calculated from the elastic analysis, to define the stress norm as $H = \boldsymbol{\sigma}^0 : \boldsymbol{I}_d : \boldsymbol{\sigma}^0$. Such method is simple to use but will ignore the effect of reinforcement to local plastic field in microscope. As is mentioned in the Mori-Tanaka's assumption, the macroscopic matrix stress/strain is equal to the microscopic far-field strain/stress, therefore by simply using the macroscopic matric stress σ^0, i.e. microscopic far field stress, the local disturbance of stress near the particles is ignored. However, the local disturbance plays as a key factor to determine: 1. whether the plasticity had begun; 2. how large was the plastic strain rate and magnitude. An accurate way of defining the stress norm is needed to be both easy to use in macro level, but also incorporate the local effect of the particles' disturbance.

During the elastic modeling in Section 3.3, an ensemble average approach was used to convert the particles' interaction in microscope to the averaged relation in macroscope, such that both particle to matrix influence and particle to particle pair-wise interactions are characterized. The same idea is applied in the plastic analysis, to address the influence of the local disturbance of particle reinforcement in an ensemble average way. For a particular particle configuration $\boldsymbol{\mathcal{G}}$, the ensemble average stress norm of matrix phase is defined following Ju and Chen's (1994c) framework:

$$\langle H \rangle_m(\boldsymbol{X}) = H^0 + \int_{\boldsymbol{\mathcal{G}}} \{H(\boldsymbol{x}|\boldsymbol{\mathcal{G}}) - H^0\} P(\boldsymbol{\mathcal{G}}) d\boldsymbol{\mathcal{G}} \tag{3.38}$$

with the first term H^0 being the stress norm of the macroscopic matrix stress $\boldsymbol{\sigma}^0$ as

$$H^0 = \boldsymbol{\sigma}^0 : \boldsymbol{I}_d : \boldsymbol{\sigma}^0 \tag{3.39}$$

and $H(\boldsymbol{x}|\boldsymbol{\mathcal{G}}) = \boldsymbol{\sigma}:\boldsymbol{I}_d:\boldsymbol{\sigma}$ being the stress norm of the microscopic local matrix stress at location $\boldsymbol{x}$ given the particle configuration $\boldsymbol{\mathcal{G}}$, where $\boldsymbol{I}_d$ is the fourth rank deviatoric identity tensor $\boldsymbol{I}_{d\,ijkl} = \frac{1}{2}\left(\delta_{ik}\delta_{jl} + \delta_{il}\delta_{jk}\right) - \frac{1}{3}\delta_{ij}\delta_{kl}$ and $P(\boldsymbol{\mathcal{G}})$ is the probability density function of the particle configuration.

By integrating the difference of microscopic local matrix stress to the macroscopic averaged matrix stress, the second term addresses the ensemble averaged influence of the microscopic local variation over the whole configuration to the macroscopic plastic deformation. By incorporating the local effects, this new definition of stress norm is now suitable for the plastic analysis of composite materials.

Before plugging Eq. (3.38) into the yield function, an additional term is needed for the EIM domain. The new definition of the matrix stress norm in Eq. (3.38) is based on the idea of the ensemble average of local disturbance, and the calculation is built upon the equivalent inclusion method introduced in Section 3.2. In the EIM domain, the inhomogeneity problem is transformed into an inclusion problem with the introduction of eigenstrain. What is important is the conversion of particle phase into matrix phase to formulate a homogeneous material, instead of a composite, which means that the domain of matrix is virtually enlarged by $1/(1-\phi)$ by taking in the domain originally belonged to the particle phase. Therefore, a so-called current stress norm is defined as

$$\sqrt{\langle H \rangle} = (1-\phi)\sqrt{\langle H \rangle_m} \tag{3.40}$$

to reduce the magnitude in order to stay at the same scale with the hardening function.

The current stress norm Eq. (3.40) is plugged into Eq. (3.37) to formulate the yield function that applies to the plastic analysis of functionally graded materials. The hardening function is assumed based on the material parameters with no involvement of any micromechanical assumption, and

therefore stays unchanged. The final ensemble average form of the yield function $\bar{F}$ for two-phase FGMs is written as:

$$\bar{F}\left(\sigma, e_m^p\right) = (1-\phi)\sqrt{\langle H\rangle_m} - \sqrt{\frac{2}{3}}K\left(e_m^p\right) \tag{3.41}$$

where e_m^p is the effective yield strain for the matrix phase.

Since the matrix stress norm contains the particles' influence on the plastic deformation, accurate definition and calculation of the stress norm becomes critical to the plastic model. The evaluation based on real particle configuration $\boldsymbol{\mathcal{G}}$ is almost impossible, with too many particles and parameters coupled together. In order to simplify the modeling, higher order particle interactions in Eq. (3.38) are neglected, leaving only the first order influence of particle to matrix, to have a simplified ensemble average stress norm of the matrix phase:

$$\langle H\rangle_m(\boldsymbol{X}) = H^0 + \int_{|x-x_1|>a}\{H(\boldsymbol{x}|\boldsymbol{x}_1) - H^0\}P(\boldsymbol{x}_1)d\boldsymbol{x}_1 \tag{3.41}$$

where a is the particle's radius, $P(\boldsymbol{x}_1)$ is the probability density function with the same form as introduced in Section 3.3, and $H(\boldsymbol{x}|\boldsymbol{x}_1)$ is the stress norm at microscopic matrix location $\boldsymbol{x}$ given a particle's existence at location $\boldsymbol{x}_1$, with the definition $H(\boldsymbol{x}|\boldsymbol{x}_1) = \boldsymbol{\sigma}(\boldsymbol{x}):\boldsymbol{I}_d:\boldsymbol{\sigma}(\boldsymbol{x})$. The probability of particle's existence at location $\boldsymbol{x}_1$ is given as $P(\boldsymbol{x}_1)$ and the whole effect is integrated over the whole domain, to incorporate all the particle to matrix interactions. The microscopic matrix stress $\boldsymbol{\sigma}(\boldsymbol{x})$ is determined with the help of equivalent inclusion method introduced in Section 3.2. Specifically, with the help of Eqs. (3.1), (3.6) and (3.8), the local matrix stress is evaluated as:

$$\boldsymbol{\sigma} = \boldsymbol{\sigma^0} + \boldsymbol{\sigma'} = (\boldsymbol{I} + \boldsymbol{A}):\boldsymbol{\sigma^0} \tag{3.42}$$

where $\boldsymbol{A} = -\boldsymbol{D}:(\boldsymbol{D}^{\boldsymbol{\Omega}} - \Delta\boldsymbol{C}^{-1})^{-1}$ is the disturbance ratio of the local inhomogeneities to the far field stress. Substituting Eq. (3.42) into Eq. (3.41) yields the explicit form of ensemble average stress norm of matrix as follows:

$$\langle H\rangle_m(\boldsymbol{x}) = H^0 + \int_{|\boldsymbol{x}-\boldsymbol{x_1}|>a}\{\boldsymbol{A}^T:\boldsymbol{I_d}:\boldsymbol{A} + \boldsymbol{A}^T:\boldsymbol{I_d} + \boldsymbol{I_d}:\boldsymbol{A}\}P(\boldsymbol{x}_1)d\boldsymbol{x}_1 = \boldsymbol{\sigma}^0:\boldsymbol{T}^0:\boldsymbol{\sigma}^0 \quad (3.43)$$

Here, the components of the fourth rank tensor $\boldsymbol{T^0}$ are given by

$$T^0_{ijkl} = T^0_1\delta_{ij}\delta_{kl} + T^0_2\left(\delta_{ik}\delta_{jl} + \delta_{il}\delta_{jk}\right) \quad (3.44)$$

where

$$T^0_1 = -\frac{1}{3} + \frac{\phi\beta\left[75(1-2v_0)^2\alpha + 2\left(2-50v_0+65v_0^2\right)\beta\right]}{2025(1-v_0)^2\mu_0^2} \quad (3.45a)$$

$$T^0_2 = \frac{1}{2} + \frac{\phi\left(23-50v_0+35v_0^2\right)\beta^2}{675(1-v_0)^2\mu_0^2} \quad (3.45b)$$

and α and β are given in the Appendix at the end of this chapter, μ_0 and v_0 are the shear modulus and Poisson ratio of matrix, respectively. It is noted that the first order term from probability density function $P(\boldsymbol{x}_1)$ in Eq. (3.18) will vanish during the integration, thanks to the symmetric property of the volume integral. The probability density function can also be expanded to higher order terms to account for larger gradation of particle volume fraction, but will generate additional terms in Eq. (3.44).

Eq. (3.44) gives the stress norm that accounts for the first order particle-matrix influence. It assumes dilute particle configuration so that the disturbed strain field from each particle can be linearly superposed. When the particle volume fraction is high, the pair-wise particle interaction effect shall be considered. It is hard to directly apply the pair-wise particle interactions into the formulation. However, it is easy to utilize the relation that has already contained the pair-wise particle effect, and plugs in to convert the matrix stress norm into the right form. In the elastic

analysis, a relation can be found between the macroscopic matrix stress $\boldsymbol{\sigma}^0$ and the volume average stress $\overline{\boldsymbol{\sigma}}$ through Eqs. (3.19) and (3.20), which, although implicit, contains the pair-wise interaction effects. The connection is assumed through a fourth rank tensor $\boldsymbol{P}$ as:

$$\boldsymbol{\sigma}^0 = \boldsymbol{P}: \overline{\boldsymbol{\sigma}} \tag{3.46}$$

The next step is to derive the expression of $\boldsymbol{P}$.

For functionally graded materials, the gradation is normally along one direction, which in most cases is the thickness direction. If the thickness is virtually divided into multiple layers, Eq. (3.9) holds for each individual layer as $(\boldsymbol{\sigma}^0)^i = \boldsymbol{P}^i: (\overline{\boldsymbol{\sigma}})^i$. Although the combination of the two equations involves a first order boundary value problem and makes the fourth rank tensor $\boldsymbol{P}$ tensor implicit due to the derivative of the microscopic far field strain $\varepsilon^0_{,3}$, an implicit relation can still be assumed and determined numerically as a boundary value problem through the backward Euler's method, by solving layer by layer from the given boundary.

The way to generate the equations for tensor $\boldsymbol{P}$ will be discussed below. Through the elastic equations of Eqs. (3.19) and (3.20), it is straightforward to assume that the ensemble average stress at the current layer $(\overline{\boldsymbol{\sigma}})^i$ is related to both the matrix stress at the current layer $(\boldsymbol{\sigma}^0)^i$ and the previous layer $(\boldsymbol{\sigma}^0)^{i-1}$. Two sets of fourth order isotropic tensors $\boldsymbol{H}^i$ and $\boldsymbol{Q}^i$ are assumed as the parameters for the relationship in the i^{th} layer:

$$(\overline{\boldsymbol{\sigma}})^i = \boldsymbol{H}^i: (\boldsymbol{\sigma}^0)^i + \boldsymbol{Q}^i: (\boldsymbol{\sigma}^0)^{i-1} \tag{3.47}$$

with

$$\boldsymbol{H}^i = H_1^i\left(\delta_{ik}\delta_{jl} + \delta_{il}\delta_{jk}\right) + H_2^i\delta_{ij}\delta_{kl} \tag{3.48a}$$

$$\boldsymbol{Q}^i = Q_1^i\left(\delta_{ik}\delta_{jl} + \delta_{il}\delta_{jk}\right) + Q_2^i\delta_{ij}\delta_{kl} \tag{3.48b}$$

where H_1^i, H_2^i and Q_1^i, Q_2^i are the parameters for the $\boldsymbol{H}^i$ and $\boldsymbol{Q}^i$, respectively. To achieve the numerical representation, the thickness of FGM t is divided virtually into N different layers and by combining Eqs. (3.19) and (3.20) in the elastic analysis, the theoretical expression of the $\boldsymbol{H}^i$ and $\boldsymbol{Q}^i$ writes:

$$\boldsymbol{H}^i = \{\boldsymbol{\phi C}_1 \cdot [(\boldsymbol{I} - \boldsymbol{D}^{\Omega} \cdot \Delta \boldsymbol{C})^{-1} + \phi \Delta \boldsymbol{C}^{-1} \cdot \boldsymbol{\mathcal{D}}] \cdot \boldsymbol{C}_{\boldsymbol{0}}^{-1} + (1-\phi)\boldsymbol{I}\} - \boldsymbol{Q}^i \quad (3.49a)$$

$$\boldsymbol{Q}^i = -\frac{N}{t}\phi_{,3}\boldsymbol{\phi C}_1 \cdot \Delta \boldsymbol{C}^{-1} \cdot \boldsymbol{\mathcal{F}} \cdot \boldsymbol{C}_0^{-1} \quad (3.49b)$$

Since the external loads for functionally graded materials are normally applied and transferred along gradation, the volume average stresses are the same in each layer $(\overline{\boldsymbol{\sigma}})^i = (\overline{\boldsymbol{\sigma}})^j$. Therefore, by plugging Eq. (3.46) into Eq. (3.47), the relation between different $\boldsymbol{P}^i$ is given as:

$$\boldsymbol{I} = \boldsymbol{H}^i : \boldsymbol{P}^i + \boldsymbol{Q}^i : \boldsymbol{P}^{i-1} \quad (3.50)$$

A boundary value problem is thus formulated to numerically solve the fourth rank tensor $\boldsymbol{P}$, to convert the matrix norm into a form with pair-wise particle interactions.

For the case of 100% matrix material at the boundary $i = 1$, the volume average stress $\overline{\boldsymbol{\sigma}}$ equals the matrix stress, making $\boldsymbol{P}^0 = \boldsymbol{I}$. For the case where the particle volume fraction ϕ does not start from 0% (say 10%), the boundary condition $\boldsymbol{P}^0$ can be formulated by dropping the $\boldsymbol{Q}$ term in Eq. (3.49a), i.e. no gradation effect considered in the first layer, making the equation:

$$\boldsymbol{P}^0 = \{\boldsymbol{\phi C}_1 \cdot [(\boldsymbol{I} - \boldsymbol{D}^{\Omega} \cdot \Delta \boldsymbol{C})^{-1} + \phi \Delta \boldsymbol{C}^{-1} \cdot \boldsymbol{\mathcal{D}}] \cdot \boldsymbol{C}_{\boldsymbol{0}}^{-1} + (1-\phi)\boldsymbol{I}\} \quad (3.51)$$

Therefore, the fourth rank tensor $\boldsymbol{P}$ can be numerically defined layer by layer, making the ensemble average matrix stress norm also numerically determined layer by layer. The discrete form of the matrix stress norm is then written as:

$$\langle \boldsymbol{H} \rangle_{\boldsymbol{m}}^i(\boldsymbol{x}) = \overline{\boldsymbol{\sigma}} : \overline{\boldsymbol{T}}^i : \overline{\boldsymbol{\sigma}} \quad (3.52)$$

where the fourth order tensor $\overline{\boldsymbol{T}}^i$ is defined as:

$$\overline{\boldsymbol{T}}^i = \boldsymbol{P}^i : \boldsymbol{T}^0 : \boldsymbol{P}^i \tag{3.53}$$

Finally, the yield function for FGMs considering the pair-wise particle interaction effect becomes:

$$\bar{F}^i(\overline{\boldsymbol{\sigma}}, e^p) = (1-\phi)\sqrt{\overline{\boldsymbol{\sigma}} : \overline{\boldsymbol{T}}^i : \overline{\boldsymbol{\sigma}}} - \sqrt{\frac{2}{3}} K(e^p) \tag{3.54}$$

It is noted that the yielding function is for the composite, although written in terms of matrix phase, because the equivalent inclusion method has been applied during the derivation of the stress norm part. The second part of the yielding function, the hardening function $K(e^p)$, also indicated the hardening of the whole composite. Since the FGMs we considered in the scope of this study also have the plasticity in the matrix phase, the hardening function $K(e^p)$ follows:

$$K(e^p) = K\left(e_m^p\right) = \left[\sigma_Y + h\left(e_m^{p\,i}\right)^q\right] \tag{3.55}$$

where σ_Y, h and q are the yielding stress and hardening parameters for the matrix phase, and e^p is the effective plastic strain for the matrix phase. The final form of the yielding function is written as:

$$\bar{F}^i\left(\overline{\boldsymbol{\sigma}}, e_m^{p\,i}\right) = (1-\phi)\sqrt{\overline{\boldsymbol{\sigma}} : \overline{\boldsymbol{T}}^i : \overline{\boldsymbol{\sigma}}} - \sqrt{\frac{2}{3}}\left[\sigma_Y + h\left(e_m^{p\,i}\right)^q\right] \tag{3.56}$$

The associated flow rule is assumed, and the macroscopic plastic strain in each layer is determined as:

$$\left(\dot{\bar{\boldsymbol{\varepsilon}}}^p\right)^i = \dot{\lambda}\frac{\partial \bar{F}^i}{\partial \overline{\boldsymbol{\sigma}}} = \dot{\lambda}(1-\phi)\frac{\overline{\boldsymbol{T}}^i : \overline{\boldsymbol{\sigma}}}{\sqrt{\overline{\boldsymbol{\sigma}} : \overline{\boldsymbol{T}} : \overline{\boldsymbol{\sigma}}}} \tag{3.57}$$

Accordingly, the effective plastic strain for the composite is:

$$(\dot{e}^p)^i = \sqrt{\frac{2}{3}\left(\dot{\bar{\boldsymbol{\varepsilon}}}^p\right)^i : \left(\dot{\bar{\boldsymbol{\varepsilon}}}^p\right)^i} = \dot{\lambda}(1-\phi)\sqrt{\frac{2}{3}\frac{(\overline{\boldsymbol{\sigma}} : \overline{\boldsymbol{T}})' : (\overline{\boldsymbol{\sigma}} : \overline{\boldsymbol{T}})}{\overline{\boldsymbol{\sigma}} : \overline{\boldsymbol{T}} : \overline{\boldsymbol{\sigma}}}} \tag{3.58}$$

The effective plastic strain for the matrix phase is:

$$\left(\dot{e}_m^p\right)^i = \frac{\dot{e}^p}{1-\phi} = \dot{\lambda}\sqrt{\frac{2}{3}\frac{(\overline{\boldsymbol{\sigma}} : \overline{\boldsymbol{T}})' : (\overline{\boldsymbol{\sigma}} : \overline{\boldsymbol{T}})}{\overline{\boldsymbol{\sigma}} : \overline{\boldsymbol{T}} : \overline{\boldsymbol{\sigma}}}} \tag{3.59}$$

So far, the plastic behavior of functionally graded materials considering pair-wise particle interactions is fully defined, and the traditional plastic algorithms can be applied here for the determination of plastic strain and strain rate. The macroscopic total strain is the volumetric average of the particle and matrix as:

$$\langle \boldsymbol{\varepsilon} \rangle = (1-\phi)\boldsymbol{\varepsilon}_m + \phi \boldsymbol{\varepsilon}_p \tag{3.60}$$

where the matrix strain is the combination of its elastic and plastic part $\boldsymbol{\varepsilon}_m = \boldsymbol{\varepsilon}_m^e + \boldsymbol{\varepsilon}_m^p$, and the total strain of particle only contains elastic part $\boldsymbol{\varepsilon}_p = \boldsymbol{\varepsilon}_p^e$. The elastic part $\boldsymbol{\varepsilon}_m^e$ and $\boldsymbol{\varepsilon}_p^e$ are determined with the help of elastic algorithm described in Section 3.3, while the plastic part $\boldsymbol{\varepsilon}_m^p$ is fully defined by Eqs. (3.56) to (3.57).

If the macroscopic volumetric average stress $\overline{\boldsymbol{\sigma}}$ is known, the plasticity is stress driven and the consistency condition requires the yield function Eq. (3.56) smaller or equal to zero, which determines the effective plastic strain directly. In case of the strain-driven plasticity, return mapping algorithm is applied to perform the stress update, during which Newton's method or Bisection can be used to determine the $\dot{\lambda}$ from consistency condition. Specifically, in each loading step the trial stress in every layer $(\Delta\sigma^{tr})^i$ corresponding to the loading step ΔF is computed via the elastic algorithm in Section 3.3, which is plugged into Eq. (3.56) to see if the consistency condition holds based on the parameters in the previous loading step:

$$\bar{F}^i\left(\overline{\boldsymbol{\sigma}}, e_m^p\right) = (1-\phi)\sqrt{\overline{\boldsymbol{\sigma}} : \overline{\boldsymbol{T}}^i : \overline{\boldsymbol{\sigma}}} - \sqrt{\frac{2}{3}}\left[\sigma_Y + h\left(e_m^{p\,i}\right)^q\right] \leq 0 \tag{3.61}$$

If the consistency condition holds true in every layer, then the FGM stays at the elastic state or plastic unloading. If the yield function is larger than zero in a layer, $\bar{F}^i\left(\overline{\boldsymbol{\sigma}}, e_m^p\right) > 0$, then plastic strain occurs and the material parameters need to be updated, where the discrete form of Eqs. (3.57)

and (3.58) are plugged into the consistency condition to solve for the $\dot{\lambda}$ with the Newton's method or the bisection method.

3.5.2 Drucker-Prager yielding, associate flow rule and isotropic hardening

The Drucker-Prager yielding criteria considers the effect of hydrostatic pressure towards the material yielding. Therefore, the yielding function is different with the von-Mises model. As is discussed in the HDPE modeling in Subsection 2.5.3, the first stress invariant I_1 is incorporated to represent the hydrostatic pressure. The yield function of homogeneous material with isotropic hardening under microscope is written as:

$$F = \sqrt{3J_2} + aI_1 - \sigma_y - h(e^p)^q \tag{3.62}$$

As is described in Subsection 3.5.1, the ensemble average process is needed to connect the microscope to the macroscope, where traditional plasticity theory can be applied to solve the problem. Therefore yield function for the Drucker-Prager model is written as:

$$F(\boldsymbol{\sigma}, e^p) = \sqrt{H} - a\hat{I}_1 - b \tag{3.63}$$

The ensemble average form of the stress components follows Eq. (3.40), while the hydrostatic pressure term $\hat{I}_1$ needs special attention. The parameter a is the material constants determined through experiments and b represents the yielding and hardening described in Subsection 3.5.1. In the case of isotropic hardening, $b = K = \sigma_Y + h(e^p)^q$.

Following the procedure of ensemble average, the hydrostatic pressure term $\hat{I}_1$ writes:

$$\hat{I}_1 = trace\left(\boldsymbol{\sigma}^0 + \int_{\boldsymbol{\mathcal{G}}} \boldsymbol{\sigma}' \cdot P(\boldsymbol{\mathcal{G}}) d\boldsymbol{\mathcal{G}}\right) \tag{3.64}$$

where $\boldsymbol{\sigma}^0$ is the prescribed far field stress in microscope, which is averaged to the average matrix stress in macroscope, $\boldsymbol{\sigma}'$ describes the disturbed stress from particles in microscope, and $P(\boldsymbol{\mathcal{G}})$ is the probability density function of a given particle configuration $\boldsymbol{\mathcal{G}}$.

From Eqs. (3.18) and (3.42), Eq. (3.64) can be further written as:

$$\hat{I}_1 = trace\left\{\boldsymbol{\sigma}^0 + \left[\int_{|\boldsymbol{x}-\boldsymbol{x}_1|} \boldsymbol{A}\cdot\frac{3}{4\pi a^3}\left(\phi + e^{-\boldsymbol{x}/\delta}\cdot\phi_{,3}\cdot x_3\right)d\boldsymbol{x}_1\right]\cdot\boldsymbol{\sigma}^0\right\} \quad (3.65)$$

where $\boldsymbol{A} = -\boldsymbol{D}:(\boldsymbol{D}^{\boldsymbol{\Omega}} - \Delta\boldsymbol{C}^{-1})^{-1}$. Fortunately, the integration inside the square brackets gives the value of zero and the term vanishes in the derivation, leaving only the $\boldsymbol{\sigma}^0$ in the trace. Therefore, micromechanics-based yield function under the Drucker-Prager criteria is written as:

$$F(\boldsymbol{\sigma}, e^p) = (1-\phi)\sqrt{\langle H\rangle_m} - a\cdot trace(\boldsymbol{\sigma}^0) - b \quad (3.66)$$

The definition of matrix stress norm $\langle H\rangle_m$ follows Eq. (3.38) and varies with different plastic models. The matrix stress $\boldsymbol{\sigma}^0$ is then converted into the volume average stress $\overline{\boldsymbol{\sigma}}$ with the aid of Eq. (3.46) to incorporate the pair-wise particle effect, so that the yielding function under the Drucker-Prager plastic model is fully defined. It is worth mentioning that under the Mori-Tanaka's scheme, the macroscopic matrix stress shares the same value of the microscopic far field stress, which means that the inhomogeneities' influence will only disturb the local stress field and will cancel out over the whole domain. Therefore, the vanishing terms after integration is consistent with the physics.

3.6 Thermo-elastoplastic modeling of functionally graded materials

It is shown in Section 3.4 that the temperature change will have a big effect to the elastic behavior of the functionally graded materials. It has been observed in many applications that the temperature induced thermal residual stresses can cause big deformation and sometimes result in failure of the structure. Therefore, the thermo-elastoplastic modeling of the FGMs is necessary for the understanding of the FGM performance in some extreme conditions.

Since in the building application, the temperature variation is slow and the relative temperature difference is relatively stable, the quasi-static temperature change is assumed in this section to demonstrate the effect of temperature change to the plastic behavior of functionally graded materials. It is known that the temperature change will introduce a thermal strain related to the temperature and coefficient of thermal expansion. The thermal strain is hydrostatic with identical value in all the three major directions. For the case of homogeneous composite such as the particle reinforced metal matrix composite, the spherical particle shape with the hydrostatic prescribed strain field will only introduce hydrostatic disturbed strain around the particles and therefore have no influence towards the von-Mises yielding function. Only the ellipsoidal particle shape will have the contribution towards the stress norm under the hydrostatic thermal strain. For the case of functionally graded materials, however, the particle volume fraction is graded along a particular direction, making the influence of particle interaction no longer uniform across the domain. Therefore, the disturbed stress field under the hydrostatic thermal strain will have the influence over the von-Mises yielding function.

As is discussed in Section 3.5, the plastic modeling requires the tracking of local stress status, and due to the local inhomogeneities' influence the normal macroscopic matrix stress cannot be directly used for the definition of stress norm in the yield function. An ensemble average stress norm of matrix phase is proposed that takes consideration of the microscopic variation of matrix stress. Since the temperature change will trigger thermal stress and change the microscopic matrix stress due to the material mismatch, the matrix stress norm is different and plastic model shall be rederived. For simplicity, the von-Mises yielding criteria with associate flow rule and isotropic hardening is considered in the following derivation. The yield function shares the same form with

Eq. (3.37) and the definition of ensemble average stress norm of the matrix is the same with Eq. (3.38) and written below for the convenience of reading:

$$\langle H\rangle_m(\boldsymbol{x}) = H^0 + \int_{|\boldsymbol{x}-\boldsymbol{x_1}|>a}\{H(\boldsymbol{x}|\boldsymbol{x_1}) - H^0\}P(\boldsymbol{x_1})d\boldsymbol{x_1} \tag{3.67}$$

where $H(\boldsymbol{x}|\boldsymbol{x_1}) = \boldsymbol{\sigma}:\boldsymbol{I}_d:\boldsymbol{\sigma}$ is the microscopic matrix stress norm and $P(\boldsymbol{x_1})$ is the probability density function with the same form as Eq. (3.18). The microscopic matrix stress is a combination of far field stress $\boldsymbol{\sigma}^0$ and the disturbed stress $\boldsymbol{\sigma}'$ and Eq. (3.41) is transformed into:

$$\langle H\rangle_m(\boldsymbol{x}) = \boldsymbol{\sigma}^0:\boldsymbol{I}_d:\boldsymbol{\sigma}^0 + \int_{|\boldsymbol{x}-\boldsymbol{x_1}|>a}\{\boldsymbol{\sigma}':\boldsymbol{I}_d:\boldsymbol{\sigma}' + \boldsymbol{\sigma}^0:\boldsymbol{I}_d:\boldsymbol{\sigma}' + \boldsymbol{\sigma}':\boldsymbol{I}_d:\boldsymbol{\sigma}^0\}P(\boldsymbol{x_1})d\boldsymbol{x_1} \tag{3.68}$$

The disturbed matrix stress $\boldsymbol{\sigma}'$ is calculated with the help of Eq. (3.24) and (3.26) as:

$$\boldsymbol{\sigma}' = \boldsymbol{C}_0:\boldsymbol{\varepsilon}' = \boldsymbol{B}:\left(\boldsymbol{\sigma}^0 - \boldsymbol{\sigma}_{eff}^T\right) \tag{3.69}$$

where the effective thermal stress is defined as $\boldsymbol{\sigma}_{eff}^T = \boldsymbol{C}_0\cdot\Delta\boldsymbol{C}^{-1}\cdot\boldsymbol{C}_1:\boldsymbol{\varepsilon}^T$, and the fourth order tensors $\boldsymbol{B} = \boldsymbol{C}_0\cdot\boldsymbol{A}\cdot{\boldsymbol{C}_0}^{-1}$, $\boldsymbol{A} = -\boldsymbol{D}^{\bar{\Omega}}:(\boldsymbol{D}^{\Omega} - \Delta\boldsymbol{C}^{-1})^{-1}$. Eq. (3.69) is plugged into Eq. (3.68) for the integration. It is noted that the third and fourth terms vanish after the integration, and the remaining first and second terms become:

$$\begin{aligned}\langle H\rangle_m(\boldsymbol{x}) &= \boldsymbol{\sigma}^0:\boldsymbol{I}_d:\boldsymbol{\sigma}^0 + \left(\boldsymbol{\sigma}^0 - \boldsymbol{\sigma}_{eff}^T\right):\left[\int_{|\boldsymbol{x}-\boldsymbol{x}_1|>a}(\boldsymbol{B}':\boldsymbol{I}_d:\boldsymbol{B})P(\boldsymbol{x}_1)d\boldsymbol{x}_1\right]:\left(\boldsymbol{\sigma}^0 - \boldsymbol{\sigma}_{eff}^T\right)\\ &= \boldsymbol{\sigma}^0:(\boldsymbol{T}^0 + \boldsymbol{I}_d):\boldsymbol{\sigma}^0 - \boldsymbol{\sigma}^0:\boldsymbol{T}^0:\boldsymbol{\sigma}_{eff}^T - \boldsymbol{\sigma}_{eff}^T:\boldsymbol{T}^0:\boldsymbol{\sigma}^0 + \boldsymbol{\sigma}_{eff}^T:\boldsymbol{T}^0:\boldsymbol{\sigma}_{eff}^T\end{aligned} \tag{3.70}$$

where the fourth order tensor $\boldsymbol{T}^0$ shares the same result as Eq. (3.44).

Comparing to the pure elastoplastic result discussed in Section 3.5, the second and third terms address the coupling effect between mechanical loading and thermal loading while the last term addresses the effect of pure thermal loading.

As is mentioned in Section 3.5, only the first order particle-matrix influence is considered in Eq. (3.70). Dilute particle configuration is assumed so that the disturbed strain field from each particle can be linearly superposed. The pair-wise particle interaction shall be considered when the volume

fraction is high. Following the same procedure, the relation between matrix stress and the volume average stress is utilized to incorporate the pair-wise particle interaction into Eq. (3.70). Through the observation in the thermo-elastic analysis in Section 3.4, the relation between the macroscopic matrix stress $\boldsymbol{\sigma}^0$ and the ensemble average stress $\overline{\boldsymbol{\sigma}}$ is assumed as:

$$\boldsymbol{\sigma}^0 = \boldsymbol{P}:\overline{\boldsymbol{\sigma}} + \boldsymbol{M} \tag{3.71}$$

where the fourth order tensor $\boldsymbol{P}$ follows the form of isotropic stiffness tensor $P_{ijkl} = P_1\delta_{ij}\delta_{kl} + P_2\left(\delta_{il}\delta_{jk} + \delta_{ik}\delta_{jl}\right)$ and $\boldsymbol{M}$ is a just second order tensor. Eq. (3.71) holds for each individual layer $(\boldsymbol{\sigma}^0)^i = \boldsymbol{P}^i:(\overline{\boldsymbol{\sigma}})^i + \boldsymbol{M}^i$. However, the derivative of far field strain $\varepsilon^0_{,3}$ makes the relation implicit, where the backward Euler's method can be used to numerically determine the $\boldsymbol{P}$ and $\boldsymbol{M}$ in each layer along the gradation. Similar to the procedure discussed in Section 3.5, the way to generate equations for $\boldsymbol{P}$ and $\boldsymbol{M}$ is through the thermo-elastic equations. Combining Eqs. (3.35) and (3.36) we will have:

$$(\overline{\boldsymbol{\sigma}})^i = \boldsymbol{H}^i:(\boldsymbol{\sigma}^0)^i + \boldsymbol{Q}^i:(\boldsymbol{\sigma}^0)^{i-1} + \boldsymbol{S}^i \tag{3.72}$$

where i denotes the i^{th} layer along the thickness, and

$$\boldsymbol{H} = \{\boldsymbol{\phi C}_1 \cdot [(\boldsymbol{I} - \boldsymbol{D}^{\Omega} \cdot \Delta\boldsymbol{C})^{-1} + \phi\Delta\boldsymbol{C}^{-1} \cdot \boldsymbol{\mathcal{D}}] \cdot \boldsymbol{C}_{\boldsymbol{0}}^{-1} + (1-\phi)\boldsymbol{I}\} - \boldsymbol{Q} \tag{3.73a}$$

$$\boldsymbol{Q} = -\frac{N}{t}\phi_{,3}\phi\boldsymbol{C}_1 \cdot \Delta\boldsymbol{C}^{-1} \cdot \boldsymbol{\mathcal{F}} \cdot \boldsymbol{C}_0^{-1} \tag{3.73b}$$

$$\begin{aligned}\boldsymbol{S} = -T(1-\phi)\alpha_0\boldsymbol{C}_0:\boldsymbol{\delta} - \phi\boldsymbol{C}_1 \cdot (\boldsymbol{I} - \boldsymbol{D}^{\Omega} \cdot \Delta\boldsymbol{C})^{-1}:[\alpha_1 T\boldsymbol{\delta} + \boldsymbol{D}^{\Omega} \cdot \boldsymbol{C}_0:\boldsymbol{\varepsilon}^T] \\ -\phi^2\boldsymbol{C}_1 \cdot \Delta\boldsymbol{C}^{-1} \cdot \boldsymbol{\mathcal{D}}:[\alpha_1 T\boldsymbol{\delta} + \Delta\boldsymbol{C}^{-1} \cdot \boldsymbol{C}_0:\boldsymbol{\varepsilon}^T]\end{aligned} \tag{3.73c}$$

in which t is the thickness and N denotes the number of layers along gradation. Since the load is transferred along gradation, the ensemble average stresses are the same in each layer $(\overline{\boldsymbol{\sigma}})^i = (\overline{\boldsymbol{\sigma}})^j$. Therefore, the relation between different $\boldsymbol{P}^i$ is given as:

$$\boldsymbol{I} = \boldsymbol{H}^i \cdot \boldsymbol{P}^i + \boldsymbol{Q} \cdot \boldsymbol{P}^{i-1} \tag{3.74}$$

$$\mathbf{0} = \boldsymbol{H}^i : \boldsymbol{M}^i + \boldsymbol{Q}^i : \boldsymbol{M}^{i-1} + \boldsymbol{S}^i \tag{3.75}$$

The boundary at $i = 1$ corresponds to the 100% matrix material, such that an explicit equation can be formulated to calculate $\boldsymbol{P}^0$ and $\boldsymbol{M}^0$. For FGMs of which the particle volume fraction does not start from 0% (say 10%), the boundary condition can be formulated by dropping the $\boldsymbol{Q}$ term in Eqs. (3.74) and (3.75), which assumes the gradation effect is neglected in the first layer.

After the coefficients $\boldsymbol{P}^i$ and $\boldsymbol{M}^i$ are determined numerically in each layer, the new stress norm in terms of ensemble average stress is written as:

$$\langle \boldsymbol{H} \rangle_{\boldsymbol{m}}^i(\boldsymbol{x}) = \overline{\boldsymbol{\sigma}} : \overline{\boldsymbol{T}}_1 : \overline{\boldsymbol{\sigma}} + \overline{\boldsymbol{\sigma}} : \overline{\boldsymbol{T}}_2 + \overline{\boldsymbol{T}}_3 : \overline{\boldsymbol{\sigma}} + \overline{\boldsymbol{T}}_4 \tag{3.76}$$

where

$$\overline{\boldsymbol{T}}_1^i = \boldsymbol{P}^i \cdot (\boldsymbol{T}^0 + \boldsymbol{I_d}) \cdot \boldsymbol{P}^i \tag{3.77a}$$

$$\overline{\boldsymbol{T}}_2 = \boldsymbol{P}^i \cdot (\boldsymbol{T}^0 + \boldsymbol{I_d}) : \boldsymbol{M}^i - \boldsymbol{P}^i \cdot \boldsymbol{T}^0 : \boldsymbol{\sigma}_{eff}^T \tag{3.77b}$$

$$\overline{\boldsymbol{T}}_3 = \boldsymbol{M}^i : (\boldsymbol{T}^0 + \boldsymbol{I_d}) \cdot \boldsymbol{P}^i - \boldsymbol{\sigma}_{eff}^T : \boldsymbol{T}^0 \cdot \boldsymbol{P}^i \tag{3.77c}$$

$$\overline{\boldsymbol{T}}_4 = \boldsymbol{M}^i : (\boldsymbol{T}^0 + \boldsymbol{I_d}) : \boldsymbol{M}^i + \boldsymbol{\sigma}_{eff}^T : \boldsymbol{T}^0 : \boldsymbol{\sigma}_{eff}^T - \boldsymbol{M}^i : \boldsymbol{T}^0 : \boldsymbol{\sigma}_{eff}^T - \boldsymbol{\sigma}_{eff}^T : \boldsymbol{T}^0 : \boldsymbol{M}^i \tag{3.77d}$$

Similar to the physical meaning of Eq. (3.70), the first term represents the effect from pure mechanical loading, the last term represents the pure thermal loading, while the second and third terms represent the coupling of mechanical and thermal loading.

Therefore, with the definition of Eq. (3.37) the yield function for FGMs becomes:

$$\bar{F}^i\left(\overline{\boldsymbol{\sigma}}, e_m^p\right) = (1-\phi)\sqrt{\langle \boldsymbol{H} \rangle_{\boldsymbol{m}}^i(\boldsymbol{x})} - \left[\sigma_Y + h\left(e_m^{p\,i}\right)^q\right] \tag{3.78}$$

Following the associative flow rule, the macroscopic plastic strain in each layer is determined by:

$$\dot{\boldsymbol{\varepsilon}}^p = \dot{\lambda}\frac{\partial \overline{\boldsymbol{F}}}{\partial \overline{\boldsymbol{\sigma}}} = \dot{\lambda}(1-\phi)\frac{\overline{\boldsymbol{T}}_1 : \overline{\boldsymbol{\sigma}} + \frac{1}{2}(\overline{\boldsymbol{T}}_2 + \overline{\boldsymbol{T}}_3)}{\sqrt{\overline{\boldsymbol{\sigma}} : \overline{\boldsymbol{T}} : \overline{\boldsymbol{\sigma}}}} \tag{3.79}$$

Accordingly, the effective plastic strain for the matrix is:

$$\dot{e}_m^p = \frac{\dot{e}^p}{1-\phi} = \frac{1}{1-\phi}\sqrt{\frac{2}{3}\dot{\boldsymbol{\varepsilon}}^p : \dot{\boldsymbol{\varepsilon}}^p} \tag{3.80}$$

The temperature effect to the elastoplastic deformation of functionally graded materials is fully defined. The traditional plastic analysis algorithms can be applied onto the yield function Eq. (3.78) for further determination of plastic deformation rate and magnitude.

3.7 Verification and validation

3.7.1 Verification with PRMMC theory

The elastoplastic behavior of FGM was not well studied in the literature and there was not existing theory for the verification, however, the plastic behavior of particle-reinforced metal matrix composites (PRMMC) has been well documented and discussed. PRMMCs are widely used as they can exhibit nearly isotropic properties and are easier to process using standard metallurgical processing such as powder metallurgy or casting routes. The reinforcing particles are assumed to be uniformly distributed among the metal matrix to exhibit an overall homogeneous mechanical behavior, which can be considered a special case of functionally graded material with constant particle volume fraction along the gradation. Specifically, experiments conducted by Yang et al. (1991) are used for the validation. Micromechanics based elastoplastic behavior algorithm of PRMMC in the paper of Ju and Chen (1994c) is also compared for the verification. In the experiment, uniaxial loading is applied to the Al/4Mg alloy reinforced with SiC particles, where the material properties for the matrix is $E_0 = 75\text{GPa}, v_0 = 0.33$ and for the particle $E_1 = 420\text{GPa}, v_1 = 0.17$. The hardening parameters for the matrix is given as $\sigma_Y = 46\text{MPa}$, $h = 320\text{MPa}$ and $q = 0.265$. Four types of particle volume fractions $\phi = 0\%, 17\%, 30\%$ and 48% are investigated. Since the macroscopic ensemble average stress equals to the applied stress and is

known $\bar{\boldsymbol{\sigma}} = (\bar{\sigma}_{11}, 0, 0, 0, 0, 0)$. The effective plastic strain e_m^p can be directed computed from Eq. (35). The total strain can be fully determined with the help of Eqs. (16), (17), (36) and (38). Yang's experimental results, Ju's theoretical predictions and the prediction of the proposed algorithm are plotted in Figure 23 for comparison. The dashed line is the theoretical prediction based on present theory, the triangles represent the result from Ju and Chen's [178] theoretical prediction and the circular dots are the experimental result from Yang's experiment.

Very good agreement is achieved among the proposed theory, Ju and Chen's (1994c) theory and the experiment for PRMMC. The proposed theory slightly underestimates the total deformation compared with Ju's result, but perfectly captures the experiment deformation when $\phi = 48\%$. It is noted that both Ju's theory and the present theory share the same fundamental derivation. The small discrepancy is resulted from the different formulation of pair-wise interaction effect to the definition of microscopic stress field and ensemble average stress norm, where a more straightforward calculation is achieved in the present theory.

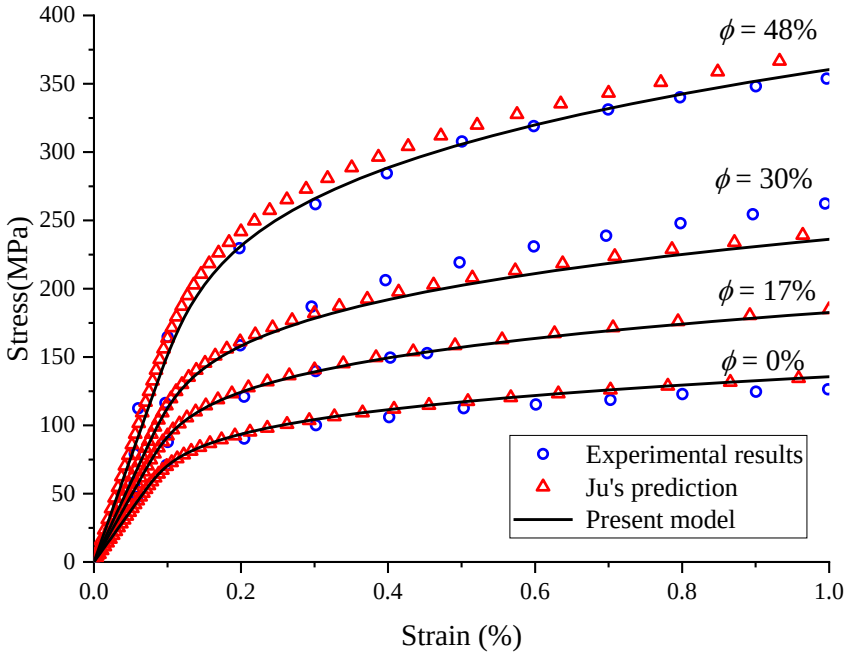

Figure 23 Theoretical prediction and experimental data of uniaxial plastic deformation of PRMMC

3.7.2 Validation with FGM experiments

In the previous sections we have discussed the great potential to harvest solar energy efficiency by developing a BIPVT roofing panel with FGMs as an essential component. The FGMs were made by coarse aluminum powder and HDPE through the vibration method. Coarse aluminum powder (Al-111) was chosen to mix with the finer HDPE powder. Since the BIPVT panel is designed to function as the roof, the thorough understanding of its elastoplastic behavior is necessary to fully utilize its potential. In this section, the experimental testing is described and discussed with a comparison to the theoretical prediction from the micromechanics approach.

Table 8 The dimension and weight information of the FGM samples

Sample #	Height (in)	Width (in)	Depth (in)	Weight (g)
1	0.527	0.522	0.561	3.396
2	0.532	0.536	0.522	3.299
3	0.520	0.519	0.525	3.161
4	0.537	0.541	0.536	3.426
Average	0.529	0.530	0.536	3.321

Since the FGM plates are designed to be very thin, with the maximum thickness no more than 1 in, the tensile test samples cannot be made with the testing standard. Therefore, only compression tests are carried out for the validation. Four FGM samples are cut from a plate for the uniaxial compression test, with its dimension and weight information listed in Table 8. The samples are uniaxially compressed with the Instron 5984 34k Universal Testing Machine inside the Carleton Laboratory of Columbia University. The samples are loaded with the speed of 0.02 in/min until 0.06-inch total deformation is reached, where the approximate total deformation is about 10%. In

the meantime, a high-resolution photo is taken at the beginning of each loading test, to obtain the volume fraction distribution of aluminum particles for theoretical prediction. The experiment setup is shown in Figure 10 (a).

The stress-strain curve of experimental results and numerical results are plotted in Figure 24. The experimental results of all samples are in dot marker with the error bar represents the maximum deviation of all samples. Numerical results with the true particle distribution is also given in Figure 24, together with the linear distribution proposed by Chen et al. (2016), and a referential quadratic distribution, marked in solid line, dash line and dot-dash line, respectively.

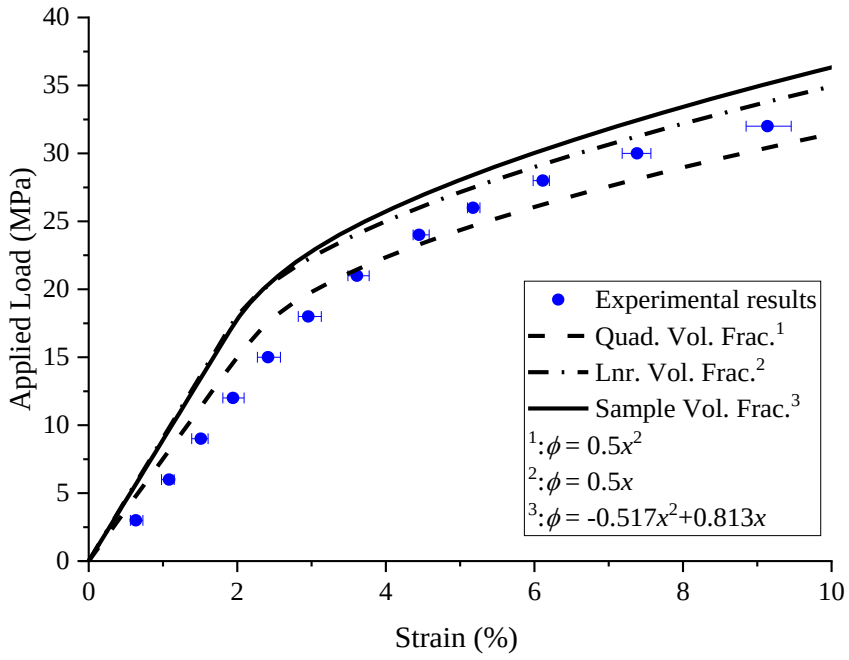

Figure 24 Elastoplastic behavior of FGM in the experiments and prediction

It is shown that the experimental data exhibit similar elastoplastic behavior with a narrow deviation over the whole loading process. The present theoretical elastoplastic prediction based on the true particle distribution tends to slightly underestimate the overall deformation but captures the trend of behavior very well. The prediction mismatch happens majorly in the elastic stage and becomes

not that obvious during the plastic stage. According to best of the authors' knowledge, the underestimation of deformation may be resulted from the debonding effect between aluminum particle and HDPE matrix and the potential air void inside the sample [194], [195]. Firstly, the two phases are assumed to be perfectly bonded and free of defect like air void in theoretical framework. However, the connection between aluminum and HDPE may not be that strong. Although vacuumed during the manufacturing, air bubbles are still very likely to be trapped inside, given the high viscosity of HDPE. Secondly, the proposed algorithm is developed based on the assumption that the particle shape being spherical, which cannot be perfectly satisfied in the real world. Overall, the proposed elastoplastic algorithm of FGM captures the real elastoplastic behavior of FGM very well and can be used for further investigation and industry prediction. It is worth noting that the derivation is based on Cauchy strain theory. For large plastic deformation [196], quadratic terms are needed in the strain definition.

3.8 Case studies

Volume fraction, in general, is one of the main factors that represents the FGM properties. Based on the procedure mentioned above, when a uniaxial loading is applied to the Al/HDPE FGM, the effect of volume fraction distribution is studied in two cases: (1) different overall particle volume fractions with quadratic and linear distribution functions; (2) the same overall particle volume fraction with different quadratic distribution functions. In this section, the FGMs are assumed as mixture of Al as particle and HDPE as matrix with maximum phase volume fraction remains smaller than 50%, to avoid the phase transition between particle and matrix. The mechanical parameters, which are $E_0 = 550\ \text{MPa}, \nu_0 = 0.3, \sigma_Y = 17.6\ \text{MPa}, h = 67.5\ \text{MPa}, q = 0.5444$ for

HDPE matrix, and $E_1 = 70\ \text{GPa}, v_1 = 0.33$ for Al particles, are collected in Section 4. The effective Young's modulus E_e for the elastic behavior, the offset yield stress $\sigma_{0.2}$ and the corresponding total strain $\varepsilon_{0.2}$ for the plastic behavior are defined and calculated for comparison. The offset yield stress $\sigma_{0.2}$ is defined as the stress state corresponding to 0.2% plastic strain and has been used in many literatures [197]–[200] for the measurement of plastic behavior.

3.8.1 Effect of different volume fractions

Figure 26 gives the elastoplastic predictions of FGMs under different overall particle volume fraction, with the quadratic and linear distribution function. The overall particle volume fraction ranges from 10% to 25%. The effective Young's modulus E_e, the offset yield stress $\sigma_{0.2}$ and the corresponding total strain $\varepsilon_{0.2}$ are listed in Table 9 and Table 10 for comparison. It is seen that the effective Young's modulus E_e is strongly affected by the overall volume fraction, indicating the overall volume fraction has a strong effect to the elastic behavior of the FGM. The effective Young's modules E_e will rise 1.95% with every 1% increase of the overall particle volume fraction. The offset yield stress $\sigma_{0.2}$ remain stable with variation smaller than 3% and can thus be considered as independent to the overall particle volume fraction. However, the corresponding total strain $\varepsilon_{0.2}$ is significantly reduced to 40% with the increase of the overall stiffness. The difference between quadratic and linear distribution, under the same overall volume fraction, is less than 3% for all the three mechanical parameters. It is also worth mentioned that the prediction based on the linear particle distribution, given by Chen et al [142] provides similar behavior prediction with the quadratic particle distribution and can be used as a simplified estimation of the particle distribution, from the elastoplastic perspective.

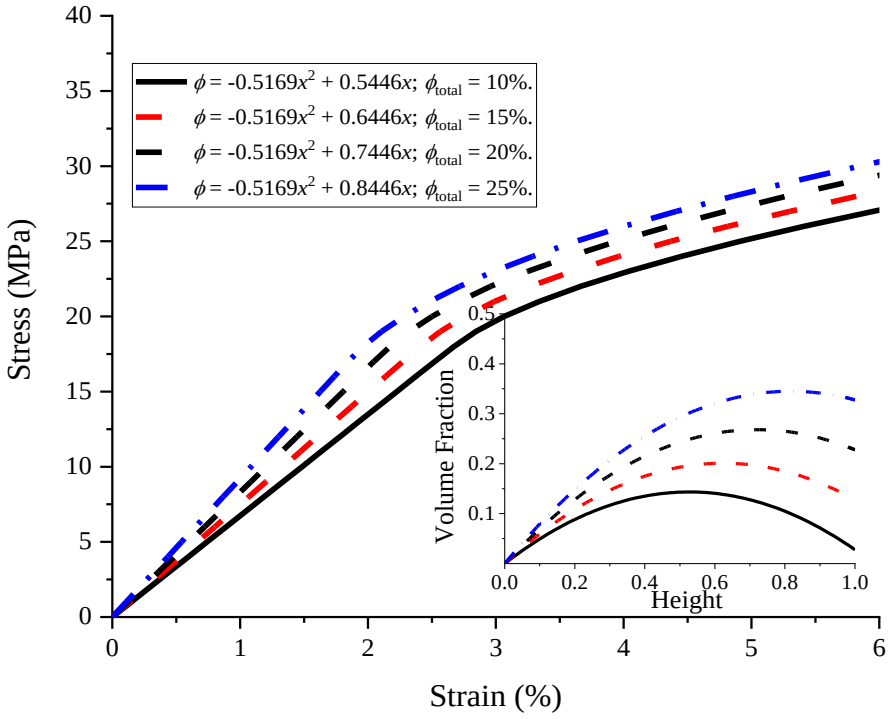

Figure 25 Stress-strain curve of Al/HDPE composites of different overall particle volume fraction with quadratic distribution function

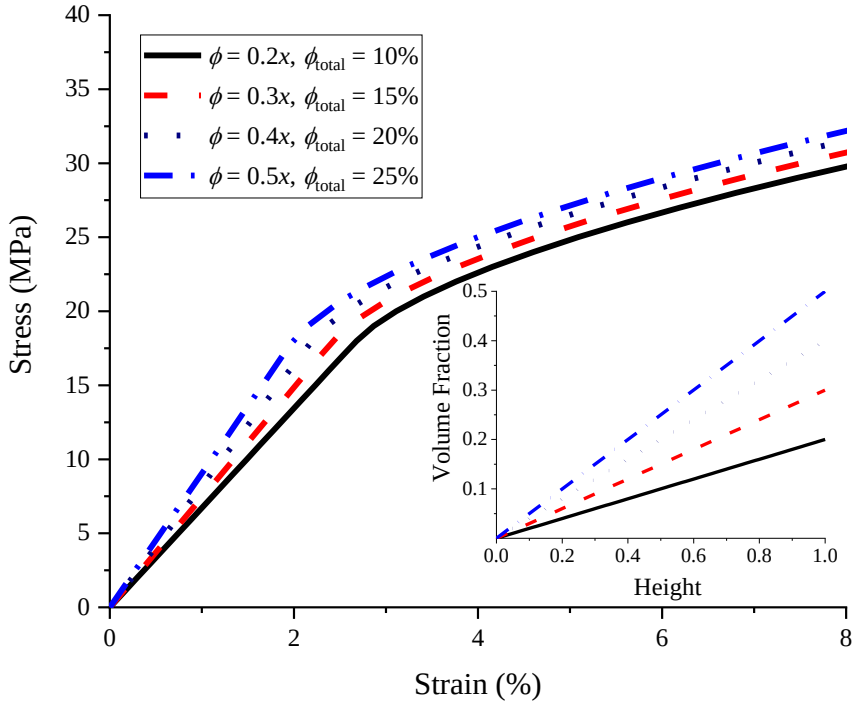

Figure 26 Stress-strain curve of Al/HDPE composites of different overall particle volume fraction with linear distribution function

Table 9 Comparison of E_e, $\sigma_{0.2}$ and $\varepsilon_{0.2}$ under different phase volume fractions with a quadratic distribution

volume fractions	E_e (MPa)	Comparison -	$\sigma_{0.2}$ (MPa)	comparison -	$\varepsilon_{0.2}$ %	comparison -
10%	673.942	0.00%	20.607	0.00%	3.258	0.00%
15%	748.342	11.04%	20.936	1.60%	2.998	-7.98%
20%	830.767	23.27%	21.002	1.92%	2.728	-16.26%
25%	921.982	36.80%	20.835	1.11%	2.460	-24.49%

Table 10 Comparison of E_e, $\sigma_{0.2}$ and $\varepsilon_{0.2}$ under different phase volume fractions with a linear distribution

volume fractions	E_e (MPa)	Comparison -	$\sigma_{0.2}$ (MPa)	comparison -	$\varepsilon_{0.2}$ %	comparison -
10%	671.9657	0.00%	20.2911	0.00%	3.21967	0.00%
15%	742.4855	10.49%	20.3984	0.53%	2.94731	-8.46%
20%	820.0698	22.04%	20.4014	0.54%	2.68777	-16.52%
25%	905.3679	34.73%	20.2798	-0.06%	2.43995	-24.22%

3.8.2 Effect of different quadratic distribution functions

In order to further study the effect of particle distribution function, Figure 27 illustrates the elastoplastic predictions under the same overall particle volume fraction but different quadratic distributions, which are listed in the legend. The overall particle volume fraction is equal to the measured result in the Section 4. The overall effective Young's modulus E_e, the overall offset yield stress $\sigma_{0.2}$ and the corresponding total strain $\varepsilon_{0.2}$ are listed in Table 11 for comparison. Since the overall particle volume fraction remains unchanged, and the particle distribution configuration is restricted to and varied from the authentic particle distribution formulation, the mechanical properties for both elastic and plastic stages are weakened with the increase of the gradation. The maximum difference is less than 3% for the effective Young's modulus E_e and about 6% for the offset yield stress $\sigma_{0.2}$. Together with the comparison in Subsection 2.5.1, it is therefore concluded that the slight variation in particle distribution function under the same overall volume fraction will not generate big difference in mechanical behaviors, as long as a similar trend is followed. However, for some extreme cases where particles are overly sedimented to formulate a delaminated composite, or insufficiently sedimented with almost homogeneous particle distribution along gradation, big difference in plastic deformation is expected and need further investigation.

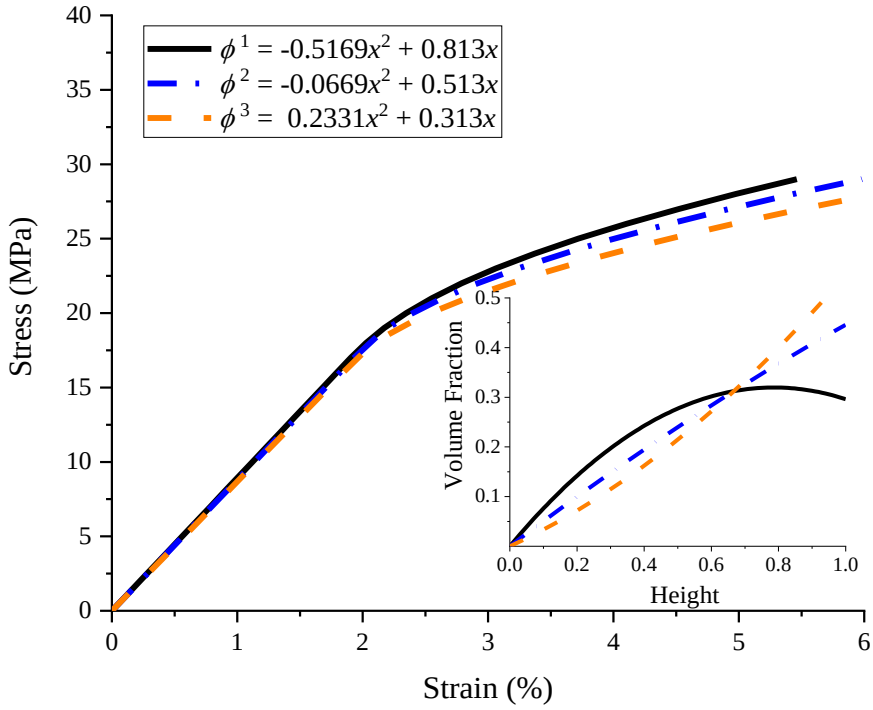

Figure 27 Stress-strain curve of Al/HDPE composites with different quadratic distributed function at the same overall particle volume fraction at 23.42%

Table 11 Comparison of E_e, $\sigma_{0.2}$ and $\varepsilon_{0.2}$ under different quadratic distributed functions

distribution function	E_e (MPa)	comparison -	$\sigma_{0.2}$ (MPa)	comparison -	$\varepsilon_{0.2}$ %	comparison -
ϕ^1	892.16	0.00%	20.89	0.00%	2.542	0.00%
ϕ^2	880.00	-1.36%	20.45	-2.12%	2.524	-0.70%
ϕ^3	867.74	-2.74%	19.62	-6.11%	2.461	-3.19%

3.8.3 Effect of different volume fraction function

Figure 28 gives the elastoplastic predictions of FGMs under different particle distributions, which include uniform, root, quadratic, linear and sigmoid, respectively. The overall particle volume fractions are the same with the samples in the experiment, which is 23.42%. The effective Young's modulus E_e, the offset yield stress $\sigma_{0.2}$ and the corresponding total strain $\varepsilon_{0.2}$ are listed in Table

12 for comparison. Different from the discussion in [201], the particle distributions are more versatile, where extreme cases such as the homogeneously mixed and overly sedimented cases are both considered. The overall composite stiffness reaches strongest under the uniform particle distribution and is gradually weakened with the increase of particle distribution order. The overly sedimented FGM, which is represented by the sigmoid function, shows the weakest material stiffness in the plot. The effective Young's modulus E_e remains almost the same, with the variation smaller than 6%. However, the offset yield stress $\sigma_{0.2}$ shows much greater variation up to around 37%. It is concluded that the particle gradation has small effect on the elastic behavior but exhibits a large influence on the plastic behavior of FGMs.

It is worthwhile to point out that although the homogeneous mixture provides a better plastic behavior, the special advantage of material gradation is jeopardized. One of the greatest advantages of FGMs is the capability to tailor the particle distribution for the optimal design that considers both thermal and elastoplastic behavior of FGM panels.

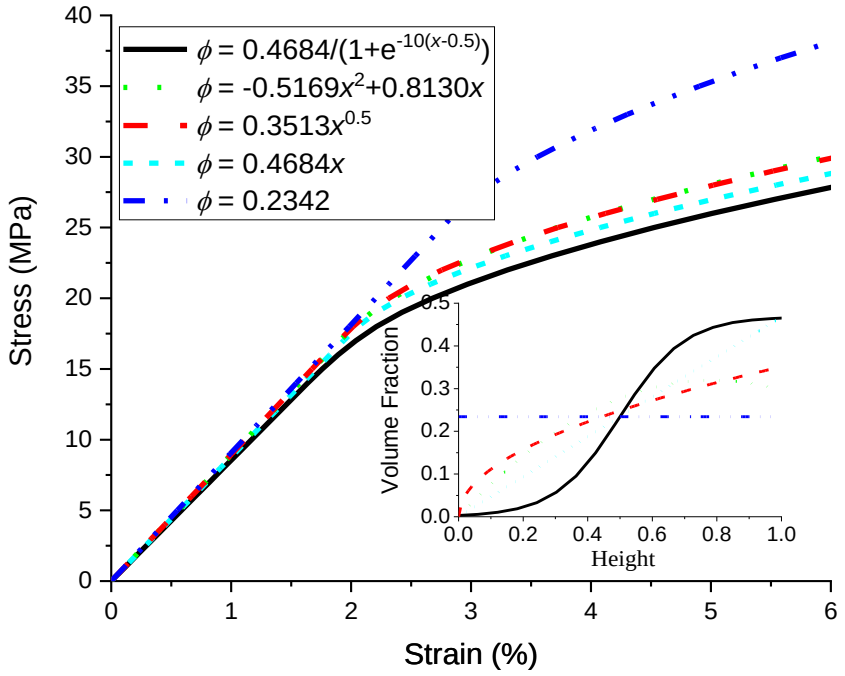

Figure 28 Stress-strain curve of Al/HDPE composites with different types distributed function at the same overall particle volume fraction at 23.42%

Table 12 Comparison of E_e, $\sigma_{0.2}$ and $\varepsilon_{0.2}$ under different types of distribution functions

distribution function	E_e (MPa)	comparison -	$\sigma_{0.2}$ (MPa)	comparison -	$\varepsilon_{0.2}$ %	comparison -
uniformed	907.14	0.00%	29.34	0.00%	3.434	0.00%
root	895.48	-1.28%	21.03	-28.32%	2.548	-25.80%
quadratic	892.16	-1.65%	20.89	-28.78%	2.542	-25.98%
linear	877.54	-3.26%	20.34	-30.66%	2.518	-26.67%
sigmoid	854.65	-5.79%	18.67	-36.37%	2.384	-30.58%

3.8.4 Effect of elastic constants

Apart from the overall volume fraction and distribution, the relative stiffness of particle and matrix also has an important effect to the overall elastoplastic behavior of FGMs. In Figure 29, the effect of Young's modulus ratio to the dimensionless mechanical properties are calculated based on the

particle volume fraction in [201], which is plotted in the legend. The mechanical properties are divided by its corresponding value under pure matrix stage to reach its dimensionless phases. Figure 29 uncovers the phenomenon that the monotonically increasing of particle stiffness will have a gradually weakened contribution to the overall stiffness. It is seen from the plot that all the overall effective mechanical properties grow almost linearly with the Young's modulus ratio when it is smaller than 8, and gradually stabilize after the ratio is larger than 15, which means that particles with stiffness 100 times stronger than the matrix will have similar contribution to the overall stiffness with the particle 15 times stronger. It is interesting that the increase of particle stiffness does not guarantee the linear increase of overall effective stiffness, and its strengthening effect quickly fades out when the stiffness ratio is higher than ~20. It is also straightforward to conclude that an optimal selection of particle stiffness exists, from the elastoplastic point of view, to avoid the potential waste of particle stiffness. It is also worth to mention that matrix stiffness plays an important role in the overall effective stiffness and shall not be neglected in the elastoplastic design.

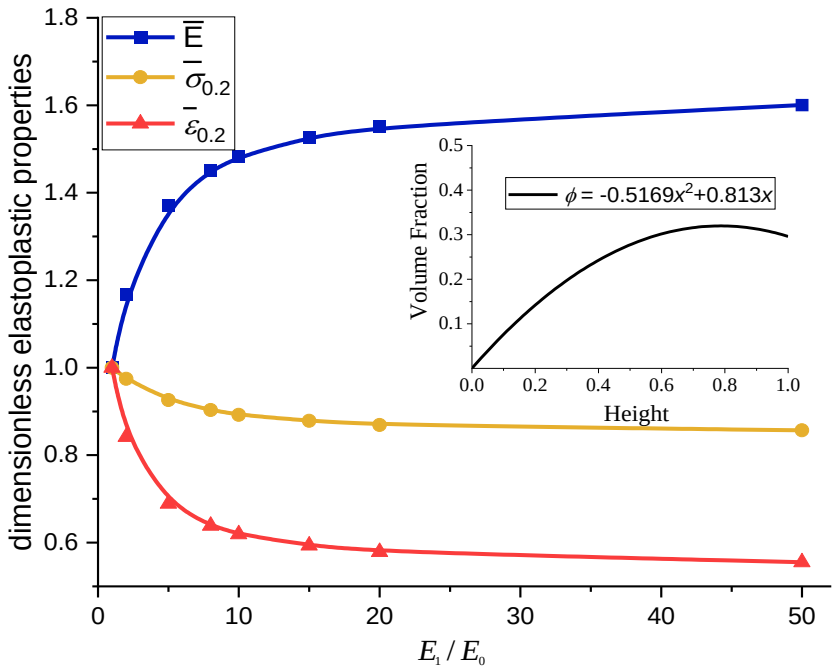

Figure 29 Dimensionless overall effective elastoplastic properties vary with E_1/E_0, where E_1 and E_0 are Young's modulus of particle and matrix, respectively

3.9 Conclusions

In this chapter, the equivalent inclusion method is introduced to convert the inhomogeneity problem into inclusion problem, with the help of a prescribed eigenstrain. The method is extended to the elastic and thermoelastic analysis of two phase functionally graded materials, with the consideration of pair-wise particle interactions. Such micromechanics-based algorithm provides a theoretical approach to study the strain and stress field and grants incomparable insights to the interactions between particles and matrix. Based on the equivalent inclusion method, a theoretical algorithm is proposed in this chapter to deal with the vacancy in the elastoplastic modeling of the functionally graded materials. Originally the particles' effect to the plastic deformation of matrix is difficult to quantify. The equivalent inclusion method provides an unique perspective to convert

the microscopic interaction and influence to the macroscope, thus formulating an ensemble averaged form of the yield function. The algorithm is studied for both von-Mises yielding and Drucker-Prager yielding, under isotropic hardening and associate flow rule. The thermo-elastoplastic analysis is also conducted to quantify the quasi-static thermal influence on the plastic deformation. The proposed theory is verified with other algorithms and validated by the experimental data. The proposed theory shreds light on the plastic modeling of FGM and serves as valuable reference to the future study of graded composite materials. The case studies are carried out to quantify the influence of volume fraction, distribution, and relative elastic constants, which grant insight to the future FGM design and engineering.

3.10 Appendix

The fourth order tensor D_{ijkl} is [185]

$$D_{ijkl} = \begin{cases} \dfrac{\rho^3}{60\mu^0(1-v^0)} \begin{bmatrix} (5-3\rho^2)\delta_{ij}\delta_{kl} - (5-10v^0+3\rho^2)\left(\delta_{ik}\delta_{jl}+\delta_{il}\delta_{jk}\right) \\ -15(1-\rho^2)\left(\delta_{ij}n_k n_l + \delta_{kl}n_i n_j\right) \\ -15(v^0-\rho^2)\left(\delta_{ik}n_j n_l + \delta_{il}n_j n_k + \delta_{jk}n_i n_l + \delta_{jl}n_i n_k\right) \\ +15(5-7\rho^2)n_i n_j n_k n_l \end{bmatrix} & \text{for } r > a \ \ (\boldsymbol{D}^{\bar{\Omega}}) \\ \dfrac{1}{30\mu^0(1-v^0)}\left[\delta_{ij}\delta_{kl} - (4-5v^0)\left(\delta_{ik}\delta_{jl}+\delta_{il}\delta_{jk}\right)\right] & \text{for } r \le a \ \ (\boldsymbol{D}^{\Omega}) \end{cases}$$

where $r, \rho,$ and n_i are defined as:

$$\begin{cases} r = (x_i x_i)^{\frac{1}{2}} \\ \rho = \dfrac{a}{r} \\ n_i = \dfrac{x_i}{r} \end{cases}$$

The fourth order tensor L_{ijkl} for the pair-wise particle interaction is:

$$L_{ijkl} = l_1\delta_{ij}\delta_{kl} + l_2\left(\delta_{ik}\delta_{jl} + \delta_{il}\delta_{jk}\right) + l_3\left(\delta_{ij}n_k n_l + \delta_{kl}n_i n_j\right)$$
$$+ l_4\left(\delta_{ik}n_j n_l + \delta_{il}n_j n_k + \delta_{jk}n_i n_k + \delta_{jl}n_i n_k\right) + l_5 n_i n_j n_k n_l$$

where the coefficients $c_i (i = 1,2, \dots, 5)$ are defined as

$$l_1 = \frac{-d_1(2d_2 + 4d_4 + d_5) + d_3^2}{4d_2[d_1(3d_2 + 4d_4 + d_5) + d_2(2d_2 + 2d_3 + 4d_4 + d_5) - d_3^2]} + \frac{\alpha}{2\beta(3\alpha + 2\beta)}$$

$$l_2 = \frac{1}{4d_2} - \frac{1}{4\beta}$$

$$l_3 = \frac{-d_1(4d_4 + d_5) - 2d_2d_3 - d_3^2}{4d_2[d_1(3d_2 + 4d_4 + d_5) + d_2(2d_2 + 2d_3 + 4d_4 + d_5) - d_3^2]}$$

$$l_4 = -\frac{d_4}{4d_2(d_2 + d_4)}$$

$$l_5 = \frac{d_2(8d_3d_4 + 3d_3^2 - 3d_1d_5 - 2d_2d_5 + 2d_4d_5 + 8d_4^2) + d_1d_4(4d_4 + d_5) - d_3^2d_4}{4d_2(d_2 + d_4)[d_1(3d_2 + 4d_4 + d_5) + d_2(2d_2 + 2d_3 + 4d_4 + d_5) - d_3^2]}$$

in which

$$d_1 = \alpha - \frac{\rho^3}{60\mu^0(1 - v^0)}(5 - 3\rho^2)$$

$$d_2 = \beta + \frac{\rho^3}{60\mu^0(1 - v^0)}(5 - 10v^0 + 3\rho^2)$$

$$d_3 = \frac{\rho^3}{4\mu^0(1 - v^0)}(1 - \rho^2)$$

$$d_4 = \frac{\rho^3}{4\mu^0(1 - v^0)}(v^0 - \rho^2)$$

$$d_5 = -\frac{\rho^3}{4\mu^0(1 - v^0)}(5 - 7\rho^2)$$

and

$$\alpha = -\frac{\lambda^1 - \lambda^0}{2(\mu^1 - \mu^0)[3(\lambda^1 - \lambda^0) + 2(\mu^1 - \mu^0)]} - \frac{1}{30\mu^0(1 - v^0)}$$

$$\beta = \frac{1}{4(\mu^1 - \mu^0)} + \frac{4 - 5v^0}{30\mu^0(1 - v^0)}$$

The explicit expressions of $\boldsymbol{\mathcal{D}}$ and $\boldsymbol{\mathcal{F}}$ introduced in Eq. (3.19) are

$$\boldsymbol{\mathcal{D}} = \int_{2a}^{\infty} \frac{3}{4\pi a \rho^2} \int_{\Sigma} \boldsymbol{L}(\mathbf{0}, \boldsymbol{x}) d\omega dx$$

$$\boldsymbol{\mathcal{F}} = \int_{2a}^{\infty} \frac{3a}{4\pi \rho^4} e^{-x/\delta} \int_{\Sigma} \boldsymbol{L}(\mathbf{0}, \boldsymbol{x}) n_3^2 d\omega dx$$

where $d\omega$ is the surface element on the unit sphere Σ centered at the origin of the coordinates, and that

$$\int_{\Sigma} L_{ijkl}(\mathbf{0}, \boldsymbol{x}) d\omega = \frac{4\pi}{15}(15l_1 + 10l_3 + l_5)\delta_{ij}\delta_{kl} + \frac{4\pi}{15}(15l_2 + 10l_4 + l_5)\left(\delta_{ik}\delta_{jl} + \delta_{il}\delta_{jk}\right)$$

$$\int_{\Sigma} L_{ijkl}(\mathbf{0}, \boldsymbol{x}) n_3^2 d\omega$$

$$= \frac{4\pi}{105}[35l_1 + 14l_3 + l_5 + 2(7l_3 + l_5)(\delta_{I3} + \delta_{K3})]\delta_{ij}\delta_{kl}$$

$$+ \frac{4\pi}{105}\left(35l_2 + 14l_4 + l_5 + 2(7l_4 + l_5)\left(\delta_{I3} + \delta_{J3}\right)\right)\left(\delta_{ik}\delta_{jl} + \delta_{il}\delta_{jk}\right)$$

Chapter 4 Structure analysis of BIPVT plate on high order plate theory

4.1 Overview

Because of the gradual change of aluminum and HDPE's proportion across the thickness direction, the thermal expansion coefficient of the FGM varies in the thickness direction. Considerable curling deformation was found in the final product of the designed FGM panel when it was cooled down from the higher processing temperature (140^0C). Extra deformation may also exist in field applications due to a considerable variance of service temperatures. In this sense, the structural integrity of the BIPVT panel significantly relies on the thermal deformation of the FGM layer. In the current prototype, the FGM panel is mechanically flattened by external load and glued to another structural layer to remain flat. To address this issue, one needs to accurately predict the thermos-mechanical performance of the designed FGM panel and understand the amount of external load needed for the flat surface, in order to secure the integrity of the assembled BIPVT panel.

Extensive studies have been conducted in the literature to predict the thermo-mechanical behavior on FGM beams, plates or shells by the first order shear deformable theories (FSDT) [202], [203], higher order shear deformable theories (HSDT) [204]–[206] and refined beam or plate theories [207], [208]. Circular FGM plates are widely employed as engineering structural components and perfect for understanding the thermal-mechanical behavior, but are relatively overlooked in comparison with the numerous studies about beams, rectangular plates and shells. Among the existing theories for the circular plates, the FSDT is the most widely used one [209]. However, the traction free condition cannot be satisfied in the FSDT due to the assumed constant shear strain

across the thickness direction. To avoid such conflict, higher order shear deformable theories (HSDT) were often developed [210], [211]. However, the application of the HSDT generally leads to a more accurate prediction of the global response, it requires much more computational efforts. As the first step to understand the thermo-mechanical behavior of the solar panel, a circular FGM plate is considered for simplification, where an explicit and exact solution can be obtained due to its axisymmetric configuration. Currently, most studies in this area are only suitable for simple isotropic materials [212]–[214]. To the authors' knowledge, no relevant closed-form solutions for an FGM circular plate subjected to thermo-mechanical loadings has been developed yet. To improve the accuracy of the FSDT and to reduce the complexity of HSDT, an explicit solution based on the refined plate theory (RPT) is developed in this study for the FGM circulate plate under asymmetric thermo-mechanical loading. The RPT assumes a separation of the displacement from bending and shear parts [215]–[217], which not only reduces the number of unknown variables but also shows a clearer physical meaning. Compared with the FSDT, the RPT leads to a parabolic shear deformation distribution across the thickness direction thus automatically satisfy the traction free conditions. Thus, it provides more accurate solutions than FSDT but with fewer unknowns than HSDT [218].

4.2 Theoretical modeling

A circular FGM panel with radius r_0 is considered as Figure 30. The cylindrical coordinates r, θ and z are applied in this analysis, where r-axis is taken radially outward from the center of the plate, θ-axis along the circumference of the plate and z-axis perpendicular to the mid-plane of the plate. It is noted that the mid-plane and neutral plane of the FGM plate usually does not

coincide, because the distribution of material properties is normally not symmetric along thickness. However, since we are going to use the integrated form of properties, it does not matter which plane to use to build up the coordinate.

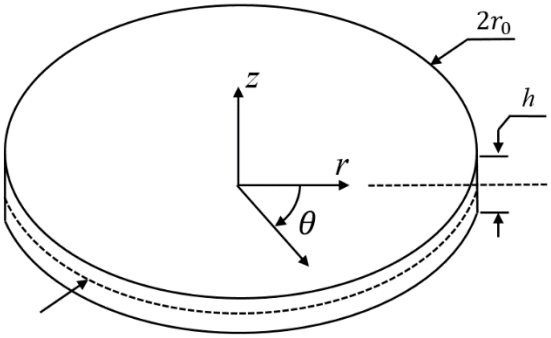

Figure 30 Configuration of a circular FGM plate with a radius of r_0 and the thickness h

4.2.1 Displacement assumptions

To formulate the problem and derive the solution, the following assumptions are made in this model [219], [220]:

- Small deformation is assumed and thus geometric nonlinearity is not considered;
- The transverse normal stress σ_{zz} can be neglected in comparison with the in-plane stresses
- The out-of-plane deflection w can be divided into two components as bending w_b and shear w_s. While the in-plane displacement is consisted of extension u_0, bending u_b and shear u_s.

Therefore, we can write the displacement components as follows:

$$\begin{aligned} w &= w_b + w_s \\ u &= u_0 + u_b + u_s \end{aligned} \tag{4.1}$$

The bending component u_b is assumed to be similar to the displacements given in the classical plate theory, i.e.

$$u_b = -z\frac{dw_b}{dr} \tag{4.2}$$

The shear component u_s, however, gives rise to the parabolic variation of shear strains through the thickness of the plate such that the shear stresses σ_{rz} and $\sigma_{\theta z}$ are zero at the top and bottom surfaces of the plate [215].

$$u_s = h\left[\frac{1}{4}\left(\frac{z}{h}\right) - \frac{5}{3}\left(\frac{z}{h}\right)^3\right]\frac{dw_s}{dr} \tag{4.3}$$

4.2.2 Kinematics

According to the assumptions, the displacement of the axisymmetric FGM plate based on the refined plate theory can be written as:

$$\begin{cases} u_r(r) = u_0(r) - z\frac{dw_b(r)}{dr} + h\left[\frac{1}{4}\frac{z}{h} - \frac{5}{3}\left(\frac{z}{h}\right)^3\right]\frac{dw_s(r)}{dr} \\ w(r) = w_b(r) + w_s(r) \end{cases} \tag{4.4}$$

The strains are related to the displacements by linear kinematic equations [221]:

$$\begin{gathered} \varepsilon_r = \frac{\partial u_r}{\partial r}, \quad \varepsilon_\theta = \frac{1}{r}\left(u_r + \frac{\partial u_\theta}{\partial \theta}\right), \quad \varepsilon_z = \frac{\partial w}{\partial z} \\ \gamma_{r\theta} = \frac{1}{r}\frac{\partial u_r}{\partial \theta} + \frac{\partial u_\theta}{\partial r} - \frac{u_\theta}{r} \\ \gamma_{\theta z} = \frac{\partial u_\theta}{\partial z} + \frac{1}{r}\frac{\partial u_z}{\partial \theta} \\ \gamma_{rz} = \frac{\partial u_r}{\partial z} + \frac{\partial u_z}{\partial r} \end{gathered} \tag{4.5}$$

Therefore, the strains are written as:

$$\begin{Bmatrix} \varepsilon_{rr} \\ \varepsilon_{\theta\theta} \end{Bmatrix} = \begin{Bmatrix} \varepsilon_{rr}^0 \\ \varepsilon_{\theta\theta}^0 \end{Bmatrix} + z\begin{Bmatrix} K_r^b \\ K_\theta^b \end{Bmatrix} + f\begin{Bmatrix} K_r^s \\ K_\theta^s \end{Bmatrix}, \quad \{\gamma_{rz}\} = g\{\gamma_{rz}^s\} \tag{4.6}$$

where

$$\begin{Bmatrix}\varepsilon_{rr}^{0}\\ \varepsilon_{\theta\theta}^{0}\end{Bmatrix}=\begin{Bmatrix}\frac{du_0}{dr}\\ \frac{u_0}{r}\end{Bmatrix},\begin{Bmatrix}K_r^b\\ K_\theta^b\end{Bmatrix}=\begin{Bmatrix}-\frac{d^2w_b}{dr^2}\\ -\frac{dw_b}{rdr}\end{Bmatrix},\begin{Bmatrix}K_r^s\\ K_\theta^s\end{Bmatrix}=\begin{Bmatrix}-\frac{d^2w_s}{dr^2}\\ -\frac{dw_s}{rdr}\end{Bmatrix},\{\gamma_{rz}^s\}=\begin{Bmatrix}\frac{dw_s}{dr}\end{Bmatrix}$$
$$f=-\frac{1}{4}z+\frac{5}{3}z\left(\frac{z}{h}\right)^2,\ g=5\left[\frac{1}{4}-\left(\frac{z}{h}\right)^2\right] \tag{4.7}$$

4.2.3 Constitutive equations

The total strain ε can be divided into two parts: mechanical strain ε^M and thermal strain ε^T.

$$\begin{pmatrix}\varepsilon_{rr}\\ \varepsilon_{\theta\theta}\\ \gamma_{rz}\end{pmatrix}=\begin{pmatrix}\varepsilon_{rr}^{(M)}\\ \varepsilon_{\theta\theta}^{(M)}\\ \gamma_{rz}^{(M)}\end{pmatrix}+\begin{pmatrix}\varepsilon_{rr}^{(T)}\\ \varepsilon_{\theta\theta}^{(T)}\\ \gamma_{rz}^{(T)}\end{pmatrix}=\begin{pmatrix}\varepsilon_{rr}^{(M)}\\ \varepsilon_{\theta\theta}^{(M)}\\ \gamma_{rz}^{(M)}\end{pmatrix}+\Delta T\begin{pmatrix}\alpha\\ \alpha\\ 0\end{pmatrix} \tag{4.8}$$

Here ΔT stands for the temperature variation that causes thermal strain and α stands for the Thermal Expansion Coefficient (TEC) of the material point, which varies in the gradation direction. For the axisymmetric problem with $\sigma_{zz}=0$, the constitutive equations can be reduced into three equations, which can be written in matrix form as:

$$\begin{pmatrix}\sigma_{rr}\\ \sigma_{\theta\theta}\\ \sigma_{rz}\end{pmatrix}=\frac{E(z)}{1-\nu^2}\begin{bmatrix}1 & \upsilon & 0\\ \upsilon & 1 & 0\\ 0 & 0 & \frac{1-\upsilon}{2}\end{bmatrix}\begin{pmatrix}\varepsilon_{rr}\\ \varepsilon_{\theta\theta}\\ \gamma_{rz}\end{pmatrix}-\Delta T\frac{E(z)}{1-\upsilon}\begin{pmatrix}\alpha(z)\\ \alpha(z)\\ 0\end{pmatrix} \tag{4.9}$$

Notice that both the Young's modulus $E(z)$ and TEC $\alpha(z)$ vary in the thickness direction due to the material gradation, while the Poisson ratio is studied and proved to have much less influence on the deflection than that of Young's modulus and is often assumed to be constant along the thickness [222], [223].

4.2.4 Governing equations

The governing equation can be derived via the principle of virtual displacements. The total potential energy can be written as [224]:

$$\pi=\frac{1}{2}\int_V(\sigma_r\varepsilon_r+\sigma_\theta\varepsilon_\theta+\sigma_{rz}\gamma_{rz})dV-\int_\Omega q(w_s+w_b)d\Omega \tag{4.10}$$

Then the governing equation can be obtained by the variational principle on u_0, w_s and w_b, and be written in terms of internal forces as:

$$\begin{cases} -(rN_r)' + N_\theta = 0 \\ -(rM_r^b)'' + \left(M_\theta^b\right)' - q = 0 \\ -(rM_r^s)'' + (M_\theta^s)' - (rQ_{rz})' - q = 0 \end{cases} \tag{4.11}$$

where the internal forces are defined as

$$\begin{aligned} (N_r, M_r^b, M_r^s) &= \int_{-\frac{h}{2}}^{\frac{h}{2}} (\sigma_r, z\sigma_r, f\sigma_r) dz \\ \left(N_\theta, M_\theta^b, M_\theta^s\right) &= \int_{-\frac{h}{2}}^{\frac{h}{2}} (\sigma_\theta, z\sigma_\theta, f\sigma_\theta) dz \\ Q_{rz} &= \int_{-\frac{h}{2}}^{\frac{h}{2}} \sigma_{rz} dz \end{aligned} \tag{4.12}$$

Combining the constitutive relation (4.9), one can have the internal forces in terms of displacements.

$$\begin{Bmatrix} N_r \\ N_\theta \\ M_r^b \\ M_\theta^b \\ M_r^s \\ M_\theta^s \end{Bmatrix} = \begin{bmatrix} A_{11} & A_{12} & B_{11} & B_{12} & B_{11}^s & B_{12}^s \\ A_{12} & A_{11} & B_{12} & B_{11} & B_{12}^s & B_{11}^s \\ B_{11} & B_{12} & D_{11} & D_{12} & D_{11}^s & D_{12}^s \\ B_{12} & B_{11} & D_{12} & D_{11} & D_{12}^s & D_{11}^s \\ B_{11}^s & B_{12}^s & D_{11}^s & D_{12}^s & H_{11}^s & H_{12}^s \\ B_{12}^s & B_{11}^s & D_{12}^s & D_{11}^s & H_{12}^s & H_{11}^s \end{bmatrix} \begin{Bmatrix} \varepsilon_{rr}^0 \\ \varepsilon_{\theta\theta}^0 \\ K_r^b \\ K_\theta^b \\ K_r^s \\ K_\theta^s \end{Bmatrix} - \begin{Bmatrix} N^T \\ N^T \\ M_b^T \\ M_b^T \\ M_s^T \\ M_s^T \end{Bmatrix}, \quad Q_{rz} = G_{11}\gamma_{rz}^s \tag{4.13}$$

where

$$A_{11} = \int_{-\frac{h}{2}}^{\frac{h}{2}} \frac{E}{1-v^2} dz \ , \ B_{11} = \int_{-\frac{h}{2}}^{\frac{h}{2}} z \frac{E}{1-v^2} dz \ , \ B_{11}^s = \int_{-\frac{h}{2}}^{\frac{h}{2}} f \frac{E}{1-v^2} dz \ , \ D_{11} = \int_{-\frac{h}{2}}^{\frac{h}{2}} z^2 \frac{E}{1-v^2} dz \ , \ D_{11}^s =$$

$$\int_{-\frac{h}{2}}^{\frac{h}{2}} fz \frac{E}{1-v^2} dz, H_{11}^s = \int_{-\frac{h}{2}}^{\frac{h}{2}} f^2 \frac{E}{1-v^2} dz, G_{11} = \int_{-\frac{h}{2}}^{\frac{h}{2}} g \frac{E}{2(1+v)} dz$$

$$N^T = \int_{-\frac{h}{2}}^{\frac{h}{2}} \Delta T \frac{E(z)\alpha(z)}{1-v} dz, M_b^T = \int_{-\frac{h}{2}}^{\frac{h}{2}} z\Delta T \frac{E(z)\alpha(z)}{1-v} dz, M_s^T = \int_{-\frac{h}{2}}^{\frac{h}{2}} f\Delta T \frac{E(z)\alpha(z)}{1-v} dz$$

By substituting equations (4.13) and (4.7) back into the governing equation (4.11), the equilibrium equation in terms of displacement can be obtained:

$$\begin{cases} A_{11} r \frac{d}{dr}\left[\frac{1}{r}\frac{d}{dr}(ru_0)\right] - B_{11} r \frac{d}{dr}\left[\frac{1}{r}\frac{d}{dr}(rw_b')\right] - B_{11}^s r \frac{d}{dr}\left[\frac{1}{r}\frac{d}{dr}(rw_s')\right] = 0 \\ -B_{11}\frac{1}{r}\frac{d}{dr}\left\{r\frac{d}{dr}\left[\frac{1}{r}\frac{d}{dr}(ru_0)\right]\right\} + D_{11}\nabla^2\nabla^2 w_b + D_{11}^s\nabla^2\nabla^2 w_s = q \\ -B_{11}^s\frac{1}{r}\frac{d}{dr}\left\{r\frac{d}{dr}\left[\frac{1}{r}\frac{d}{dr}(ru_0)\right]\right\} + D_{11}^s\nabla^2\nabla^2 w_b + H_{11}^s\nabla^2\nabla^2 w_s = G_{11}\nabla^2 w_s + q \end{cases} \tag{4.14}$$

where the axisymmetric Laplace operator ∇^2 is defined as

$$\nabla^2 = \left(\frac{d^2}{dr^2} + \frac{1}{r}\frac{d}{dr}\right) = \frac{1}{r}\frac{d}{dr}\left(r\frac{d}{dr}\right) \tag{4.15}$$

4.2.5 Explicit solution

The first equation in equation (4.14) provides the relation among u_0 to w_b and w_s, and therefore the governing equation can be simplified as:

$$\begin{cases} \zeta_1\nabla^2\nabla^2 w_b + \zeta_2\nabla^2\nabla^2 w_s = q \\ \zeta_3\nabla^2\nabla^2 w_b + \zeta_4\nabla^2\nabla^2 w_s = G_{11}\nabla^2 w_s + q \end{cases} \tag{4.16}$$

where

$$\begin{cases} \zeta_1 = D_{11} - B_{11}\frac{B_{11}}{A_{11}} \\ \zeta_2 = D_{11}^s - B_{11}\frac{B_{11}^s}{A_{11}} \\ \zeta_3 = D_{11}^s - B_{11}^s\frac{B_{11}}{A_{11}} \\ \zeta_4 = H_{11}^s - B_{11}^s\frac{B_{11}^s}{A_{11}} \end{cases} \tag{4.17}$$

By rearranging the terms of equation (4.16) and introducing a new variable $w_k = w_b + \frac{\zeta_2}{\zeta_1}w_s$, the governing equation can be further decoupled into:

$$\begin{cases} \nabla^2\nabla^2 w_k = \frac{q}{\zeta_1} \\ \nabla^2\nabla^2 w_s - \zeta_6\nabla^2 w_s = \frac{q}{\zeta_7} \end{cases} \tag{4.18}$$

where $\zeta_6 = \frac{G_{11}\zeta_1}{\zeta_4\zeta_1 - \zeta_2\zeta_2}$, $\zeta_7 = \frac{\zeta_4\zeta_1 - \zeta_2\zeta_2}{\zeta_1 - \zeta_2}$.

Notice that the first governing equation in Eq. (4.18) is exactly the same with the Kirchhoff Plate Theory. Its solution can be used directly. The second equation can be solved with the modified Bessel functions. If only a concentrated point load P is applied at the center of the circular panel, the governing equation (4.18) will be decoupled to the corresponding homogeneous form and with the following solutions:

$$\begin{cases} w_k = \xi_1 lnr + \xi_2 r^2 lnr + \xi_3 r^2 + \xi_4 \\ w_s = \eta_1 I_0(\kappa r) + \eta_2 K_0(\kappa r) + \eta_3 lnr + \eta_4 \end{cases} \tag{4.19}$$

where $\kappa^2 = \zeta_6$. $I_0(r)$ and $K_0(r)$ are the modified Bessel functions of order zero. The modified Bessel functions of the first and second kind can be written in explicit form as:

$$I_0(x) = \sum_{m=0}^{\infty} \frac{x^{2m}}{2^{2m} m! \Gamma(m+1)} = 1 + \frac{x^2}{2^2} + \frac{x^4}{2^4 (2!)^2} + \frac{x^6}{2^6 (3!)^2} + \cdots \tag{4.20a}$$

$$K_0(x) = -\left\{ ln\left(\frac{1}{2}x\right) + \gamma \right\} I_0(x) + \frac{\frac{1}{4}x^2}{(1!)^2} + \left(1 + \frac{1}{2}\right) \frac{\left(\frac{1}{4}x^2\right)^2}{(2!)^2} + \left(1 + \frac{1}{2} + \frac{1}{3}\right) \frac{\left(\frac{1}{4}x^2\right)^3}{(3!)^2} + \cdots \tag{4.20b}$$

The particular solution depends on the form of external load. If the externally applied load can be expanded in a polynomial form based on the Taylor's series, the particular solution can be assumed as polynomial form combining with the terms of same order, then the unknown constants can be fully determined by letting the coefficients at the same order to be zero.

On the other hand, if distributed load is applied over the plate surface, the particular solution can be determined following the procedure mentioned above as:

$$\begin{cases} w_k = \frac{q_0}{64\zeta_1} r^4 \\ w_s = -\frac{q_0}{4\zeta_6 \zeta_7} r^2 \end{cases} \tag{4.21}$$

Therefore, the final solution can be written as:

$$\begin{cases} w_k = \xi_1 lnr + \xi_2 r^2 lnr + \xi_3 r^2 + \xi_4 + \frac{q_0}{64\zeta_1} r^4 \\ w_s = \eta_1 I_0(\kappa r) + \eta_2 K_0(\kappa r) + \eta_3 lnr + \eta_4 - \frac{q_0}{4\zeta_6 \zeta_7} r^2 \end{cases} \tag{4.22}$$

With the aid of the first equation in (4.14), one can further determine the lateral displacement u_0:

$$u_0 = \frac{B_{11}}{A_{11}} w_k{}' + \left(\frac{B_{11}^S}{A_{11}} - \frac{\zeta_2}{\zeta_1}\frac{B_{11}}{A_{11}}\right) w_s' + \frac{\psi_1}{2} r + \psi_2 \frac{1}{r} \tag{4.23}$$

where ψ_1 and ψ_2 are the integration constants that can be determined by boundary conditions.

4.2.6 Boundary conditions and solutions

The simply supported boundary condition is considered here for both concentrated point load and the uniformly distributed load.

Concentrated point load

The simply supported boundary conditions for concentrated point force F at the center of the plate can be written as:

$$r = 0 \begin{cases} \dfrac{dw_k}{dr} = 0 \\ \dfrac{dw_s}{dr} = 0 \\ u_0 = 0 \\ \dfrac{d}{dr}(\nabla^2 w_k) = \dfrac{F}{2\pi r}\dfrac{1}{\zeta_1} \\ \dfrac{d}{dr}(\nabla^2 - \zeta_6) w^s = \dfrac{F}{2\pi r}\dfrac{1}{\zeta_7} \end{cases} \qquad r = r_0 \begin{cases} w_k = 0 \\ w_s = 0 \\ M_r^k = 0 \\ M_r^s = 0 \\ N_r = 0 \end{cases} \tag{4.24}$$

The fourth and fifth boundary condition at the center of the plate is based on the effective shear forces defined in [225].

By applying the boundary conditions above, one can fully determine the 10 unknown constants. The exact solution of the bending and the shear deflection can be written as:

$$\begin{cases} w_k = \frac{F}{8\pi}\frac{1}{\zeta_1}(r^2 lnr - r_0^2 lnr_0) + \xi_3(r^2 - r_0^2) \\ w_s = \eta_1[I_0(\kappa r) - I_0(\kappa r_0)] - \frac{F}{2\pi\kappa^2\zeta_7}[K_0(\kappa r) + lnr - K_0(\kappa r_0) - lnr_0] \\ u_0 = \frac{FB_{11}}{8\pi A_{11}\zeta_1}(2rlnr + r) + 2\frac{B_{11}}{A_{11}}\xi_3 r + \zeta_8\eta_1\kappa I_1(\kappa r) + \frac{F\zeta_8}{2\pi\kappa^2\zeta_7}\left[\kappa K_1(\kappa r) - \frac{1}{r}\right] + \frac{N^T}{A_{11}(1+v)} r \end{cases} \tag{4.25}$$

where $\zeta_8 = \left(\frac{B_{11}^S}{A_{11}} - \frac{\zeta_2}{\zeta_1}\frac{B_{11}}{A_{11}}\right)$

The explicit solution of coefficients ξ_3 and η_1 are shown in the Appendix at the end of this chapter. After determining the bending deflection and the shear deflection, the total deflection can be calculated by

$$w = w_k + \left(1 - \frac{\zeta_2}{\zeta_1}\right) w_s \tag{4.26}$$

Uniformly distributed load over the plate

The simply supported boundary conditions for the uniformly distributed load q_0 can be written as:

$$r = 0: \begin{cases} \frac{dw_k}{dr} = 0 \\ \frac{dw_s}{dr} = 0 \\ u_0 = 0 \\ Q_{rz}^k = \frac{d}{dr}(\nabla^2 w_k) = 0 \\ \frac{d}{dr}(\nabla^2 - \zeta_6) w^s = 0 \end{cases} \qquad r = r_0: \begin{cases} w_k = 0 \\ w_s = 0 \\ M_r^k = 0 \\ M_r^s = 0 \\ N_r = 0 \end{cases} \tag{4.27}$$

By applying the boundary conditions above, one can fully determine the 10 unknown constants. The exact solution of the bending and the shear deflection can be written as:

$$\begin{cases} w_k = \xi_3(r^2 - r_0^2) + \frac{q_0}{64\zeta_1}(r^4 - r_0^4) \\ w_s = \eta_1[I_0(\kappa r) - I_0(\kappa r_0)] - \frac{q_0}{4\zeta_6\zeta_7}(r^2 - r_0^2) \\ u_0 = \frac{B_{11}}{A_{11}}\left(2\xi_3 r + \frac{q_0}{16\zeta_1} r^3\right) + \left(\frac{B_{11}^s}{A_{11}} - \frac{\zeta_2}{\zeta_1}\frac{B_{11}}{A_{11}}\right)\left(\kappa\eta_1 I_1(\kappa r) - \frac{q_0}{2\zeta_6\zeta_7} r\right) + \frac{N^T}{(1+\nu)A_{11}} r \end{cases} \tag{4.28}$$

The explicit solution of coefficients ξ_3 and η_1 are shown in the Appendix at the end of this chapter.

4.3 Experiments

Experiments have been conducted to validate the present model for a circular FGM panel. As a reference, the CPT and FSDT have also been extended to FGM plates and been used to compare with the present model. Finite element analysis (FEA) was carried out as well to verify the theoretical results.

4.3.1 FGM circular plate fabrication

The FGM was made by coarse aluminum powder and high-density polyethylene (HDPE) through the vibration method. Coarse aluminum powder (Al-111) was chosen to mix with the finer high-density polyethylene (HDPE) powder. The desired gradation of the AL-HDPE FGM in terms of volume fraction of aluminum to the FGM is to be from 0 to 50% across its thickness. Aiming at this gradation, a mixing design of the FGM with an appropriate volume ratio of Al to HDPE as 1:3 was determined after a series of tries and comparisons, and the ethanol added for the mixing was chosen by the weight ratio of ethanol to the mixed powder as 28%. The detailed mix design and fabrication processes are summarized in Figure 31 [99]. The component materials were measured and placed in a sequence of HDPE, Al and ethanol, and then mixed in a mixer for about 6 minutes (Figure 31 (a)).

Figure 31 Fabrication process of the FGM panel: (a) Mixing of Al articles and HDPE powder with ethanol; (b) Vibration and sedimentation; (c) Heating and degassing; and (d) Cured FGM panel after cooling down

Figure 32 Microstructure of the FGM panel containing aluminum particles dispersed in the HDPE matrix with the concentration changing in the thickness direction

The mixed suspension was then dumped into an aluminum mold and vibrated for about 15 seconds as shown in (Figure 31 (b)). Thereafter, the mixed suspension was kept in the mold allowing further sedimentation of Al particles in the suspension. After the ethanol was completely drained off from the suspension, the graded Al-HDPE mixed composite with the aluminum mold were placed in a vacuum oven and heated up to a temperature of 170 °C. When the HDPE was fully melt, a degassing process was applied (Figure 31(c)) to take away as much air voids as possible in order that the thermal conductivity of the FGM will be maximized. The sample was removed from the mold when the temperature cools down to the room temperature. Due to the different thermal expansion coefficient of the FGM panel across its thickness direction resulted from the material gradation, certain thermal deformations will always exist right after it taken out from the mold, leading to a curved FGM panel as shown in Figure 31 (d). The cross section of one sample element (12.7 mm height × 20.3 mm width) cut from the FGM panel is shown in Figure 32, which shows that a well-controlled graded FGM was achieved by the proposed vibration and sedimentation combined approach. According to the gradation analysis of the present FGM, a linear gradation of the components along its thickness direction was obtained, which can be expressed via the

relationship between the volume fraction of the aluminum to HDPE (ϕ) and its height location (z/h) as:

$$\phi = \frac{47.44\frac{z}{h}+3}{0.97-0.47\frac{z}{h}} \tag{4.29}$$

4.3.2 Material characterizations

In order to characterize the material properties of the FGM, six groups of samples with six different volume fractions of Al to HDPE (10%, 20%, 30%, 40%, 50%, and 60%) were prepared. The modulus of the composites were obtained through tensile test on six groups of coupon samples with dimensions of 228.6 mm (length) × 25.4 mm (width) × 12.7 mm (thickness) as shown in Figure 33 (a). The determined modulus of the composites with different volume fractions are shown in Figure 33 (b). It shows that, as the volume fraction of Al particles increases, the modulus of the Al-HDPE composites increases until a plateau stage is reached where the volume fraction reaches about 40%. It was observed from the test that the higher volume fraction of the Al particles, more air voids were found in the particulate composite samples [99], leading to a decreasing tensile modulus when the volume fraction of Al particles are higher than 50%. When the volume fraction of Al particles getting further higher, say ≥ 60%, no quality sample can be obtained since there was not enough HDPE powder to solidify the composite during the sintering process afterwards.

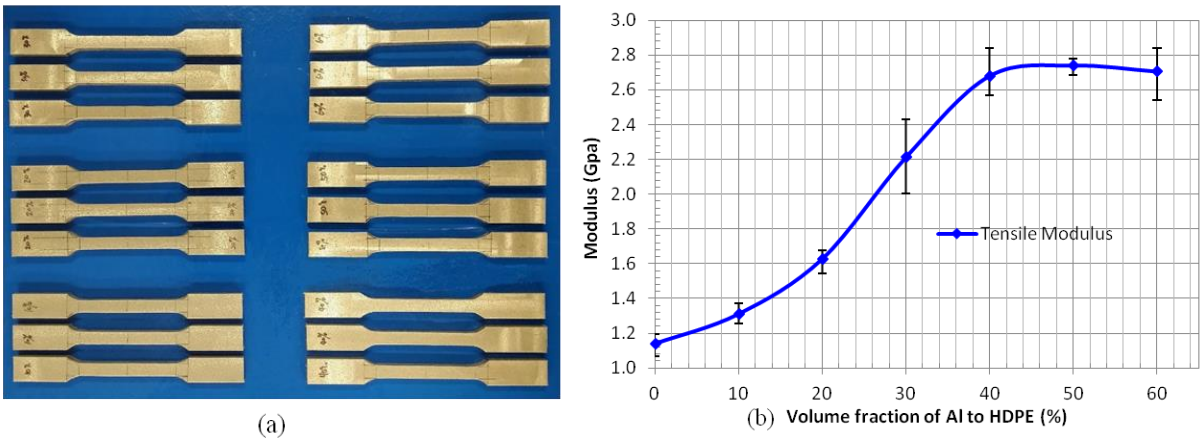

Figure 33. Tensile test: (a) prepared samples; and (b) modulus with respect to volume fraction of Al to HDPE

The thermal expansion coefficient (TEC) was determined by measuring the thermal expansion of the composites through the Orton Dilatometer machine. Six groups of samples with dimensions of 9.525 mm diameter × 25.4 mm length were prepared with four replications for each group as shown in Figure 34 (a). Percent linear change (PLC) curves of each sample over the scanning temperature (40 ℃ to 100 ℃) were obtained first. In order to obtain the TECs in an overall sense over this temperature range, the TEC of each sample was determined by the linear regression of the PLC curve (i.e., equaling to the slope of the regressed line), which are shown in Figure 34 (b).

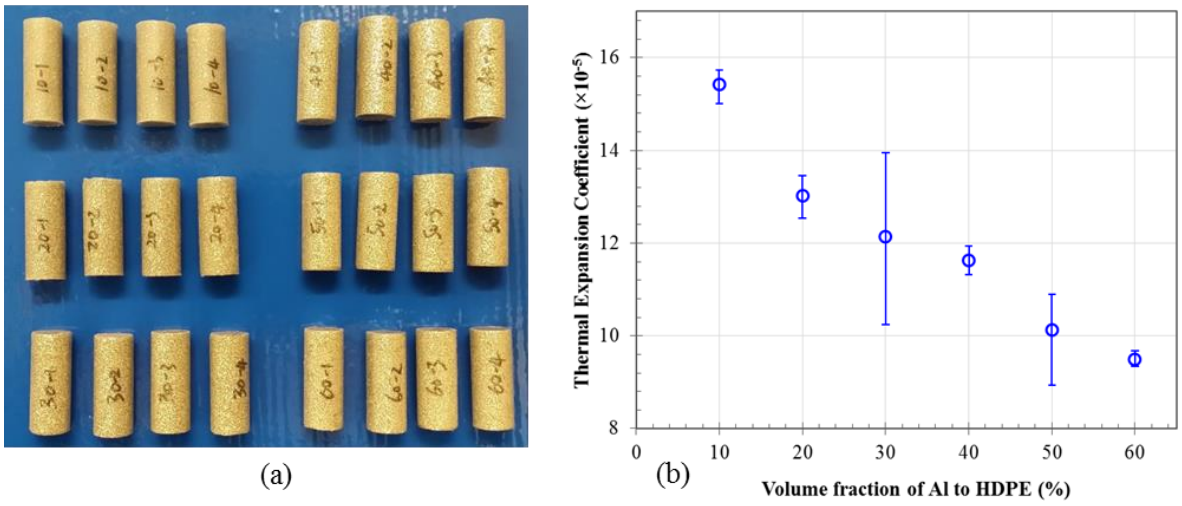

Figure 34 Thermal coefficient test: (a) prepared samples; and (b) thermal expansion coefficients with respect to volume fraction of Al to HDPE

Based on the relationship between the modulus (or TEC) of the FGM and the volume fraction of Al to HDPE as shown in Figure 33 and Figure 34, and the relationship between the volume fraction of the Al to HDPE (ϕ) and its height location (z/h) shown in Eq. (4.29), the gradation of the modulus (or TEC) of the FGM panel across its thickness direction are shown in Figure 35 (a) and (b), respectively, which are determined by the regression analysis and can be mathematically expressed as:

$$\begin{cases} E(z) = 277.8\phi^4 - 59150\phi^3 + 3.269\times10^6\phi^2 - 1.805\times10^7\phi + 1.179\times10^9 \ \ (Pa) \\ \alpha(z) = -1.116\times10^{-6}\phi + 158.9\times10^{-6} \end{cases} \quad (4.30)$$

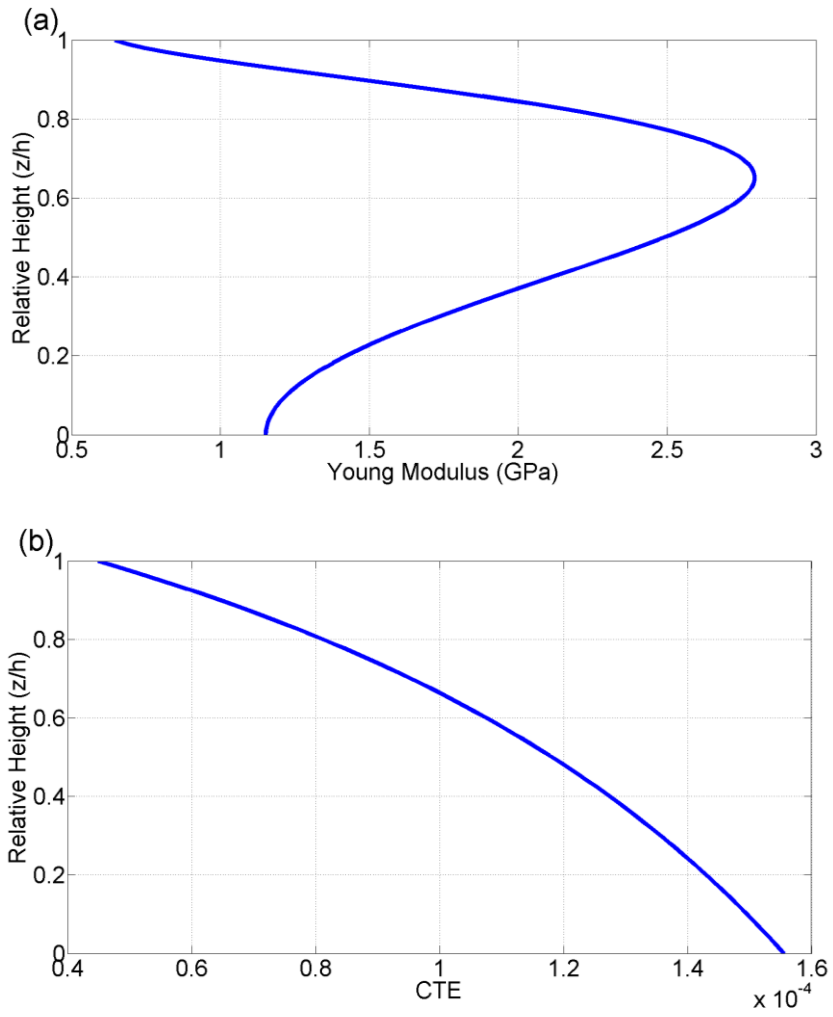

Figure 35 Material gradations across the thickness of the FGM panel: (a) Young's modulus; and (b) Thermal expansion coefficient (TEC)

4.3.3 Thermal deflection measurement

The circular FGM panel with a radius of 147.3 mm and thickness of 12.7 mm was cut from the cured FGM panel. The thermal deflection of the FG circular panel due to the gradation of material properties was measured by a Laser Displacement Sensor (LDS) which is shown in Figure 36. The LDS sends a pulse of laser light to a target surface and detects the reflection with a high accuracy of 0.02%. The LDS is linked to the LabVIEW software and configured with a 5 Hz sampling frequency. During the measurement, the circular plate was divided equally into 24 regions by 12

lines across the center with an intersectional angle of 15°. The measured relative distance along the 12 lines were analyzed to depict the deflection of the FGM panel.

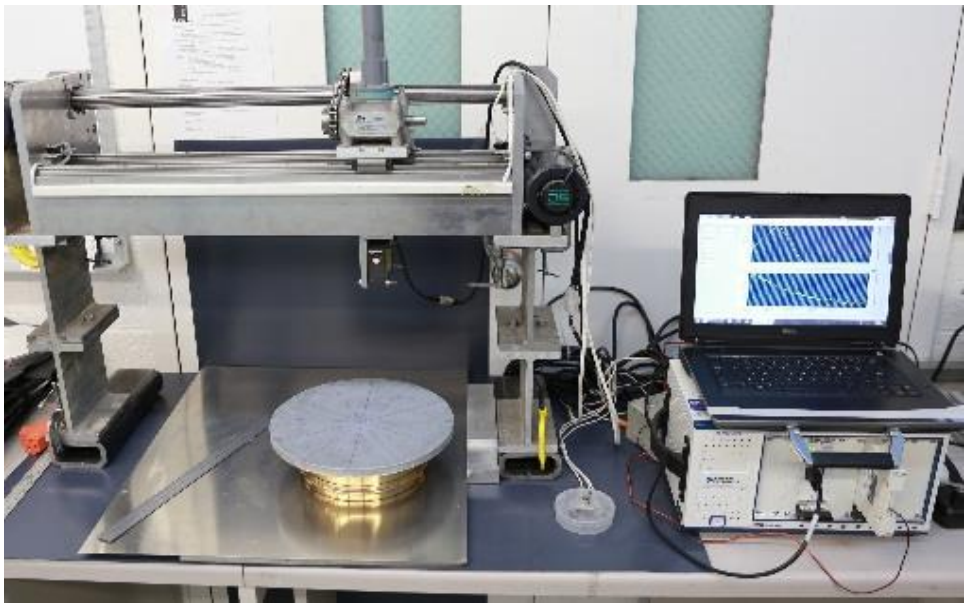

Figure 36 Thermal deflection measurement by the LDS

The recorded twelve sets of data are simulated by quadratic function, with a typical curvature shown in Figure 37. The thickness of the cured FGM panel is not exactly the same across the whole panel, the average thickness of the panel is about 12.7 mm with a coefficient of variation of ~3%. The slight ununiformed thickness of the panel makes the measured thermal deflection not exactly axisymmetric to the center of the panel. The maximum deflections of the six curves are listed in Table 13. The maximum deflection of the panel is taken as an average of the maximum deflections of the six simulated functions.

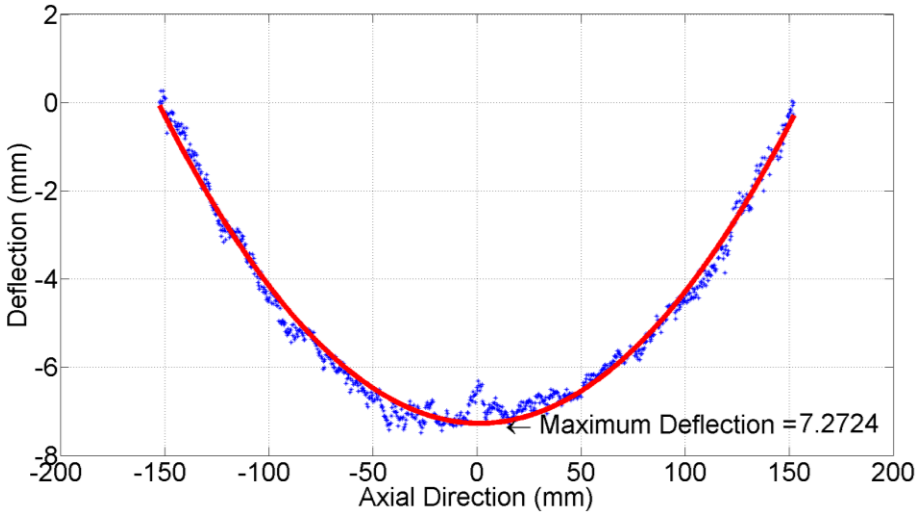

Figure 37 Thermal deflection of the FGM panel

Table 13 Maximum deflection of six curves

Curvature Number	1	2	3	4	5	6	Ave.
Deflection (mm)	6.48	6.91	7.20	7.61	7.59	6.94	
Curvature Number	7	8	9	10	11	12	7.06
Deflection (mm)	6.71	6.85	6.78	7.31	7.15	7.27	

4.3.4 Compression Test

Compression test was conducted on the curved circular FGM panel in order to obtain the external loading required to flatten the FGM panel. The determined force is used to calculate the theoretical deflection via the proposed model, which will be applied to compare with the measured thermal deflection.

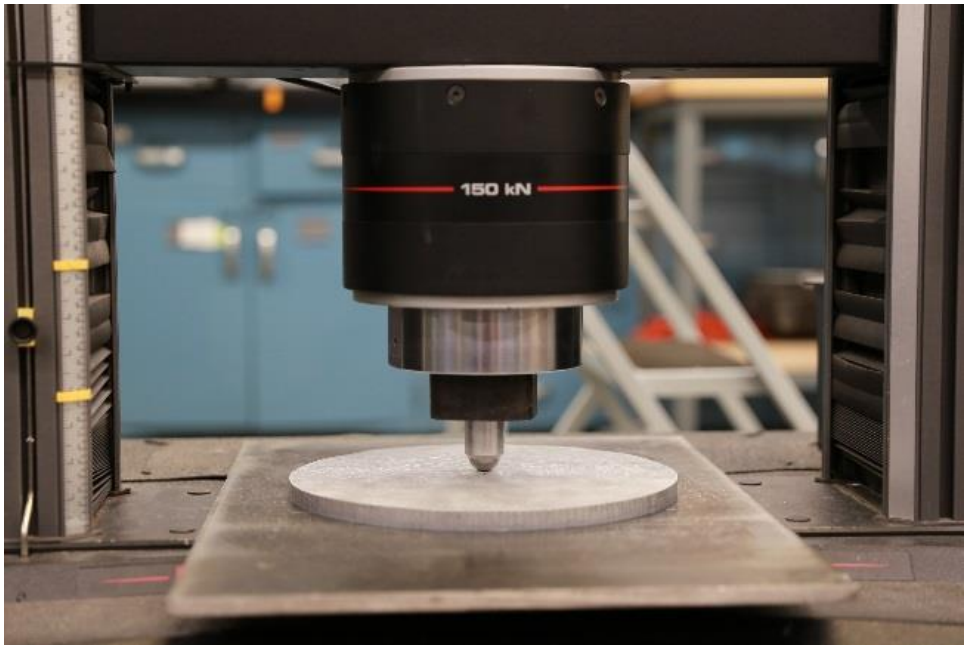

Figure 38 Point-load compression test on the curved FGM panel.

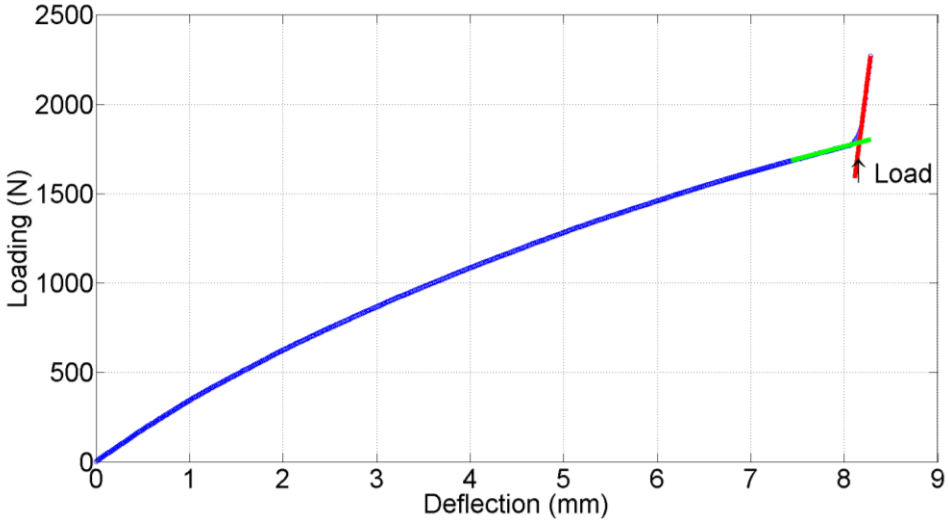

Figure 39 The deflection-loading curve of the circular FGM panel subjected to a center-pointed load

The FGM panel was loaded under the universal testing machine as shown in Figure 38. The loading point is of a ball shape head. The circular panel, with its edge smoothed and smeared with lubricant oil, was placed on a flat smooth steel plate. The applied load and the loading head displacement

were simultaneously recorded via the data acquisition system, which is shown in Figure 39. It shows that the deformation of the FGM panel gradually increases with the increasing loading. The peak load that is required to flatten the curved FGM panel is identified by the sudden change of the recorded load, indicated by the convex point of the deflection-loading curve as shown in Figure 39. The determined peak load is 1786 N with a corresponding deformation of 8.1 mm. Notice that this deformation is a little larger than the one measured from the LDS provided in Table 1, which is mainly resulted from the additional deformations from the loading point and the bottom edge of the FGM panel because of stress concentrations. Although the deformation measured is larger than the real one, the recorded load is the actual one that needs to make the curved FGM panel become flat, thus it will be used to validate the predicted load based on the present model that requires to be applied to make a flat FGM panel have a deformation of 7.06 mm, which is the real thermal deflection as measured in Table 13.

4.4 Comparison and verification

4.4.1 Thermal loading

The thermal deflection of the circular FGM panel due to a constant temperature drop (from 100 ºC to room temperature 25 ºC) is calculated in this section by the present model, which will be verified by the measured one provided in Table 13. As a comparison and further verification, the predictions from two conventional theories, i.e., the classic plate theory (CPT) and the FSDT will be also used to compare with the present solution. The geometry and material properties of the FGM panel that were characterized in Section 3 are used in the modeling. It's worthy to note that, under the pure thermal loading, no shear deformation in the circular FGM panel will be generated,

thus the thermal deflection predicted by the three theoretical models provide the exact same values, which is 6.65 mm. In comparison with the experimental measured (7.06 mm), the difference between the theoretical prediction and the experimental one is about 5%, which validate the present model.

4.4.2 Mechanical loading

Concentrated point load

The circular FGM panel subjected to a center-pointed mechanical load is considered in this section. In addition to the present theoretical model, the CPT and FSDT are also applied to predict the loading point deflection. The explicit solutions based on the CPT and FSDT have been also derived, which can be mathematically expressed as

$$w^{CPT} = -\left[\frac{A_{11}Fr^2(lnr-1)}{8\pi det} - \frac{A_{11}Fr_0^2(lnr_0-1)}{8\pi det}\right] + \frac{\xi^F}{4}(r^2 - r_0^2) \tag{4.31}$$

$$w^{FSDT} = -\frac{A_{11}F}{8\pi det}(r^2 lnr - r_0^2 lnr_0) + \left(\frac{A_{11}F}{8\pi det} + \frac{\xi^F}{4}\right)(r^2 - r_0^2) + \frac{F}{2\pi K A_{33}}(lnr - lnr_0) \tag{4.32}$$

where

$\xi^F = \frac{2}{(1+v)det}\left[B_{11}N^T - A_{11}M_b^T + A_{11}\frac{F}{8\pi}(2lnr_0 + 1) + A_{11}\frac{vF}{8\pi}(2lnr_0 - 1)\right]$, $det = A_{11}D_{11} - B_{11}^2$, and K is the shear coefficient in the FSDT which is usually taken as $K = \frac{5}{6}$.

Finite Element Analysis (FEA) was also conducted through the commercial software package ABAQUS 6.13 to further validate the present solution. In FEA, the axisymmetric element CAX4 was applied to mesh an axisymmetric beam, which was discretized into thirty two homogeneous layers with equal thickness but different material properties to approximate the continuous gradation across the thickness direction of the FGM panel. The material properties were assigned

for each layer along the thickness direction by matching them according to the gradation determined in Figure 35.

To optimize the element distribution, gradient element was employed along both the thickness and radial direction of the axisymmetric beam, leading to a much denser element distribution at the center and two ends, where the concentrated point load and boundary conditions are applied, respectively. The number of seeds along the thickness in each layer varies gradually from two seeds at the upper and bottom boundary to five seeds at the center. Totally about 138 thousand elements were generated for the whole structure. In order to simulate a simply supported boundary condition, the axisymmetric beam was constrained in the vertical direction and an axisymmetric boundary condition is applied at the inner surface. A point load of 1786 *N* measured in subsection 3.4 was applied.

The comparison among the CPT, FSDT, the present model and FEA on the deflection of the axisymmetric FGM panel subjected to concentrated point load is shown in Figure 40. It shows that all the four solutions agree very well throughout the span of the axisymmetric panel expect a small region close to the center of panel where concentrated load is applied. While within this small region (about 1/8 of the whole span), it is shown from Figure 40 that the CPT slightly underestimates the deflection as it completely ignores all shear deformation developed in the panel. At the panel center where the concentrated load is applied, infinity large deflection are predicted by all three theoretical models (CPT, FSDT and present model), which represents the singularity point. In the vicinity to the singularity point, Figure 40 indicates that the prediction by the present model approaches to the real one (measurement = 7.06 mm) more smoothly, while both the FSDT and FEM predict a more severe singularity than the present model.

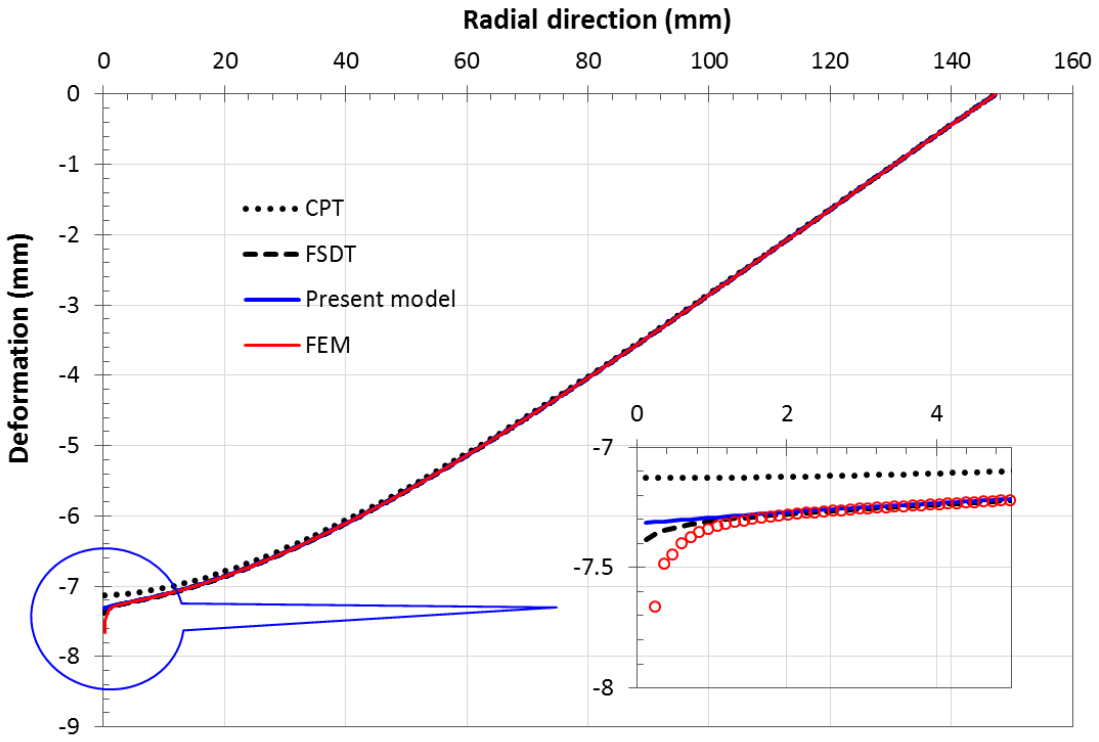

Figure 40 Comparison among different models on the deflection of the axisymmetric FGM panel subjected to concentrated point load

Uniformly distributed load

The comparison among different models on the deflection of the axisymmetric FGM panel when subjected to a uniform mechanical load is shown in Figure 41. The explicit solutions for the CPT and FSDT under uniform load can be mathematically expressed as

$$w^{CPT} = \frac{A_{11}q}{64det}(r^4 - r_0^4) + \frac{\xi^P}{4}(r^2 - r_0^2) \tag{4.33}$$

$$w^{FSDT} = \frac{A_{11}q}{64det}(r^4 - r_0^4) + \left(\frac{\xi^P}{4} + \frac{q}{4KA_{33}}\right)(r^2 - r_0^2) \tag{4.34}$$

where

$\xi^P = \frac{2}{(1+v)det}\left[B_{11}N^T - A_{11}M_b^T - A_{11}\frac{3+v}{16}qr_0^2\right]$, $det = A_{11}D_{11} - B_{11}^2$, $A_{33} = \int_{-\frac{h}{2}}^{\frac{h}{2}} \frac{E}{2(1+v)}dz$, and $K = \frac{5}{6}$ is the shear coefficient in the FSDT.

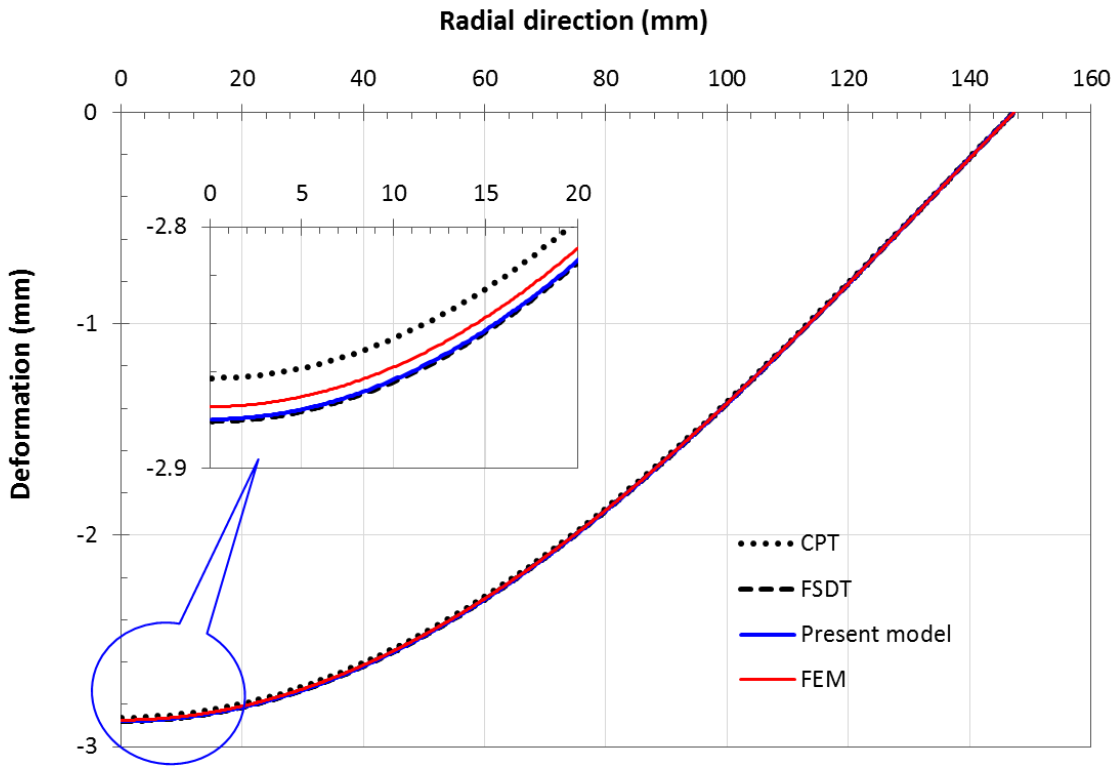

Figure 41 Comparison among different models on the deflection of the axisymmetric FGM panel subjected to uniformly distributed load

It shows again from Figure 41 that the four solutions agree well throughout the whole span of the axisymmetric panel, where the difference among different models is less than 1%. Overall, the well agreements among the present model, FSDT and FEM as shown in Figure 41 validate the present model. It's worthy to note that the considered FGM panel is quite thin (diameter: thickness = 23.2), and the shear modulus in the considered FGM panel is comparable to its Young's modulus, leading to a trivial shear deformation and a negligible difference among the four considered models. However, for moderate/thick plate, or laminated composite materials whose shear modulus are usually considerably smaller than their in-plane modulus, the shear deformation will be generally much apparent, it is thus expected that more obvious difference from the predictions among different models will be observed.

4.5 Conclusions

To understand the deformation of the FGM under thermo-mechanical loading, an axisymmetric refined plate theory was developed in this study for a circular FGM panel subjected to thermo-elastic loading. The closed-form solutions for the circular panel under different loadings (thermal, concentrated point, and uniformly distributed load) were provided. The derivation and exact solution of the refined plate theory is much simpler than other high order plate theories. Sample preparation and material characterization of the considered FGM panel were presented, and the experiments on the structural performances of the circular panel under thermo-mechanical loadings were subsequently conducted to validate the present model. As a comparison, explicit solutions based on the conventional CPT and FSDT were also developed. Finite element analyses (FEA) were conducted to further verify the present model for the circular FGM panel under different loading conditions.

The comparison results show that, (1) under pure thermal loading where no shear deformation involved in the circular FGM panel, the thermal deflection predicted by the three theoretical models (CPT, FSDT and the present refined theory) provide the exact same values, which agree well with the experimental result with a difference less than 5%; (2) under mechanical loading (both concentrated point load and uniformly distributed load), the three theoretical models generally agree well with the FEA predictions, except that the CPT slightly underestimates the deflection while the FSDT predict a more severe singularity within a small region (about 1/8 of the whole span) to the loading point. In general, all three theoretical models are able to provide acceptable predictions on the deflection of the circular FGM panel under thermos-mechanical loading.

The plate theory predicts the structural performance based on the distribution of material properties, which can be predicted based on the micromechanics model introduced in Chapter 3, given the volume fraction distribution of the reinforcement. Such process can also be reversed to tailor the volume fraction distribution needed to satisfy a specific loading requirement, which can provide significant value to the design and engineering.

4.6 Appendix

4.6.1 Concentrated point load

The displacements of functionally graded plate under concentrated load F are determined as:

$$\begin{cases} w_k = \dfrac{F}{8\pi}\dfrac{1}{\zeta_1}(r^2 lnr - r_0^2 lnr_0) + \xi_3(r^2 - r_0^2) \\ w_s = \eta_1[I_0(\kappa r) - I_0(\kappa r_0)] - \dfrac{F}{2\pi\kappa^2\zeta_7}[K_0(\kappa r) + lnr - K_0(\kappa r_0) - lnr_0] \\ u_0 = \dfrac{FB_{11}}{8\pi A_{11}\zeta_1}(2rlnr + r) + 2\dfrac{B_{11}}{A_{11}}\xi_3 r + \zeta_8\eta_1\kappa I_1(\kappa r) + \dfrac{F\zeta_8}{2\pi\kappa^2\zeta_7}\left[\kappa K_1(\kappa r) - \dfrac{1}{r}\right] + \dfrac{N^T}{A_{11}(1+v)}r \end{cases}$$

While the coefficient ξ_3 and η_1 are calculated as:

$$\begin{pmatrix} \xi_3 \\ \eta_1 \end{pmatrix} = \begin{bmatrix} a_{11} & a_{12} \\ a_{21} & a_{22} \end{bmatrix}^{-1} \begin{pmatrix} f_1 \\ f_2 \end{pmatrix}$$

where:

$a_{11} = 2\left(B_{11}\frac{B_{11}}{A_{11}} - D_{11}\right)(1+v)$, $a_{12} = \left[B_{11}\left(\frac{B_{11}^S}{A_{11}} - \frac{\zeta_2}{\zeta_1}\frac{B_{11}}{A_{11}}\right) - \left(D_{11}^S - \frac{\zeta_2}{\zeta_1}D_{11}\right)\right]\left[\kappa^2 I_0(\kappa r_0) - (1-v)\frac{\kappa}{r_0}I_1(\kappa r_0)\right]$,

$a_{21} = 2\left(B_{11}^S\frac{B_{11}}{A_{11}} - D_{11}^S\right)(1+v)$, $a_{22} = \left[B_{11}^S\left(\frac{B_{11}^S}{A_{11}} - \frac{\zeta_2}{\zeta_1}\frac{B_{11}}{A_{11}}\right) - \left(H_{11}^S - \frac{\zeta_2}{\zeta_1}D_{11}^S\right)\right]\left[\kappa^2 I_0(\kappa r_0) - (1-v)\frac{\kappa}{r_0}I_1(\kappa r_0)\right]$,

$f_1 = -\left(B_{11}\frac{B_{11}}{A_{11}} - D_{11}\right)\frac{F}{8\pi}\frac{1}{\zeta_1}[(2lnr_0 + 3) + v(2lnr_0 + 1)] + \left[B_{11}\left(\frac{B_{11}^S}{A_{11}} - \frac{\zeta_2}{\zeta_1}\frac{B_{11}}{A_{11}}\right) - \left(D_{11}^S - \frac{\zeta_2}{\zeta_1}D_{11}\right)\right]\frac{F}{2\pi\kappa^2\zeta_7}\left[\kappa^2 K_0(\kappa r_0) + (1 - v)\frac{\kappa}{r_0}K_1(\kappa r_0) - (1-v)\frac{1}{r_0^2}\right] + M_b^T - \frac{N^T}{A_{11}}B_{11}$,

$f_2 = -\left(B_{11}^S\frac{B_{11}}{A_{11}} - D_{11}^S\right)\frac{F}{8\pi}\frac{1}{\zeta_1}[(2lnr_0 + 3) + v(2lnr_0 + 1)] + \left[B_{11}^S\left(\frac{B_{11}^S}{A_{11}} - \frac{\zeta_2}{\zeta_1}\frac{B_{11}}{A_{11}}\right) - \left(H_{11}^S - \frac{\zeta_2}{\zeta_1}D_{11}^S\right)\right]\frac{F}{2\pi\kappa^2\zeta_7}\left[\kappa^2 K_0(\kappa r_0) + (1 - v)\frac{\kappa}{r_0}K_1(\kappa r_0) - (1-v)\frac{1}{r_0^2}\right] + M_s^T - \frac{N^T}{A_{11}}B_{11}^S$,

4.6.2 Uniformly distributed load

The displacements of functionally graded plate under uniformly distributed load q_0 are determined as:

$$\begin{cases} w_k = \xi_3 r^2 - \xi_3 r_0^2 + \dfrac{q_0}{64\zeta_1} r^4 - \dfrac{q_0}{64\zeta_1} r_0^4 \\ w_s = \eta_1 I_0(\kappa r) - \dfrac{q_0}{4\zeta_6\zeta_7} r^2 - \eta_1 I_0(\kappa r_0) + \dfrac{q_0}{4\zeta_6\zeta_7} r_0^2 \\ u_0 = \dfrac{B_{11}}{A_{11}}\left(2\xi_3 r + \dfrac{q_0}{16\zeta_1} r^3\right) + \left(\dfrac{C_{11}}{A_{11}} - \dfrac{\zeta_2}{\zeta_1}\dfrac{B_{11}}{A_{11}}\right)\left(\kappa\eta_1 I_1(\kappa r) - \dfrac{q_0}{2\zeta_6\zeta_7} r\right) + \dfrac{N^T}{(1+v)A_{11}} r \end{cases}$$

While the coefficients ξ_3 and η_1 are calculated as:

$$\begin{pmatrix} \xi_3 \\ \eta_1 \end{pmatrix} = \begin{bmatrix} a_{11} & a_{12} \\ a_{21} & a_{22} \end{bmatrix}^{-1} \begin{pmatrix} f_1 \\ f_2 \end{pmatrix}$$

where:

$a_{11} = 2(1+v)\left(B_{11}\frac{B_{11}}{A_{11}} - D_{11}\right)$,

$a_{12} = \left[B_{11}\left(\frac{B_{11}^S}{A_{11}} - \frac{\zeta_2}{\zeta_1}\frac{B_{11}}{A_{11}}\right) - \left(D_{11}^S - \frac{\zeta_2}{\zeta_1}D_{11}\right)\right]\left[\kappa^2 I_0(\kappa r_0) - (1-v)\kappa\frac{I_1(\kappa r_0)}{r_0}\right]$,

$a_{21} = 2(1+v)\left(B_{11}^S\frac{B_{11}}{A_{11}} - D_{11}^S\right)$,

$a_{22} = \left[B_{11}^S\left(\frac{B_{11}^S}{A_{11}} - \frac{\zeta_2}{\zeta_1}\frac{B_{11}}{A_{11}}\right) - \left(H_{11}^S - \frac{\zeta_2}{\zeta_1}D_{11}^S\right)\right]\left[\kappa^2 I_0(\kappa r_0) - (1-v)\kappa\frac{I_1(\kappa r_0)}{r_0}\right]$,

$f_1 = M_b^T - \frac{N^T}{A_{11}}B_{11} + \left[B_{11}\left(\frac{B_{11}^S}{A_{11}} - \frac{\zeta_2}{\zeta_1}\frac{B_{11}}{A_{11}}\right) - \left(D_{11}^S - \frac{\zeta_2}{\zeta_1}D_{11}\right)\right](1+v)\frac{q_0}{2\zeta_6\zeta_7} - \left(B_{11}\frac{B_{11}}{A_{11}} - D_{11}\right)(3+v)\frac{q_0}{16\zeta_1}r_0^2$,

$f_2 = M_s^T - \frac{N^T}{A_{11}}B_{11}^S + \left[B_{11}^S\left(\frac{B_{11}^S}{A_{11}} - \frac{\zeta_2}{\zeta_1}\frac{B_{11}}{A_{11}}\right) - \left(H_{11}^S - \frac{\zeta_2}{\zeta_1}D_{11}^S\right)\right](1+v)\frac{q_0}{2\zeta_6\zeta_7} - \left(B_{11}^S\frac{B_{11}}{A_{11}} - D_{11}^S\right)$.

Chapter 5 Design and demonstration of a thermoelectric-powered wireless sensor platform in window frames for the smart building envelope

5.1 Overview

The energy efficiency improvement of buildings can be achieved with the help of a smarter building management system, which requires the continuous and accurate monitoring of the internal and external environment. The wireless sensor network can fulfill such functionalities but would need stable and long-term power supply for the sensors and controllers. The energy harvesting technologies provide a good solution to elongate the battery lifetime and to reduce the maintenance cost of the wireless sensor network (WSN), where solar cells, piezoelectric elements, and thermoelectric elements can be used to to convert light, vibration, and heat energy into electricity. The building envelope, as the barrier between the interior and the exterior of a building, features considerably exposure to the interior and exterior of buildings and is therefore crucial to the energy harvesting application in the smart building management. The thermal energy harvesting from the building envelope, although rarely seen as an independent energy harvesting approach, is a perfect energy source for the wireless sensor platform. The traditional window/façade system the R-value, to quantify the performance of its thermal resistance. The higher the R-value, the better the energy efficiency, and less energy needed to stabilize the room temperature. The thermal bridging and infiltration losses shall be minimized as much as possible, to break down the energy exchange across the building surface. Therefore, thermal break can be easily formulated across the window cross section, which is schematically drawn in Figure 42 as an example in winter seasons. The huge temperature difference on the two sides of the window

provides great potential for the thermal energy harvesting through the thermoelectric generator (TEG).

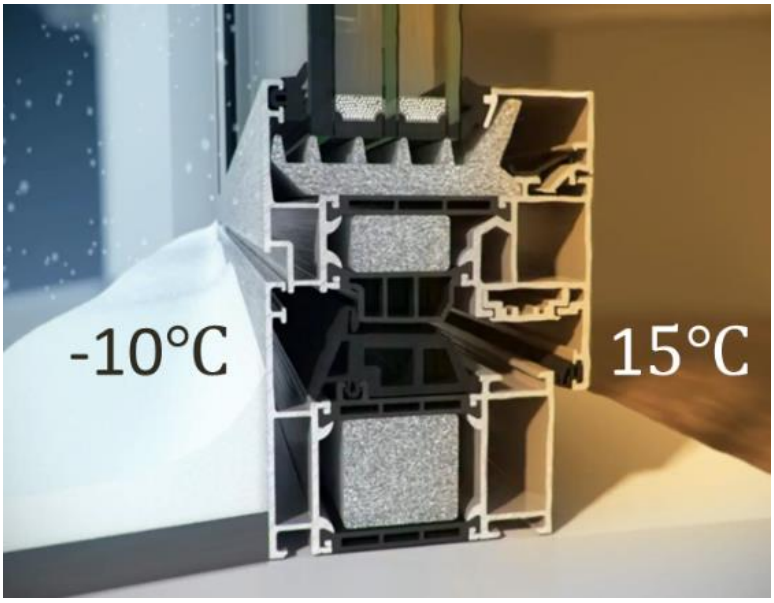

Figure 42 Temperature difference potential across the façade

In this chapter, a thermoelectric-powered wireless sensor platform designed for the next generation of the smart building envelope is proposed and prototyped within a window frame. The platform was designed entirely inside the frame with no wired connections to the outside, therefore having no compromise of the outlook. With a slight modification of the internal profile and thermal performance, the platform achieves energy equilibrium between energy consumption and harvesting and provides the solution to the limited battery lifetime of the wireless sensor network. Comprehensive discussions of the design methodology are conducted and elaborated for both the energy harvesting and the wireless sensing subsystems. Corresponding lab tests are conducted rigorously to prove the feasibility and to demonstrate the performance of the platform. An energy equilibrium algorithm is proposed based on the field test result to predict the battery energy level, such that the self-powered feature can be achieved in any environment by proper engineering of

key design parameters. The optimal battery capacity can also be determined through the cyclic amplitude of the battery energy projection. The design methodology and the energy equilibrium algorithm serve as a valuable guidance for the future design and engineering of the energy harvesting based wireless sensor network. The success of this project provides the continuous monitoring of the environment and valuable information for the optimal control of the building management system, such that significant savings can be achieved without jeopardizing the interior comfort.

The rest of this chapter is organized as follows. Section 5.2 presents the thermal energy harvesting design inside the confined window frame. Section 5.3 discusses the design methodology of the thermoelectric-powered wireless sensor network platform and the energy equilibrium algorithm. The specific design issues and the corresponding test performance of both the wireless sensor network unit and the energy harvesting unit are addressed in Subsection 5.3.1, while the theoretical discussion of the energy equilibrium algorithm is presented in Subsection 5.3.2 based on the design methodology. In Section 5.4, the field test of the TPWSN unit inside a window frame is conducted and discussed, where the amounts of energy consumption and energy harvesting are continuously monitored and calculated. Following the test results, Section 5.5 presents the energy equilibrium design and the battery performance prediction based on the historical temperature data in New York City, such that the eternal lifetime can be achieved from the energy perspective. Section 5.6 summarizes this chapter with conclusive remarks.

5.2 Thermal energy harvesting inside window frame

As the skin of buildings, window and facades are responsible for the thermal isolation to keep the internal environment stable. Such thermal isolation is achieved by the thermal resistive foams and

isolators embedded between the metal frames, as is demonstrated in Figure 43. Therefore, large temperature difference is observed across the profile, especially between the B-C surface, providing great potential for thermal energy harvesting. The thermoelectric generator (TEG) is applied to transform the temperature difference into electricity. The TEG is made with many thermocouples connected in series, and is schematically illustrated in Figure 44. Each thermocouple consists of a pair of N-type and P-type semiconductor to converse the temperature difference to electric voltage based on the Seebeck effect. It unearths the connection between the heat and electricity such that when temperature gradient is applied onto the connected thermocouples, heated electrons will flow over from hot side toward the cooler side to formulate the current and thus output voltage. Although the voltage produced from a single thermocouple is only a few microvolts per kelvin of temperature difference, thousands of them can be connected in series to magnify the output power. Unfortunately, the efficiency of the thermocouples is restricted by the Carnot factor and usually lies within 3~6% [226].

The small dimension and thermal-gradient based mechanism make TEG the perfect solution for the energy harvesting in the window frame. The length and width of a TEG can be customized with tailored allocation of thermocouples. The thickness, however, is usually made very thin, approximately 2-4 mm. It is because the thermal couples are like fixed-fixed beam and will be easily buckled and broken under large length-to-width ratio. It is possible to customize a thickness up to 6-8 mm, but the cost could rise significantly, according to the authors' survey with the vendors. The TEGs along will not fill in the space of the window frames and thus a thermal connector is needed for the heat transfer between window and TEG. Therefore, the design methodology for the thermal energy harvester is discussed in this section to achieve the optimal objective inside the confined window frame.

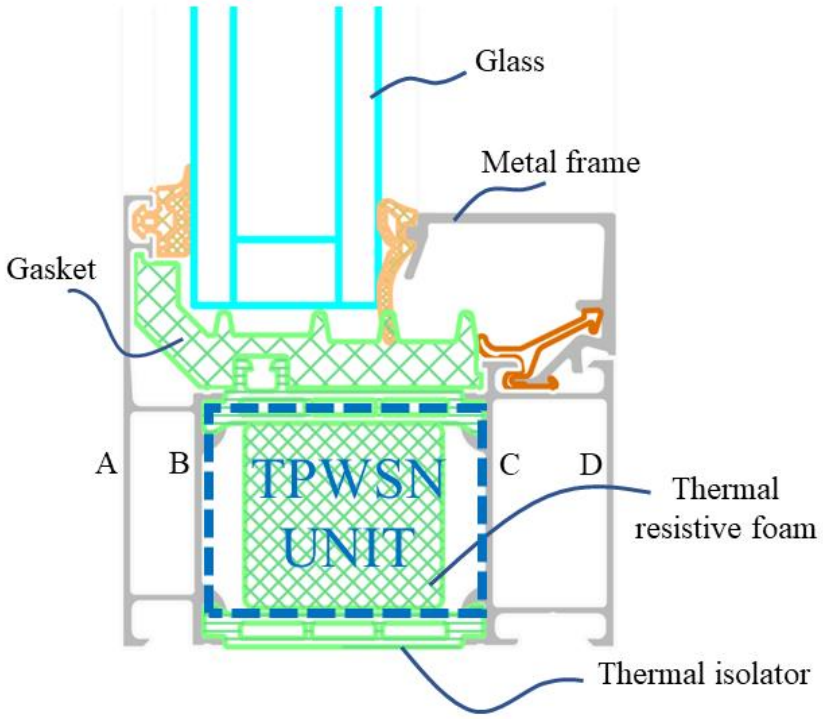

Figure 43 Schematic design of TPWSN unit inside window system

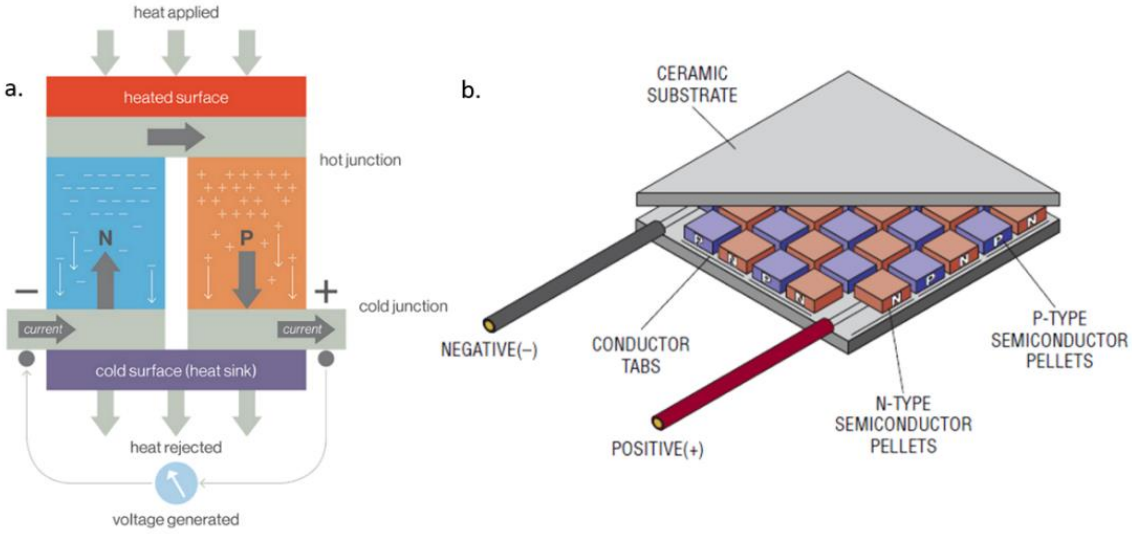

Figure 44 The structure of thermocouple and thermoelectric generator [227]

The power output of a TEG P_{TEG} is dependent on the number of thermocouples and the power output from each thermocouple. The number of thermocouples is linearly proportional to the

surface area of the TEG, A_{TEG}, while the individual power output is quadratically proportional to the temperature difference applied on the two sides of the TEG, ΔT_{TEG}, because both the voltage and current output are linearly proportionally to the temperature difference:

$$P_{TEG} \propto A_{TEG} \cdot (\Delta T_{TEG})^2 \tag{5.1}$$

It is straightforward to see that the temperature difference ΔT_{TEG} is maximized by filling the remaining of the space with the thermal conductive materials, like metals, so that the maximum amount of thermal gradient is conducted onto the TEG surfaces. However, the solid metal connector will greatly increase the weight of the window frame if multiple units are implemented. Therefore, the weight of the corresponding thermal connectors, ω_{TC}, is taken into the consideration. The objective function for the optimal design is thus proposed as:

$$Obj = \frac{P_{TEG}}{(\omega_{TC})^{\alpha}} \propto \frac{A_{TEG} \cdot (\Delta T_{TEG})^2}{(\omega_{TC})^{\alpha}} \tag{5.2}$$

where the α is a scaling factor that indicates the importance of the weight comparing to the power output. The larger the α, the more important it is of the weight over the power output. The determination of the α depends on the valuation of the weight and the energy harvesting. The α can be set at a big value to emphasize the importance of weight optimization, when the energy is abundant.

Finite element models are constructed to optimize the objective function and to achieve the most efficient design, with respect to the surface area A_{TEG}, the temperature difference ΔT_{TEG}, and the weight ω_{TC}. The space inside the window frame is measured at 42.5 mm × 25 mm and the thickness of the TEG is set as 3 mm. The surface area depends on the angle of the TEGs placement, and the largest surface area corresponds to the diagonal direction. In the scope of this research, the Schuco AWS 75 window frame is used for the prototype, and the diagonal direction corresponds

to 60° of the TEG placement angle. Therefore, in the Finite Element Analysis, angles ranging from 0° to 60° are investigated with an increment of 15°. The temperature difference depends on the internal structure of the thermal connector. The solid, three-bridge, one bridge, and hollow structure for the internal connectors are investigated. The width of the bridges and the surroundings is set at 1.5 mm. For simplicity, the five models with different TEG placement angles in the three-bridge design scenario is shown in Figure 45. Similar designs of the TEG placement angle are applied to the solid, one-bridge, and hollow thermal connector, where the designs for the 45-degree are demonstrated in Figure 46. A total of 20 models are constructed in the ABAQUS for the heat analysis. The extrusion length is set at 60 mm for all the models.

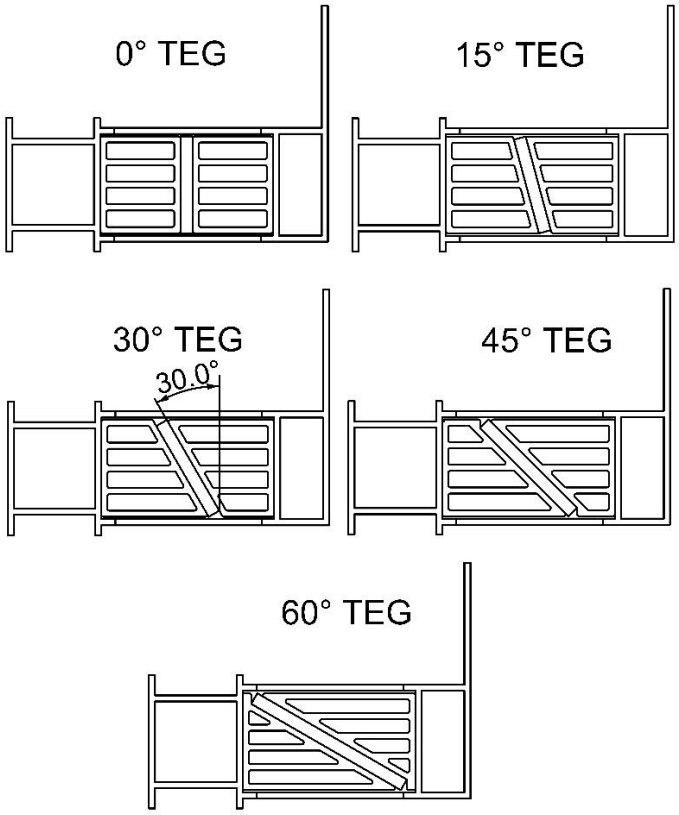

Figure 45 The five models with different TEG angles and three-bridge thermal connector design

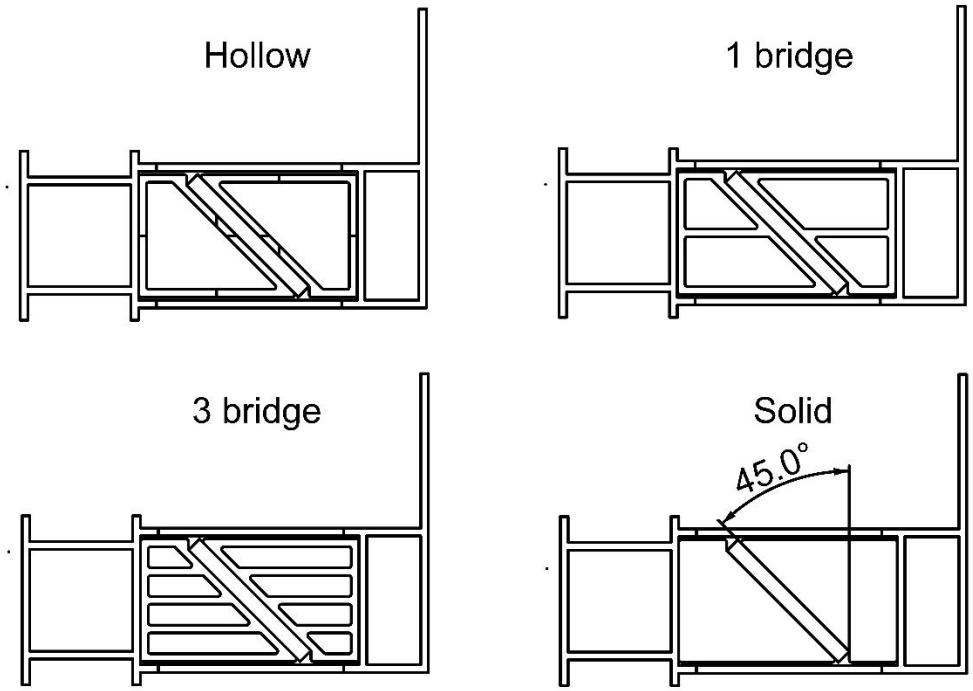

Figure 46 The four models with different thermal connector designs and 45-degree TEG angle

Table 14 Thermal conductivities of materials in the finite element model

Materials	Aluminum	TEG	Thermal isolator (PA66)
Thermal conductivities (W/m-K)	160	1.7	0.3

The steady state heat transfer analysis is conducted. The top surface indicates the in-room temperature with the boundary condition at 25 ℃ and the bottom surface indicates the out-of-room temperature with the boundary condition at -3 ℃. The material properties are listed in the Table 14. The thermal radiation and convection are neglected in the analysis since the thermal conduction plays the dominant part. The thermal conduction of the air inside the frame is also neglected for simplicity. The temperature information on the TEG surfaces are extracted from each Finite Element model for comparison. Figure 47 shows the temperature distribution for the three-bridge

model, under different TEG placement angles. The normalized location is used since different TEG placement angle will change the length of the TEGs. The temperature difference ΔT_{TEG} becomes smaller with the increase of the placement angle, but the temperature distributions on the top and bottom surfaces stay close to parallel. Figure 48 shows the temperature distribution for the 45-degree angle, with the four thermal connector designs. It is observed that for the solid connector design, the temperature distributed uniformly over the surface, while for the hollow connector design, the temperature difference follows the parabolic trend with the symmetric line at the center of the TEG. It is also worth to point out that the three-bridge design is already very close to the result of the solid design.

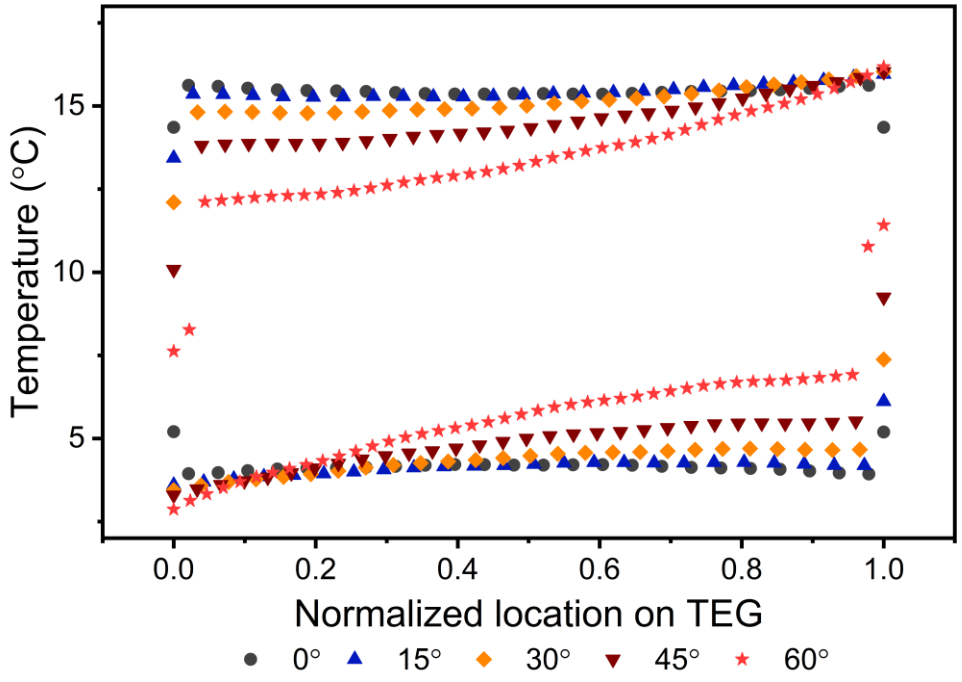

Figure 47 Temperature distribution on TEG for the three-bridge models

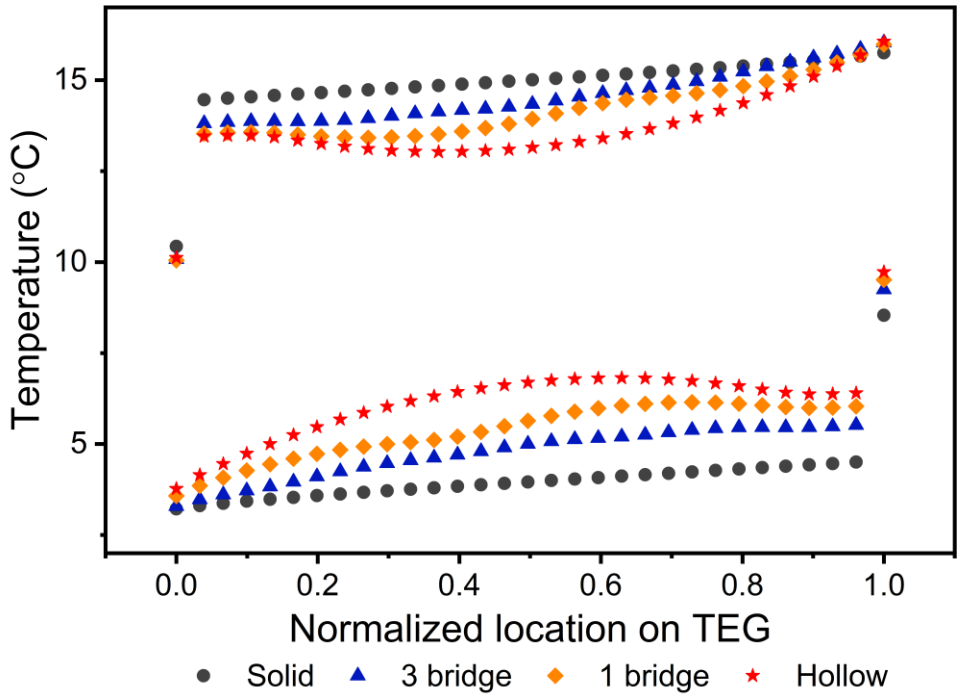

Figure 48 Temperature distribution on TEG for the 45-degree placement angle models

The temperature difference, the surface area, and the weight of the thermal connectors are extracted to calculate the objective function in Eq. (5.2). The normalized value in every design is listed in Figure 49, with the scaling factor ranging from 0, 0.5, and 1. It is observed that the most efficient design is always the case with 0 degree placement angle. Although the tilted placement of TEG elongates the contact surface, the compromise of the temperature difference is larger, and in return reduces the overall power output. The temperature difference has the second order contribution to the power output, while the contact surface is the first order term. Therefore, the contribution of the additional contact surface does not outperform the second order loss of the temperature difference. The scaling factor α determines the importance of additional weight to energy harvesting. The $\alpha = 0$, 0.5, and 1 indicates that the additional weight has no importance, half the importance and the same importance over the energy harvesting, and would recommend the solid,

three-bridge, and one-bridge structure for design of the thermal connector. After careful discussion with our industrial collaborator, the α is determined as 0.5, indicating the weight is half the importance of the power output, and therefore the three-bridge design the best performing design for our needs.

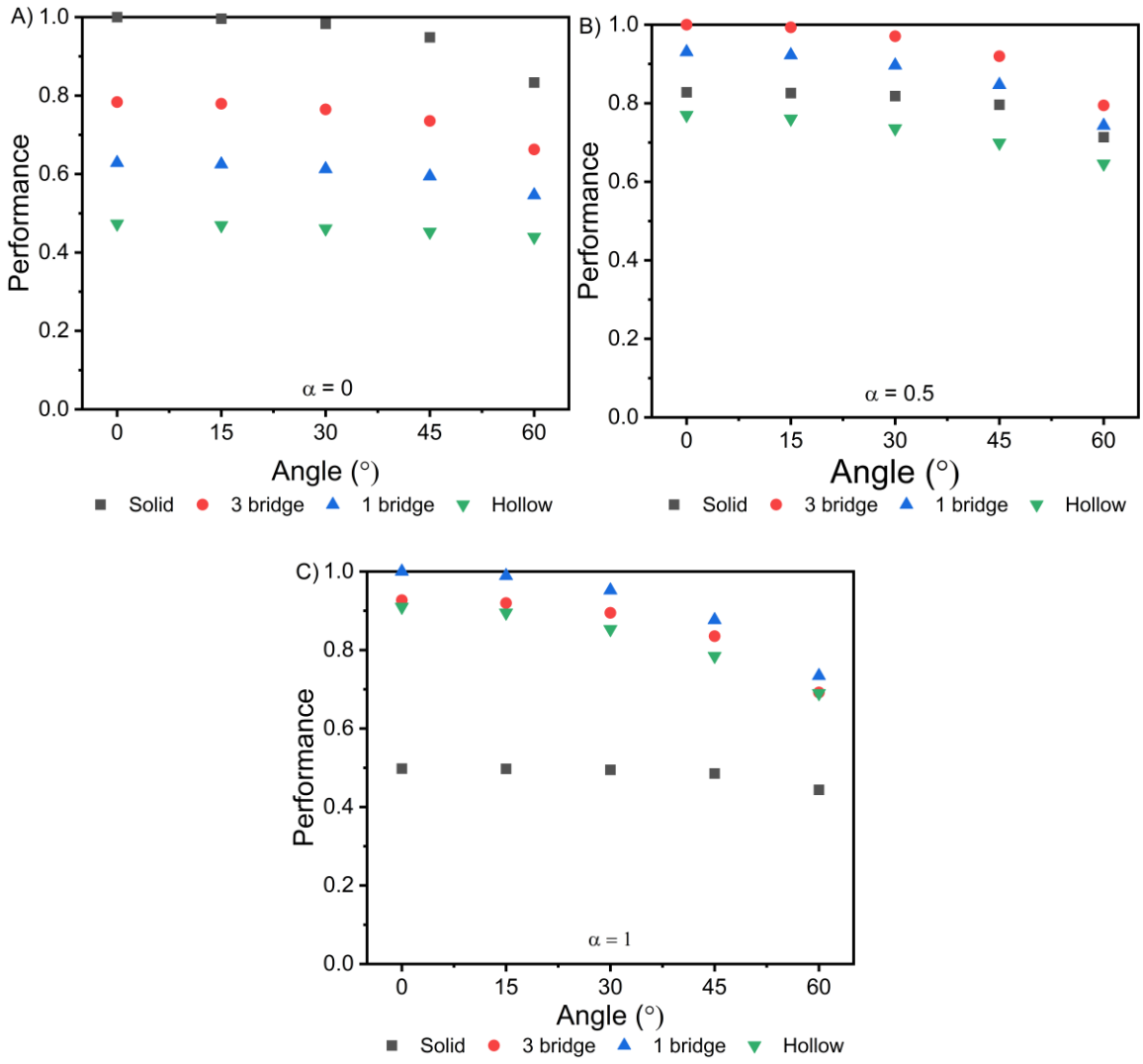

Figure 49 A) Normalized performance when $\alpha = 0$; B) Normalized performance when $\alpha = 0.5$; C) Normalized performance when $\alpha = 1$

The three-bridge structure with the 0-degree design generates best performing design when the scaling factor $\alpha = 0.5$. Unfortunately, the size of the available TEG on the market does not fit the

dimension restriction of the window frame. Therefore, the TEG with 30×30 mm dimension is selected with the three-bridge and 45-degree design, which will compromise the overall efficiency by approximately 8%. Two TEGs are connected in series and attached with the thermal connectors made by 3D printed aluminum to formulate an energy harvester unit with the depth of 60 mm, as is shown in Figure 50(A). The energy harvester unit is designed to be inside the window frame as illustrated by the 3D model generated in Rhinoceros in Figure 50 (B). The two sides of the energy harvester unit are attached to the two aluminum frames of the window to direct the temperature gradient from the window frame to the TEG. In the prototype, two energy harvester units are manufactured and implemented into the window frame, which is shown in Figure 51. Therefore, a total of four TEGs sized $30 \text{ mm} \times 30 \text{ mm} \times 3.7 \text{ mm}$ are implemented and connected in series for the test. The TEGs are manufactured by the Custom Thermoelectric and modeled 1261G-7L31-04CL. The thermal resistive plastic and foam shown in Figure 42 are removed from the window frame, formulating rectangular holes for the implementation. The spacing between holes is set as twice of the width of the energy harvester unit, to minimize the interactions between units.

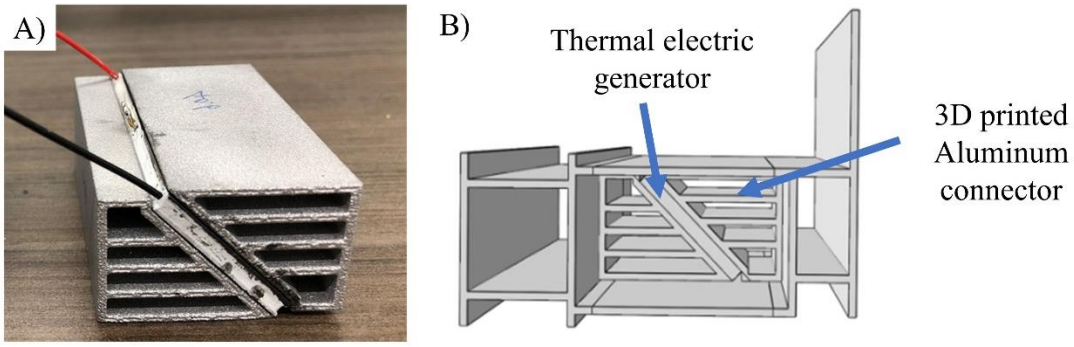

Figure 50 A) Energy harvester unit; B) 3D model inside the window frame

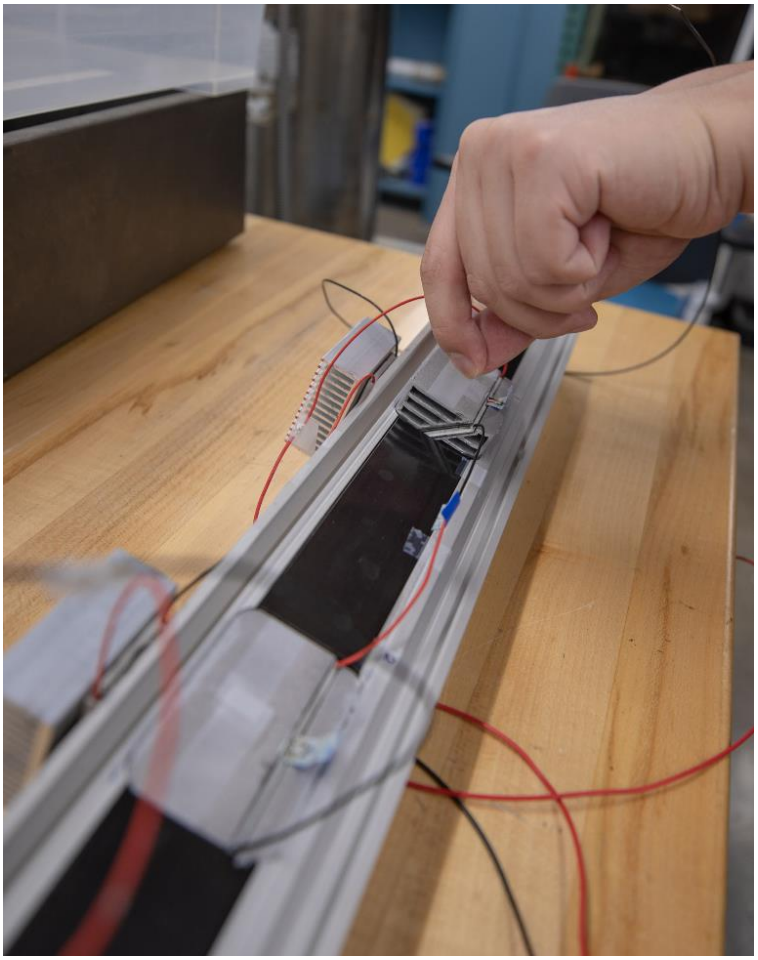

Figure 51 Energy harvesting unit implemented into the window frame

5.3 TPWSN system design and energy equilibrium algorithm

5.3.1 TPWSN system design

Thanks to the energy supply from the thermal energy harvester in the previous section, the design of the thermoelectric-powered wireless sensor network (TPWSN) becomes feasible. The architecture of the TPWSN is schematically plotted in Figure 52. The energy harvesting subsystem consists of harvesters for energy conversion, energy management circuits for optimal energy extraction, voltage boosting and regulation, and the rechargeable battery for the off-peak seasons.

The harvested energy is consumed by the processing subsystem, wireless communication subsystem and the sensing subsystem inside the wireless sensor network unit. The processing subsystem is connected with both the sensing subsystem for environment monitoring and the wireless communication subsystem for data transmission. The data from a TPWSN node will be sent out to an external server for permanent storage, which will serve as valuable information for the optimal heating, ventilation, and air conditioning (HVAC) control and building management. In an ideal TPWSN, the energy harvesting subsystem should collect as much energy as possible and transfer the dynamic power source into the stable voltage output from the battery. The processing subsystem shall consume as less energy as possible for itself, while feeding the majority of power to connected sensors and wireless communication subsystem. The following discussion will continue with a bottom up approach and discuss the design methodology in both energy harvesting and the wireless sensor network units separately. The components used in the system architecture is illustrated in Figure 53, with each part elaborated in the following subsections. In Section 5.4, the two systems are integrated, and the field test is conducted to demonstrate the performance.

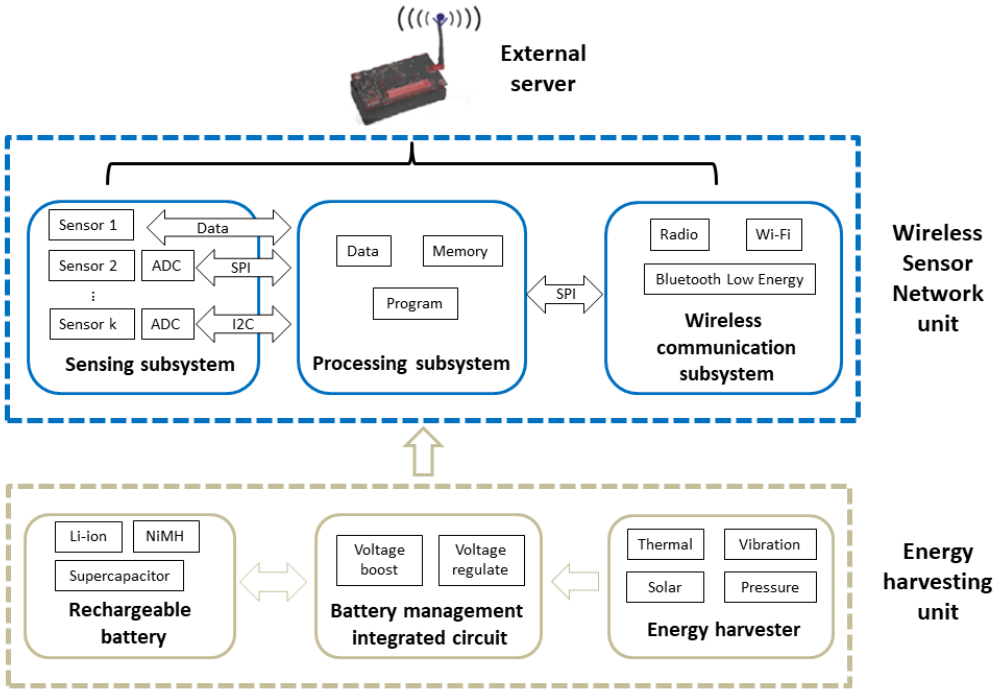

Figure 52 Architecture of the thermoelectric-powered wireless sensor network (TPWSN)

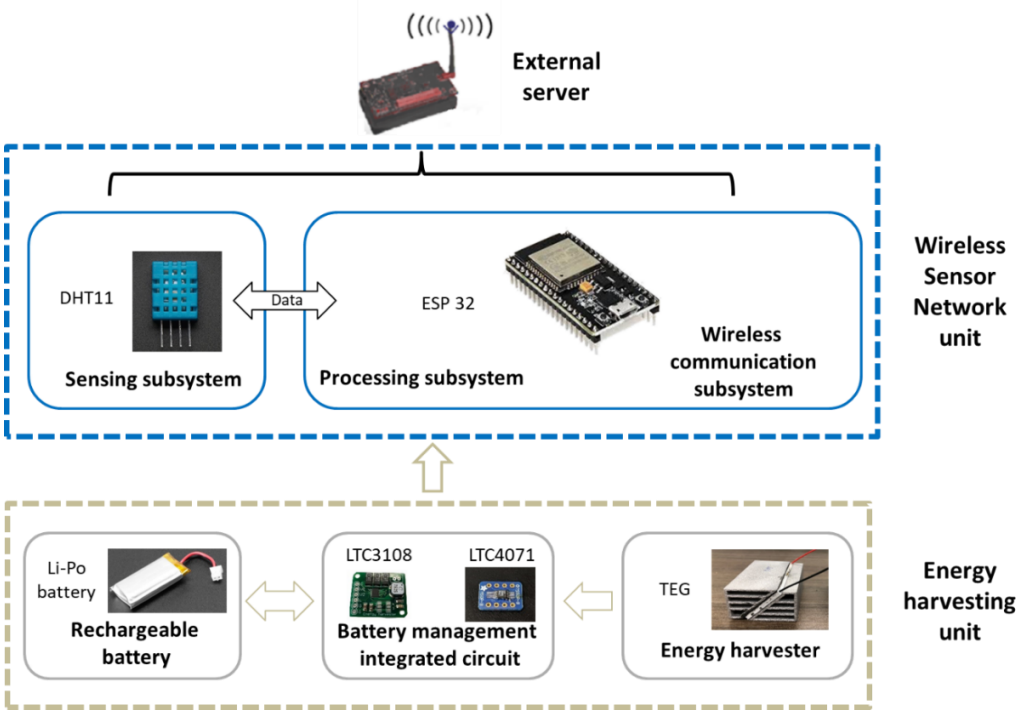

Figure 53 Components used in the system architecture of the TPWSN

5.3.1.1 Wireless sensor network unit

The energy harvesting unit extract the energy from the ambient environment and feed to the wireless sensor network unit for the data measurement and wireless communication. The wireless sensor network unit is consisted of the processing subsystem, the sensing subsystem and the wireless communication subsystem. The low-cost, low-power consumption system-on-chip (SOC) microcontroller ESP 32 is selected for the data collection, preprocessing and wireless communication of the system, which is shown in Figure 54a. The functionality block diagram of the ESP 32 is shown in Figure 54b. The ESP 32 is a super powerful SOC created and developed by Espressif and manufactured by TSMC with 40 nm process technique. Both analog and digital signal can be read through the 40 general purpose input and output channel on the chip. The ESP 32 supports both light sleep and deep sleep. In light sleep mode, the main core is paused while the RTC and the co-processor are still active. While in deep sleep mode, all the functionalities are forced to sleep except the real time clock (RTC) block and the ULP co-processor. The co-processor can also be power off for further power reduction [228]. Every memory will be wiped out during the deep sleep except the recovery memory in RTC block. A time clock can also be set to wake up the system automatically after a preset time period. A specific ESP 32 model named FireBeetle is selected for the test. FireBeetle is a model optimized in the deep sleep mode for the minimum energy consumption. It is a model optimized in the deep sleep mode for the minimum energy consumption. The advertised current consumption in the deep sleep mode can reach as low as 10 uA, and the lowest measured consumption is approximately 50 uA, which outperforms most of the SOC in the market. The DHT11 is selected as the low-cost and the low-energy-consumption sensor

for the temperature and moisture measurement. Wi-Fi is selected as the approach for the wireless communication, to send out the data and logged onto the clouds.

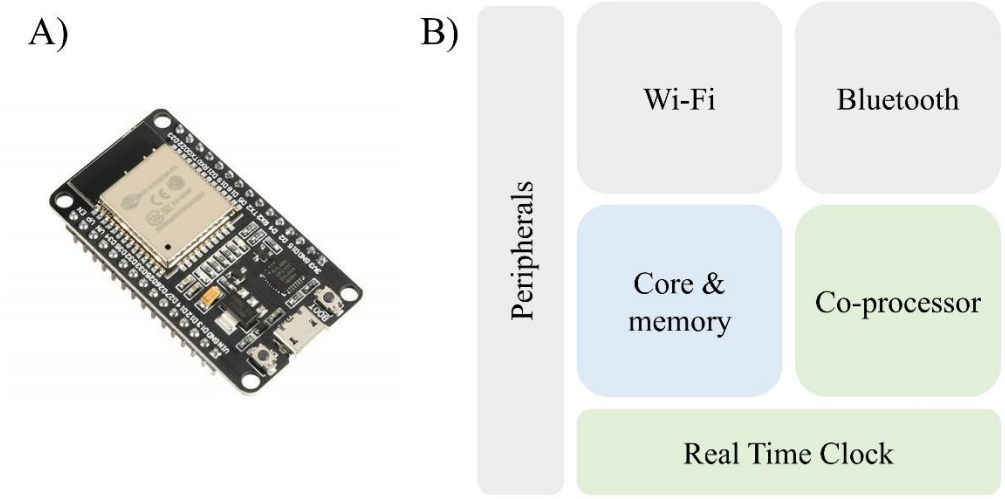

Figure 54 A). ESP 32 chip; B). ESP 32 functionality block diagram

As the brain of the system, the ESP 32 is responsible for the data reading, preliminary calculation and the wireless communication to the outside server. The schematic drawing of the procedure and corresponding functionality is shown in Figure 55. The ESP 32 is set to extract digital signal from DHT 11 every N seconds of deep sleep, and finish preliminary calculation to convert signal into temperature and moisture measurement, which will then be wirelessly sent out and logged onto Google sheets with the help of the online proxy, the IFTTT. The IFTTT stands for “If This Than That” and is a free web-based service to create chains of simple conditional statement, called applets, which can trigger changes in and from web services such as Gmail, Facebook, Instagram and Pinterest. The whole process will complete in 7 seconds (depending on the connection speed to local Wi-Fi), after which the system will go into deep sleep to loop over the whole process again and again.

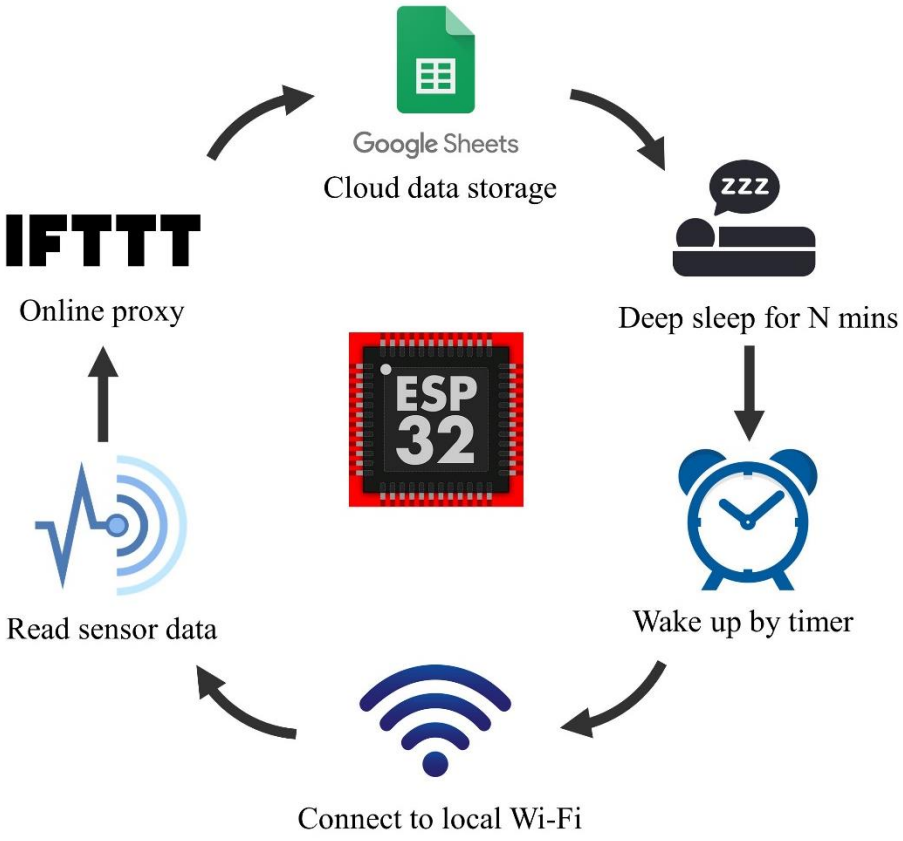

Figure 55 Schematic description of procedures in ESP 32

The current consumption of an ESP 32 can be as low as 70 mA in the awake mode and 45 uA in the deep sleep mode. It is worth point out that the instantaneous consumption can reach 450 mA during the wake-up process, which casts challenge to the energy supply unit and is a bottleneck for the energy unit design and engineering. If the start-up current requirement were not met, the system will fail to operate and continuously leak current until reset. A current shunt is designed to monitor the current consumption with the data acquisition system. The 3.1 ohms resistor with the maximum power limit of 5 W is used to sustain the instantaneous current and provide enough voltage for the DAQ to capture. The ESP 32 is programmed to cycle at every 5 minutes and totally seven cycles are documented, with the sampling frequency at 10 Hz. The current consumed in both

awake and deep mode is plotted in Figure 56 and the current in the first awake mode is enlarged in Figure 57. It is clearly seen that the regular awake mode consumes approximately 40 mA and the Wi-Fi mode consumes 115 mA. The average energy consumption in both awake and deep sleep modes are presented in the Table 15. The awake mode consumes approximately 70 mA while the deep sleep mode consumes 45 uA. The time needed for the awake mode majorly depends on the connection to the local Wi-Fi network and the average time spent is 7 seconds. Therefore, the total power consumed is calculated as

$$P_{cycle} = \frac{V_{awake} \cdot I_{awake} \cdot t_{awake} + V_{sleep} \cdot I_{sleep} \cdot t_{sleep}}{t_{awake} + t_{sleep}} \quad (5.3)$$

The power consumption can be tailored to fit the availability from the energy harvesting by controlling the t_{sleep}.

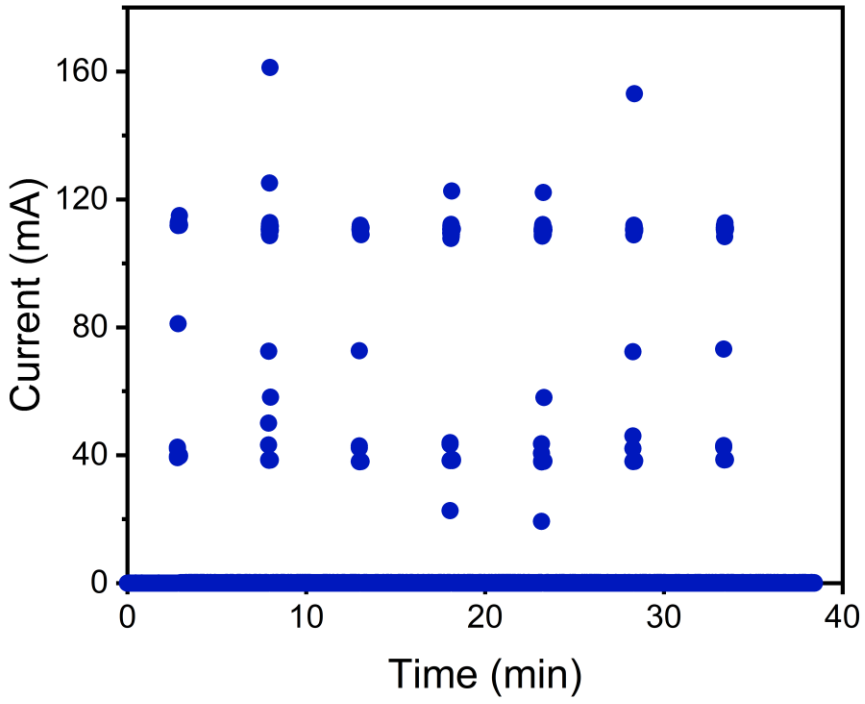

Figure 56 Current consumption of ESP 32 in both awake and deep sleep mode

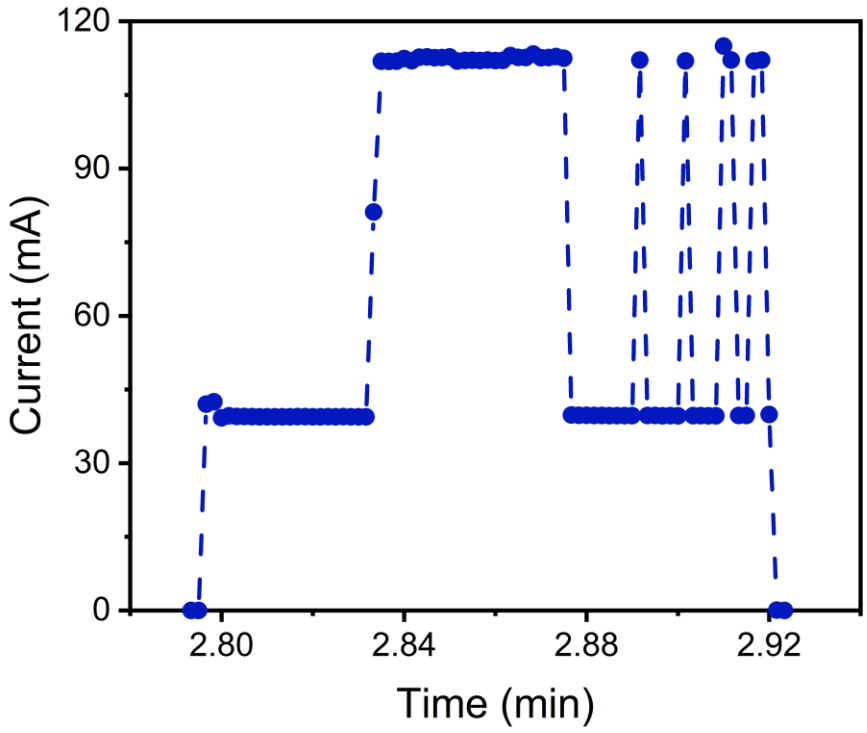

Figure 57 Current consumption of ESP 32 during the awake mode in the first cycle

Table 15 ESP 32 current consumption and awake time measurements

Cycle	1	2	3	4	5	6	7	Average
Awake time (s)	7.5	6.1	6.1	8.4	8.3	6.2	6.2	7.0
Awake current (mA)	70.30	75.16	71.57	63.12	66.34	72.35	70.89	69.96
Deep sleep current (uA)	42.69	46.21	44.34	46.13	43.82	45.10	44.80	44.73

A parametric study of the lifetime for a 500 mAh battery is conducted based on the awake and sleep data of ESP 32 and shown in the Table 16. It is seen that the power consumption reaches 0.67 mW for the deep sleep time of 1 hours, and the corresponding lifetime can be more half a year. Despite the low sampling frequency, the battery lifetime is still relatively short comparing to the life of civil structures. The demand for the energy harvesting is strong for the energy equilibrium state.

Table 16 Battery lifetime parametric study on ESP 32

Deep sleep time	5 minutes	30 minutes	1 hour	2 hours	4 hours
Averaged power consumption (mW)	6.07	1.17	0.67	0.42	0.29
1000 mAh battery lifetime (day)	12.70	65.93	115.25	184.45	263.75

5.3.1.2 Energy harvesting unit

The thermoelectric generators transform the thermal energy from temperature difference into electricity, so that the thermoelectric-powered design is practically feasible for the WSN units. However, since the TEGs depend on the temperature difference between indoor and outdoor, the power supply is dynamic across the year. Moreover, the voltage output from TEGs is very small due to the limited temperature difference and energy conversion rate. It is not possible to reach the battery recharging threshold by TEG alone. Therefore, the voltage boosting and regulating circuit LTC3108 is applied for a stable energy supply.

The LTC 3108, as shown in Figure 58 (left), is a highly integrated DC/DC converter for the energy harvesting that can boost up the voltage from 20 mV to 5 V. The energy efficiency of the LTC 3108 is tested with the input voltage ranging from 50 mV to 1V and plotted in Figure 59, where a maximum efficiency at 70% is reached when the input is around 70 mV. The efficiency drops to 40% when the input voltage is 100 mV, and even lower with higher input voltage. The LTC3108 is designed for the voltage boosting and regulation. In order to permanently store the harvested energy, a battery management circuit is needed to help store the energy and to protect the battery from damage.

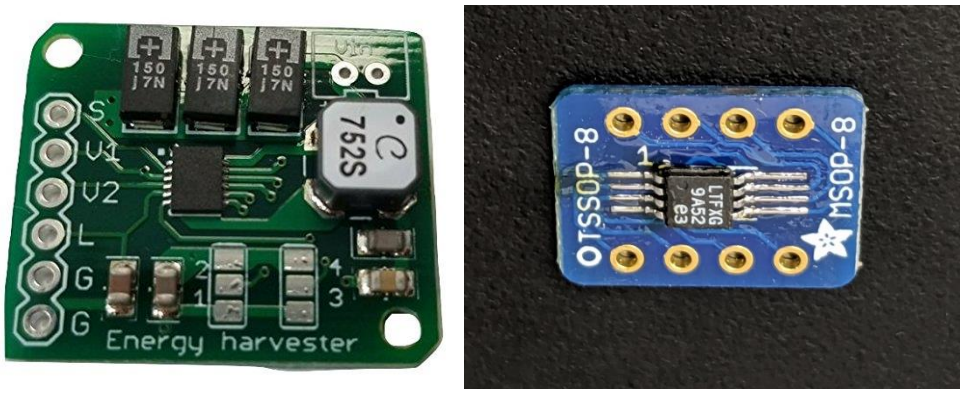

Figure 58 The voltage boosting and regulating circuit LTC3108 (left) and the battery management circuit LTC4071 (right)

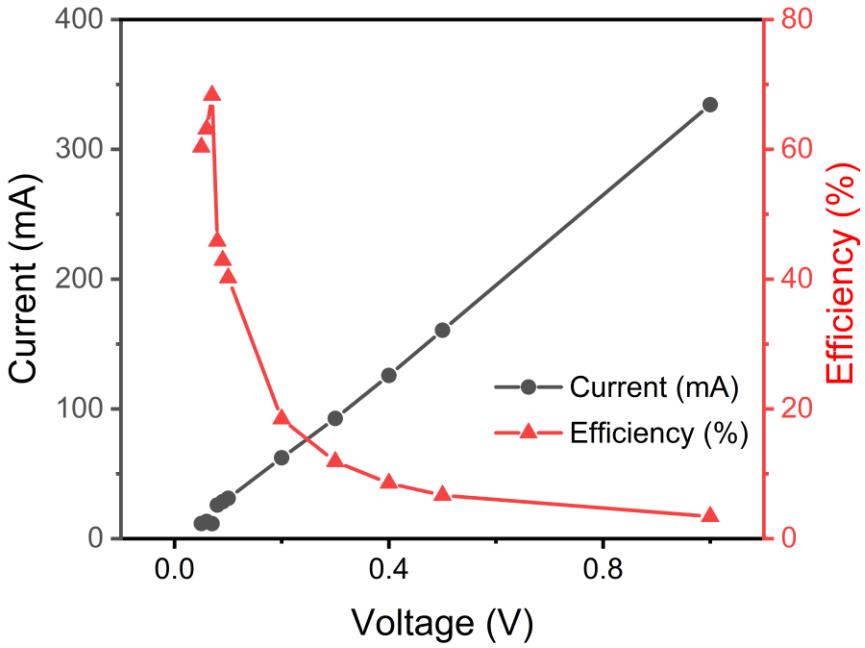

Figure 59 LTC 3108 energy conversion efficiency

The LTC4071, as is shown in Figure 58 (right), is the battery management system with the operating current from 550 nA to 50 mA. It allows the charging of batteries from very low current, under continuous or intermittent charging sources and has both overcharging and discharging protections. Therefore, it is well suited to charge low capacity Li-Ion or thin film batteries in energy harvesting applications. The LTC4071 is used together with the LTC3108 to boost, regulate and

manage the voltage for the battery charging. A diode is applied between LTC3108 and LTC4071 to regulate the current direction and avoid the energy leaking. It is worth to mention that the voltage of the whole circuit is controlled by the LTC4071, and that the LTC3108 output usually does not reach 5 V but depends on the need of the battery charging process.

The energy supply from TEG depends on the indoor and outdoor temperature and is dynamic across the year. In order to achieve the continuous functionality of the system, an energy storage unit is needed to store energy during the peak season and to supply energy in the off season. There exist a lot of discussions about the advantages and disadvantages of different types of batteries. The Li-Po battery is used in this chapter thanks to its high energy capacity, density and efficiency. The 100 mAh battery is used during the lab test to capture the charging process. It will be discussed in the Section 5.5 that a 500 mAh capacity is good capacity for New York to achieve the energy equilibrium stage. Theoretically, the battery life can reach eternity from the energy point of view. The main consideration for the application is the limit of the battery cycle life. Since the unit is designed to stay inside the confined chamber for decades without maintenance, the system will be out of energy story unit when the cycle life is reached. However, in the scope of this chapter, the cycle life is not discussed.

5.3.2 Energy equilibrium algorithm

In energy harvesting, one design methodology is to treat the harvested energy as a supplement to the battery energy and to maximize its lifetime. Another design mode is to use the harvested energy at an appropriate rate such that the system continues to operate perennially, which is called the energy-neutral operation. A harvesting node is said to achieve energy-neutral operation if a desired performance level can be supported forever. A naïve approach would be to require the minimum energy supply at any instant larger than the maximum power required. Advanced approaches

would engineer the energy supply from the periodical viewpoint and achieve a balance by harvest and store in the peak season and supply for the off season. Since the ambient temperature cycles with the period of a year, the lifetime of a node will reach eternity if the energy-neutral operation can be achieved in a yearly period. As long as the battery can survive the cycling, the energy-neutral condition is satisfied, and the lifetime of a node will reach eternity. In this subsection, an energy equilibrium algorithm is proposed based on the test measurements to predict the battery energy level, so as to achieve the energy equilibrium across a year. A case study based on the New York City weather conditions is conducted in Section 5.5 to guide the energy equilibrium design and engineering.

Two constrains for the battery level must be satisfied in order to achieve the energy equilibrium condition: a) the energy level of battery cannot be lower than zero, for the functioning of the system and the health of the battery; b) energy level of the battery is better to stay below the maximum capacity, to avoid the wasting of the harvested energy. The two constrains are written as:

$$\begin{cases} B(t) = B(0) + \int_0^t P_H(\xi)\, d\xi - \int_0^t P_C(\xi)\, d\xi - \int_0^t P_{leak}\, d\xi > 0, \exists t \in (0,T) \\ B(t) = B(0) + \int_0^t P_H(\xi)\, d\xi - \int_0^t P_C(\xi)\, d\xi - \int_0^t P_{leak}\, d\xi \le \hat{B}, \exists t \in (0,T) \end{cases} \tag{5.4}$$

where the $B(t)$ is the battery energy level at any time t and the $\hat{B}$ is the maximum energy the battery can sustain; P_H, P_C and P_{leak} stand for the power of harvesting, consumption and leakage of battery, respectively; T is the time scale of the analysis.

The analysis based on continuous time steps is necessary when the energy harvesting and consumption have close periods. For the case where the energy harvesting period (1 year) is much larger than the prescribed energy consumption period (hours or minutes), the analysis in continuous time steps brings too much detail into the calculation. Such problem can be avoided by

analyzing with discrete time steps. The constrains in Eq. (5.4) are converted to the corresponding discrete form as addressed below:

$$\begin{cases} B(t) = B(0) + \sum_{i=0}^{t/\Delta t} P_H(i)\Delta t - \sum_{i=0}^{t/\Delta t} P_C(i)\Delta t - \sum_{i=0}^{t/\Delta t} P_{leak}\Delta t > 0, \exists t \in (0,T) \\ B(t) = B(0) + \sum_{i=0}^{t/\Delta t} P_H(i)\Delta t - \sum_{i=0}^{t/\Delta t} P_C(i)\Delta t - \sum_{i=0}^{t/\Delta t} P_{leak}\Delta t \leq \hat{B}, \exists t \in (0,T) \end{cases} \quad (5.5)$$

The Δt is the prescribed time step for the analysis, e.g. $\Delta t = 1$ hour for the analysis based on the temperature measurement data with precision to 1 hour. It is worth pointing out that Δt may not be the same with the period of energy consumption (e.g. the energy consumption loops every 2 hours but the Δt can be 1 hour). The total time t may not be divisible by the step Δt, but since t is usually much larger than Δt, the remaining of the division has limited influence on the overall performance and is thus neglected in the equation.

For the energy harvesting based on the thermoelectric generator, the harvested power is linearly proportional to the area of the TEG surface A_{TEG} and the number of TEGs n_{TEG}. It is also quadratically proportional to the temperature difference ΔT_{TEG}, since both voltage and current are linearly dependent on the ΔT_{TEG}. Therefore, the power of energy harvesting is addressed as:

$$P_H = \frac{n_{TEG}}{\tilde{n}} \frac{A_{TEG}}{\tilde{A}_{TEG}} \tilde{P}_H \left(\frac{\Delta T_{TEG}}{\Delta \tilde{T}_{TEG}}\right)^2 \eta \quad (5.6)$$

where η stands for the energy conversion efficiency in the voltage boosting, regulating and battery charging process, and $\tilde{\cdot}$ indicates the results and parameters measured in the test. For the TEGs integrated into the window frame, the temperature difference of TEG is directly related to the temperature difference of the window frame by the reduction factor λ:

$$\Delta T_{TEG} = \frac{\Delta T_{win}}{\lambda} \quad (5.7)$$

Therefore, the total energy harvested is addressed in discrete form as:

$$\sum_{i=0}^{t/\Delta t} P_H(i)\Delta t = \sum_{i=0}^{t/\Delta t} \frac{n_{TEG}}{\tilde{n}} \frac{A_{TEG}}{\tilde{A}_{TEG}} \tilde{P}_H \left[\frac{\Delta T_{win}(i)}{\lambda \cdot \Delta \tilde{T}_{TEG}}\right]^2 \eta \Delta t \tag{5.8}$$

It is seen that only the window temperature difference ΔT_{win} is a function of time step i, all the other parameters are constant once the testing and product configuration are been determined. The total energy harvested is therefore simplified into:

$$\sum_{i=0}^{t/\Delta t} P_H(i)\Delta t = \frac{n_{TEG}}{\tilde{n}} \frac{A_{TEG}}{\tilde{A}_{TEG}} \tilde{P}_H \frac{\eta \Delta t}{\lambda^2 \cdot \Delta \tilde{T}_{TEG}^2} \sum_{i=0}^{t/\Delta t} \Delta T_{win}^2(i) \tag{5.9}$$

The harvested energy is consumed by the wireless sensor network unit at the rate of P_C, which is an averaged value depending on the awake mode P_a and the deep sleep mode P_s

$$P_C = \frac{P_a \cdot t_a + P_s \cdot t_s}{t_a + t_s} = P_s + (P_a - P_s)\frac{t_a}{t_a + t_s} \tag{5.10}$$

where t_a and t_s stand for the time spent during the awake mode and the deep sleep mode. The awake mode is like the fixed cost of power while the sleep mode is like the variable cost of power, which can be controlled to tailor the overall power consumption level. Since the P_a, P_s, and t_a cannot be manipulated, the only variable that can control the averaged power consumption is the time for the deep sleep mode t_s. The overall power consumption is a power function of the deep sleep time to the order of -1, which indicates that the influence is large at the beginning and gradually attenuate and converges to the deep sleep consumption. The sum of the power consumption is written as:

$$\sum_{i=0}^{t/\Delta t} P_C(i)\Delta t = \sum_{i=0}^{t/\Delta t} \left[P_s + (P_a - P_s)\frac{t_a}{t_a + t_s}\right] \cdot \Delta t \tag{5.11}$$

It is worth pointing out that the power consumption is averaged over the cycle and that the consumption cycle may not coincide with the prescribed time step for the analysis. Therefore, the discrete form of the battery energy level is thus written as:

$$B(t) = B(0) + \frac{n_{TEG}}{\tilde{n}} \frac{A_{TEG}}{\tilde{A}_{TEG}} \tilde{P}_H \frac{\eta \Delta t}{\lambda^2 \cdot \Delta \tilde{T}_{TEG}^2} \sum_{i=0}^{t/\Delta t} \Delta T_{win}^2(i) - \sum_{i=0}^{\frac{t}{\Delta t}} \left[P_s + (P_a - P_s) \frac{t_a}{t_a + t_s} \right] \cdot \Delta t - \sum_{i=0}^{t/\Delta t} P_{leak} \Delta t \quad (5.12)$$

The corresponding iterative form is written as:

$$B(m) = B(m-1) + \frac{n_{TEG}}{\tilde{n}} \frac{A_{TEG}}{\tilde{A}_{TEG}} \tilde{P}_H \frac{\eta \Delta t}{\lambda^2 \cdot \Delta \tilde{T}_{TEG}^2} \Delta T_{win}^2(m\Delta t) - \left[P_s + (P_a - P_s) \frac{t_a}{t_a + t_s} \right] \cdot \Delta t - P_{leak} \Delta t \quad (5.13)$$

Once the initial condition $B(0)$ is given, the battery energy level $B(t)$ can be projected based on the temperature measurement data. The battery constraints in Eqs. (5.5) shall be checked and followed during the analysis.

5.4 System integration and performance demonstration

The energy harvesting unit and the wireless sensor network unit are integrated together to formulate a complete TPWSN system, and is tested for the energy balance between harvesting and consumption. The flow chart of the system is shown in Figure 60. The energy output from TEGs is boosted and regulated by LTC3108, after which it is directed to LTC4071 for the battery charging. A diode is connected between LTC3108 and LTC4071 to control the current direction so that the energy inside the battery will not leak back into LTC3108 and wasted. One 3.7 V 100 mAh Adafruit Lithium-Ion Polymer (Li-Po) battery is used in the test, for the energy storage and supply to the wireless sensor network unit. In order to generate a stable temperature gradient across the window frame, the bottom of the window frame is immersed into the ice water for the cooling, and the top is attached with a water bath tunnel for the warming. The testing configuration is demonstrated in Figure 61 with a data acquisition system for the continuous monitoring of the temperature profile and the battery energy level.

The temperature of the water bath is controlled at 40 ℃ for a stable temperature profile over time in the lab test, where the ambient temperature is 22℃. Other water bath temperature will result in a monotonic increasing or decreasing over time. The charging of the battery is quantified by the increase of the battery voltage. Since the amount of harvested energy is small, a small capacity battery is applied to magnify the charging process so that the charging can be observed during the test.

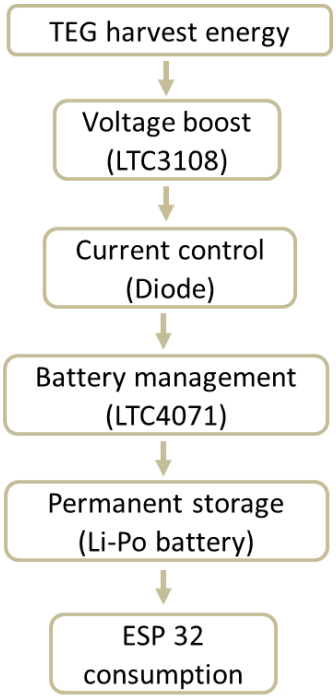

Figure 60 The flow chart of the energy harvesting and energy consumption

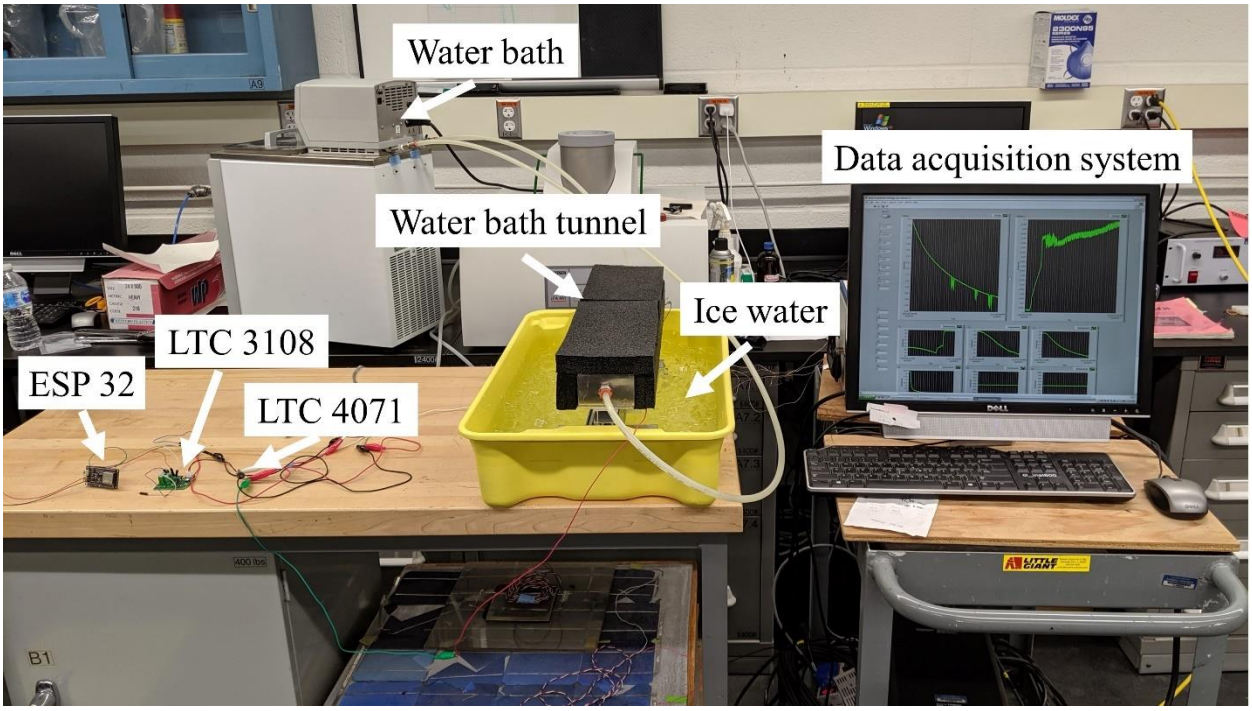

Figure 61 The testing configuration for the thermoelectric-powered wireless sensor network unit

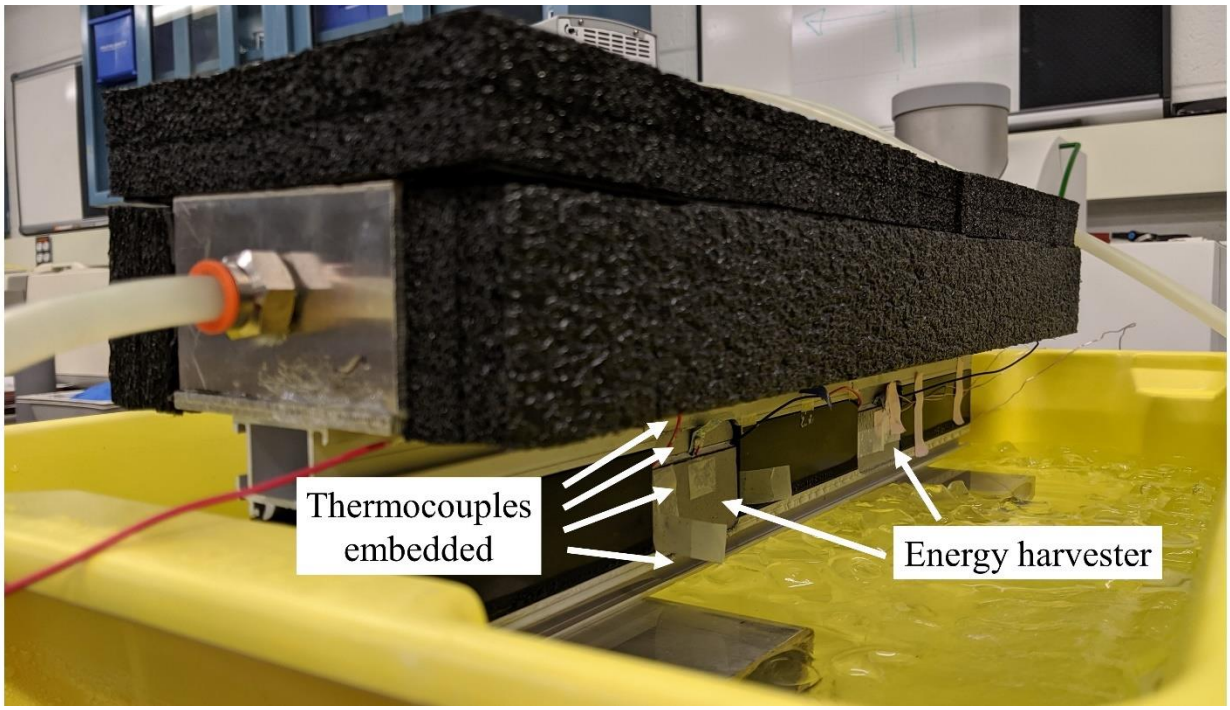

Figure 62 Experimental configuration with implementation of TEG units inside the window

The temperature distribution across the window frame is continuously monitored by the data acquisition system, with the locations of the thermocouples indicated in Figure 62. The temperature profile of the window and the TEG is plotted in Figure 63. It is seen that under the warm water supply, the heat transfer across the window frame reaches a stable balance. The temperature information of the four thermocouples is 24 ℃, 11 ℃, 5 ℃, and 2.5 ℃, corresponding to the top side of the window, the top side of the TEG, the bottom side of the TEG, and the bottom side of the window. The absolute value of the temperature distribution is of limited value since it is significantly influenced by the boundary conditions. The relative temperature difference $\lambda = \Delta T_{TEG}/\Delta T_{win} = 3.5$ is much more valuable because it is only influenced by the internal structures between the TEG and the window frame. It is expected that the λ will stay stable under in different boundary conditions and thus can be used to predict the energy harvesting in the energy equilibrium analysis.

The voltage output from four TEGs is measured and plotted with respect to the temperature difference in Figure 64, where a linear trend line of voltage-temperature is observed. The temperature difference applied on TEG is around 5 ℃ and the voltage output stabilize at 0.1 volt. An additional test is conducted to measure the current output from TEGs since the direct current measurement from DAQ is not easy. The supercapacitors are connected directly to the LTC3108 to calculate the amount of energy harvested from TEGs. It is measured that 3 hours are needed to fully charge two identical supercapacitors at 2.7 V and 1 F. The energy efficiency of LTC3108 is approximately 40% with the voltage input at 100 mV, the current output from the four TEGs are calculated as 15 mA. The total power output can also be determined as $P = V \times I = 1.5$ mW.

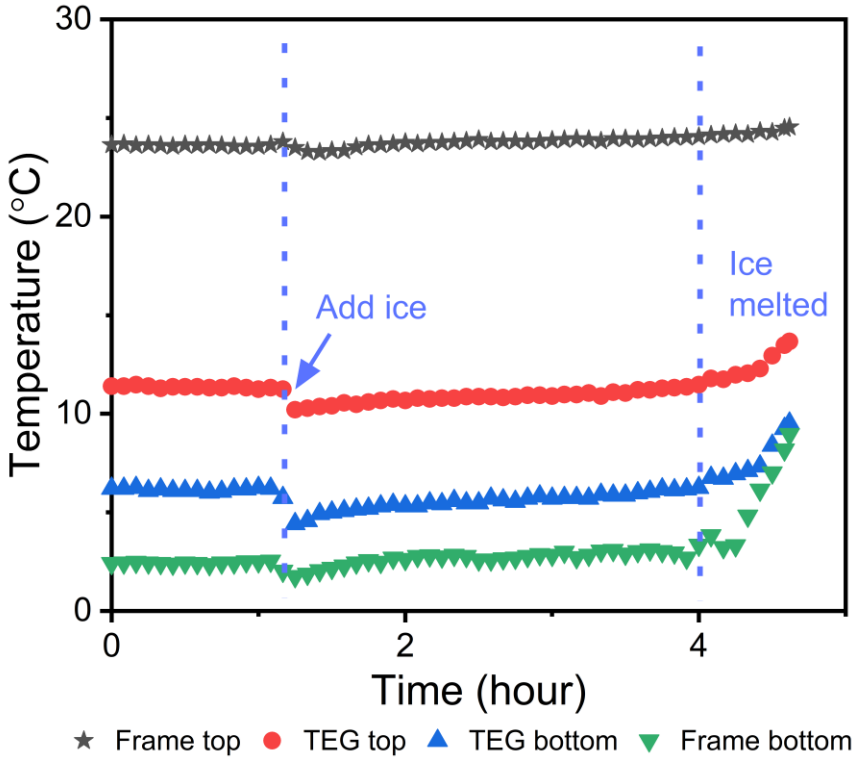

Figure 63 Temperature distribution to time inside the window frame

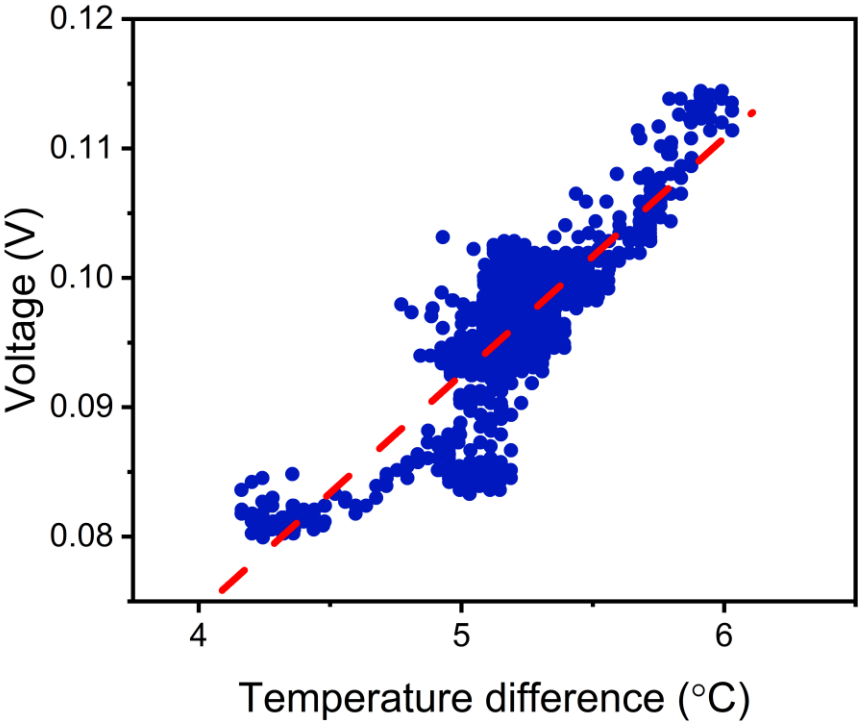

Figure 64 The voltage output directly from TEGs

The voltage of the circuit is controlled by the battery, due to its high energy density. The battery voltage is measured at 3.8 volt and the voltage, current, power and energy efficiency of all the components are listed in the Table 17. The total power stored into the battery is thus calculated at 0.51 mW, and the total energy efficiency is calculated as

$$\eta = \eta_{3108} \times \eta_{diode} \times \eta_{4071} = 33.4\% \tag{5.14}$$

Considering the period of the ESP 32 cycle of 2 hours, the total energy harvested into the battery is calculated as 0.27 mAh.

Table 17 Energy harvesting voltage, current and efficiency

	Voltage/mV	Current/mA	Power/mW	Efficiency
TEG	100	15	1.5	
LTC3108	4300	0.140	0.6	40%
Diode	3800	0.140	0.54	88%
LTC4071	3800	0.135	0.51	95%

The battery voltage level is continuously monitored by the data acquisition system and plotted in Figure 65. It is seen that the start-up of ESP 32 will quickly drain a lot of power from battery, causing a significant drop of voltage level. The ESP 32 then goes to the deep sleep mode, and the battery voltage gradually stabilizes and increase. In order to see whether the battery is being charged or not, the deep sleep period within the two cycles are taken out and plotted separately in Figure 66. It is seen that approximately 0.001 V of battery voltage is raised in the 2 hours charging period, which concludes the battery charging at a slow but continuous pace. The energy harvesting during this specific testing configuration outperforms the energy consumption and stores additional energy into the battery for future usages. The testing configuration and results serve as the reference in the energy equilibrium modeling in the next section, where the guide for the thermoelectric-powered design is provided and discussed.

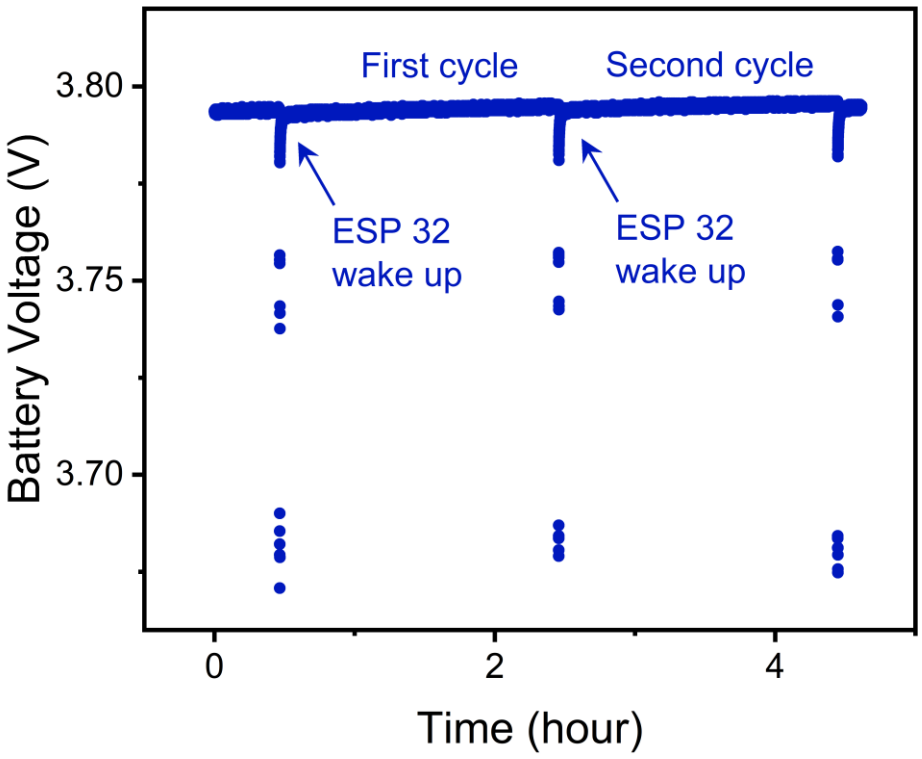

Figure 65 The voltage level of the Li-Po battery based on TEG energy harvesting

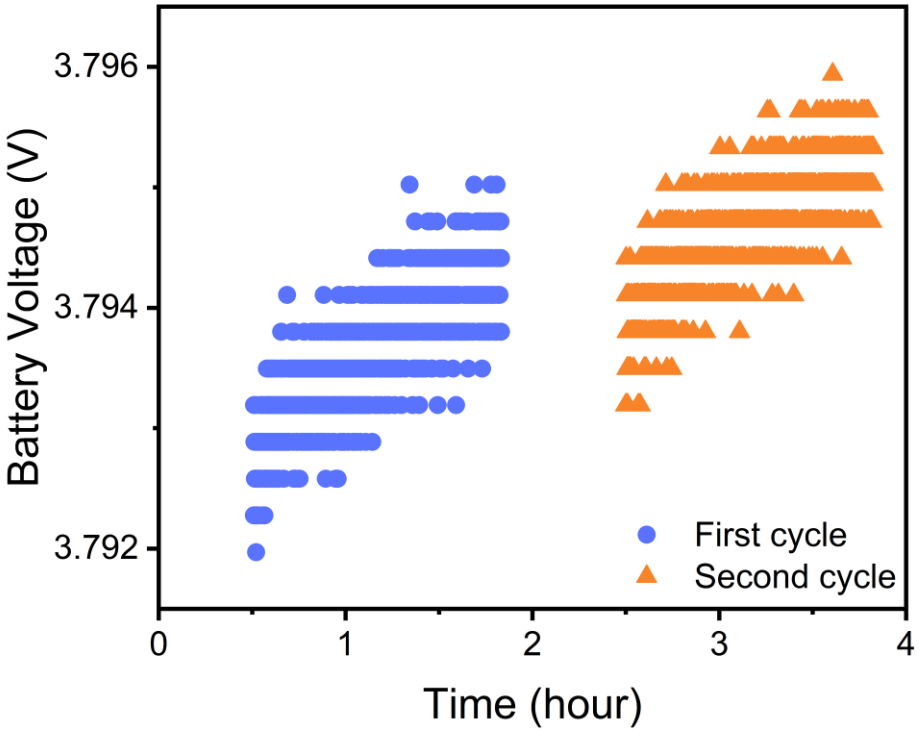

Figure 66 The voltage level of the Li-Po battery in two charging cycles

5.5 Case study for the battery level prediction

Following the testing configuration discussed in the previous section, the parameters in the energy harvesting test are recorded as $\tilde{n} = 4$, $A_{TEG} = \tilde{A}_{TEG} = 9$ cm^2, $\tilde{P}_H = 1.5$ mW, $\Delta\tilde{T}_{TEG} = 5$ ℃, $\lambda \cong 3.5$, and $\eta = \eta_{3108} \cdot \eta_{4071} \cdot \eta_{diode} = 0.334$. The power consumption based on the ESP 32 system is measured in Section 5.3 that the awake current consumption is $P_a = 70$ mA and the deep sleep consumption is $P_s = 45$ uA, under the voltage of 3.7 V. The average time needed for the data extraction and wireless communication is 7 seconds. It is seen from the energy equilibrium analysis that only two variables, the number of TEGs n_{TEG} and the deep sleep time t_s, can be used to achieve the balance between harvesting and the consumption.

The historical temperature data from the beginning of 2016 to the mid of 2019 measured 2 meters above ground in the New York City Central Park is plotted in Figure 67 and utilized for the energy equilibrium analysis. The temperature data is measured every hour and therefore the analysis time step $\Delta t = 1$ hour. As is mentioned before, the outside of the window frame is assumed to share the same temperature with the ambient environment. The inside of the frame is assumed to have the 70°F, the indoor temperature value described in the building code. Since the LTC3108 can only take the direct current, instead of the alternating current, the energy harvesting will occur only when the ambient temperature is smaller than 21 ℃. The summer days when the ambient temperature is larger than 21 ℃ will not contribute to the battery energy level but only drain the battery for the supply of wireless sensor network unit.

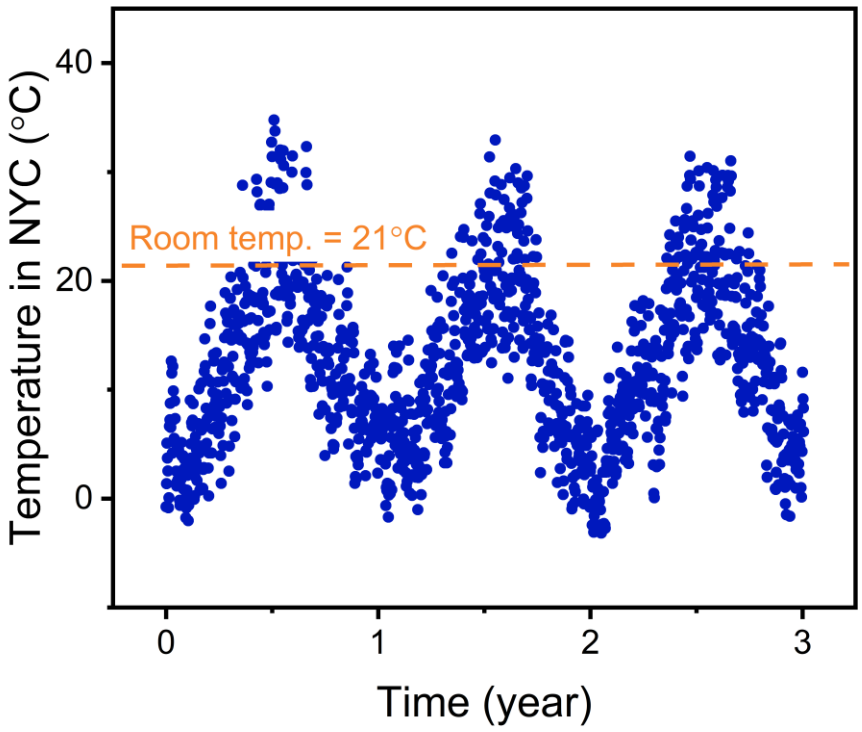

Figure 67 The historical New York City Central Park temperature measurement with precision of 1 hour

The energy equilibrium analysis is applied to predict the battery energy level based on the historical temperature data. In the scope of this case study, the initial battery level is set at 100 mAh and the deployment time is the first day of a year, when the ambient temperature is low, and the energy harvesting is at its maximum potential. The battery level predictions based on the different t_s and n_{TEG} are determined and plotted in Figure 68. It is seen that the energy equilibrium state can be discovered by playing around with the variables. The battery capacity can also be determined by looking at difference of local maximum and minimum in a single cycle. The rule of thumb for the energy equilibrium design is to have a slightly upgrowing curve to avoid the battery depletion and the wasting of energy due to the limited battery size. Among the four scenarios, the case with $t_s = 2$ hrs and $n_{TEG} = 4$ can achieve the balance between energy harvesting and consumption without wasting much energy. The corresponding battery capacity would be 500 mAh, slightly larger than

the difference between local maximum and minimum of 400 mAh. The battery initial energy depends on both the setting of the energy harvester and the deployment date of the system. If the system is installed in summer, more initial energy would be needed to cover the consumption till the harvesting seasons.

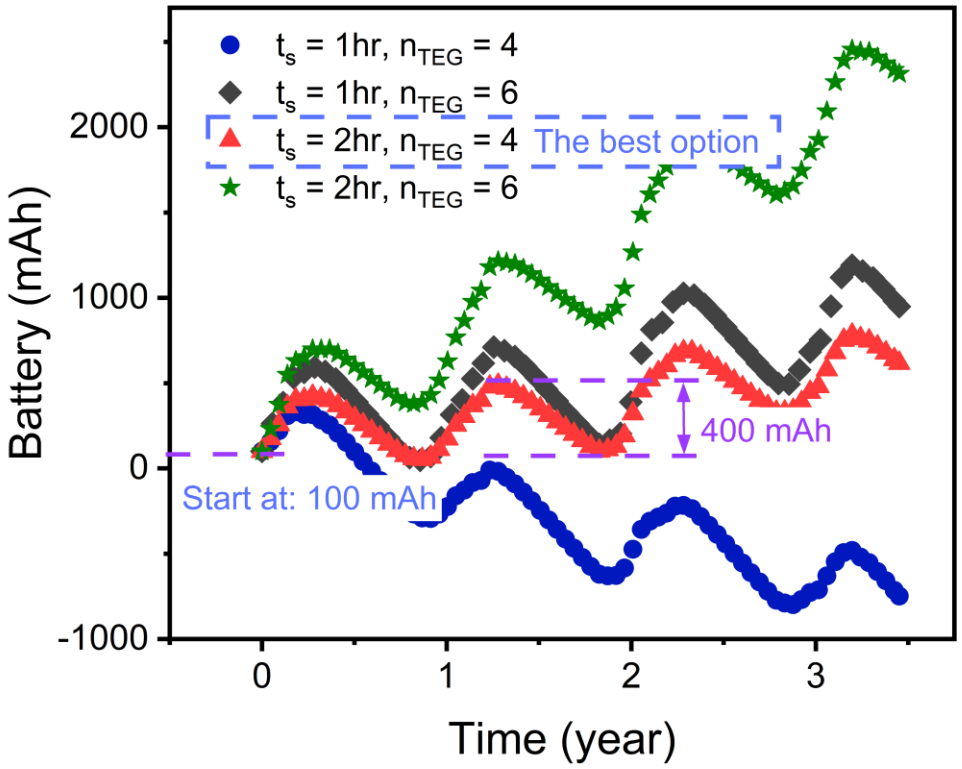

Figure 68 Battery level prediction based on the historical temperature data of New York City

5.6 Conclusions

This chapter presents a thermoelectric-powered wireless sensor network system with prototype and tests based on the thermal energy harvesting in the window frame. The corresponding energy equilibrium analysis is proposed to achieve the balance between energy harvesting and the energy consumption. The TPWSN system formulates a platform for the application of different sensors

for the next generation of smart building management system and provides guidance for the future designs and engineering of the smart building envelope.

The wireless sensor network unit and the energy harvesting unit are investigated separated and then integrated together. An ESP 32 based WSN unit is designed and implemented with a temperature and moisture sensor DHT 11. The Wi-Fi is used as the wireless communication technique to log data into clouds. The deep sleep mode of the ESP 32 is activated to balance the energy consumption and the energy harvesting. The overall power consumption depends on the ratio of awake and deep sleep time and can be as low as 0.67 mW if the system is awake one time per hour. The thermoelectric generators are used to convert the energy from temperature gradient into the electrical form. A special 3D printed aluminum thermal connector is designed through finite element analysis to better transfer temperature gradient onto the TEG surfaces. A voltage boosting integrated circuit LTC3108 is used to boost up and stabilize the ultra-small voltage. The battery management circuit LTC4071 is applied to regulate the voltage input for the battery charging. The Lithium-ion polymer battery is used for the energy storage from the energy harvesters. The overall energy conversion rate reaches 33% for the battery charging, and 1.5 mW power supply for the configuration based on 5.5 ℃ on four TEGs with 9 cm^2 surface. The energy harvesting and wireless sensor network systems are integrated together for the performance test and prototyping. The temperature gradient controlled by the ice water and the water bath tunnel. The temperature distribution across the window section, as well as the voltage outputs of TEGs and battery, are monitored through the data acquisition system. If is found that about 30% of temperature difference will be transferred onto the TEG surfaces based on the current thermal connection inside the window. Linear trends have been observed between the output voltage and the applied temperature difference, for both open and close circuit.

A test-based energy equilibrium model is proposed to reach the balance between the energy harvesting and consumption. The number of TEGs and the deep sleep time are identified as the key variables to control the energy equilibrium design. The case study based on the New York City historical temperature data is conducted and the energy equilibrium state is reached with four TEGs and the sampling period of 2 hours. The energy equilibrium design does not have a unique solution and the variables can be modified to accommodate the design and engineering needs. The battery capacity can also be determined through the analysis, which serves as valuable reference for the design and engineering.

Chapter 6 Design and demonstration of a Sun-powered window blinds for the smart building envelope

6.1. Introduction

As is mentioned in the previous chapter, the smart building management provides the solution to achieve the optimal interior comfort with minimal energy consumption, which would require both smart controlling algorithms and continuously monitored environmental data. The bottleneck for continuous monitoring of the environment is the limited sensor lifetime due to the limited battery capacity. Therefore, the energy harvesting provides a good solution to elongate the battery lifetime and to reduce the cost and time in both installation and maintenance. The thermoelectric powered wireless sensor network system was proposed and prototyped in the Chapter 5, as the platform that can eternally provide energy supply for different sensors. The system is completely inside the confined window frame so as to not jeopardize the outlook of the window/façade. The sensing application usually would not require too much power and therefore the thermoelectric-powered platform introduced in Chapter 5 is good for most of the environmental monitoring work. However, the data acquisition is the first step of the smart building management and is followed up the analysis by the algorithms and the response by the actuators. The actuators consume much more power than the sensors and therefore require a more robust energy harvesting technology for the self-powered feature.

Solar energy harvesting is by far one of the most developed and promising energy harvesting technology in the recent decades. Since first invented in 1946, the modern solar cell industry has gone through three generations of development, with the efficiency up to 40% [229]. Among them, the silicon wafer solar cell, as the first-generation product, occupied most of the industry. The

second-generation solar cells use the thin-film technologies that significantly reduces the light absorbing layer from the 350 μm to the order of 1 μm [230]. The newest generation solar cell, although not commercialized yet, can reach an efficiency much higher than the previous generations [231]. During the past decade, a wide range of photovoltaic applications has appeared in the building sector, especially for building envelope, owing to the possibility of building integration and the huge energy demand from building components.

Two major classifications are defined for the building photovoltaic systems: building integrated photovoltaic (BIPV) and building attached photovoltaic (BAPV) [232]. The BIPV is considered as a functional part of the building structure, or architecturally integrated into the building design. The most widely seen BIPV product is the BIPV roof, which is used to replace the original building roof, or to fit with a specific roof solution produced by the manufacturer [54]. The BIPV roof integrates the solar panels into the roof to provide both energy harvesting capability and the structural capability for anticipated building roof loads. The concept of the building integrated photovoltaic thermal roof is later proposed to both harvest the additional thermal energy and cool down the PV for a better energy conversion rate [23], [53], [98], [233], [234]. The BIPV is also applied to the window/façade thanks to the development of transparent and semi-transparent solar cells, such that it can be integrated into the window/façade glass for both shading and energy harvesting purposes [235]–[238]. The transparency level varies from 16% to 41% for various models [54]. The BAPV is used as an add-on to the building and is not directly related to the building's structural design. In other words, the BAPV systems are usually standing or rack-mounted onto the superstructure such as building roof or curtain walls [239]–[241]. Although it is

less studied in the academia, the BAPV is widely applied to the industry thanks to its cost and retrofit advantages.

The shading system, as an important attachment to the building window/façade systems, is significantly exposed to the exterior environment and therefore is the perfect location for the BAPV systems. However, there has been limited research and application of photovoltaic to the shading system. A recent PV-shading system called Lumiduct was proposed by attaching the concentrating photovoltaic module to the double-skin façade [242]. It optically concentrates the sunlight to a restricted area of solar cells to satisfy the needs of transparency and diffusivity. The Lumiduct has the potential for the self-powered media wall with integrated LED lights, but suffers from the limited area of PV cells for energy harvesting and the large size of the system for applications with limited space. Another PV-integrated shading system was proposed by attaching the second-generation solar cells onto the window blinds, and the study was conducted from the technical, economic, and political aspects for potential applications in Korea [243]. However, the authors did not discuss the technical details of this idea nor did they consider the additional heat dissipated from the solar cells into the building. In addition, the authors focused on the energy generation from the window blind but failed to consider the smart management system that could be constructed from the harvested energy.

In this chapter, a novel smart window system is designed and demonstrated with the goal of improving the energy efficiency of the building envelop by harvesting and preserving solar energy, promoting the energy dissipation, sensing the surrounding environment and automatically controlling the window unit for optimal performance. As shown in Figure 69, the smart window system consists of the window blinds covered with flexible PV cells on one side and porous coating on the opposite side for heat dissipation, and a motor and a micro-controller that control the

shading the blinds automatically based on the sensed data. The harvested energy from solar cells will self-power the operation and provide energy for additional power needs. The heat absorbed by the PV cells will be rejected via the reflective coating made of porous PVdF-HFP, which can drop the temperature by 5~8 °C in summer, improving the overall energy efficiency. The sensed data will serve as valuable information for the building management system for the optimization of the overall energy efficiency.

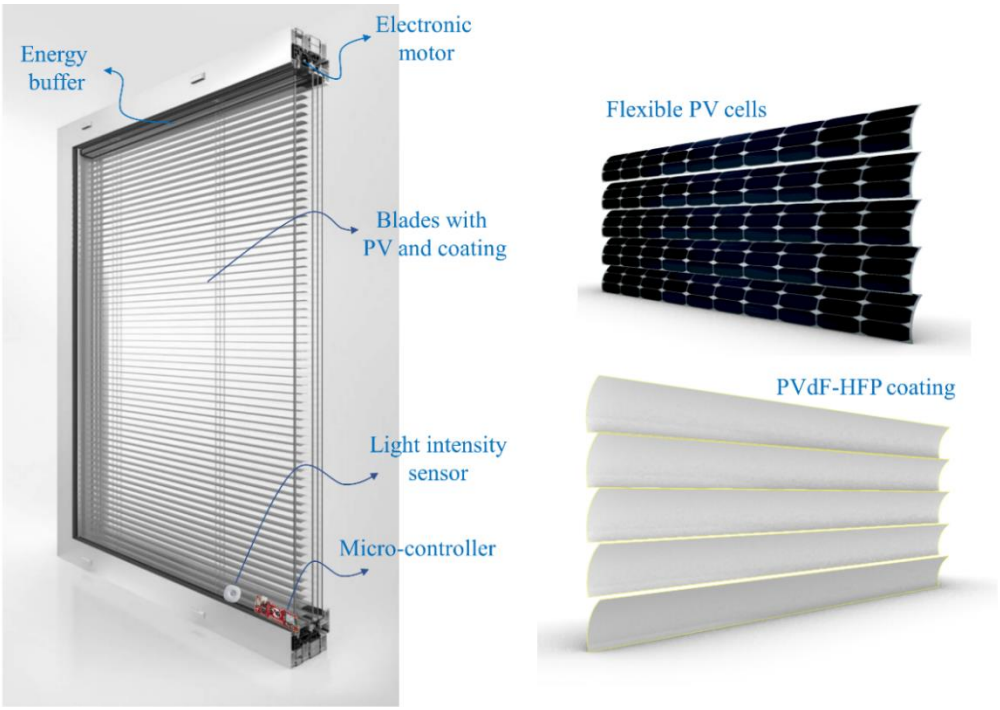

Figure 69 Schematic drawing of (left) the smart window unit, (top right) the PV cells, and (c) the porous coating for heat absorption.

6.2 Design, fabrication and performance quantification of the smart window blind

The smart window blind system is designed with five subsystems as shown in Figure 70: the battery and power management subsystem for the energy storage and management; the sensors and microcontroller subsystem for the environmental monitoring and the optimal control; the

motor subsystem for the lifting, lowering and rotating of the window blind; and the window blind that contains both the solar energy harvesting subsystem on the one side for solar energy harvesting; and the thermal reflective coating subsystem on the other side for the heat ejection under high temperature. The system is designed and demonstrated based on the blinds system of the Schuco AWS120 window, with a physical dimension of 0.9× 1.5 m. The motor integrated in the blind system is the DCD22-2-E double shaft motor with a fixed 24 volt voltage input that can provide the nominal torque of 0.6 N · m. The nominal current consumption from the motor is 320 mA, which corresponds to 7.7 W of nominal power consumption. The starting current of the motor is 1.45 A, such that the instantaneous power consumption is up to 34.8 W. The following subsections will discuss the design the demonstration of the remaining subsystems in detail.

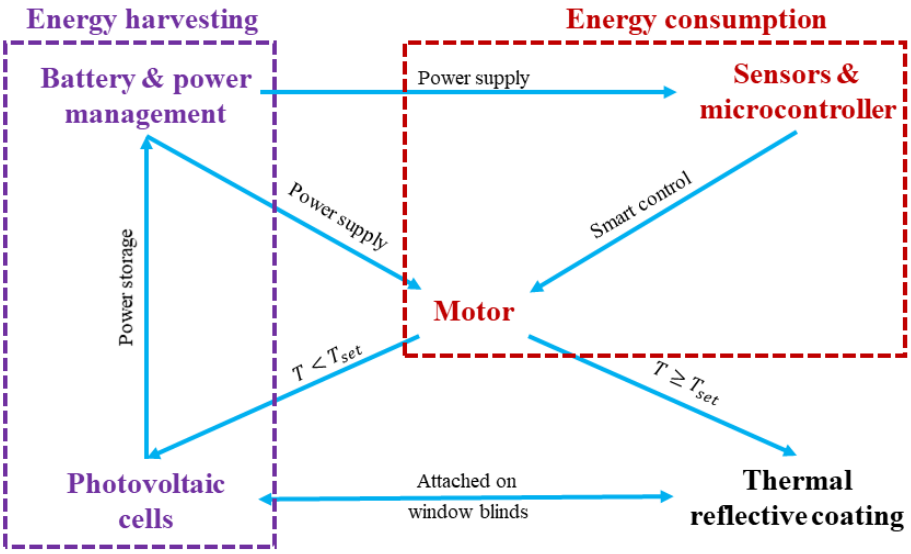

Figure 70 Smart window blind system architecture

6.2.1 Photovoltaic cells integrated window blinds

The solar energy harvesting is achieved through the photovoltaic cells attached on the aluminum blind slats. The thin-film photovoltaic cells manufactured by PowerFilm with a model number

MP3-25 are glued to the window slats during the fabrication. The MP3-25 is a thin-film amorphous solar cell with great flexibility, under a compromise of the efficiency. The claimed efficiency is around 5% on its website [244], which is much lower than traditional silicon solar cells. The operating voltage of each PV cell is 3 V and the maximum voltage is 4.6 V, while the nominal power output is 90 mW. Each blind slat is covered by 5 pieces of PV cells connected in series such as to boost up the voltage output. The open-circuit voltage is around 14 V under in-door lighting, and around 19 V under the solar simulator. Eighteen pieces of slats were fabricated with PV cells and integrated into the window blind system as shown in Figure 71. The slats are connected in parallel to boost up the current output for the energy harvesting. Around 3 mA of short-circuit current is generated under in-room lighting and 400-850 mA under the solar simulator, with a solar irradiation of 850-1700 W/m^2.

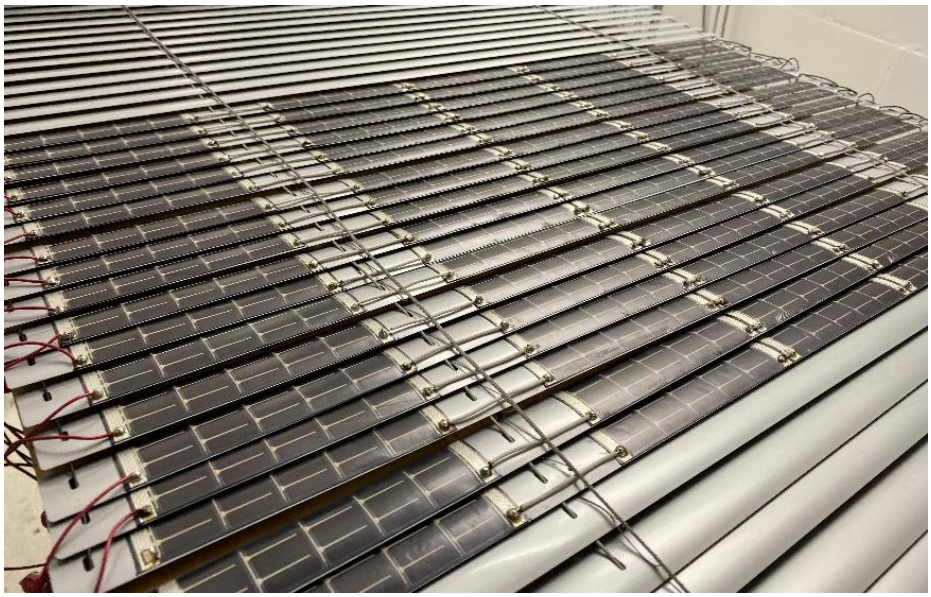

Figure 71 PV integrated smart window blind

In order to identify the maximum power output and the corresponding external resistance, the IV curve is measured by the Seaward PV210 solar tracer under different solar irradiation generated

by the ATLAS MHG Solar Simulator with 4000 W maximum power output, which is shown in Figure 72. Since the PV efficiency varies with the change of temperature, a thermocouple is attached to the surface of the slats to continuously monitor the PV temperature with a data acquisition system (DAQ). A pyranometer is placed close to the system and connected to the DAQ to monitor the solar irradiation. Since the detector of the pyranometer is slightly higher than the PV cells, the measured solar irradiation is slightly larger than the received irradiation on the PV cells.

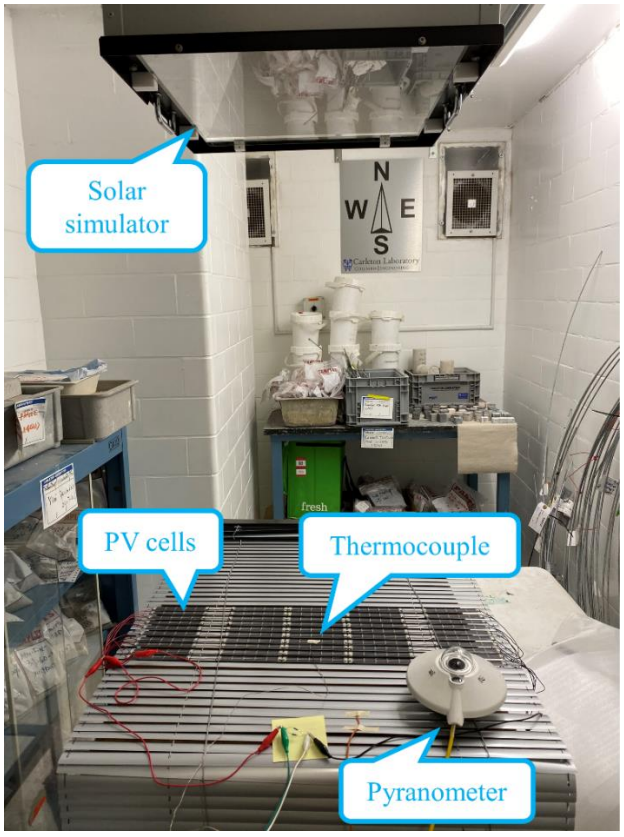

Figure 72 Test configuration for the maximum power output of solar window blind

The effects of temperature and solar irradiation on the PV power outputs are tested. Since the exposure of the solar irradiation will increase the PV temperature and thus reduce the power output, the temperature influence is addressed first by fixing the solar irradiation and testing the IV curve

under different temperature conditions. The I-V curves under 1263 W/m^2 solar irradiation and different temperature condition are plotted in Figure 73 (left). It is seen that the temperature influences more on the open-circuit voltage output but has limited impact on the short-circuit current output. The corresponding relationships between the power output to the external resistance are shown in Figure 73 (right), from which it is observed that the power outputs lie between 6 W to 6.5 W, and that the 20℃ temperature difference will generate approximately 6% power output reduction. The optimal power output points and the corresponding external resistances are captured from Figure 73 (right), and plotted against the different temperature conditions in Figure 74. The linear relationships to the temperature are observed for both the optimal power output and the external resistance.

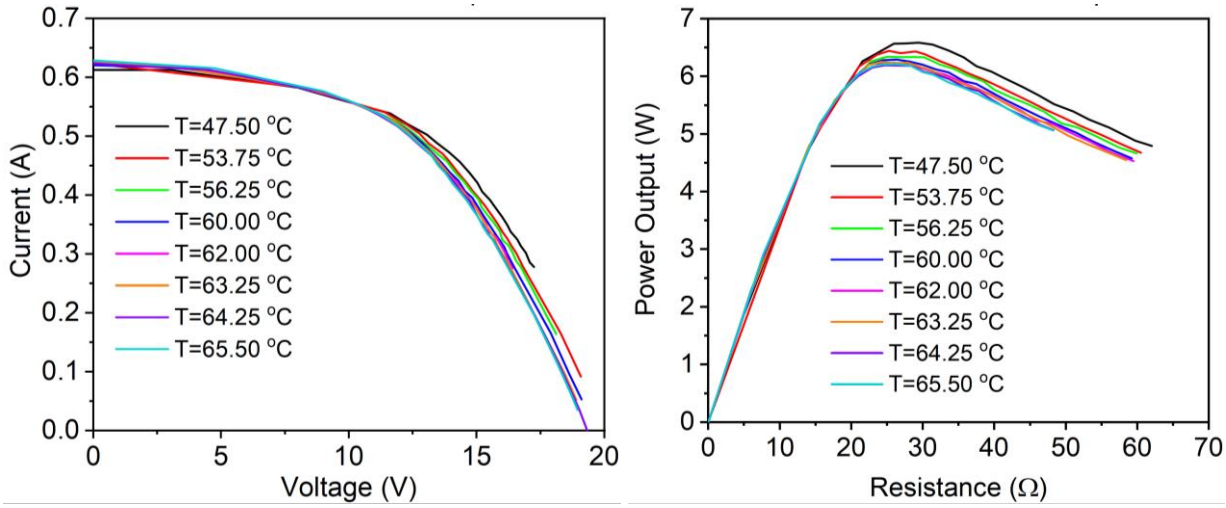

Figure 73 Current and voltage relationships (left) and power output and external resistance relationships (right) under 1263 W/m^2 solar irradiation and different temperature conditions

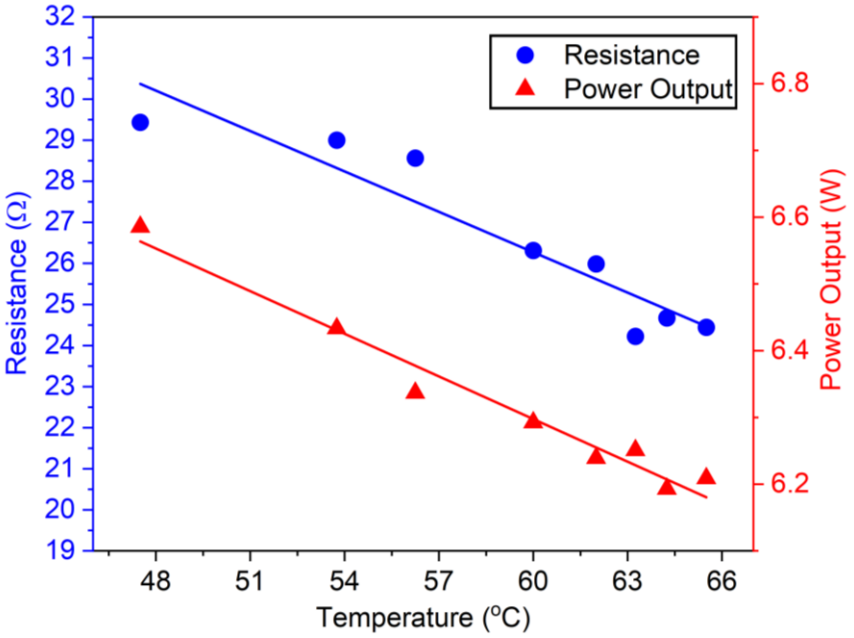

Figure 74 Temperature influence on the optimal power output and external resistance under 1263 W/m^2 solar irradiation

After the temperature effects are addressed, the solar irradiation effects on the I-V curve and the optimal power output can be also address. Similar tests are carried out under different solar irradiation level from 859 W/m^2 to 1709 W/m^2 after the temperature gradually stabilized. The temperature effect can be offset by the relationships obtains in Figure 74. The I-V curves are plotted in Figure 75 (left), and it is observed that the solar irradiation will have a big effect on the short-circuit current, while almost no influence on the open-circuit voltage, after considering the temperature effect. The corresponding power output to the external resistance is given in Figure 75 (right), from which a clear liner trend is observed between the optimal power output and the solar irradiation. The relationships between the power output and the external resistance to the solar irradiation are plotted in Figure 76. Therefore, the best power output and the corresponding resistance can be projected at any location and in any time, given the solar irradiation and the

temperature condition, with the help of bilinear interpolation and extrapolation of the current test results.

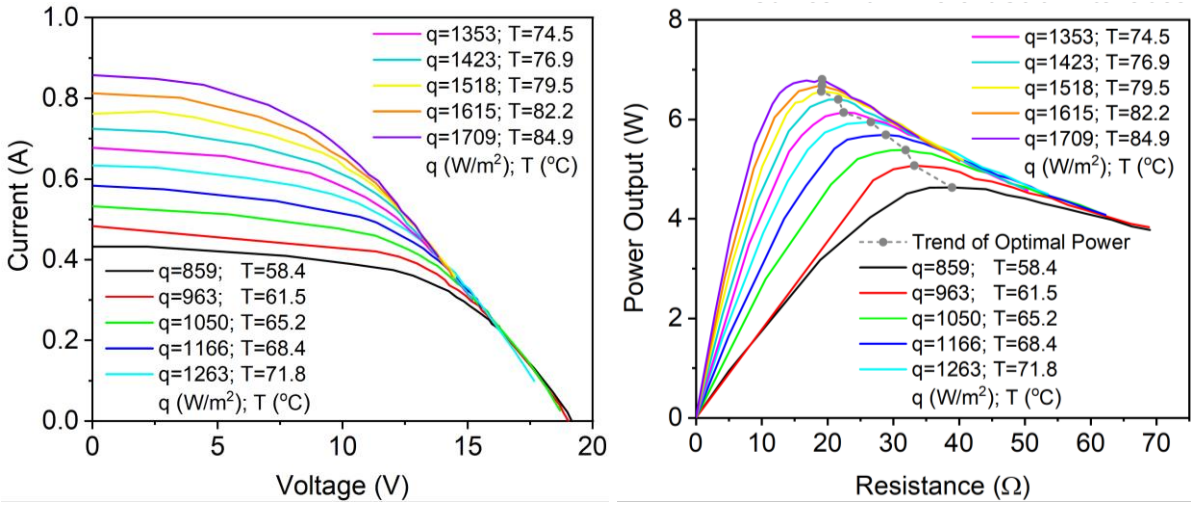

Figure 75 Current and voltage relationships (left) and power output and external resistance (right) under different solar irradiation levels

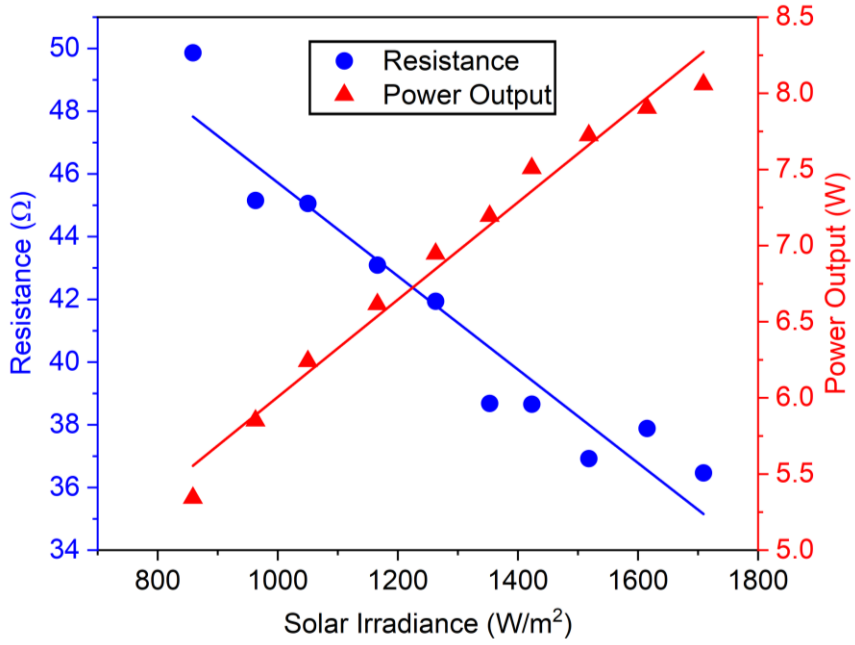

Figure 76 Solar irradiation influence on the optimal power output and external resistance

The optimal power output under every solar irradiation condition is extracted to compare with the input power from the solar simulator, such that the overall efficiency of the PV cells is calculated and listed in Table 18. It is seen that the overall efficiency lies around 2%, and gradually attenuates to 1.5% with the increase of the input power, due to the increase of the PV temperature. The tested efficiency is lower than the claimed 5% and is due to the potential overlapping of the window blinds and the high temperature during the test. In the real application, the overlapping cannot be avoided, but the solar irradiation will be much smaller, which means the temperature is much lower than the measured level. Therefore, it is projected that the efficiency in the real application will be around 2.5% given the direct solar irradiation measurement.

Table 18 The input and output power of PV cells and the corresponding efficiency

Solar irradiation (W/m^2)	859	963	1050	1166	1263	1353	1423	1518	1615	1709
Area (m^2)	0.26	0.26	0.26	0.26	0.26	0.26	0.26	0.26	0.26	0.26
Input power (W)	220	247	269	299	324	347	365	389	414	438
Temperature (℃)	58.4	61.5	65.2	68.4	71.8	72.6	75.0	77.6	80.3	83.0
Output power (W)	4.63	5.07	5.38	5.69	5.95	6.14	6.40	6.56	6.69	6.78
Efficiency (%)	2.10	2.05	2.00	1.90	1.84	1.77	1.75	1.69	1.61	1.55

6.2.2 PVdF-HFP porous coating and the corresponding performance

The PVdF-HFP coating is a hierarchically porous poly(vinylidene fluoride-co-hexafluoropropene) coatings with excellent passive daytime radiative cooling (PDRC) capability. Its high hemispherical solar reflectance and long-wave infrared emittances allow for sub-ambient temperature drops of ~6 °C and cooling powers of ~96 $\mathrm{W/m^{-2}}$ under solar intensities of 890 and 750 $\mathrm{W/m^{-2}}$, respectively [245]. In the PVdF-HFP coating process, a primer layer is first applied on the window blind surface to enhance the bonding strength, which takes approximately 10

minutes to dry. Then, the polymer coating is presented via a commercial spray gun Flexio 590 from Wagner Spraytech. The polymer coating is initially liquid. After being exposed to the air, it turns to a white-colored porous solid film quickly. The polymer coating is applied 6 to 76 times with an interval of 10 minutes to let the previous coating layer dry. In the end, additional 1 to 2 hours are needed for the coating to dry completely. Five window blinds are applied with the PVdF-HFP coating as is shown in Figure 77. The front of the window blinds is covered with PV cells as described in Figure 71. The five coated window blinds are integrated into the window system and tested under the solar simulator so as to quantify the cooling performance of the coating.

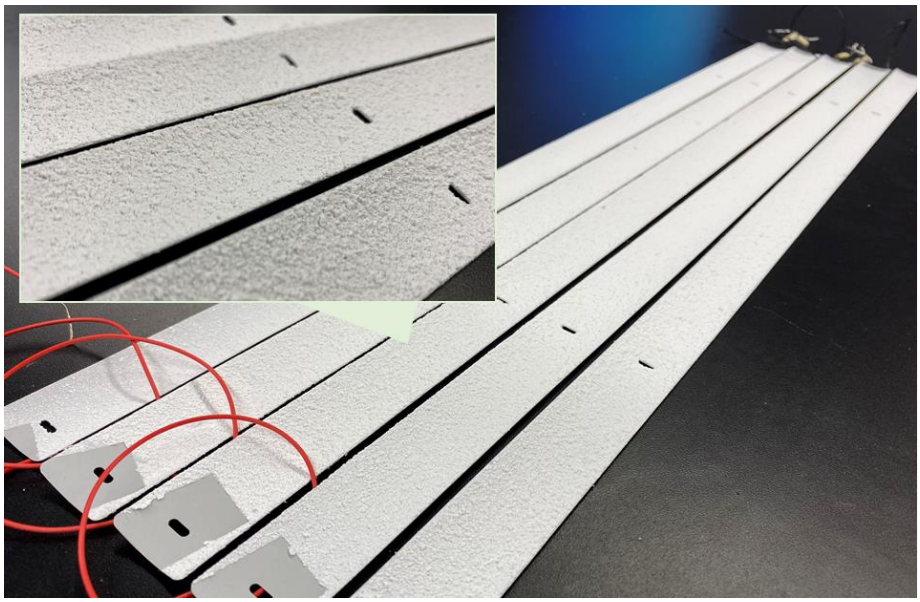

Figure 77 PVdF-HFP coating on the other side of the window blind

Similar testing configuration as described in Figure 72 is set up for the test of window blinds with the PVdF-HFP coating. As is shown in Figure 78, five coated PV blinds and five original PV blinds are integrated into the system for comparison. Two testing tables are bridged together with metal frames to generate the empty space for the heat dissipation of the PVdF-HFP coating. Both coated PV blinds and the original PV blinds are sitting on top of the metal frame and right below the solar

simulator. Thermocouples are attached at the center of third PV blinds and connected to the data acquisition system for the temperature measurement over time. Six different levels of solar irradiation ranging from 780 to 1700 W/m^2 are casted onto the window blinds to increase the surface temperature. The surface temperature gradually stabilized after 5 mins of the applied solar irradiation and the measurements are taken for both coated and un-coated PV blinds, which are plotted in Figure 79. Thanks to the PVdF-HFP coating, clear temperature reduction has been observed in the tests and the maximum drop can be as much as 7.6℃ under the solar irradiation of 1700 W/m^2, which corresponds to 9.31% of the temperature reduction and approximately 4% of additional PV output power. Less significant improvement is expected under weaker solar irradiation, and under the solar irradiation of 780 W/m^2, a 4℃ reduction of the surface temperature can be observed. It is worth to mention that the testing room is confined space with limited air ventilation, and the room temperature could reach 35℃ under 850 W/m^2 of irradiation, which compromises the passive cooling performance of the coating. A larger temperature reduction could be expected for the application in the open space.

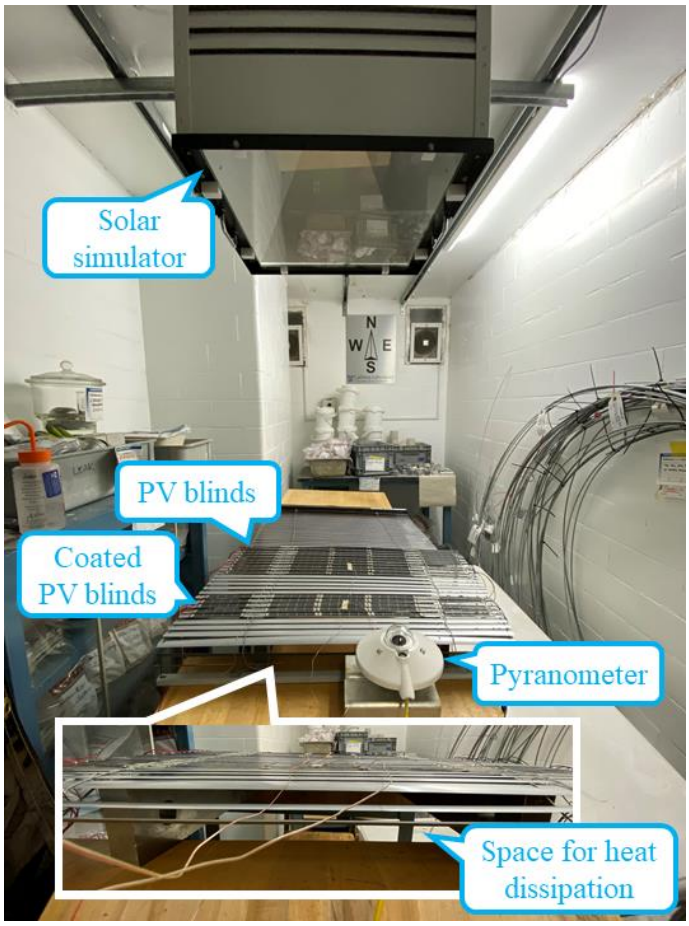

Figure 78 Test configuration of PVdF-HFP coating window blinds

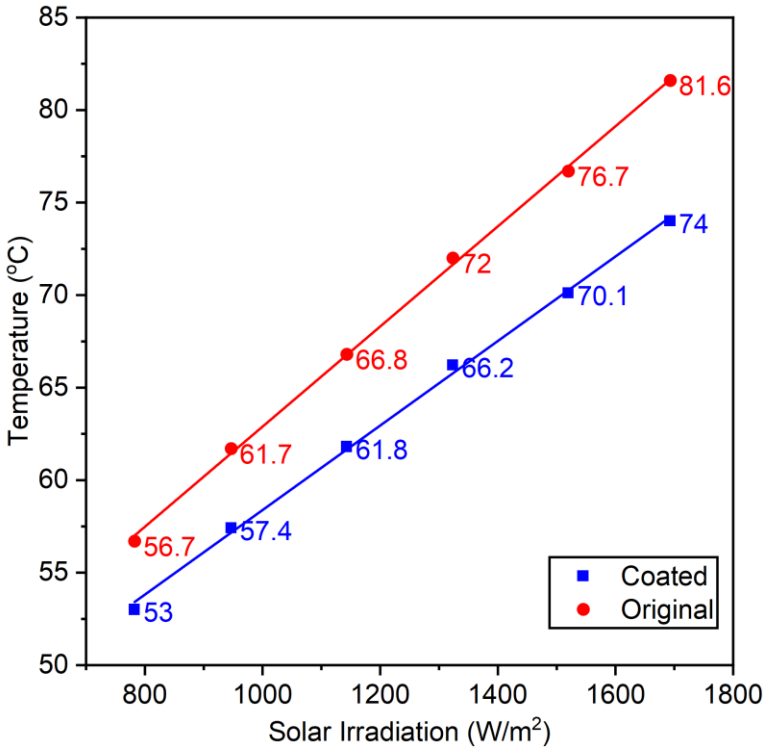

Figure 79 Coated and un-coated PV blinds temperature under different solar irradiation

6.2.3 Energy storage and battery management system

Considering the dynamics of the power output, voltage regulation is needed to stabilize the energy supply from the solar window blinds to the battery. The LTC3780 buck boost converter is applied to stabilize and regulate the voltage. The LTC3780 will automatically adjust internal resistance to best extract the power output from the PV cells. The voltage output from the solar cells is first taken down to 12 V to charge 3×18650 battery which is shown in Figure 81 and has the capacity of 3×1600 mAh. The voltage is then taken up to 24 V with the help of a fixed-ratio voltage booster for the power supply of the DCD22-2-E motor. The reason for not directly boosting the voltage to charge the 24 V battery pack is that the boost mode of the LTC3780 has much lower efficiency than the buck mode, and that the boost mode has a minimum output current requirement that the

system cannot satisfy. The schematic drawing of the energy management and storage system is shown in Figure 80. The tests are conducted under two different solar irradiation intensities, 760 W/m^2, and 1190 W/m^2, each for approximately 20 mins.

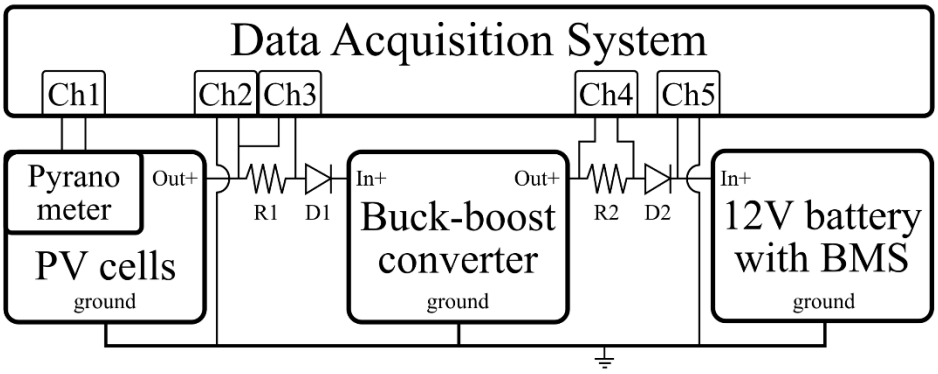

Figure 80 Schematic drawing of energy management and storage system from PV to battery

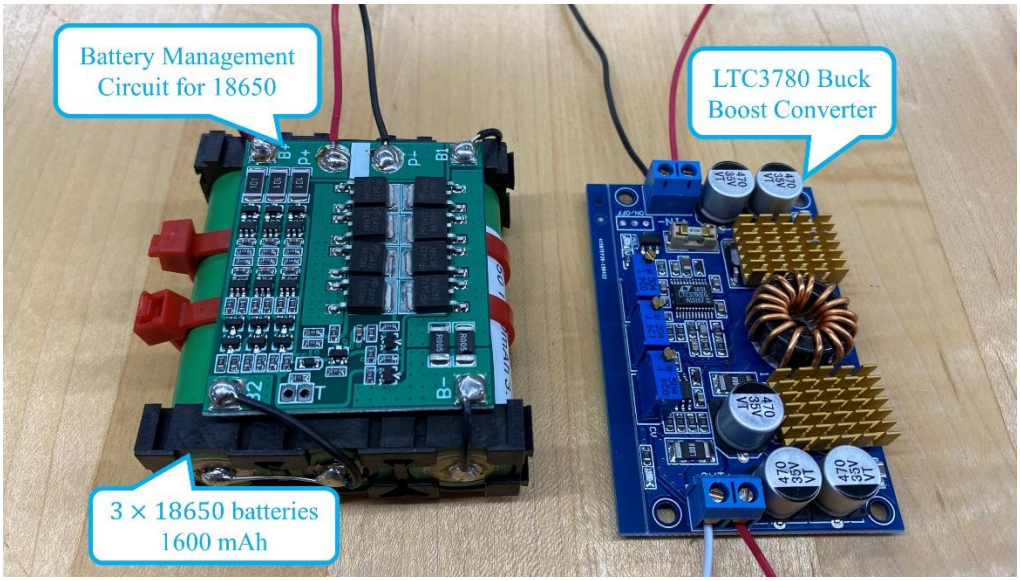

Figure 81 The 18650 battery pack and the LTC3780 buck boost converter

Each PV-integrated slat is connected with a N4007 diode to prevent the reverse current consumed by other PV cells. The N4007 diode will consume approximately 0.7 V. A resistor of 1.7 ohms is placed between the PV cells and the LTC3780 to monitor the direct current output with the help

of the Data Acquisition (DAQ) system. The measurement frequency is set at 20 data per second. The current and power measurements directly from the PV cells are plotted in Figure 82. Combined with the maximum power output in Figure 75 (right), the total available power, the power into the converter, and the wasted power due to the diode, resistor and the algorithm are calculated and listed in the Table 19, where an overall efficiency of 75% - 80% is achieved in the lab testing. If the resistor is removed, the efficiency can increase by approximately 3.5%. It is also seen that the current and the power distribution follow a similar pattern, which means that the voltage output is stable given the solar irradiation. The average voltage outputs for both cases are 11.95 V. While the optimal voltage corresponding to the maximum power output can be obtained from Figure 75 (left), which is 13.43 V and 12.82 V for $I = 858.6\ W/m^2$ and $I = 1166\ W/m^2$, correspondingly. It is worth to mention that the current output from the PV is intermittent. The current measurement from in Figure 82 is the moving average of the surrounding 10 seconds of measurement.

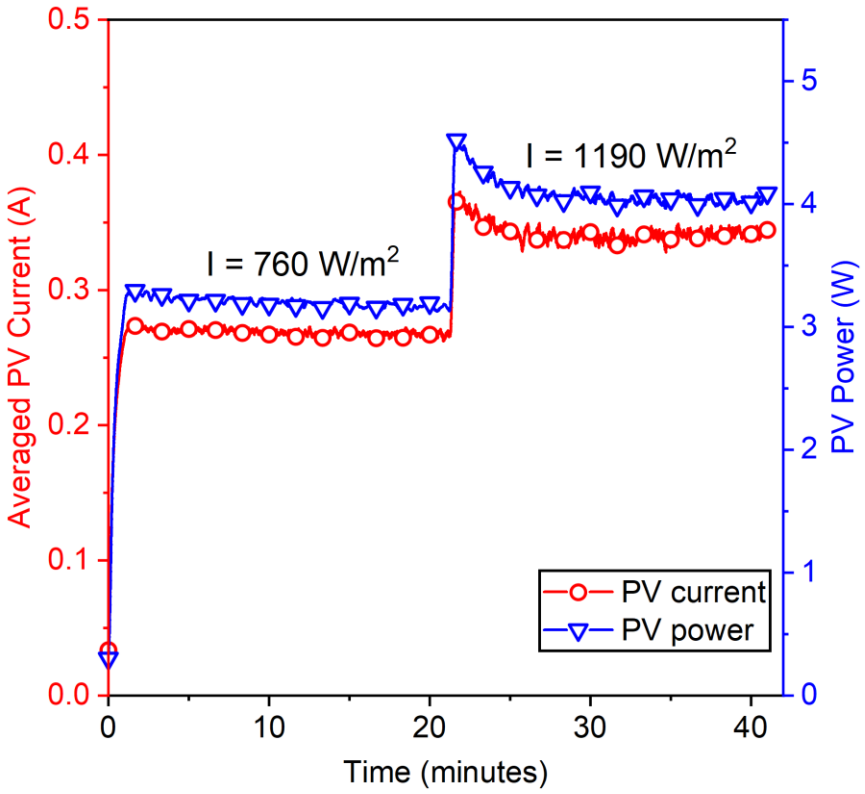

Figure 82 Current and power output from the PV cells

Table 19 Power consumption and efficiency from PV cells

Solar intensity (W/m^2)	760	1190
Total available power (W)	4.00	5.50
Power consumed by diode (W)	0.19	0.24
Power consumed by resistor (W)	0.12	0.20
Miscellaneous waste (W)	0.49	1.02
Power into converter (W)	3.20	4.04
Power efficiency	80%	74%

The energy from the PV cells are collected and voltage-regulated by the LTC3780, and is sent to the battery management system for the permanent energy storage. In order to know the efficiency of the LTC3780 and the battery management circuit, the measurement of current directly from the PV cells and measurement of the current charged into the battery are plotted in Figure 83 for comparison. The current measurements fluctuate over a short period of time in both cases, due to

the limited power the PV cells can provide. In order to have a better observation of the process, a detailed observation of the cycle is plotted in Figure 84. It is seen that the current before and the after the LTC3780 follows the same dynamic pattern. The battery charging current increases as the PV output current increases, and decreases as the PV current decreases. Such behavior is due to the dynamic of LTC3780 internal resistance. The LTC3780 swipes its internal resistance to capture the maximum power input from the PV cells. It also tries to satisfy the constant current requirement from the user. When the minimum constant current value is not met, the LTC3780 will continue to swipe its internal resistance and therefore causing the fluctuation of the current measurement. With the increase of the input power, the LTC3780 will provide greater proportion of the high-level current output and eventually provide the continuous current output. It is seen that the proportion of the high-current phase is largely increased in the 1190 $\mathrm{W/m^2}$ case than the 760 $\mathrm{W/m^2}$ case while the maximum value of peaks are very close to each other. It is worth to mention that the harvested energy in the real application will be much smaller than the lab test condition, due to the indirect sunlight and the weaker light intensity, therefore the current fluctuation will be likely to occupy the majority of time in the application. The energy conversion rate will be compromised and further optimization of the voltage regulating system shall be conducted and studied in the future.

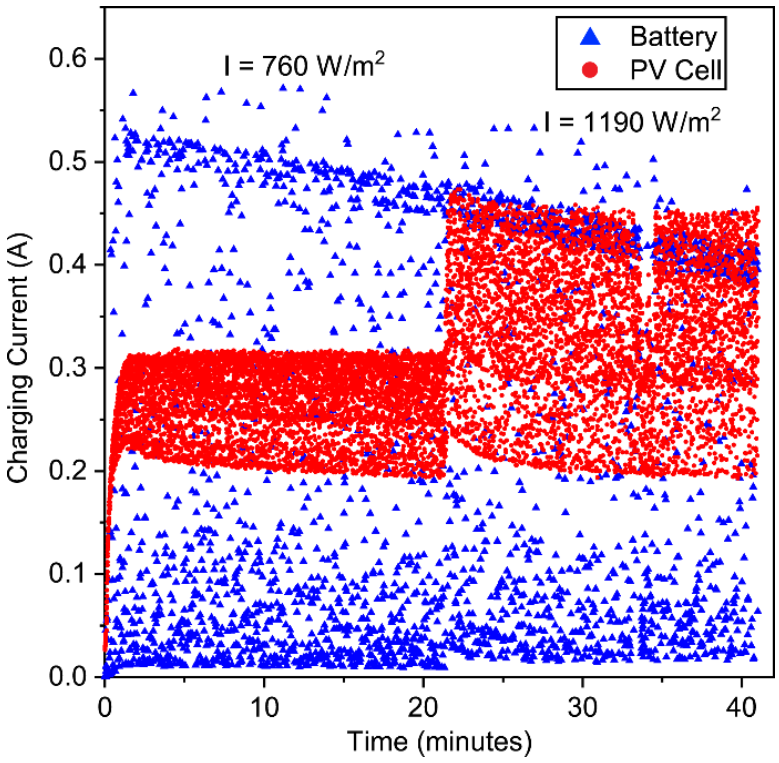

Figure 83 PV output current and battery charging current

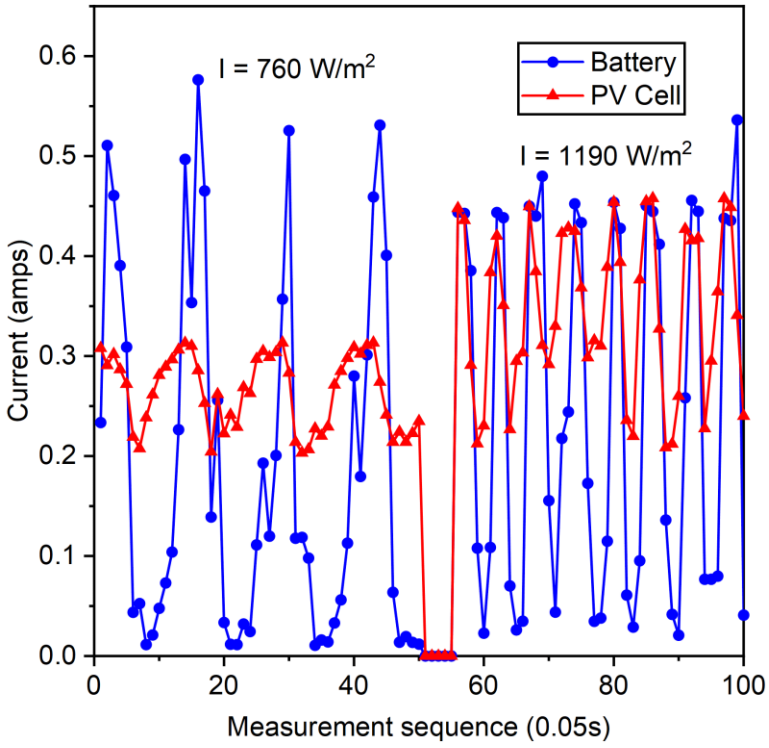

Figure 84 Detailed cycles of PV output current and battery charging current

The intermittent current measurements in Figure 83 are transformed to a continuous distribution via a moving average over the surrounding 10 seconds of measurements and are plotted in Figure 85. The averaged result is relatively stable across the testing period and the into-battery current of 0.27 amps and 0.34 amps is observed for the light intensity 760 W/m^2, and 1190 W/m^2, respectively. The detailed voltage and current measurements, as well as the power and efficiency analysis are listed in Table 20. It is seen that an overall 70% of efficiency is achieved for both cases from the PV output to the battery. The 30% of the energy loss comes from the energy converter, the battery management system, diode, and the resistor. It is worth to mention that the input voltage and the output voltage of the buck booster converter are very close in the test, and a slight difference of system efficiency is expected if the input voltage deviates from the output voltage.

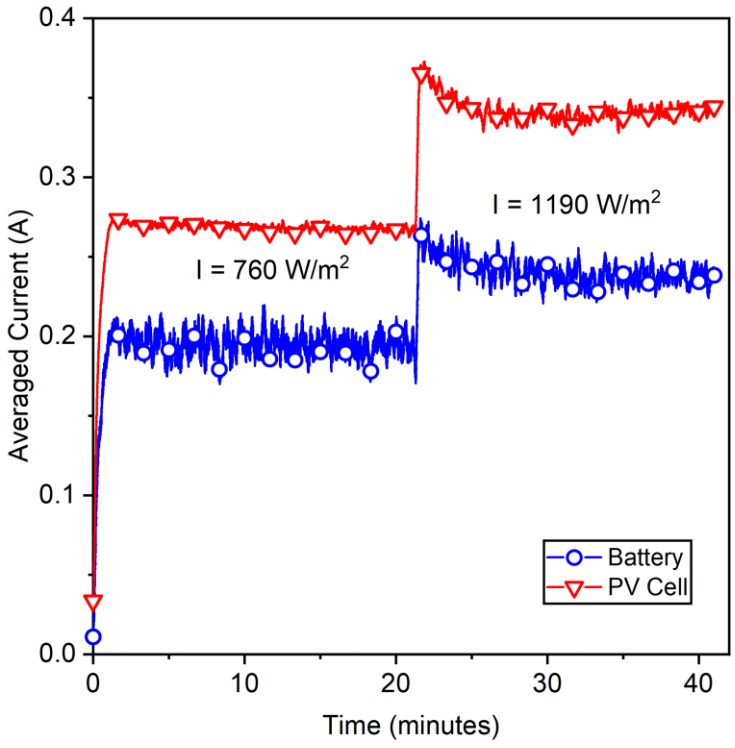

Figure 85 Moving averaged result of PV output current and battery charging current

Table 20 Power consumption and efficiency from convert to battery

Scenario		Light intensity = 760 W/m^2	Light intensity = 1190 W/m^2
Before LTC3780	Voltage (V)	11.90	11.90
	Current (A)	0.27	0.34
	Power (W)	3.20	4.04
After LTC3780	Battery voltage (V)	11.80	11.80
	Current into Battery (A)	0.19	0.24
	Power into battery (W)	2.30	2.83
	Diode consumed (W)	0.14	0.17
	Resistor consumed (W)	0.06	0.10
Efficiency		71.88%	69.98%

The overall energy efficiency of the system reaches 58% and 52% under 760 $\mathrm{W/m^2}$ and 1190 $\mathrm{W/m^2}$ of solar irradiation intensity. Although the energy input of the second test is 1.56 times larger than the first test, as quantified by the rate of solar irradiation intensity, the overall current charged into the battery is 1.26 times larger, as quantified by the current. The additional amount of energy is dissipated into the environment via the heating of the PV cells, the loss of the converter, the diode, and the resistor. In order to see the energy storage process, the battery voltage is recorded and plotted in Figure 86, where the first 20 mins is under the 760 $\mathrm{W/m^2}$ and the last 20mins is under the 1190 $\mathrm{W/m^2}$. The battery voltage keeps increasing during the 40 mins of testing period, and fluctuates at a period close to 1 min. Although no significant change of the battery voltage increase rate has been observed, the overall charging process goes smoothly and is at the rate of approximately 0.7 volt/hour.

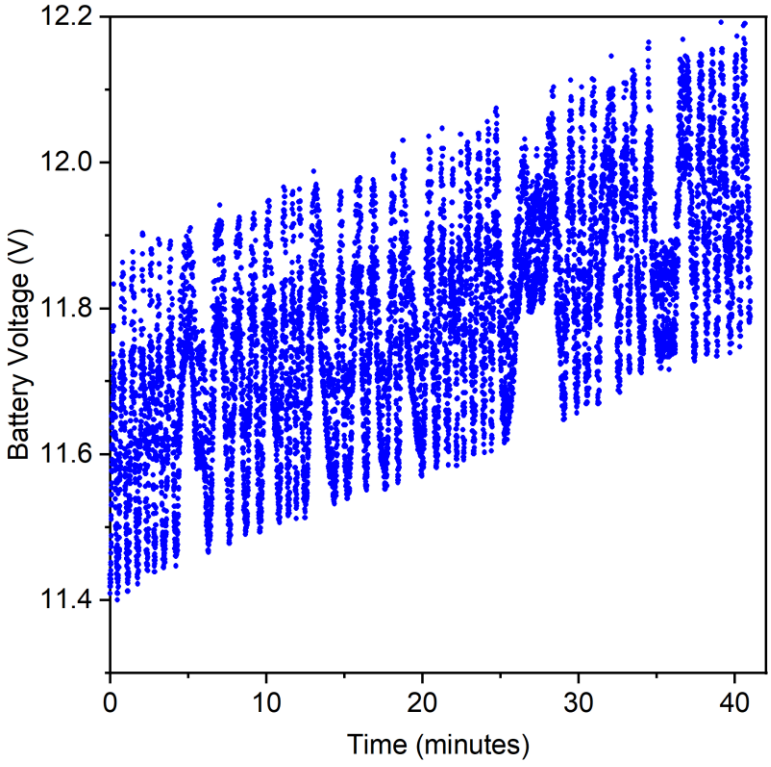

Figure 86 Battery voltage measurement over 40 mins

6.2.4 Sensing and controlling system

The photovoltaic cells attached on the window blinds harvest solar energy into electricity, but also absorb the solar thermal and heat up the internal temperature. The out-facing solar cells in a hot summer day will significantly increase the temperature and compromise the internal comfort. The excessive heat absorption can be rejected by letting the back of the window blinds facing outside, where the radiative cooling capability of the porous PVdF-HFP coating can be fully utilized for the heat ejection. A smart controlling system is thus needed to balance the solar harvesting and the system cooling.

The Arduino Uno R3 development board is used as the microcontroller to collect the temperature measurements from the thermometer and to conduct logical decisions as when to rotate the window blinds. An H-bridge is used to switch the polarity of the applied voltage on the motor, such that

the rotating direction of the motor can be digitally controlled by the signal from the microcontroller. The physical components of the Arduino Uno and the H-bridge are shown in Figure 87 and the schematic drawing of the connection is shown in Figure 88. The input signal is connected to the lower side of the H-bridge. Ranging from left to right one can find the 24 V power input from battery, the ground, and 5 V signal input from the Arduino Uno. The output sides are located on the left and right of the H-bridge, both of which are connected to the motor with one serving as the positive and the other as ground. The output signal is equal to the 24 V power input and the polarity is controlled via the 5 V signal input. The deep sleep mode is activated in the Arduino Uno and for every 8 seconds, the system will wake up from the deep sleep to collect the temperature measurement from the thermometer. It will compare the temperature measurement to the preset temperature thresholds and decide whether to send out the signal for the motor control, after which it will go back to deep sleep and wait for another cycle.

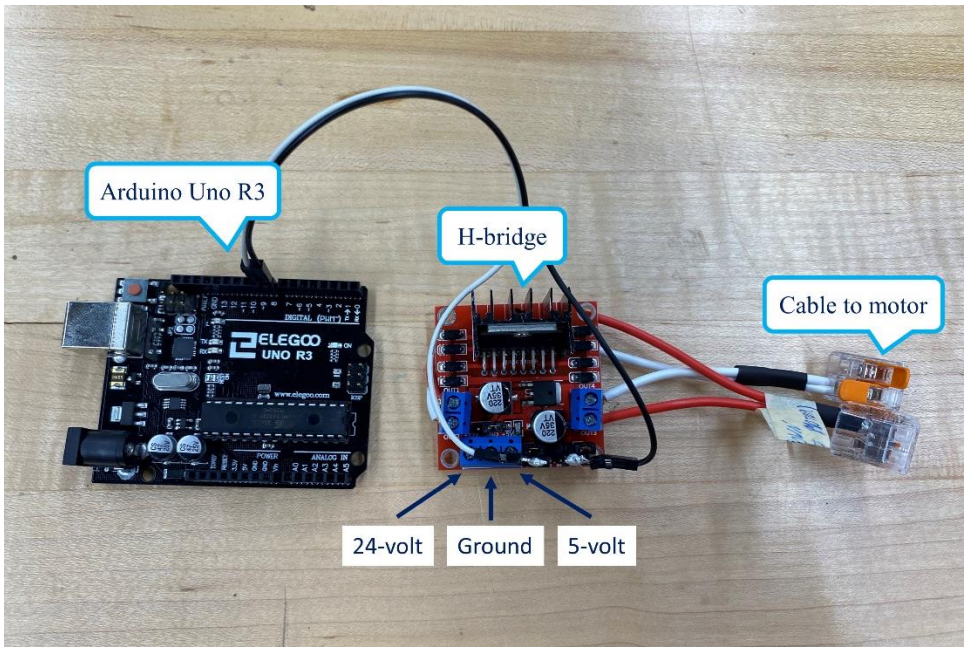

Figure 87 The Arduino Uno R3 and the H-bridge

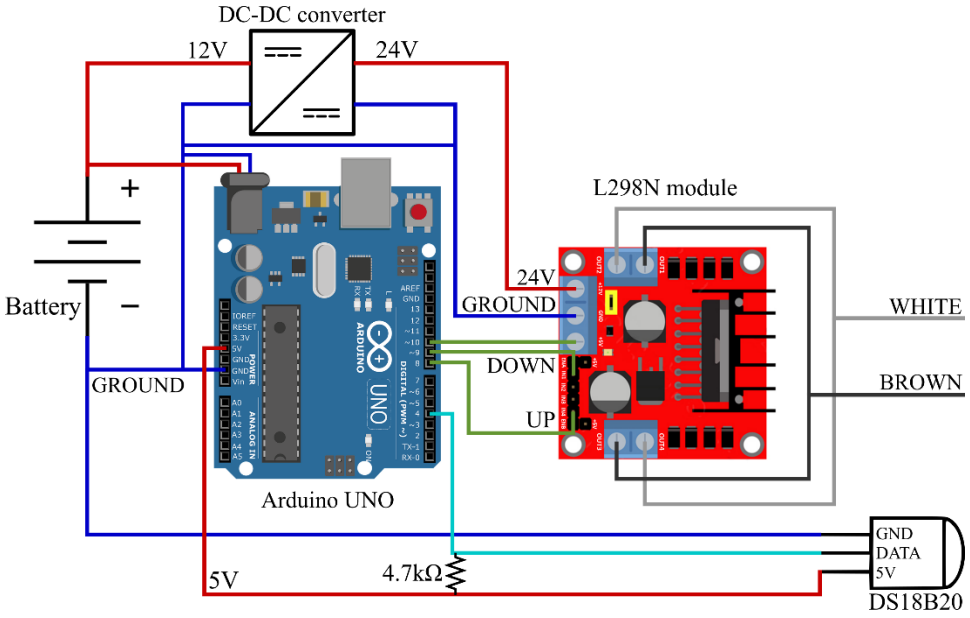

Figure 88 Schematic drawing of the connections in the controlling system

The 18B20 digital thermometer is used for the temperature monitoring and attached onto the PV surface as shown in Figure 89. The window blinds are hung vertically from the ceiling and three-point fixed with nylon rope, such that the motor can be used to rotate, lift and lower the blinds. The ATLAS MHG Solar Simulator is used to artificially cast solar irradiation in order to test and calibrate the performance of the controlling system. The simulator is placed horizontally on a testing table for the horizontal irradiation and adjusted at a distance 45 inches away from the blinds. The lowest solar irradiation output is chosen and the equivalent solar irradiation of 760 W/m^2 is received by the window blinds. It is worth to mention the that window blinds cannot rotate 180° due to the mechanical connection to the motor. The schematic drawing of the blind is shown in Figure 90 and a maximum of 144° is expected for the rotation. Also, a slight compromise of the cooling performance is expected since the non-PV side can only face the ground and rather than the sky.

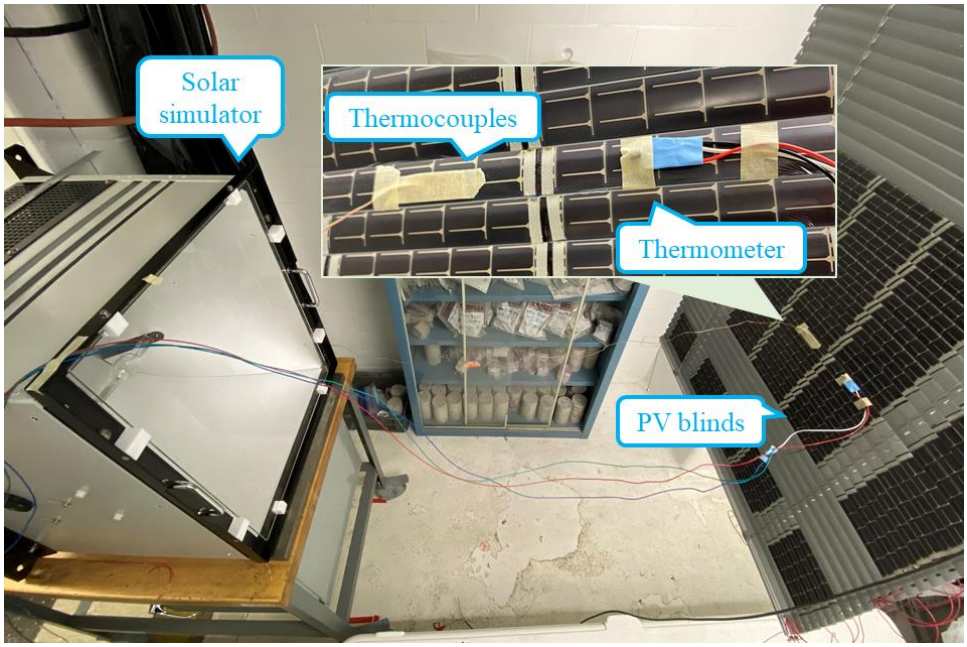

Figure 89 Test configuration of the solar simulator and the window blinds

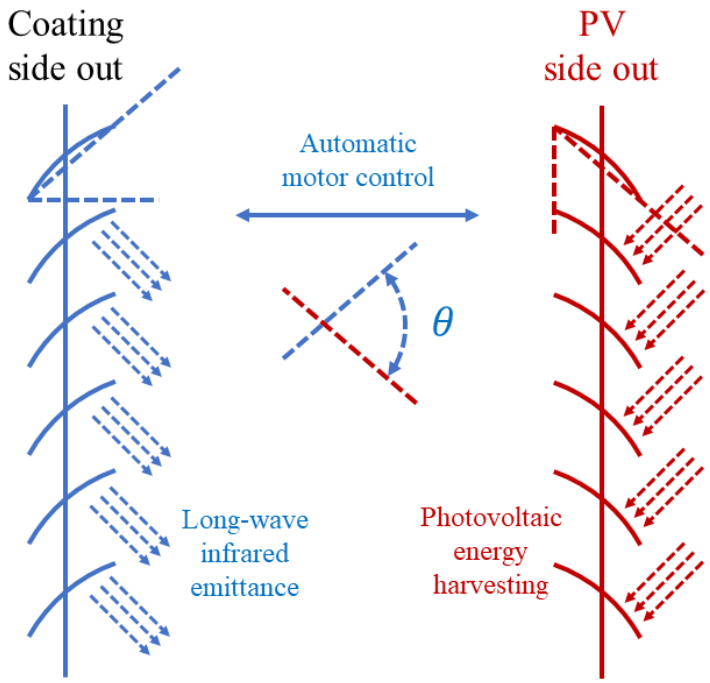

Figure 90 The rotating mechanism of the smart window blinds

Two temperature thresholds $T_{high} = 47\,℃$ and $T_{low} = 42\,℃$ are predefined in the microcontroller, such that the cooling process starts when the temperature measurement is higher than T_{high}, and the PV harvesting resumes when the temperature measurement is lower than T_{low}. The thermometer measurement is not readable for a standalone system with no wireless communication, and thus the thermocouple is attached to the same window blind as shown in Figure 89, to serve as an indicator of the surface temperature. The measurements from the thermocouple and thermometer are recorded via the data acquisition system and the Arduino Uno, respectively, and plotted in Figure 91 for comparison. Although the thermocouple measurement is slightly different with the thermometer, the dynamics of the temperature variation are successfully captured in both measurements. Therefore, the thermocouple is used as the indicator of the surface temperature and the motor control when the thermometer measurement is not available.

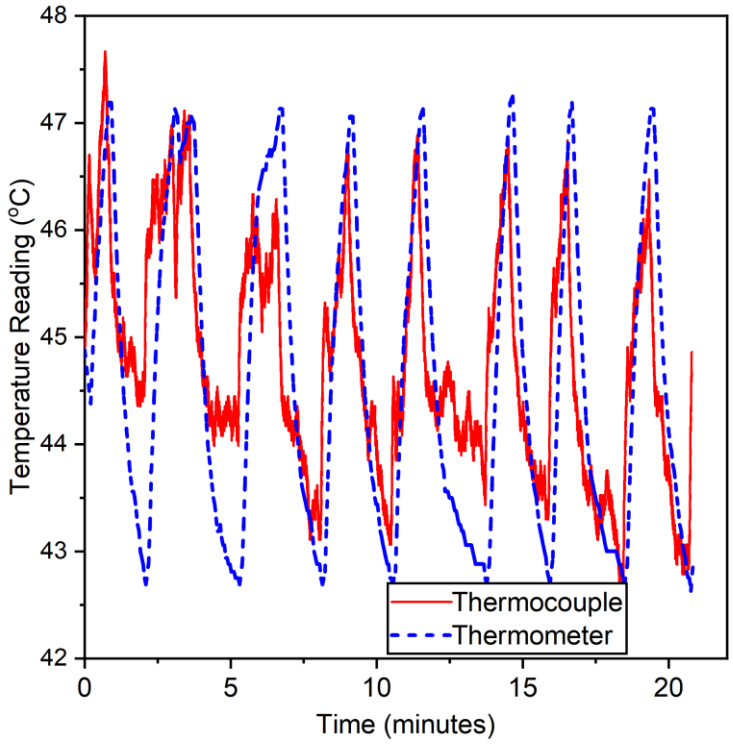

Figure 91 Temperature measurement from thermocouple and thermometer

The current output from the battery is monitored via the voltage measurement of a 1.43 ohm 25 W resistor via the data acquisition system. Since the voltage from the battery is fixed at 12 V, the battery current output represents the total energy consumption. In Figure 92 the dynamic of the battery current output and the temperature variation are plotted in blue and red dots, respectively. Whenever the surface temperature reaches the preset threshold temperature points, the H-bridge is open and the motor is activated for the rotation, which is observed as the sudden peak current in Figure 92. An enlarged plot of the current consumption is shown in Figure 93, where the current consumptions for the deep sleep mode, the awake mode, and the motor control mode are clearly distinguished. The deep sleep mode consumes approximately 25 mA and lasts for 8 seconds, after which the Arduino Uno is waken by its internal clock and measures the temperature from the connected thermometer. The awake mode takes less than 1 second and consumes 37 mA on average. When the temperature requirement is met and the motor control is activated, an intravenously current increase to 270 mA is observed and lasts for about 2 seconds, which corresponds to 6 Joule of energy in total. The overall energy consumption of the controlling unit is shown in Table 21. The deep sleep mode, the awake mode, and the motor control mode consumes 0.30, 0.44, and 3.24 W of power, respectively. It is worth to mention that the 12 V battery pack is connected directly to the Arduino Uno, which enlarges the power consumption. Less power is expected if a high-efficiency step down voltage converter is added between the battery and the Arduino Uno. It is also worth to point out that the performance of the deep sleep mode of Arduino Uno is not outstanding, and that the deep sleep mode of the ESP32 FireBeetle mentioned in the Chapter 5 consumes as low as 50 nA and can significantly improve the energy saving of the controlling unit.

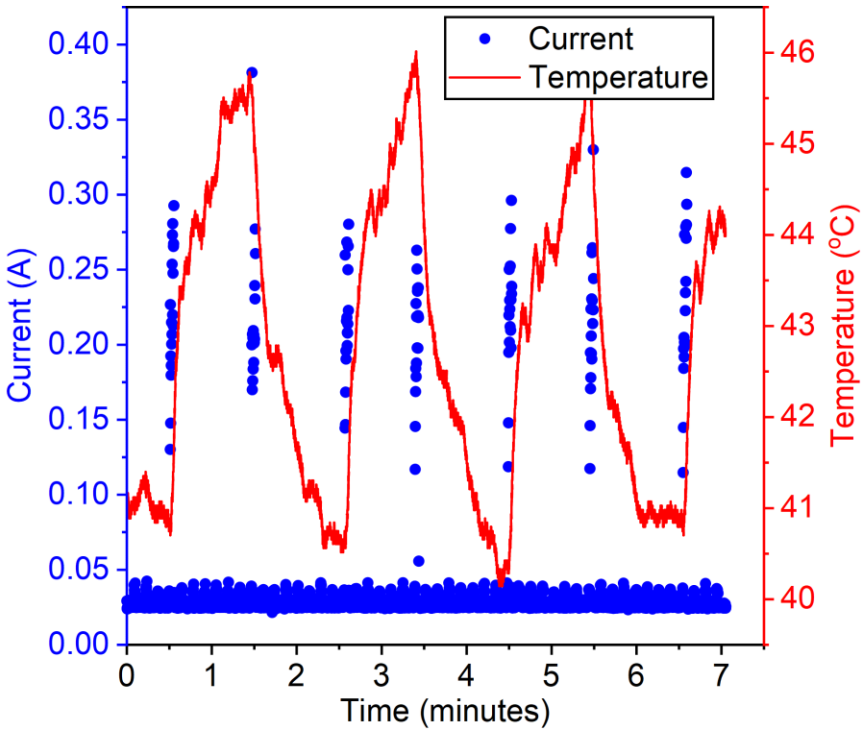

Figure 92 The temperature measurement and the system energy consumption of the smart window blinds

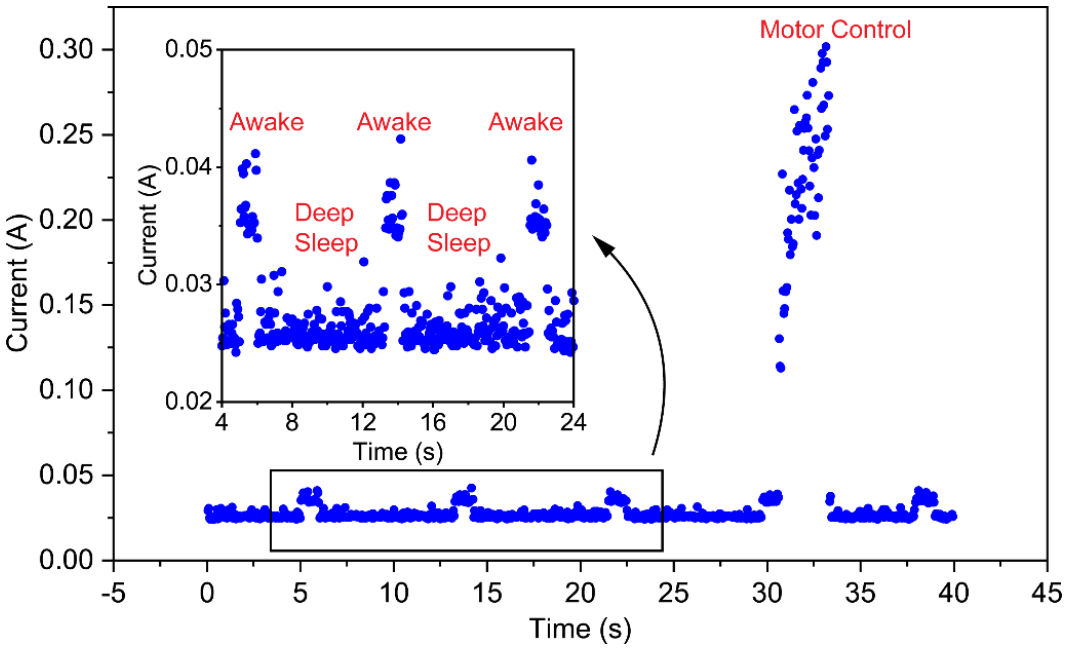

Figure 93 The detailed energy consumption for deep sleep, awake and the motor control mode

Table 21 Energy consumption of the smart window blinds controlling unit

	Deep sleep	Awake	Motor control
Voltage (V)	12	12	12
Current (mA)	25	37	270
Power (W)	0.30	0.44	3.24

6.3 Energy equilibrium analysis

The self-powered function is an important feature for the proposed sun-powered smart window blinds, after which the abundant energy can be used as the power output for small appliances or for more complicated monitoring and smart controls. Therefore, the energy equilibrium analysis of the solar energy harvesting and the system power consumption is an important step. Similar to the methodology described in Chapter 5, the energy level in the battery is traced throughout a prescribed period T, which is typically a year, to aid the engineering design and to predict the system performance. The amount of energy charged into the battery E_{bat} is decomposed into the harvested power P_{har} and the consumed power P_{con} as described below

$$E_{bat} = (P_{har} - P_{con}) \times T \tag{6.1}$$

where P_{har} and P_{con} are described in detail below. A case study based on the New York City measurements will be discussed as an example of the energy equilibrium design and engineering.

6.3.1 Harvested power into battery

The harvested power into the battery comes from the photovoltaic cells on the window blinds, and is written as

$$P_{har} = I_{siwb} \times A_{PV} \times \eta_{PV} \times \eta_{BM} \tag{6.2}$$

where I_{siwb} is the solar irradiation on window blinds, A_{PV} is the area of the photovoltaic cells, η_{PV} and η_{BM} represent the energy efficiency of the photovoltaic cells and the battery management

system, respectively. The area of the photovoltaic cells A_{PV} depends on the applications and the current window size of $A_{PV} = 0.9\ \text{m} \times 1.5\ \text{m} = 1.35\ \text{m}^2$ is used for estimation. The $\eta_{PV} = 2\%$ and $\eta_{BM} = 55\%$ is estimated based on the tests conducted in Section 6.2.

The solar irradiation on window blinds I_{siwb} is originated from the direct solar irradiation from the sun. One way to estimate the I_{siwb} is to start from the irradiation output from the sun, and combined with the sun zenith angle, which varies by time and date, to determine the available irradiation. However, this approach does not incorporate local weather conditions, and needs to incorporate the data at different time of a single day, which is too complicated to model accurately. A more practical approach is to estimate based on the local solar energy stations, which has already considered the local weather conditions and the sunlight angle at different time by providing an averaged data over a month. Empirically, the Average Tilt at Latitude (ATaL) angle will often produce the optimum energy output [246]. It is defined as the total amount of solar radiation received per unit area by a surface that is tilted toward the equator at an angle equal to the current latitude and is used as a variable to calculate the direct solar irradiation. It is worth to mention that the measurements from the solar station is based on the south-facing solar panels. For applications under other directions, a reduction factor is needed to the solar irradiation level, to also incorporate the scattering of the atmosphere and the reflection of surrounding architectures.

Theoretically, the optimal angle for the solar energy harvesting is the plane perpendicular to the solar irradiation, as indicated by the dash line in Figure 94, the schematic drawing of the angles between the sun and the earth. The earth's axis results in an angle between the earth–sun line and the earth's equatorial plane and is called the solar declination ξ, which ranges from -23.45° to 23.45° from winter to summer and is represented as [247]:

$$\xi = 23.45 \sin\left[\frac{2\pi}{365}(284 + N)\right] \tag{6.3}$$

where N is the date of a year starting from January 1st. The geographical location is represented by the local latitude ϕ, ranging from $-90°$ to $90°$ from south pole to the north.

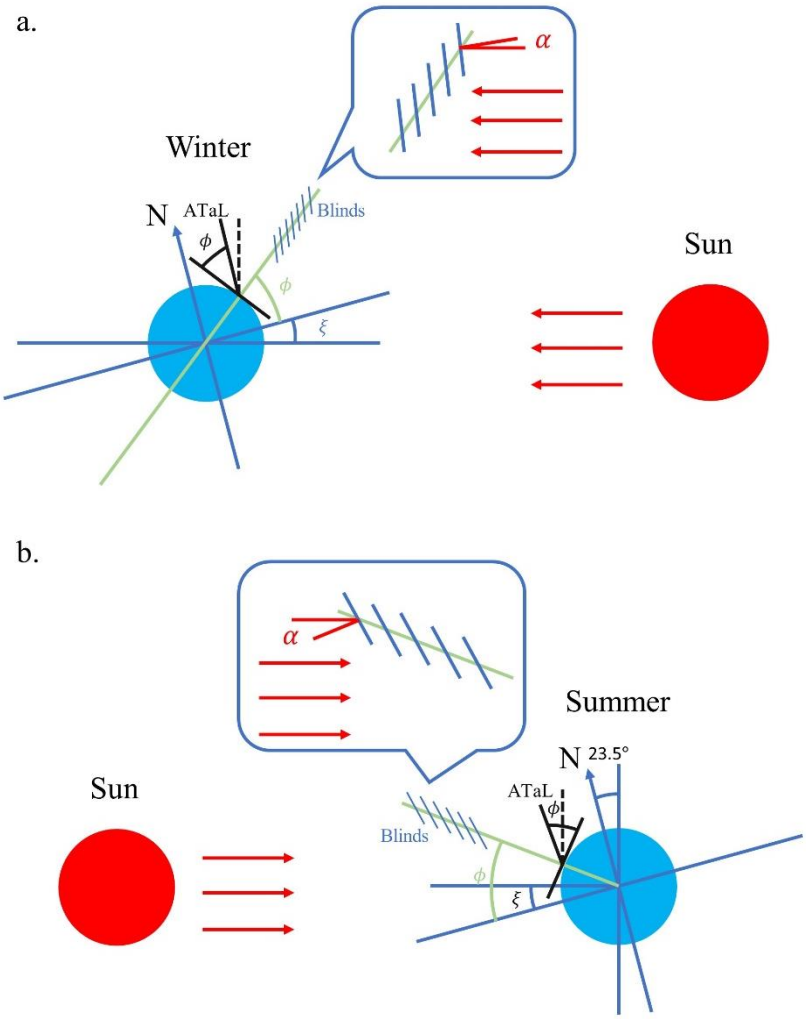

Figure 94 Sunlight and window blinds angle in a. winter and b. summer

With the help of the solar declination and the local latitude, the maximum solar irradiation I_0 that can be received by the dash line in Figure 94 is determined via the ATaL position measurement I_{ATaL} as

$$I_0 = \frac{I_{\mathrm{ATaL}}}{\cos\xi} \tag{6.4}$$

Considering the buildings are perpendicular to the ground, the placement of the window blinds is also vertical, as represented by the green line in Figure 94. Considering the maximum rotational angle of the window blinds θ as indicated in Figure 90, the solar irradiation perpendicular to the window blinds can be calculated as

$$I_{siwb} = I_0 \cos\alpha = I_{ATaL} \frac{\cos\left(\phi+\xi-\frac{\theta}{2}\right)}{\cos\xi} \tag{6.5}$$

The total harvested power into the battery P_{har} can therefore be easily determined.

6.3.2 Consumed power from battery

The energy consumption of the system is majorly consisted of the motor consumption and the microcontroller consumption. The motor is responsible for both rotational and translational motion of the window blinds. The energy consumption of the microcontroller is decomposed into the awake mode and the deep sleep mode. Therefore, the consumed power P_{con} is written as:

$$P_{con} = P_{MOT} + P_{CTL} = P_{mo}\left(\frac{t_{rot}}{T_{rot}} + \frac{t_{trans}}{T_{trans}}\right) + \frac{P_{aw}t_{aw}+P_{ds}t_{ds}}{t_{aw}+t_{ds}} \tag{6.6}$$

where P_{mo} is the power consumption of the motor for both rotational and translational motions, which consumes equal amount according to the test; t_{rot} and t_{trans} are the time taken for a rotational or translational motion, respectively, within a prescribed period T_{rot} and T_{trans}; $P_{aw}, t_{aw}, P_{ds},$ and t_{ds} are the power consumption and time for the awake and deep sleep mode, respectively.

The motion of the blinds is automated by the microcontroller and is related to the prescribed temperature thresholds, the surrounding environments, and human interactions. An activation of a rotation will take approximately 2 seconds with the averaged power consumption of 3.24 W, which makes $t_{rot} = 2$ s and P_{mo}=3.24 W. The period T_{rot} is the averaged time needed for a single

activation of the rotation and is dependent on the prescribed temperature thresholds and the surround environment. One design methodology is to prescribe the temperature thresholds, so that the T_{rot} can be determined depending on the surrounding environment. This methodology would require rigorous testing on different environments. Another methodology is to prescribe the T_{rot} so as to prescribe how many rotations within a certain period of time, such that the temperature thresholds can later calculated and continuously updated based on the surroundings. In the second approach, machine learning algorithms can be implemented to predict the temperature threshold based on either the temperature prediction from the Internet, or the local environmental measurements from the attached sensors. In the scope of this research, the T_{rot} is prescribed as 1 mins from the test conducted in Figure 92, which means the rotational control of the blinds is activated in every 1 mins on average. The T_{rot} in the real application will be much smaller because of the weaker solar irradiation and better air ventilation. The translational motion of the blinds, including the lifting and lowering of the blinds, is highly dependent on the human interference and is difficult to predict. Therefore, the translational motion by human interaction is neglected in the scope of this study. Unlike the motor, the power consumption from the microcontroller is more stable and less influenced by the surroundings. It is divided into the deep sleep mode and the awake mode. The ratio between the deep sleep time and the awake time $\gamma = t_{ds}/t_{aw}$ can be modified to control the power consumption from the microcontroller. Therefore, Eq. (6.6) can be further simplified as:

$$P_{con} = P_{mo}\frac{t_{rot}}{T_{rot}} + \left[P_{ds} + (P_{aw} - P_{ds})\frac{1}{1+\gamma}\right] \tag{6.7}$$

in which the period of the rotational motion T_{rot} and the ratio between the deep sleep time and the awake time γ are two variables to control the overall power consumption.

6.3.3 Energy equilibrium analysis based on New York

The New York City is chosen as the demonstration of the energy equilibrium analysis. The average energy received per day in each month is obtained from the local solar energy stations [ref] from the solar panels at the ATaL angle to the sun. The New York City latitude ϕ is obtained and the average solar declination angle ξ is calculated with the help of Eq. (6.3). The projected energy onto the window blinds is therefore calculated with the help of Eq. (6.4) and (6.5) and listed in Table 22. The solar irradiation intensity I_i $(i = ATaL, 0, siwb)$ can be directly calculated from the E_i $(i = ATaL, 0, siwb)$ by dividing 24 hour/day as the average over a day. The average energy received by the ATaL angle E_{ATaL}, the optimal angle E_0, and the window blinds E_{siwb} are plotted in Figure 95 for a straightforward distribution over months. It is seen that the summer months contributes the majority of the solar irradiation over a year and that the available energy in the summer is more than 2.5 times the lowest season in winter. It is interesting to point out that in the summertime in the north hemisphere, the sunlight is almost in parallel with the vertical building skins, which could potentially waste the abundant solar energy if the PV is attached directly to the building skin. However, a placement angle θ is introduced by the design of the window blinds, as described in Figure 90, and this angle compensates the harm from the vertical building skin and brings the PV cells closer to the direct solar irradiation. It is worth to point out that when maximum α is smaller than 0, the perpendicular solar irradiation onto the window blinds can be achieved by adjusting the rotational angle of the motor, and therefore achieving the optimal solar energy harvesting from the photovoltaic cells.

Table 22 Solar irradiation and angles in New York

Month	Jan	Feb	Mar	Apr	May	Jun
E_{ATaL} (kWh/m^2/d)	3.61	4.45	4.92	5.05	5.24	5.31
ξ (°)	-20.40	-13.09	-2.34	9.30	18.40	22.61
ϕ_{NY} (°)	40.72	40.72	40.72	40.72	40.72	40.72
E_0 (kWh/m^2/d)	3.85	4.57	4.92	5.12	5.52	5.75
α (°)	-51.68	-44.38	-33.62	-21.98	-12.88	-8.67
E_{siwb} (kWh/m^2/d)	2.39	3.27	4.10	4.75	5.38	5.69
Month	Jul	Aug	Sep	Oct	Nov	Dec
E_{ATaL} (kWh/m^2/d)	5.46	5.28	5.10	4.26	3.44	3.34
ξ (°)	20.65	13.01	1.95	-9.64	-18.67	-22.60
ϕ_{NY} (°)	40.72	40.72	40.72	40.72	40.72	40.72
E_0 (kWh/m^2/d)	5.83	5.42	5.10	4.32	3.63	3.62
α (°)	-10.64	-18.27	-29.33	-40.92	-49.95	-53.88
E_{siwb} (kWh/m^2/d)	5.73	5.15	4.45	3.27	2.34	2.13

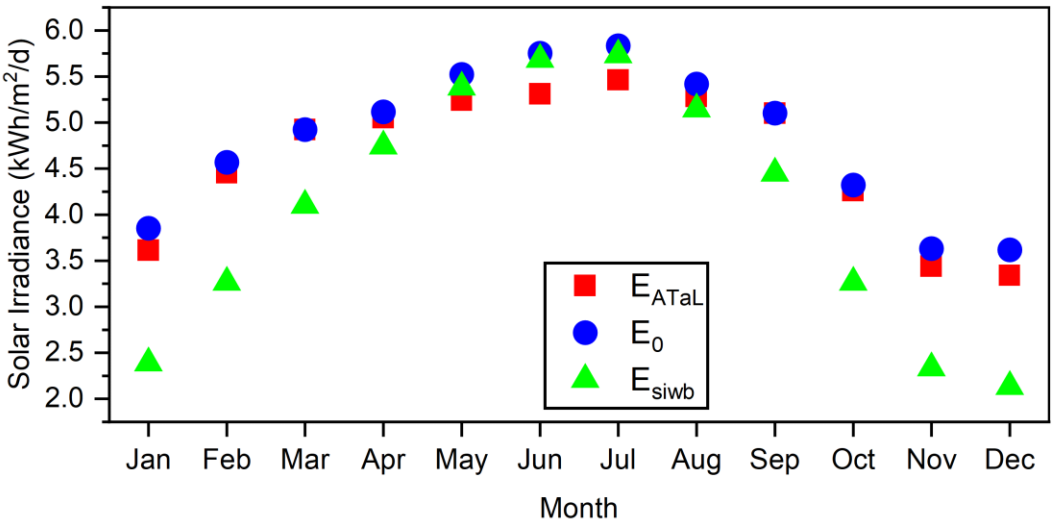

Figure 95 Average Tilt at Latitude, direct, and window blinds solar irradiation in New York

The harvested power into the battery P_{har} can be calculated from the E_{siwb} in Table 22, with the help of Eq. (6.2). The consumed power from the battery P_{con} is determined from Eq. (6.7), with the prescribed $\gamma = 7$ and $T_{rot} = 1$ min obtained from the tests. The harvested, consumed power is listed in Table 23, together with the projected energy that can be saved in a month. It is concluded that the harvested power is much larger than the power needed for the motor and microcontroller, and the energy equilibrium can be easily satisfied with any sized battery. The power efficiency of the system, defined as the remaining power divided by the total harvested power, is between 70% to 90%, indicating that the harvested power is 3 to 9 times larger than needed power from the motor and the controller. The efficiency could be improved by the larger rotational period T_{rot}, via the optimization of the temperature control, or a better microcontroller with less deep sleep consumption, such as the ESP32 introduced in Chapter 5. Since the power consumption of the deep sleep mode for the Arduino Uno R3 is not much different to the awake mode, the increase of the sleep-awake ratio γ will not improve the energy consumption significantly. The monthly saved energy is also calculated to quantify the amount of energy charged into the battery, and as an indicator of the energy budget for the translational motion of the window blinds and for other connected devices in the future. The abundant energy projection validates the feasibility of the design and indicates the great application potentials, from being the platform for a wide range of sensors to serving as the energy hub of various smart home devices in the future.

Table 23 Harvested, consumed and saved energy of the smart window blind

Month	Jan	Feb	Mar	Apr	May	Jun
E_{siwb} (kWh/m^2/d)	2.39	3.27	4.10	4.75	5.38	5.69
η_{PV}	0.02	0.02	0.02	0.02	0.02	0.02
η_{BM}	0.55	0.55	0.55	0.55	0.55	0.55
Area (m^2)	1.50	1.50	1.50	1.50	1.50	1.50
P_{har}	1.64	2.25	2.82	3.26	3.70	3.91
P_{MOT}	0.11	0.11	0.11	0.11	0.11	0.11
P_{CTL}	0.32	0.32	0.32	0.32	0.32	0.32
P_{con}	0.43	0.43	0.43	0.43	0.43	0.43
P_{remain}	1.22	1.82	2.39	2.84	3.28	3.48
Efficiency (%)	0.74	0.81	0.85	0.87	0.89	0.89
Monthly saved energy (kWh/M)	0.88	1.31	1.72	2.04	2.36	2.51
Month	Jul	Aug	Sep	Oct	Nov	Dec
E_{siwb} (kWh/m^2/d)	5.73	5.15	4.45	3.27	2.34	2.13
η_{PV}	0.02	0.02	0.02	0.02	0.02	0.02
η_{BM}	0.55	0.55	0.55	0.55	0.55	0.55
Area (m^2)	1.50	1.50	1.50	1.50	1.50	1.50
P_{har}	3.94	3.54	3.06	2.24	1.61	1.47
P_{MOT}	0.11	0.11	0.11	0.11	0.11	0.11
P_{CTL}	0.32	0.32	0.32	0.32	0.32	0.32
P_{con}	0.43	0.43	0.43	0.43	0.43	0.43
P_{remain}	3.52	3.11	2.63	1.82	1.18	1.04
Efficiency (%)	0.89	0.88	0.86	0.81	0.74	0.71
Monthly saved energy (kWh/M)	2.53	2.24	1.90	1.31	0.85	0.75

6.4 Conclusions

A novel sun-powered smart window system is design, fabricated and tested in this chapter, with the flexible photovoltaic cells attached on one side and PVdF-HFP passive cooling coating attached on the other side. Comprehensive tests are conducted to quantify the performance of the flexible PV cells, and its linear relation to the temperature and the solar irradiation. The open-circuit voltage, short-circuit current, and the optimal power output is measured via a commercial solar tracer, such that the optimal power output and the corresponding external resistance can always be determined given the applied solar irradiation and the temperature. The energy efficiency of the flexible PV cell is determined around 2%, because of its thin thickness, physical flexibility, and the overlap of the window blinds. The cooling performance of the PVdF-HFP passive cooling coating is also quantified via the stable temperature measurement under different solar irradiation, where a 4% to 9% temperature reduction is observed thanks to the help of the coating. Better performance can be anticipated in the real application because of weaker solar irradiation and better air ventilation. Because of the intermittency of the solar energy, the voltage regulation and battery management systems are designed and tested with a 12 V 18650 battery pack. Two tests are conducted under different solar irradiation intensities and a stable 55% efficiency is achieved from the PV into the battery. The controlling system is built based on the Arduino Uno R3 microcontroller and connected to a thermometer for the temperature measurement. Automated control of the window blinds is achieved depending on the prescribed temperature thresholds and the current temperature measurement. The deep sleep mode is activated, and the corresponding energy consumptions are recorded in each phase. The energy equilibrium analysis is proposed based on the testing data. The methodology to predict the available solar energy onto the window blinds is also proposed, which utilizes the measurements from local solar

energy stations to incorporate the influence of local weather conditions and solar zenith angles within a day. The energy harvesting capability of the smart window blinds far outweighs the power needed for the controller and the motor based on the energy equilibrium analysis, and the abundant energy validates the feasibility and robustness of the system and proves its wide application to various sensors and applications.

Chapter 7 Conclusions and future work

7.1 Summary

This dissertation systematically presents the design, modeling and engineering of smart building envelope systems, in order to achieve the optimal interior comfort with minimal energy expenditure. Both building roof and window/façade systems are investigated for the smart response towards the dynamic environment, in passive and active response, respectively.

A building-integrated photovoltaic thermal (BIPVT) panel is proposed for the building roof systems, which incorporates the photovoltaic cells, functionally graded composite panel and water tubes as the main components. The photovoltaic cells convert solar energy into electric form for the building consumption. The functionally graded composite panel made of high-density polyethylene and aluminum prevents the heat from entering the building and directs the heat to the water tubes embedded inside the panel for the thermal energy harvesting, such that the warm water can be used for energy supply and that the efficiency of PV can be improved. The design, fabrication and properties of the BIPVT system is discussed and a novel image-based, non-destructive analysis method is developed to statistically captures the authentic particle distribution of the FGM. An equivalent inclusion method (EIM) based algorithm is proposed to model the elastoplastic behavior of the FGM by an ensemble average approach to capture the particle's influence on the plastic behavior of the matrix. The algorithm is cross verified by other algorithms and validated by experiments and is extended to thermal and viscoelastic problems. A high order plate theory is also proposed to better capture the thermo-mechanical performance of the BIPVT panel made of functionally graded materials. The shearing and bending behaviors are decomposed,

solved independently, and combined to formulate the final solution, which is verified by other models and validated by the experiments.

Two smart window systems are proposed to actively monitor and control the building environment. The energy harvesting techniques are investigated to convert energy from ambient environment into electricity for the power supply of sensing and control. The thermal energy harvesting inside the window frame and the solar energy harvesting on the window blinds are designed, manufactured and tested in two smart window systems, respectively. The harvested energy is voltage-regulated and stored into rechargeable batteries for the consumption in low seasons. Wireless data transfer and cloud storage is achieved for the data obtained from the monitoring and the overall power consumption can be tailored by manipulating the ratio between sleep and awake. The energy equilibrium is achieved between the harvesting and consumption and an algorithm is proposed to aid the energy design, such that the system can theoretically be alive until physical failure of components.

7.2 Key results

In this work, the key results are presented in the following four parts: the micromechanics-based elastoplastic modeling of a two-phase functionally graded material, the high order plate theory for the circular plate made of FGM, the thermal energy harvesting methodology for the self-powered wireless sensing platform, and the solar energy harvesting methodology for the self-powered wireless sensing platform.

7.2.1 Elastoplastic modeling of functionally graded materials

Recently, an innovative water-based BIPVT roofing system was proposed to for both solar and thermal energy harvesting, with the help of a high-density polyethylene based and aluminum particle reinforced functionally graded panel. The panel is designed to replace the original building roof, and thus responsible for both structural support and the thermal energy harvesting. It goes under significant mechanical forces from external wind load, snow load, and dead load, as well as thermomechanical forces from temperature change. Therefore, the thermo-elastoplastic modeling of the particle reinforced FGM is very important for a wide industrial application of the panel. However, the particle's influence on the elastoplastic behavior of the matrix material is very hard to capture and quantify, and therefore making it difficult to theoretically model the plastic behavior of the functionally graded materials.

A complete elastoplastic modeling methodology of FGM is given in this dissertation, with the consideration of pair-wise particle interactions. The elastic model of FGM is first introduced based on the equivalent inclusion method, where the particle's effect is represented by the introduction of an eigenstrain. The pair-wise particle interaction is obtained by comparing the strain field of two-particle case and the one-particle case. The microscopic relations are integrated to the macroscope via the Mori-Tanaka's assumption, in order to formulate a connection between particle and matrix. An ensemble average approach was used to convert the particles' interaction in microscope to the averaged relation in macroscope, such that both particle to matrix influence and particle to particle pair-wise interactions are characterized. An ordinary differential equation is achieved to represents the relation between the internal stress field to the external load, which can be solved via numerical methods such as the backward Euler's method.

The idea of the equivalent inclusion method extends to the plastic modeling of the FGM, by formulating an ensemble average form of the matrix stress norm in the macroscale that incorporate the local disturbance of particle reinforcement in the microscale. The replacement of the particle inhomogeneity by the matrix phase introduces a scaling factor related to the particle volume fraction, and thus defines a so-called current stress norm in the final form of the yield function. The explicit form of the yield function is derived based on the relationship found in the elastic modeling and arrives at an isotropic fourth order tensor. The pair-wise particle interaction is incorporate to the model via the relation between the internal stress field and the external load, from an ordinary differential equation that can be solved numerically. Therefore, the EIM-based yield function that considers the particle's pair-wise interaction and the influence on the matrix is obtained, which can be directly applied with the classic plasticity theory to solve the elastoplastic behavior of the functionally graded materials. If the macroscopic volumetric average stress $\bar{\boldsymbol{\sigma}}$ is known, the plasticity is stress driven and the consistency condition requires the yield function smaller than or equal to zero, which determines the effective plastic strain directly. In case of the strain-driven plasticity, return mapping algorithm is applied to perform the stress update, during which Newton's method or Bisection can be used to determine the $\dot{\lambda}$ from consistency condition. Such equivalent inclusion based elastoplastic modeling is studied for both von-Mises yielding criteria and the pressure dependent yielding criteria. The ensemble average form of the pressure dependent term is also discussed and derived. The temperature effect is taken into consideration for both elastic and elastoplastic analysis, by the introduction of an additional eigenstrain term in the constitutive equation. The temperature change will introduce three additional terms in the stress norm, with one term indicating the pure thermal loading and the other two representing the coupling between mechanical and thermal loading.

To the best of the author's knowledge, there exists no available algorithm for the elastoplastic modeling of functionally graded materials. Therefore, the proposed method is downgraded to compare with a model for the particle-reinforced metal matrix composite, a non-graded form of the FGM, for the verification, where a good agreement is achieved. The experimental validation is also conducted with the Al/HDPE based FGM, in which an innovative non-destructive method is proposed to statistically capture the particle volume fraction distribution. Good accordance between the experiment and the modeling is observed in the plastic region, while a slight underestimation is recorded in the elastic region. Overall, the proposed elastoplastic algorithm of FGM captures the real elastoplastic behavior of FGM very well and can be used for further investigation and industry prediction. Cases studies are carried out to quantify the influence of the volume fraction distribution, and the variation of material properties to the overall elastoplastic performance.

7.2.2 FGM plate theory

The equivalent inclusion based algorithm gives the theoretically modeling tool to capture and predict the thermal and elastoplastic behavior of functionally graded materials. The BIPVT roof utilizes the functionally graded material as a panel to support structural loads and to prevent the heating from entering the room. Therefore, a high order plate theory is proposed to study for the thermo-mechanical performance of the circular FGM panel made of Al/HDPE FGM, in order to provide structural design guideline for the BIPVT panels.

The material characterizations of the FGM panel is conducted. The distributions of Young's modulus and thermal expansion coefficient along the thickness are presented and discussed. The manufacturing of the panel undergoes a 120 ℃ temperature drop, which casts a big thermomechanical loading to curves the panel surface. The thermal-induced deflections are

measured with laser displacement sensor along eight segments to obtain an averaged overall deformation. In the theoretical modeling, the deflections from bending and shearing are separated. The shear strain components are assumed to follow a parabolic variation across the thickness, while the bending components follows the solution from classical plate theory. Temperature induced thermal strain is integrated into the constitutive equations, and the governing equations are formulated via variational principle on extension, bending deflection and shearing deflection. Theoretical solutions are obtained with the help of the modified Bessel function under different loading and boundary conditions. Closed-form solutions for the circular panel under different loadings (thermal, concentrated point, and uniformly distributed load) are provided. The derivation and exact solution of the refined plate theory is much simpler than other high order plate theories. Sample preparation and material characterization of the FGM panel are presented. Experiments on the structural performances of the circular panel under thermo-mechanical loadings are subsequently conducted to validate the present model. Explicit solutions based on the conventional classical plate theory and the first order plate theory are also developed as a comparison. Finite element analyses (FEA) were conducted to further verify the present model for the circular FGM panel under different loading conditions. The comparison results show that, (1) under pure thermal loading where no shear deformation involved in the circular FGM panel, the thermal deflection predicted by the three theoretical models provide the exact same values, which agree well with the experimental result with a difference less than 5%; (2) under mechanical loading (both concentrated point load and uniformly distributed load), the solution from the proposed high order plate theory lies between the classical plate theory, where the shear is overlooked, and the first order plate theory, where the shear is overestimated, and therefore gives a better prediction for plates complicated material composition.

The combination of the elastoplastic modeling and the plate theory can serve as the guidance for the BIPVT panel design. In order to replace the original building roof, the proposed BIPVT panel must satisfy the loading requirement, the deformation limit of the ASCE standard, while providing the optimal thermal insulation towards the external heat. The strength of the functionally graded material can be predicted by the micromechanics based elastoplastic analysis with the volume fraction. Therefore, the volume fraction of the aluminum reinforcement can be reversely determined given the loading requirements. The corresponding elastic properties can be quickly estimated based on the overall volume fraction. The distribution of the volume fraction can then be tailored to satisfy the deformation limit while maximizing the thermal insulation, such that the heat is locked into the water tubes for energy harvesting. The plastic deformation can also be predicted given the volume fraction distribution in case the panel goes into some extreme loading conditions.

7.2.3 Thermoelectric powered wireless sensing platform

The building-integrated photovoltaic thermal roof can harvest solar and thermal energy simultaneously in a very high efficiency but fails to actively respond to the dynamic environment. The active adaptation to the environment requires the continuous knowledge of the environment and the smart controlling center to respond accordingly. A new thermoelectric-powered wireless sensing network (TPWSN) platform, embedded inside the window/façade, is introduced and developed for the environmental sensing and the control of a smart building system. The TPWSN continuously monitors the building environment and provides data for the optimization of the building energy consumption and indoor comfort. In addition, the self-powered wireless sensing significantly simplifies the installation and maintenance of the system with considerable savings

of time and cost. The window/façade are selected as the place for the platform because they are the first and the most critical barrier for the heat exchange between buildings and environment. The platform is hidden entirely inside the frame with no wired connections to the outside, therefore having no compromise of the outlook.

The environmental monitoring is carried out by a system-on-chip with ultra-low energy consumption, which is powered by the energy harvesting system with a rechargeable battery. The data is wirelessly transferred to the external server through the local Wi-Fi network. The energy harvesting unit utilizes the thermoelectric generator to convert the thermal gradient into electricity by leveraging the temperature difference between the two sides of a window system. Twenty different internal structures are investigated under commercial finite element software ABAQUS for the heat transfer analysis, in order to optimize a specially designed objective function that incorporate the energy output from the thermal electric generator and the additional weight introduced to the system. The three-bridge model with 45° placement angle of the TEG is chosen as the final design. Two units are manufactured and implemented into the window frame, each unit with two TEGs at the size of $30mm \times 30mm$. The voltage regulator LTC3108 is used to boost the ultra-low voltage output from TEG to high voltage, and the battery management circuit LTC4071 is used to direct the energy into battery with both overcharge and over-discharge protection. The total energy efficiency reaches 33.4% from the energy harvester to the battery. The microcontroller ESP32 FireBeetle is chosen as the CPU for the sensing platform, which enjoys the ultra-low energy consumption under the deep sleep mode. The overall energy consumption can be manipulated via the ratio of sleep and awake time. The Wi-Fi is used as the wireless communication protocol for the data transmission to the external server and the cloud.

The energy balance between consumption and harvesting is achieved in the lab testing configuration, and the battery charging process is recorded when the temperature difference on TEG reaches 7℃. An energy balance algorithm is proposed based on the designed configuration to permanently supply the energy consumption through harvesting. The number of TEGs and the ratio between the sleep and awake time are selected as the controllable variables to achieve the energy balance. The battery energy level can be projected at any time given the temperature histogram, such that the system design could be tailored to any geographic location. The architecture of the design, the testing result of the system, and the energy equilibrium analysis in this chapter can serve as a valuable reference and guideline for future smart building envelope projects.

7.2.4 Sun-powered smart window blinds

A novel sun-powered smart window system is designed, fabricated and tested, with the flexible photovoltaic cells attached on one side and PVdF-HFP passive cooling coating attached on the other side. Comprehensive tests are conducted to quantify the open-circuit voltage, short-circuit current, and the optimal power output of the flexible PV cells. Linear relations between performance to the temperature and solar irradiation are also obtained, which can be used to project the power output in the future. The cooling performance of the PVdF-HFP passive cooling coating is also quantified via the testing under different solar irradiations, and 4% to 9% temperature reduction is observed under different intensities. The voltage regulation and battery management systems are designed and tested with a 12-volt 18650 battery pack, which could reach a stable 55% energy efficiency from the PV into the battery. The controlling system is built based on the Arduino Uno R3 microcontroller and connected to a thermometer for the temperature measurement. Automated control of the window blinds is achieved depending on the prescribed

temperature thresholds and the current temperature measurement. The energy equilibrium analysis is proposed and demonstrated with the measurements from the local solar energy stations in New York City to incorporate the influence of local weather conditions and solar zenith angle. The energy harvesting provides much more power than the needed energy supply from the microcontroller and the motor. The abundant energy validates the feasibility and the robustness of the system and proves its wide application potentials to various sensors and applications.

7.3 Future work

Improvement of the BIPVT roof will be conducted in the future in both theoretical modeling and system design. The modeling of the BIPVT involves the elastoplastic algorithm and the high order plate theory for the functionally graded material panel. The equivalent inclusion method based elastoplastic algorithm is extended to the theoretically discussion of thermo-elastoplastic and viscoelastic modeling. The cross verification and experimental validation will be conducted in future to prove the accuracy of the algorithm. The plate theory gives the projection of how much external force is needed to flatten the curved panel, and can be combined with the elastoplastic modeling to study the local plastic deformation under the external force. Recently a design with foamed aluminum and phase change materials provides similar structural and thermal performance with the proposed FGM structure, and further study could be conducted to compare the pros and cons.

The self-powered wireless sensing platform has achieved the self-powered feature with the help of thermoelectric harvesting, but the energy efficiency is still relatively low. The temperature difference transferred to the TEG surfaces is only 1/3 of the total potential on the window, and the efficiency of charging is also 1/3 from the TEG to the battery. Future improvement is needed to

tailor the TEG thickness to the window space, so as to get rid of the thermal connector in order to increase the heat transfer efficiency. The improvement of the energy storage efficiency could be achieved by optimizing the inductance on LTC3108 and the voltage management throughout the charging, where a potential 50% improve could be expected. The Bluetooth Low Energy (BLE) and the Radio Frequency (RF) could be investigated as the wireless communication tools to reduce the energy consumption and improve the system performance.

The sun-powered smart window utilizes the second generation of solar cells for the self-powering of the window blind motor, but the overall harvesting efficiency is only 2%, which shall be investigated for improvement in the future. The current controlling system has 24-volt motor, which cast a lot of challenges for the power supply and energy management. More efficient motor with lower voltage could be investigated to provide better efficiency of the system and a smarter controlling system in the future. The current microcontroller of Arduino Uno R3 could be replaced by the ESP32 so as to incorporate the wireless communication function and to improve the performance of the deep sleep mode, which can significantly reduce the energy consumption of the system. The platform can be extended to various sensors and applications and more designs and engineering are needed.

With the help of all energy harvesting approaches and the optimized control and management of all building components, the energy independent house is made possible, which would significantly increase the energy efficiency and green house gas footprint in the future.

References

[1] US Department of Energy, "Quadrennial Technology Review 2015-An Assessment of Energy Technologies and Research Opportunities, Chapter 1: Energy Challenges," US Department of Energy, 2015.

[2] US Department of Energy, "Quadrennial Technology Review 2015-An Assessment of Energy Technologies and Research Opportunities, Chapter 5: Increasing Efficiency of Building Systems and Technologies," US Department of Energy, 2015.

[3] M. Manic, D. Wijayasekara, K. Amarasinghe, and J. J. Rodriguez-Andina, "Building Energy Management Systems: The Age of Intelligent and Adaptive Buildings," *IEEE Industrial Electronics Magazine*, vol. 10, no. 1, pp. 25–39, Mar. 2016, doi: 10.1109/MIE.2015.2513749.

[4] Energy Information Administration (EIA), "Annual Energy Review 2014-With Projections to 2040," Department of Energy, Washington, DC: U.S, 2014. [Online]. Available: http://www.eia.gov/outlooks/archive/aeo14/pdf/0383(2014).

[5] Energy Information Administration (EIA), "Manufacturing Energy Consumption Survey 2010," Washington DC, 2013.

[6] W. M. Kroner, "An intelligent and responsive architecture," *Automation in Construction*, vol. 6, no. 5, pp. 381–393, Sep. 1997, doi: 10.1016/S0926-5805(97)00017-4.

[7] M. Wigginton and J. Harris, *Intelligent Skins*. Routledge, 2013.

[8] J. Yang and H. Peng, "Decision support to the application of intelligent building technologies," *Renewable Energy*, vol. 22, no. 1, pp. 67–77, Jan. 2001, doi: 10.1016/S0960-1481(00)00085-9.

[9] J. Böke, U. Knaack, and M. Hemmerling, "State-of-the-art of intelligent building envelopes in the context of intelligent technical systems," *Intelligent Buildings International*, vol. 11, no. 1, pp. 27–45, Jan. 2019, doi: 10.1080/17508975.2018.1447437.

[10] M. A. Berawi, P. Miraj, M. S. Sayuti, and A. R. B. Berawi, "Improving building performance using smart building concept: Benefit cost ratio comparison," *AIP Conference Proceedings*, vol. 1903, no. 1, p. 030001, Nov. 2017, doi: 10.1063/1.5011508.

[11] S. B. Sadineni, S. Madala, and R. F. Boehm, "Passive building energy savings: A review of building envelope components," *Renewable and Sustainable Energy Reviews*, vol. 15, no. 8, pp. 3617–3631, Oct. 2011, doi: 10.1016/j.rser.2011.07.014.

[12] M. Ciampi, F. Leccese, and G. Tuoni, "Energy analysis of ventilated and microventilated roofs," *Solar Energy*, vol. 79, no. 2, pp. 183–192, Aug. 2005, doi: 10.1016/j.solener.2004.08.014.

[13] A. B. Besir and E. Cuce, "Green roofs and facades: A comprehensive review," *Renewable and Sustainable Energy Reviews*, vol. 82, pp. 915–939, Feb. 2018, doi: 10.1016/j.rser.2017.09.106.

[14] M. Shafique, R. Kim, and M. Rafiq, "Green roof benefits, opportunities and challenges – A review," *Renewable and Sustainable Energy Reviews*, vol. 90, pp. 757–773, Jul. 2018, doi: 10.1016/j.rser.2018.04.006.

[15] J. Han, L. Lu, and H. Yang, "Investigation on the thermal performance of different lightweight roofing structures and its effect on space cooling load," *Applied Thermal Engineering*, vol. 29, no. 11, pp. 2491–2499, Aug. 2009, doi:

10.1016/j.applthermaleng.2008.12.024.
[16] A. Synnefa, M. Santamouris, and I. Livada, “A study of the thermal performance of reflective coatings for the urban environment,” *Solar Energy*, vol. 80, no. 8, pp. 968–981, Aug. 2006, doi: 10.1016/j.solener.2005.08.005.
[17] S. Guichard, F. Miranville, D. Bigot, B. Malet-Damour, K. Beddiar, and H. Boyer, “A complex roof incorporating phase change material for improving thermal comfort in a dedicated test cell,” *Renewable Energy*, vol. 101, pp. 450–461, Feb. 2017, doi: 10.1016/j.renene.2016.09.018.
[18] A. Jayalath, L. Aye, P. Mendis, and T. Ngo, “Effects of phase change material roof layers on thermal performance of a residential building in Melbourne and Sydney,” *Energy and Buildings*, vol. 121, pp. 152–158, Jun. 2016, doi: 10.1016/j.enbuild.2016.04.007.
[19] H.-M. Chou, C.-R. Chen, and V.-L. Nguyen, “A new design of metal-sheet cool roof using PCM,” *Energy and Buildings*, vol. 57, pp. 42–50, Feb. 2013, doi: 10.1016/j.enbuild.2012.10.030.
[20] M. Saffari, C. Piselli, A. de Gracia, A. L. Pisello, F. Cotana, and L. F. Cabeza, “Thermal stress reduction in cool roof membranes using phase change materials (PCM),” *Energy and Buildings*, vol. 158, pp. 1097–1105, Jan. 2018, doi: 10.1016/j.enbuild.2017.10.068.
[21] H. M. Yin, D. J. Yang, G. Kelly, and J. Garant, “Design and performance of a novel building integrated PV/thermal system for energy efficiency of buildings,” *Solar Energy*, vol. 87, pp. 184–195, Jan. 2013, doi: 10.1016/j.solener.2012.10.022.
[22] C. S. Malvi, D. W. Dixon-Hardy, and R. Crook, “Energy balance model of combined photovoltaic solar-thermal system incorporating phase change material,” *Solar Energy*, vol. 85, no. 7, pp. 1440–1446, Jul. 2011, doi: 10.1016/j.solener.2011.03.027.
[23] T. N. Anderson, M. Duke, G. L. Morrison, and J. K. Carson, “Performance of a building integrated photovoltaic/thermal (BIPVT) solar collector,” *Solar Energy*, vol. 83, no. 4, pp. 445–455, Apr. 2009, doi: 10.1016/j.solener.2008.08.013.
[24] T. Yang and A. K. Athienitis, “A review of research and developments of building-integrated photovoltaic/thermal (BIPV/T) systems,” *Renewable and Sustainable Energy Reviews*, vol. 66, pp. 886–912, Dec. 2016, doi: 10.1016/j.rser.2016.07.011.
[25] K. Vats and G. N. Tiwari, “Energy and exergy analysis of a building integrated semitransparent photovoltaic thermal (BISPVT) system,” *Applied Energy*, vol. 96, pp. 409–416, Aug. 2012, doi: 10.1016/j.apenergy.2012.02.079.
[26] M. Rabani, V. Kalantar, A. A. Dehghan, and A. K. Faghih, “Experimental study of the heating performance of a Trombe wall with a new design,” *Solar Energy*, vol. 118, pp. 359–374, Aug. 2015, doi: 10.1016/j.solener.2015.06.002.
[27] M. Tunç and M. Uysal, “Passive solar heating of buildings using a fluidized bed plus Trombe wall system,” *Applied Energy*, vol. 38, no. 3, pp. 199–213, Jan. 1991, doi: 10.1016/0306-2619(91)90033-T.
[28] X. Qu and X. Zhao, “Previous and present investigations on the components, microstructure and main properties of autoclaved aerated concrete – A review,” *Construction and Building Materials*, vol. 135, pp. 505–516, Mar. 2017, doi: 10.1016/j.conbuildmat.2016.12.208.
[29] M. Jerman, M. Keppert, J. Výborný, and R. Černý, “Hygric, thermal and durability properties of autoclaved aerated concrete,” *Construction and Building Materials*, vol. 41, pp. 352–359, Apr. 2013, doi: 10.1016/j.conbuildmat.2012.12.036.
[30] Z. O. Pehlivanlı, İ. Uzun, Z. P. Yücel, and İ. Demir, “The effect of different fiber

reinforcement on the thermal and mechanical properties of autoclaved aerated concrete," *Construction and Building Materials*, vol. 112, pp. 325–330, Jun. 2016, doi: 10.1016/j.conbuildmat.2016.02.223.
[31] F. Kuznik and J. Virgone, "Experimental assessment of a phase change material for wall building use," *Applied Energy*, vol. 86, no. 10, pp. 2038–2046, Oct. 2009, doi: 10.1016/j.apenergy.2009.01.004.
[32] J. Xie, W. Wang, J. Liu, and S. Pan, "Thermal performance analysis of PCM wallboards for building application based on numerical simulation," *Solar Energy*, vol. 162, pp. 533–540, Mar. 2018, doi: 10.1016/j.solener.2018.01.069.
[33] E. Leang, P. Tittelein, L. Zalewski, and S. Lassue, "Numerical study of a composite Trombe solar wall integrating microencapsulated PCM," *Energy Procedia*, vol. 122, pp. 1009–1014, Sep. 2017, doi: 10.1016/j.egypro.2017.07.467.
[34] S. Barbosa and K. Ip, "Perspectives of double skin façades for naturally ventilated buildings: A review," *Renewable and Sustainable Energy Reviews*, vol. 40, pp. 1019–1029, Dec. 2014, doi: 10.1016/j.rser.2014.07.192.
[35] R. A. Agathokleous and S. A. Kalogirou, "Double skin facades (DSF) and building integrated photovoltaics (BIPV): A review of configurations and heat transfer characteristics," *Renewable Energy*, vol. 89, pp. 743–756, Apr. 2016, doi: 10.1016/j.renene.2015.12.043.
[36] H. Omrany, A. Ghaffarianhoseini, A. Ghaffarianhoseini, K. Raahemifar, and J. Tookey, "Application of passive wall systems for improving the energy efficiency in buildings: A comprehensive review," *Renewable and Sustainable Energy Reviews*, vol. 62, pp. 1252–1269, Sep. 2016, doi: 10.1016/j.rser.2016.04.010.
[37] E. Cuce and S. B. Riffat, "A state-of-the-art review on innovative glazing technologies," *Renewable and Sustainable Energy Reviews*, vol. 41, pp. 695–714, Jan. 2015, doi: 10.1016/j.rser.2014.08.084.
[38] M.-H. Lee and J.-S. Cho, "Better thermochromic glazing of windows with anti-reflection coating," *Thin Solid Films*, vol. 365, no. 1, pp. 5–6, Apr. 2000, doi: 10.1016/S0040-6090(99)01112-8.
[39] A. Jonsson and A. Roos, "Visual and energy performance of switchable windows with antireflection coatings," *Solar Energy*, vol. 84, no. 8, pp. 1370–1375, Aug. 2010, doi: 10.1016/j.solener.2010.04.016.
[40] M. Ferrara, A. Castaldo, S. Esposito, A. D'Angelo, A. Guglielmo, and A. Antonaia, "AlN–Ag based low-emission sputtered coatings for high visible transmittance window," *Surface and Coatings Technology*, vol. 295, pp. 2–7, Jun. 2016, doi: 10.1016/j.surfcoat.2015.12.015.
[41] M. Kamalisarvestani, R. Saidur, S. Mekhilef, and F. S. Javadi, "Performance, materials and coating technologies of thermochromic thin films on smart windows," *Renewable and Sustainable Energy Reviews*, vol. 26, pp. 353–364, Oct. 2013, doi: 10.1016/j.rser.2013.05.038.
[42] R. Vergaz, J.-M. Sánchez-Pena, D. Barrios, C. Vázquez, and P. Contreras-Lallana, "Modelling and electro-optical testing of suspended particle devices," *Solar Energy Materials and Solar Cells*, vol. 92, no. 11, pp. 1483–1487, Nov. 2008, doi: 10.1016/j.solmat.2008.06.018.
[43] A. Ghosh, B. Norton, and A. Duffy, "Measured overall heat transfer coefficient of a suspended particle device switchable glazing," *Applied Energy*, vol. 159, pp. 362–369, Dec.

2015, doi: 10.1016/j.apenergy.2015.09.019.
[44] A. Ghosh, B. Norton, and A. Duffy, “Measured thermal performance of a combined suspended particle switchable device evacuated glazing,” *Applied Energy*, vol. 169, pp. 469–480, May 2016, doi: 10.1016/j.apenergy.2016.02.031.
[45] P. H. Shaikh, N. B. M. Nor, P. Nallagownden, I. Elamvazuthi, and T. Ibrahim, “A review on optimized control systems for building energy and comfort management of smart sustainable buildings,” *Renewable and Sustainable Energy Reviews*, vol. 34, pp. 409–429, Jun. 2014, doi: 10.1016/j.rser.2014.03.027.
[46] D. L. Marino, K. Amarasinghe, and M. Manic, “Building energy load forecasting using Deep Neural Networks,” in *IECON 2016 - 42nd Annual Conference of the IEEE Industrial Electronics Society*, 2016, pp. 7046–7051, doi: 10.1109/IECON.2016.7793413.
[47] L. Wang, E. W. M. Lee, and R. K. K. Yuen, “Novel dynamic forecasting model for building cooling loads combining an artificial neural network and an ensemble approach,” *Applied Energy*, vol. 228, pp. 1740–1753, Oct. 2018, doi: 10.1016/j.apenergy.2018.07.085.
[48] M. Q. Raza and A. Khosravi, “A review on artificial intelligence based load demand forecasting techniques for smart grid and buildings,” *Renewable and Sustainable Energy Reviews*, vol. 50, pp. 1352–1372, Oct. 2015, doi: 10.1016/j.rser.2015.04.065.
[49] Z. Chen, C. Jiang, and L. Xie, “Building occupancy estimation and detection: A review,” *Energy and Buildings*, vol. 169, pp. 260–270, Jun. 2018, doi: 10.1016/j.enbuild.2018.03.084.
[50] A. H. Kazmi, M. J. O’grady, D. T. Delaney, A. G. Ruzzelli, and G. M. P. O’hare, “A Review of Wireless-Sensor-Network-Enabled Building Energy Management Systems,” *ACM Trans. Sen. Netw.*, vol. 10, no. 4, pp. 66:1–66:43, Jun. 2014, doi: 10.1145/2532644.
[51] F. K. Shaikh and S. Zeadally, “Energy harvesting in wireless sensor networks: A comprehensive review,” *Renewable and Sustainable Energy Reviews*, vol. 55, pp. 1041–1054, 2016, doi: 10.1016/j.rser.2015.11.010.
[52] V. Devabhaktuni, M. Alam, S. Shekara Sreenadh Reddy Depuru, R. C. Green, D. Nims, and C. Near, “Solar energy: Trends and enabling technologies,” *Renewable and Sustainable Energy Reviews*, vol. 19, pp. 555–564, Mar. 2013, doi: 10.1016/j.rser.2012.11.024.
[53] H. M. Yin, D. J. Yang, G. Kelly, and J. Garant, “Design and performance of a novel building integrated PV/thermal system for energy efficiency of buildings,” *Solar Energy*, vol. 87, pp. 184–195, Jan. 2013, doi: 10.1016/j.solener.2012.10.022.
[54] A. K. Shukla, K. Sudhakar, and P. Baredar, “A comprehensive review on design of building integrated photovoltaic system,” *Energy and Buildings*, vol. 128, pp. 99–110, Sep. 2016, doi: 10.1016/j.enbuild.2016.06.077.
[55] J. Chen, Q. Qiu, Y. Han, and D. Lau, “Piezoelectric materials for sustainable building structures: Fundamentals and applications,” *Renewable and Sustainable Energy Reviews*, vol. 101, pp. 14–25, Mar. 2019, doi: 10.1016/j.rser.2018.09.038.
[56] X. Li and V. Strezov, “Modelling piezoelectric energy harvesting potential in an educational building,” *Energy Conversion and Management*, vol. 85, pp. 435–442, Sep. 2014, doi: 10.1016/j.enconman.2014.05.096.
[57] L. Zuo and X. Tang, “Large-scale vibration energy harvesting,” *Journal of Intelligent Material Systems and Structures*, vol. 24, no. 11, pp. 1405–1430, Jul. 2013, doi: 10.1177/1045389X13486707.
[58] O. H. Ando Junior, A. L. O. Maran, and N. C. Henao, “A review of the development and applications of thermoelectric microgenerators for energy harvesting,” *Renewable and*

Sustainable Energy Reviews, vol. 91, pp. 376–393, Aug. 2018, doi: 10.1016/j.rser.2018.03.052.

[59] W. Wang, V. Cionca, N. Wang, M. Hayes, B. O'Flynn, and C. O'Mathuna, "Thermoelectric Energy Harvesting for Building Energy Management Wireless Sensor Networks," *International Journal of Distributed Sensor Networks*, vol. 9, Jun. 2013, doi: 10.1155/2013/232438.

[60] M. Guan, K. Wang, D. Xu, and W.-H. Liao, "Design and experimental investigation of a low-voltage thermoelectric energy harvesting system for wireless sensor nodes," *Energy Conversion and Management*, vol. 138, pp. 30–37, Apr. 2017, doi: 10.1016/j.enconman.2017.01.049.

[61] Y.-H. Lin, K.-T. Tsai, M.-D. Lin, and M.-D. Yang, "Design optimization of office building envelope configurations for energy conservation," *Applied Energy*, vol. 171, pp. 336–346, Jun. 2016, doi: 10.1016/j.apenergy.2016.03.018.

[62] A. Emamian, S. F. Corbin, and A. Khajepour, "In-Situ Deposition of Metal Matrix Composite in Fe-Ti-C System Using Laser Cladding Process," 2011.

[63] J. M. P. Q. Delgado, Ed., *Industrial and Technological Applications of Transport in Porous Materials*. Berlin Heidelberg: Springer-Verlag, 2013.

[64] W. D. Callister and D. G. Rethwisch, *Materials Science and Engineering: An Introduction*, 10th Edition. WILLEY, 2018.

[65] Y. Yang, R. Boom, B. Irion, D.-J. van Heerden, P. Kuiper, and H. de Wit, "Recycling of composite materials," *Chemical Engineering and Processing: Process Intensification*, vol. 51, pp. 53–68, Jan. 2012, doi: 10.1016/j.cep.2011.09.007.

[66] Manalo Allan, Aravinthan Thiru, Fam Amir, and Benmokrane Brahim, "State-of-the-Art Review on FRP Sandwich Systems for Lightweight Civil Infrastructure," *Journal of Composites for Construction*, vol. 21, no. 1, p. 04016068, Feb. 2017, doi: 10.1061/(ASCE)CC.1943-5614.0000729.

[67] S. M. Bida, F. N. A. A. Aziz, M. S. Jaafar, F. Hejazi, and A. B. Nabilah, "Advances in Precast Concrete Sandwich Panels toward Energy Efficient Structural Buildings," Oct. 2018, doi: 10.20944/preprints201810.0147.v1.

[68] A. Kan and J. Hu, "Thermal performance evaluation on vacuum insulation panels in composite building envelope under large temperature variations," *Int J Low-Carbon Tech*, vol. 12, no. 1, pp. 51–53, Mar. 2017, doi: 10.1093/ijlct/ctv026.

[69] F. Qian, "Insulation and Energy-Saving Technology for the External Wall of Residential Building," *Advanced Materials Research*, 2015. https://www.scientific.net/AMR.1073-1076.1263 (accessed Oct. 29, 2019).

[70] T. D. Ngo, Q. T. Nguyen, and P. Tran, "Heat release and flame propagation in prefabricated modular unit with GFRP composite facades," *Build. Simul.*, vol. 9, no. 5, pp. 607–616, Oct. 2016, doi: 10.1007/s12273-016-0294-3.

[71] M. Smolka, V. Mózer, and P. Tofiło, "FIRE PERFORMANCE OF COMPOSITE-PANEL SEPARATION WALLS," *Applications of Structural Fire Engineering*, vol. 0, no. 0, Jan. 2016, doi: 10.14311/asfe.2015.062.

[72] R. Hay and C. P. Ostertag, "Life cycle assessment (LCA) of double-skin façade (DSF) system with fiber-reinforced concrete for sustainable and energy-efficient buildings in the tropics," *Building and Environment*, vol. 142, pp. 327–341, Sep. 2018, doi: 10.1016/j.buildenv.2018.06.024.

[73] B. Abediniangerabi, S. M. Shahandashti, B. Bell, S.-H. Chao, and A. Makhmalbaf, "Building energy performance analysis of ultra-high-performance fiber-reinforced concrete (UHP-FRC) façade systems," *Energy and Buildings*, vol. 174, pp. 262–275, Sep. 2018, doi: 10.1016/j.enbuild.2018.06.027.
[74] Nobili Andrea and Falope Federico O., "Impregnated Carbon Fabric–Reinforced Cementitious Matrix Composite for Rehabilitation of the Finale Emilia Hospital Roofs: Case Study," *Journal of Composites for Construction*, vol. 21, no. 4, p. 05017001, Aug. 2017, doi: 10.1061/(ASCE)CC.1943-5614.0000780.
[75] I. A. Ibrahim, F. A. Mohamed, and E. J. Lavernia, "Particulate reinforced metal matrix composites — a review," *J Mater Sci*, vol. 26, no. 5, pp. 1137–1156, Jan. 1991, doi: 10.1007/BF00544448.
[76] S. Ahmed and F. R. Jones, "A review of particulate reinforcement theories for polymer composites," *J Mater Sci*, vol. 25, no. 12, pp. 4933–4942, Dec. 1990, doi: 10.1007/BF00580110.
[77] M. C. Limbachiya and H. Y. Kew, *Excellence in Concrete Construction through Innovation: Proceedings of the conference held at the Kingston University, United Kingdom, 9 - 10 September 2008*. CRC Press, 2008.
[78] C. Calleri *et al.*, "Characterization of the sound insulation properties of a two-layers lightweight concrete innovative façade," *Applied Acoustics*, vol. 145, pp. 267–277, Feb. 2019, doi: 10.1016/j.apacoust.2018.10.003.
[79] H. S. Wilson and V. M. Malhotra, "Development of high strength lightweight concrete for structural applications," *International Journal of Cement Composites and Lightweight Concrete*, vol. 10, no. 2, pp. 79–90, May 1988, doi: 10.1016/0262-5075(88)90034-6.
[80] G. Song, L. Wang, L. Deng, and H. M. Yin, "Mechanical characterization and inclusion based boundary element modeling of lightweight concrete containing foam particles," *Mechanics of Materials*, vol. 91, pp. 208–225, Dec. 2015, doi: 10.1016/j.mechmat.2015.07.014.
[81] M. Naebe and K. Shirvanimoghaddam, "Functionally graded materials: a review of fabrication and properties," *Applied Materials Today*, vol. 5, pp. 223–245, 2016.
[82] A. Kawasaki and R. Watanabe, "Concept and P/M fabrication of functionally gradient materials," *Ceramics International*, vol. 23, no. 1, pp. 73–83, Jan. 1997, doi: 10.1016/0272-8842(95)00143-3.
[83] M. Koizumi, "FGM activities in Japan," *Composites B: Eng*, vol. 28, no. 1–2, pp. 1–4, 1997.
[84] H. Abramovich, *Stability and Vibrations of Thin-Walled Composite Structures*, 1 edition. Duxford ; Cambridge, MA: Woodhead Publishing, 2017.
[85] D. K. Jha, T. Kant, and R. K. Singh, "A critical review of recent research on functionally graded plates," *Composite Structures*, vol. 96, pp. 833–849, Feb. 2013, doi: 10.1016/j.compstruct.2012.09.001.
[86] S. Kumar, K. V. V. S. Murthy Reddy, A. Kumar, and G. Rohini Devi, "Development and characterization of polymer–ceramic continuous fiber reinforced functionally graded composites for aerospace application," *Aerospace Science and Technology*, vol. 26, no. 1, pp. 185–191, Apr. 2013, doi: 10.1016/j.ast.2012.04.002.
[87] C.-Y. Lee and J.-H. Kim, "Evaluation of homogenized effective properties for FGM panels in aero-thermal environments," *Composite Structures*, vol. 120, pp. 442–450, Feb. 2015, doi: 10.1016/j.compstruct.2014.10.017.

[88] J. Reinoso, M. Paggi, and R. Rolfes, "A computational framework for the interplay between delamination and wrinkling in functionally graded thermal barrier coatings," *Computational Materials Science*, vol. 116, pp. 82–95, Apr. 2016, doi: 10.1016/j.commatsci.2015.08.031.
[89] F. Kirbiyik, M. G. Gok, and G. Goller, "Microstructural, mechanical and thermal properties of Al2O3/CYSZ functionally graded thermal barrier coatings," *Surface and Coatings Technology*, vol. 329, pp. 193–201, Nov. 2017, doi: 10.1016/j.surfcoat.2017.08.025.
[90] P. Sharma, "Basics of FGM and FGPM," in *Vibration Analysis of Functionally Graded Piezoelectric Actuators*, P. Sharma, Ed. Singapore: Springer Singapore, 2019, pp. 11–17.
[91] F. Ebrahimi and E. Salari, "Size-dependent thermo-electrical buckling analysis of functionally graded piezoelectric nanobeams," *Smart Mater. Struct.*, vol. 24, no. 12, p. 125007, Oct. 2015, doi: 10.1088/0964-1726/24/12/125007.
[92] M. Saadatfar and M. Aghaie-Khafri, "Thermoelastic analysis of a rotating functionally graded cylindrical shell with functionally graded sensor and actuator layers on an elastic foundation placed in a constant magnetic field," *Journal of Intelligent Material Systems and Structures*, vol. 27, no. 4, pp. 512–527, Mar. 2016, doi: 10.1177/1045389X15573342.
[93] E. Müller, Č. Drašar, J. Schilz, and W. A. Kaysser, "Functionally graded materials for sensor and energy applications," *Materials Science and Engineering: A*, vol. 362, no. 1, pp. 17–39, Dec. 2003, doi: 10.1016/S0921-5093(03)00581-1.
[94] Y. Zhang *et al.*, "Reducing the Charge Carrier Transport Barrier in Functionally Layer-Graded Electrodes," *Angewandte Chemie International Edition*, vol. 56, no. 47, pp. 14847–14852, 2017, doi: 10.1002/anie.201707883.
[95] D. Maurya *et al.*, "Functionally Graded Interfaces: Role and Origin of Internal Electric Field and Modulated Electrical Response," *ACS Appl. Mater. Interfaces*, vol. 7, no. 40, pp. 22458–22468, Oct. 2015, doi: 10.1021/acsami.5b06544.
[96] H. M. Yin, L. Z. Sun, and G. H. Paulino, "Micromechanics-based elastic model for functionally graded materials with particle interactions," *Acta Materialia*, vol. 52, no. 12, pp. 3535–3543, Jul. 2004, doi: 10.1016/j.actamat.2004.04.007.
[97] V. Kumar and K. Balasubramanian, "Progress update on failure mechanisms of advanced thermal barrier coatings: A review," *Progress in Organic Coatings*, vol. 90, pp. 54–82, Jan. 2016, doi: 10.1016/j.porgcoat.2015.09.019.
[98] F. Chen and H. Yin, "Fabrication and laboratory-based performance testing of a building-integrated photovoltaic-thermal roofing panel," *Applied Energy*, vol. 177, pp. 271–284, 2016, doi: 10.1016/j.apenergy.2016.05.112.
[99] F. L. Chen, X. He, and H. M. Yin, "Manufacture and multi-physical characterization of aluminum/high-density polyethylene functionally graded materials for green energy building envelope applications," *Energy and Buildings*, doi: 10.1016/j.enbuild.2015.11.001.
[100] C. R. Bowen, J. Taylor, E. LeBoulbar, D. Zabek, A. Chauhan, and R. Vaish, "Pyroelectric materials and devices for energy harvesting applications," *Energy Environ. Sci.*, vol. 7, no. 12, pp. 3836–3856, Nov. 2014, doi: 10.1039/C4EE01759E.
[101] F. Suarez, A. Nozariasbmarz, D. Vashaee, and M. C. Öztürk, "Designing thermoelectric generators for self-powered wearable electronics," *Energy Environ. Sci.*, vol. 9, no. 6, pp. 2099–2113, Jun. 2016, doi: 10.1039/C6EE00456C.
[102] M. Thielen, L. Sigrist, M. Magno, C. Hierold, and L. Benini, "Human body heat for powering wearable devices: From thermal energy to application," *Energy Conversion and Management*, vol. 131, pp. 44–54, Jan. 2017, doi: 10.1016/j.enconman.2016.11.005.

[103] J. M. Donelan, Q. Li, V. Naing, J. A. Hoffer, D. J. Weber, and A. D. Kuo, "Biomechanical Energy Harvesting: Generating Electricity During Walking with Minimal User Effort," *Science*, vol. 319, no. 5864, pp. 807–810, Feb. 2008, doi: 10.1126/science.1149860.
[104] F. Invernizzi, S. Dulio, M. Patrini, G. Guizzetti, and P. Mustarelli, "Energy harvesting from human motion: materials and techniques," *Chem. Soc. Rev.*, vol. 45, no. 20, pp. 5455–5473, Oct. 2016, doi: 10.1039/C5CS00812C.
[105] M. Geisler *et al.*, "Human-motion energy harvester for autonomous body area sensors," *Smart Mater. Struct.*, vol. 26, no. 3, p. 035028, Feb. 2017, doi: 10.1088/1361-665X/aa548a.
[106] R. Rantz *et al.*, "Architectures for wrist-worn energy harvesting," *Smart Mater. Struct.*, vol. 27, no. 4, p. 044001, Mar. 2018, doi: 10.1088/1361-665X/aa94d6.
[107] F. Qian, T.-B. Xu, and L. Zuo, "Piezoelectric energy harvesting from human walking using a two-stage amplification mechanism," *Energy*, vol. 189, p. 116140, Dec. 2019, doi: 10.1016/j.energy.2019.116140.
[108] Y. Yuan and L. Zuo, "Dynamics of energy harvesting backpack with human being interaction," in *Active and Passive Smart Structures and Integrated Systems 2016*, 2016, vol. 9799, p. 97991K, doi: 10.1117/12.2219308.
[109] R. Yang, Y. Qin, C. Li, G. Zhu, and Z. L. Wang, "Converting Biomechanical Energy into Electricity by a Muscle-Movement-Driven Nanogenerator," *Nano Lett.*, vol. 9, no. 3, pp. 1201–1205, Mar. 2009, doi: 10.1021/nl803904b.
[110] Z. Li, G. Zhu, R. Yang, A. C. Wang, and Z. L. Wang, "Muscle-Driven In Vivo Nanogenerator," *Advanced Materials*, vol. 22, no. 23, pp. 2534–2537, 2010, doi: 10.1002/adma.200904355.
[111] Y. Pan *et al.*, "Modeling and field-test of a compact electromagnetic energy harvester for railroad transportation," *Applied Energy*, vol. 247, pp. 309–321, Aug. 2019, doi: 10.1016/j.apenergy.2019.03.051.
[112] H.-J. Jung, I.-H. Kim, and S.-J. Jang, "An energy harvesting system using the wind-induced vibration of a stay cable for powering a wireless sensor node," *Smart Mater. Struct.*, vol. 20, no. 7, p. 075001, May 2011, doi: 10.1088/0964-1726/20/7/075001.
[113] P. A. Østergaard and H. Lund, "A renewable energy system in Frederikshavn using low-temperature geothermal energy for district heating," *Applied Energy*, vol. 88, no. 2, pp. 479–487, Feb. 2011, doi: 10.1016/j.apenergy.2010.03.018.
[114] J. W. Matiko, N. J. Grabham, S. P. Beeby, and M. J. Tudor, "Review of the application of energy harvesting in buildings," *Meas. Sci. Technol.*, vol. 25, no. 1, p. 012002, Nov. 2013, doi: 10.1088/0957-0233/25/1/012002.
[115] B. P. Jelle, "Building Integrated Photovoltaics: A Concise Description of the Current State of the Art and Possible Research Pathways," *Energies*, vol. 9, no. 1, p. 21, Jan. 2016, doi: 10.3390/en9010021.
[116] S. Hassanli, G. Hu, K. C. S. Kwok, and D. F. Fletcher, "Utilizing cavity flow within double skin façade for wind energy harvesting in buildings," *Journal of Wind Engineering and Industrial Aerodynamics*, vol. 167, pp. 114–127, Aug. 2017, doi: 10.1016/j.jweia.2017.04.019.
[117] N. Pundhir, G. Arora, H. Pathak, and S. Zafar, "Ballistic Impact Response of HDPE/UHMWPE Polymer Composite," in *Advances in Mechanical Engineering*, Singapore, 2020, pp. 245–255, doi: 10.1007/978-981-15-0124-1_23.
[118] H. Louche, F. Piette-Coudol, R. Arrieux, and J. Issartel, "An experimental and modeling

study of the thermomechanical behavior of an ABS polymer structural component during an impact test," *International Journal of Impact Engineering*, vol. 36, no. 6, pp. 847–861, Jun. 2009, doi: 10.1016/j.ijimpeng.2008.09.007.

[119] J. A. Clarke, J. W. Hand, C. M. Johnstone, N. Kelly, and P. A. Strachan, "Photovoltaic-integrated building facades," *Renewable Energy*, vol. 8, no. 1, pp. 475–479, May 1996, doi: 10.1016/0960-1481(96)88902-6.

[120] S. J. Hayter and R. L. Martin, "Photovoltaics for Buildings Cutting-Edge PV," *UPVG Utility PV Experience (UPEx)'98, San Diego, CA (US), 09/28/1998--09/30/1998; Other Information: Supercedes report DE00012167; PBD: 5 Nov 1998*, 05-Nov-1998. https://digital.library.unt.edu/ark:/67531/metadc627444/ (accessed May 18, 2019).

[121] Y. Tripanagnostopoulos, Th. Nousia, M. Souliotis, and P. Yianoulis, "Hybrid photovoltaic/thermal solar systems," *Solar Energy*, vol. 72, no. 3, pp. 217–234, Mar. 2002, doi: 10.1016/S0038-092X(01)00096-2.

[122] T. T. Chow, J. W. Hand, and P. A. Strachan, "Building-integrated photovoltaic and thermal applications in a subtropical hotel building," *Applied Thermal Engineering*, vol. 23, no. 16, pp. 2035–2049, Nov. 2003, doi: 10.1016/S1359-4311(03)00183-2.

[123] L. Mei, D. Infield, U. Eicker, and V. Fux, "Thermal modelling of a building with an integrated ventilated PV façade," *Energy and Buildings*, vol. 35, no. 6, pp. 605–617, Jul. 2003, doi: 10.1016/S0378-7788(02)00168-8.

[124] S. Pantic, L. Candanedo, and A. K. Athienitis, "Modeling of energy performance of a house with three configurations of building-integrated photovoltaic/thermal systems," *Energy and Buildings*, vol. 42, no. 10, pp. 1779–1789, Oct. 2010, doi: 10.1016/j.enbuild.2010.05.014.

[125] A. Ibrahim, A. Fudholi, K. Sopian, M. Y. Othman, and M. H. Ruslan, "Efficiencies and improvement potential of building integrated photovoltaic thermal (BIPVT) system," *Energy Conversion and Management*, vol. 77, pp. 527–534, Jan. 2014, doi: 10.1016/j.enconman.2013.10.033.

[126] M. A. Green *et al.*, "Solar cell efficiency tables (version 50)," *Progress in Photovoltaics: Research and Applications*, vol. 25, no. 7, pp. 668–676, 2017, doi: 10.1002/pip.2909.

[127] Y. Chen, A. K. Athienitis, and K. Galal, "Modeling, design and thermal performance of a BIPV/T system thermally coupled with a ventilated concrete slab in a low energy solar house: Part 1, BIPV/T system and house energy concept," *Solar Energy*, vol. 84, no. 11, pp. 1892–1907, Nov. 2010, doi: 10.1016/j.solener.2010.06.013.

[128] K. Nagano, T. Mochida, K. Shimakura, K. Murashita, and S. Takeda, "Development of thermal-photovoltaic hybrid exterior wallboards incorporating PV cells in and their winter performances," *Solar Energy Materials and Solar Cells*, vol. 77, no. 3, pp. 265–282, May 2003, doi: 10.1016/S0927-0248(02)00348-3.

[129] O. Zogou and H. Stapountzis, "Energy analysis of an improved concept of integrated PV panels in an office building in central Greece," *Applied Energy*, vol. 88, no. 3, pp. 853–866, Mar. 2011, doi: 10.1016/j.apenergy.2010.08.023.

[130] B. Kundakci Koyunbaba and Z. Yilmaz, "The comparison of Trombe wall systems with single glass, double glass and PV panels," *Renewable Energy*, vol. 45, pp. 111–118, Sep. 2012, doi: 10.1016/j.renene.2012.02.026.

[131] S. Xu, W. Liao, J. Huang, and J. Kang, "Optimal PV cell coverage ratio for semi-transparent photovoltaics on office building façades in central China," *Energy and Buildings*, vol. 77, pp. 130–138, Jul. 2014, doi: 10.1016/j.enbuild.2014.03.052.

[132] L. Gaillard, S. Giroux-Julien, C. Ménézo, and H. Pabiou, “Experimental evaluation of a naturally ventilated PV double-skin building envelope in real operating conditions,” *Solar Energy*, vol. 103, pp. 223–241, May 2014, doi: 10.1016/j.solener.2014.02.018.
[133] T. N. Anderson, M. Duke, J. K. Carson, R. Künnemeyer, and B. Smith, “The development of a novel large area building integrated solar collector for pool heating,” in *48th Annual Conference of the Australian Solar Energy Society*, 2010, Accessed: 09-Nov-2019. [Online]. Available: https://researchcommons.waikato.ac.nz/handle/10289/4926.
[134] A. Buonomano, F. Calise, A. Palombo, and M. Vicidomini, “BIPVT systems for residential applications: An energy and economic analysis for European climates,” *Applied Energy*, vol. 184, pp. 1411–1431, Dec. 2016, doi: 10.1016/j.apenergy.2016.02.145.
[135] J.-H. Kim, S.-H. Park, J.-G. Kang, and J.-T. Kim, “Experimental Performance of Heating System with Building-integrated PVT (BIPVT) Collector,” *Energy Procedia*, vol. 48, pp. 1374–1384, Jan. 2014, doi: 10.1016/j.egypro.2014.02.155.
[136] M. J. Huang, P. C. Eames, B. Norton, and N. J. Hewitt, “Natural convection in an internally finned phase change material heat sink for the thermal management of photovoltaics,” *Solar Energy Materials and Solar Cells*, vol. 95, no. 7, pp. 1598–1603, Jul. 2011, doi: 10.1016/j.solmat.2011.01.008.
[137] M. Jun Huang, “The effect of using two PCMs on the thermal regulation performance of BIPV systems,” *Solar Energy Materials and Solar Cells*, vol. 95, no. 3, pp. 957–963, Mar. 2011, doi: 10.1016/j.solmat.2010.11.032.
[138] M. A. Kibria, R. Saidur, F. A. Al-Sulaiman, and M. M. A. Aziz, “Development of a thermal model for a hybrid photovoltaic module and phase change materials storage integrated in buildings,” *Solar Energy*, vol. 124, pp. 114–123, Feb. 2016, doi: 10.1016/j.solener.2015.11.027.
[139] S. Sharma, A. Tahir, K. S. Reddy, and T. K. Mallick, “Performance enhancement of a Building-Integrated Concentrating Photovoltaic system using phase change material,” *Solar Energy Materials and Solar Cells*, vol. 149, pp. 29–39, May 2016, doi: 10.1016/j.solmat.2015.12.035.
[140] M. J. Huang, P. C. Eames, and B. Norton, “Thermal regulation of building-integrated photovoltaics using phase change materials,” *International Journal of Heat and Mass Transfer*, vol. 47, no. 12, pp. 2715–2733, Jun. 2004, doi: 10.1016/j.ijheatmasstransfer.2003.11.015.
[141] F. L. Chen and H. M. Yin, “Fabrication and laboratory-based performance testing of a building-integrated photovoltaic-thermal roofing panel,” *Applied Energy*, vol. Under review.
[142] F. L. Chen, X. He, and H. M. Yin, “Manufacture and multi-physical characterization of aluminum/high-density polyethylene functionally graded materials for green energy building envelope applications,” *Energy and Buildings*, vol. 116, pp. 307–317, 2016.
[143] R. Seltzer, A. P. Cisilino, P. M. Frontini, and Y.-W. Mai, “Determination of the Drucker–Prager parameters of polymers exhibiting pressure-sensitive plastic behaviour by depth-sensing indentation,” *International Journal of Mechanical Sciences*, vol. 53, no. 6, pp. 471–478, Jun. 2011, doi: 10.1016/j.ijmecsci.2011.04.002.
[144] S. M. Kurtz, L. Pruitt, C. W. Jewett, R. P. Crawford, D. J. Crane, and A. A. Edidin, “The yielding, plastic flow, and fracture behavior of ultra-high molecular weight polyethylene used in total joint replacements,” *Biomaterials*, vol. 19, no. 21, pp. 1989–2003, Nov. 1998.
[145] J. S. Bergström, S. M. Kurtz, C. M. Rimnac, and A. A. Edidin, “Constitutive modeling of

ultra-high molecular weight polyethylene under large-deformation and cyclic loading conditions," *Biomaterials*, vol. 23, no. 11, pp. 2329–2343, Jun. 2002, doi: 10.1016/S0142-9612(01)00367-2.
[146] J. W. Ju and L. Z. Sun, "Effective elastoplastic behavior of metal matrix composites containing randomly located aligned spheroidal inhomogeneities. Part I: micromechanics-based formulation," *International Journal of Solids and Structures*, vol. 38, no. 2, pp. 183–201, Jan. 2001, doi: 10.1016/S0020-7683(00)00023-8.
[147] L. R. Alejano and A. Bobet, "Drucker–Prager Criterion," in *The ISRM Suggested Methods for Rock Characterization, Testing and Monitoring: 2007-2014*, R. Ulusay, Ed. Cham: Springer International Publishing, 2015, pp. 247–252.
[148] Y. Wang and Z. Huang, "A Review of Analytical Micromechanics Models on Composite Elastoplastic Behaviour," *Procedia Engineering*, vol. 173, pp. 1283–1290, Jan. 2017, doi: 10.1016/j.proeng.2016.12.159.
[149] G. P. Tandon and G. J. Weng, "A Theory of Particle-Reinforced Plasticity," *J. Appl. Mech*, vol. 55, no. 1, pp. 126–135, Mar. 1988, doi: 10.1115/1.3173618.
[150] J. R. Zuiker, "Functionally graded materials: choice of micromechanics model and limitations in property variation," *Composites Engineering*, vol. 5, no. 7, pp. 807–819, 1995.
[151] T. Mori and K. Tanaka, "Average stress in matrix and average elastic energy of materials with misfitting inclusions," *Acta metallurgica*, vol. 21, no. 5, pp. 571–574, 1973.
[152] R. Hill, "Continuum micro-mechanics of elastoplastic polycrystals," *Journal of the Mechanics and Physics of Solids*, vol. 13, no. 2, pp. 89–101, 1965.
[153] I. Tamura, "Strength and ductility of Fe-Ni-C alloys composed of austenite and martensite with various strength," in *Proceedings of the third international conference on strength of metals and alloys, 1973*, 1973, vol. 1, pp. 611–615.
[154] T. Reiter, G. J. Dvorak, and V. Tvergaard, "Micromechanical models for graded composite materials," *Journal of the Mechanics and Physics of Solids*, vol. 45, no. 8, pp. 1281–1302, 1997.
[155] T. Reiter and G. J. Dvorak, "Micromechanical models for graded composite materials: II. Thermomechanical loading," *Journal of the Mechanics and Physics of Solids*, vol. 46, no. 9, pp. 1655–1673, 1998.
[156] J. Aboudi, M.-J. Pindera, and S. M. Arnold, "Higher-order theory for periodic multiphase materials with inelastic phases," *International Journal of Plasticity*, vol. 19, no. 6, pp. 805–847, 2003.
[157] S. Nemat-Nasser and M. Hori, *Micromechanics: overall properties of heterogeneous materials*, vol. 37. Elsevier, 2013.
[158] H. Nguyen-Xuan, L. V. Tran, T. Nguyen-Thoi, and H. C. Vu-Do, "Analysis of functionally graded plates using an edge-based smoothed finite element method," *Composite Structures*, vol. 93, no. 11, pp. 3019–3039, 2011.
[159] J. P. Pascon and H. B. Coda, "Large deformation analysis of functionally graded elastoplastic materials via solid tetrahedral finite elements," *Computers & Structures*, vol. 146, pp. 59–75, 2015.
[160] P. Vena, D. Gastaldi, and R. Contro, "Determination of the effective elastic–plastic response of metal–ceramic composites," *International Journal of Plasticity*, vol. 24, no. 3, pp. 483–508, 2008.
[161] P. Barai and G. J. Weng, "A theory of plasticity for carbon nanotube reinforced composites,"

International Journal of Plasticity, vol. 27, no. 4, pp. 539–559, Apr. 2011.
[162] R. Aghababaei and S. P. Joshi, "Grain size–inclusion size interaction in metal matrix composites using mechanism-based gradient crystal plasticity," *International Journal of Solids and Structures*, vol. 48, no. 18, pp. 2585–2594, 2011.
[163] R. Ortwein, B. Skoczeń, and J. P. Tock, "Micromechanics based constitutive modeling of martensitic transformation in metastable materials subjected to torsion at cryogenic temperatures," *International Journal of Plasticity*, vol. 59, pp. 152–179, 2014.
[164] M. Amirpour, R. Das, and S. Bickerton, "An elasto-plastic damage model for functionally graded plates with in-plane material properties variation: Material model and numerical implementation," *Composite Structures*, vol. 163, pp. 331–341, 2017.
[165] J. Li and G. J. Weng, "A secant-viscosity composite model for the strain-rate sensitivity of nanocrystalline materials," *International Journal of Plasticity*, vol. 23, no. 12, pp. 2115–2133, Dec. 2007, doi: 10.1016/j.ijplas.2007.03.016.
[166] S.-B. Lee, R. A. Lebensohn, and A. D. Rollett, "Modeling the viscoplastic micromechanical response of two-phase materials using Fast Fourier Transforms," *International Journal of Plasticity*, vol. 27, no. 5, pp. 707–727, May 2011.
[167] Y. Chen and S. Ghosh, "Micromechanical analysis of strain rate-dependent deformation and failure in composite microstructures under dynamic loading conditions," *International Journal of Plasticity*, vol. 32–33, pp. 218–247, May 2012.
[168] L. Brassart, L. Stainier, I. Doghri, and L. Delannay, "Homogenization of elasto-(visco) plastic composites based on an incremental variational principle," *International Journal of Plasticity*, vol. 36, pp. 86–112, 2012.
[169] J. Segurado, R. A. Lebensohn, J. LLorca, and C. N. Tomé, "Multiscale modeling of plasticity based on embedding the viscoplastic self-consistent formulation in implicit finite elements," *International Journal of Plasticity*, vol. 28, no. 1, pp. 124–140, 2012.
[170] N. Lahellec and P. Suquet, "Effective response and field statistics in elasto-plastic and elasto-viscoplastic composites under radial and non-radial loadings," *International Journal of Plasticity*, vol. 42, pp. 1–30, 2013.
[171] V. Birman and L. W. Byrd, "Modeling and analysis of functionally graded materials and structures," *Applied mechanics reviews*, vol. 60, no. 5, pp. 195–216, 2007.
[172] H. Yin and Y. Zhao, *Introduction to the Micromechanics of Composite Materials*. CRC Press, 2016.
[173] J. D. Eshelby, "The determination of the elastic field of an ellipsoidal inclusion, and related problems," *Proc. R. Soc. Lond. A*, vol. 241, no. 1226, pp. 376–396, 1957.
[174] J. D. Eshelby, "The elastic field outside an ellipsoidal inclusion," *Proc. R. Soc. Lond. A*, vol. 252, no. 1271, pp. 561–569, 1959.
[175] Z. A. Moschovidis and T. Mura, "Two-ellipsoidal inhomogeneities by the equivalent inclusion method," *Journal of Applied Mechanics*, vol. 42, no. 4, pp. 847–852, 1975.
[176] J. W. Ju and T. M. Chen, "Micromechanics and effective moduli of elastic composites containing randomly dispersed ellipsoidal inhomogeneities," *Acta Mechanica*, vol. 103, no. 1–4, pp. 103–121, 1994.
[177] J. W. Ju and T. M. Chen, "Effective elastic moduli of two-phase composites containing randomly dispersed spherical inhomogeneities," *Acta Mechanica*, vol. 103, no. 1–4, pp. 123–144, 1994.
[178] J. W. Ju and T.-M. Chen, "Micromechanics and effective elastoplastic behavior of two-phase

metal matrix composites," *Journal of engineering materials and technology*, vol. 116, no. 3, pp. 310–318, 1994.
[179] J. W. Ju and K. H. Tseng, "Effective elastoplastic behavior of two-phase ductile matrix composites: a micromechanical framework," *International Journal of Solids and Structures*, vol. 33, no. 29, pp. 4267–4291, 1996.
[180] J. W. Ju and K. H. Tseng, "Effective elastoplastic algorithms for ductile matrix composites," *Journal of engineering mechanics*, vol. 123, no. 3, pp. 260–266, 1997.
[181] J. W. Ju and L. Z. Sun, "Effective elastoplastic behavior of metal matrix composites containing randomly located aligned spheroidal inhomogeneities. Part I: micromechanics-based formulation," *International Journal of Solids and Structures*, vol. 38, no. 2, pp. 183–201, 2001.
[182] L. Z. Sun and J. W. Ju, "Effective elastoplastic behavior of metal matrix composites containing randomly located aligned spheroidal inhomogeneities. Part II: applications," *International Journal of Solids and Structures*, vol. 38, no. 2, pp. 203–225, 2001.
[183] L. Z. Sun and J. W. Ju, "Elastoplastic modeling of metal matrix composites containing randomly located and oriented spheroidal particles," *Journal of applied mechanics*, vol. 71, no. 6, pp. 774–785, 2004.
[184] M. M. Gasik, "Micromechanical modelling of functionally graded materials," *Computational Materials Science*, vol. 13, no. 1–3, pp. 42–55, 1998.
[185] H. M. Yin, L. Z. Sun, and G. H. Paulino, "Micromechanics-based elastic model for functionally graded materials with particle interactions," *Acta Materialia*, vol. 52, no. 12, pp. 3535–3543, 2004.
[186] G. H. Paulino, H. M. Yin, and L. Z. Sun, "Micromechanics-based interfacial debonding model for damage of functionally graded materials with particle interactions," *International Journal of Damage Mechanics*, vol. 15, no. 3, pp. 267–288, 2006.
[187] H. M. Yin, G. H. Paulino, W. G. Buttlar, and L. Z. Sun, "Effective thermal conductivity of functionally graded particulate nanocomposites with interfacial thermal resistance," *Journal of Applied Mechanics*, vol. 75, no. 5, p. 051113, 2008.
[188] S. P. Gurrum, J.-H. Zhao, and D. R. Edwards, "Inclusion interaction and effective material properties in a particle-filled composite material system," *J Mater Sci*, vol. 46, no. 1, pp. 101–107, Jan. 2011, doi: 10.1007/s10853-010-4844-2.
[189] G. Song, "Inclusion Based Boundary Element Method for Modeling and Simulation of Composite Materials," Ph.D., Columbia University, United States -- New York, 2017.
[190] F. Chen and H. Yin, "Fabrication and laboratory-based performance testing of a building-integrated photovoltaic-thermal roofing panel," *Applied Energy*, vol. 177, pp. 271–284, 2016.
[191] Lin Qiliang, Zhang Liangliang, Chen Fangliang, and Yin Huiming, "Micromechanics-Based Elastoplastic Modeling of Functionally Graded Materials with Pairwise Particle Interactions," *Journal of Engineering Mechanics*, vol. 145, no. 5, p. 04019033, May 2019, doi: 10.1061/(ASCE)EM.1943-7889.0001603.
[192] J. C. Simo and T. J. Hughes, *Computational inelasticity*, vol. 7. Springer Science & Business Media, 2006.
[193] J. Yang, S. M. Pickard, C. Cady, A. G. Evans, and R. Mehrabian, "The stress/strain behavior of aluminum matrix composites with discontinuous reinforcements," *Acta metallurgica et materialia*, vol. 39, no. 8, pp. 1863–1869, 1991.

[194] H. Tan, Y. Huang, C. Liu, and P. H. Geubelle, “The Mori–Tanaka method for composite materials with nonlinear interface debonding,” *International Journal of Plasticity*, vol. 21, no. 10, pp. 1890–1918, 2005.
[195] L. Brassart, H. M. Inglis, L. Delannay, I. Doghri, and P. H. Geubelle, “An extended Mori–Tanaka homogenization scheme for finite strain modeling of debonding in particle-reinforced elastomers,” *Computational materials science*, vol. 45, no. 3, pp. 611–616, 2009.
[196] G. Ayoub, F. Zaïri, M. Naït-Abdelaziz, and J. M. Gloaguen, “Modelling large deformation behaviour under loading–unloading of semicrystalline polymers: Application to a high density polyethylene,” *International Journal of Plasticity*, vol. 26, no. 3, pp. 329–347, Mar. 2010, doi: 10.1016/j.ijplas.2009.07.005.
[197] F. Barlat, D. J. Lege, and J. C. Brem, “A six-component yield function for anisotropic materials,” *International journal of plasticity*, vol. 7, no. 7, pp. 693–712, 1991.
[198] R. M. Cleveland and A. K. Ghosh, “Inelastic effects on springback in metals,” *International Journal of Plasticity*, vol. 18, no. 5–6, pp. 769–785, 2002.
[199] P. Chowdhury, H. Sehitoglu, H. J. Maier, and R. Rateick, “Strength prediction in NiCo alloys – The role of composition and nanotwins,” *International Journal of Plasticity*, vol. 79, pp. 237–258, Apr. 2016, doi: 10.1016/j.ijplas.2015.07.002.
[200] J. Samei, L. Zhou, J. Kang, and D. S. Wilkinson, “Microstructural analysis of ductility and fracture in fine-grained and ultrafine-grained vanadium-added DP1300 steels,” *International Journal of Plasticity*, 2018.
[201] L. Zhang, Q. Lin, F. Chen, and H. Yin, “Micromechanical modeling and experimental characterization for the elastoplastic behavior of a functionally graded material,” *International Journal of Plasticity*, 2018.
[202] T.-K. Nguyen, K. Sab, and G. Bonnet, “First-order shear deformation plate models for functionally graded materials,” *Composite Structures*, vol. 83, no. 1, pp. 25–36, Mar. 2008, doi: 10.1016/j.compstruct.2007.03.004.
[203] B. Mokhtar, A. Tounsi, and E. A. Adda-Bedia, “Buckling Response of Thick Functionally Graded Plates,” *Journal of Materials and Engineering Structures « JMES »*, vol. 1, no. 3, pp. 137–145, Nov. 2014.
[204] H.-T. Thai and D.-H. Choi, “Efficient higher-order shear deformation theories for bending and free vibration analyses of functionally graded plates,” *Arch Appl Mech*, vol. 83, no. 12, pp. 1755–1771, Dec. 2013, doi: 10.1007/s00419-013-0776-z.
[205] Z. Belabed, M. S. Ahmed Houari, A. Tounsi, S. R. Mahmoud, and O. Anwar Bég, “An efficient and simple higher order shear and normal deformation theory for functionally graded material (FGM) plates,” *Composites Part B: Engineering*, vol. 60, pp. 274–283, Apr. 2014, doi: 10.1016/j.compositesb.2013.12.057.
[206] S. M. Gunjal, R. B. Hajare, A. S. Sayyad, and M. D. Ghodle, “Buckling analysis of thick plates using refined trigonometric shear deformation theory,” *Journal of Materials and Engineering Structures « JMES »*, vol. 2, no. 4, pp. 159–167, Dec. 2015.
[207] S. Merdaci, A. Tounsi, M. S. A. Houari, I. Mechab, H. Hebali, and S. Benyoucef, “Two new refined shear displacement models for functionally graded sandwich plates,” *Arch Appl Mech*, vol. 81, no. 11, pp. 1507–1522, Nov. 2011, doi: 10.1007/s00419-010-0497-5.
[208] A. M. Zenkour, “A simple four-unknown refined theory for bending analysis of functionally graded plates,” *Applied Mathematical Modelling*, vol. 37, no. 20–21, pp. 9041–9051, Nov. 2013, doi: 10.1016/j.apm.2013.04.022.

[209] L. S. Ma and T. J. Wang, “Nonlinear bending and post-buckling of a functionally graded circular plate under mechanical and thermal loadings,” *International Journal of Solids and Structures*, vol. 40, no. 13–14, pp. 3311–3330, Jun. 2003, doi: 10.1016/S0020-7683(03)00118-5.
[210] S. Sahraee and A. R. Saidi, “Axisymmetric bending analysis of thick functionally graded circular plates using fourth-order shear deformation theory,” *European Journal of Mechanics - A/Solids*, vol. 28, no. 5, pp. 974–984, Sep. 2009, doi: 10.1016/j.euromechsol.2009.03.009.
[211] M. E. Golmakani and M. Kadkhodayan, “Nonlinear bending analysis of annular FGM plates using higher-order shear deformation plate theories,” *Composite Structures*, vol. 93, no. 2, pp. 973–982, Jan. 2011, doi: 10.1016/j.compstruct.2010.06.024.
[212] S. P. Lim, K. H. Lee, S. T. Chow, and N. R. Senthilnathan, “Linear and nonlinear bending of shear-deformable plates,” *Computers & Structures*, vol. 30, no. 4, pp. 945–952, 1988, doi: 10.1016/0045-7949(88)90132-0.
[213] W. Karunasena, C. M. Wang, S. Kitipornchai, and Y. Xiang, “Exact solutions for axisymmetric bending of continuous annular plates,” *Computers & Structures*, vol. 63, no. 3, pp. 455–464, May 1997, doi: 10.1016/S0045-7949(96)00328-8.
[214] A. H. Shahdadi and M. A. Hajabasi, “An analytical solution for free vibration analysis of circular plates in axisymmetric modes based on the two variables refined plate theory,” *J Mech Sci Technol*, vol. 28, no. 9, pp. 3449–3458, Sep. 2014, doi: 10.1007/s12206-014-0806-y.
[215] R. P. Shimpi, “Refined Plate Theory and Its Variants,” *AIAA Journal*, vol. 40, no. 1, pp. 137–146, 2002, doi: 10.2514/2.1622.
[216] R. P. Shimpi and H. G. Patel, “A two variable refined plate theory for orthotropic plate analysis,” *International Journal of Solids and Structures*, vol. 43, no. 22–23, pp. 6783–6799, Nov. 2006, doi: 10.1016/j.ijsolstr.2006.02.007.
[217] S.-E. Kim, H.-T. Thai, and J. Lee, “A two variable refined plate theory for laminated composite plates,” *Composite Structures*, vol. 89, no. 2, pp. 197–205, Jun. 2009, doi: 10.1016/j.compstruct.2008.07.017.
[218] S. Cheng, P. Qiao, F. Chen, W. Fan, and Z. Zhu, “Free vibration analysis of fiber-reinforced polymer honeycomb sandwich beams with a refined sandwich beam theory,” *Journal of Sandwich Structures and Materials*, p. 1099636215619841, Dec. 2015, doi: 10.1177/1099636215619841.
[219] Q. Lin, F. Chen, and H. Yin, “Experimental and theoretical investigation of the thermo-mechanical deformation of a functionally graded panel,” *Engineering Structures*, vol. 138, pp. 17–26, May 2017, doi: 10.1016/j.engstruct.2017.01.062.
[220] Chen Fangliang, Lin Qiliang, and Yin Huiming, “Thermo-Mechanical Behavior of a Novel Functionally Graded Material Panel,” *Earth and Space 2016*, pp. 847–857, doi: 10.1061/9780784479971.079.
[221] M. H. Sadd, *Elasticity, Third Edition: Theory, Applications, and Numerics*, 3 edition. Amsterdam ; Boston: Academic Press, 2014.
[222] I. Mechab, H. A. Atmane, A. Tounsi, H. A. Belhadj, and E. A. A. Bedia, “A two variable refined plate theory for the bending analysis of functionally graded plates,” *Acta Mech Sin*, vol. 26, no. 6, pp. 941–949, Sep. 2010, doi: 10.1007/s10409-010-0372-1.
[223] A. Benachour, H. D. Tahar, H. A. Atmane, A. Tounsi, and M. S. Ahmed, “A four variable

refined plate theory for free vibrations of functionally graded plates with arbitrary gradient," *Composites Part B: Engineering*, vol. 42, no. 6, pp. 1386–1394, Sep. 2011, doi: 10.1016/j.compositesb.2011.05.032.
[224] J. N. Reddy, *Theory and Analysis of Elastic Plates and Shells, Second Edition*. CRC Press, 2006.
[225] N. R. S. K. H. Lee, "Axisymmetric bending of thick circular plates," *Mechanics Research Communications*, vol. 17, no. 2, pp. 111–116, 1990, doi: 10.1016/0093-6413(90)90076-O.
[226] D. Champier, "Thermoelectric generators: A review of applications," *Energy Conversion and Management*, vol. 140, pp. 167–181, May 2017, doi: 10.1016/j.enconman.2017.02.070.
[227] D. Salerno, "Ultralow voltage energy harvester uses thermoelectric generator for battery-free wireless sensors," *Journal of Analog Innovation*, 2010.
[228] "Insight Into ESP32 Sleep Modes & Their Power Consumption," *Last Minute Engineers*, 23-Dec-2018. https://lastminuteengineers.com/esp32-sleep-modes-power-consumption/ (accessed Mar. 24, 2020).
[229] S. Sharma, K. K. Jain, and A. Sharma, "Solar Cells: In Research and Applications—A Review," *Materials Sciences and Applications*, vol. 6, no. 12, pp. 1145–1155, Dec. 2015, doi: 10.4236/msa.2015.612113.
[230] M. A. Green, "Thin-film solar cells: review of materials, technologies and commercial status," *J Mater Sci: Mater Electron*, vol. 18, no. 1, pp. 15–19, Oct. 2007, doi: 10.1007/s10854-007-9177-9.
[231] J. Yan and B. R. Saunders, "Third-generation solar cells: a review and comparison of polymer:fullerene, hybrid polymer and perovskite solar cells," *RSC Advances*, vol. 4, no. 82, pp. 43286–43314, 2014, doi: 10.1039/C4RA07064J.
[232] C. Peng, Y. Huang, and Z. Wu, "Building-integrated photovoltaics (BIPV) in architectural design in China," *Energy and Buildings*, vol. 43, no. 12, pp. 3592–3598, Dec. 2011, doi: 10.1016/j.enbuild.2011.09.032.
[233] M. S. Buker, B. Mempouo, and S. B. Riffat, "Experimental investigation of a building integrated photovoltaic/thermal roof collector combined with a liquid desiccant enhanced indirect evaporative cooling system," *Energy Conversion and Management*, vol. 101, pp. 239–254, Sep. 2015, doi: 10.1016/j.enconman.2015.05.026.
[234] V. Delisle and M. Kummert, "A novel approach to compare building-integrated photovoltaics/thermal air collectors to side-by-side PV modules and solar thermal collectors," *Solar Energy*, vol. 100, pp. 50–65, Feb. 2014, doi: 10.1016/j.solener.2013.09.040.
[235] P. K. Ng, N. Mithraratne, and H. W. Kua, "Energy analysis of semi-transparent BIPV in Singapore buildings," *Energy and Buildings*, vol. 66, pp. 274–281, Nov. 2013, doi: 10.1016/j.enbuild.2013.07.029.
[236] L. Lu and K. M. Law, "Overall energy performance of semi-transparent single-glazed photovoltaic (PV) window for a typical office in Hong Kong," *Renewable Energy*, vol. 49, pp. 250–254, Jan. 2013, doi: 10.1016/j.renene.2012.01.021.
[237] P. K. Ng and N. Mithraratne, "Lifetime performance of semi-transparent building-integrated photovoltaic (BIPV) glazing systems in the tropics," *Renewable and Sustainable Energy Reviews*, vol. 31, pp. 736–745, Mar. 2014, doi: 10.1016/j.rser.2013.12.044.
[238] J. Peng, D. C. Curcija, A. Thanachareonkit, E. S. Lee, H. Goudey, and S. E. Selkowitz, "Study on the overall energy performance of a novel c-Si based semitransparent solar

photovoltaic window," *Applied Energy*, vol. 242, pp. 854–872, May 2019, doi: 10.1016/j.apenergy.2019.03.107.
[239] B. Fina, H. Auer, and W. Friedl, "Profitability of active retrofitting of multi-apartment buildings: Building-attached/integrated photovoltaics with special consideration of different heating systems," *Energy and Buildings*, vol. 190, pp. 86–102, May 2019, doi: 10.1016/j.enbuild.2019.02.034.
[240] M. S. Karimi, F. Fazelpour, M. A. Rosen, and M. Shams, "Techno-economic feasibility of building attached photovoltaic systems for the various climatic conditions of Iran," *Environmental Progress & Sustainable Energy*, vol. 0, no. 0, p. e13239, doi: 10.1002/ep.13239.
[241] X. Wu *et al.*, "Monitoring the performance of the building attached photovoltaic (BAPV) system in Shanghai," *Energy and Buildings*, vol. 88, pp. 174–182, Feb. 2015, doi: 10.1016/j.enbuild.2014.11.073.
[242] H. Saini, R. C. G. M. Loonen, and J. L. M. Hensen, "Simulation-based performance prediction of an energy-harvesting facade system with selective daylight transmission," in *VIII International Congress on Architectural Envelopes*, 2018, pp. 213–219, Accessed: 14-Oct-2019. [Online]. Available: https://research.tue.nl/en/publications/simulation-based-performance-prediction-of-an-energy-harvesting-f-2.
[243] C. Koo, T. Hong, K. Jeong, C. Ban, and J. Oh, "Development of the smart photovoltaic system blind and its impact on net-zero energy solar buildings using technical-economic-political analyses," *ENERGY*, vol. 124, pp. 382–396, Jan. 2017, doi: 10.1016/j.energy.2017.02.088.
[244] "PowerFilm Solar OEM Components - Frequently Asked Questions | FlexSolarCells." http://www.flexsolarcells.co.uk/index_files/OEM_Components/PowerFilm-Solar-OEM-Components-FAQs.php (accessed Dec. 16, 2019).
[245] J. Mandal *et al.*, "Hierarchically porous polymer coatings for highly efficient passive daytime radiative cooling," *Science*, vol. 362, no. 6412, pp. 315–319, Oct. 2018, doi: 10.1126/science.aat9513.
[246] "Solar Energy and Solar Power in New York, NY," *Solar Energy Local*. https://www.solarenergylocal.com/states/new-york/new-york/ (accessed Dec. 28, 2019).
[247] "Solar Altitude Angle - an overview | ScienceDirect Topics." https://www.sciencedirect.com/topics/engineering/solar-altitude-angle (accessed Dec. 28, 2019).